AE3200 Design Synthesis Exercise

Final Report

Version 1.1

Pluto Orbiter, group 13

July 2018

Faculty of Aerospace Engineering

Delft University of Technology

Challenge the future

Page intentionally left blank.

Pluto Orbiter: Final Report

AE3200 Design Synthesis Exercise

Authors:	Badea, Andrei	4439767
	Barreiro, Filipe	4270053
	Daniel Noel, Alejandro	4456971
	Garrett, Geoffrey H.	4450973
	Houwink, Quint	4371232
	Kerstens, Fabio	4435796
	Turnock, Matthew	4430913
	van Beers, Eleonoor	4273427
	van Oorschot, Marijn	4439279
	Wiese, Joana	4342364

Principle Tutor:	Dr. Ir. Claudio Lettieri
Coaches:	Ir. Diana Olejnik
	Dr. Ir. Elisabetta Iorfida

Delft University of Technology

Acknowledgements

In front of you lies the final report of the Orpheus mission, a proposed orbiter mission to the Pluto-Charon system for the Design Synthesis Exercise of the Delft University of Technology. The team is grateful for receiving this unique research opportunity and would like to thank Dr. Ir Lettieri, Dr. Ir. Iorfida and Ir. Olejnik for their guidance and motivation throughout the project. Next, we would like to acknowledge teaching assistant Giacomo Acciarini for all his useful advice with respect to project management and systems engineering. As well as Dr. Ir. Castro for taking the time to help us with the preliminary structural design. For propulsion, the advice of Ir. Zandbergen and Dr. Ir. Cervone has been tremendously important for the final product. We would also like to thank Dr. DeBoy, the lead communications engineer of the New Horizons mission, for providing insight on how the spacecraft achieved its connection with Earth.

Group 13
A. Badea, F. Barreiro, A.D. Noel, G.H. Garrett, Q. Houwink, F. Kerstens, M. Turnock, E. van Beers, M. van Oorschot, J. Wiese

Executive Summary

This report covers the full preliminary design of a mission to orbit the Pluto-Charon system, including the planning of mission phases, determination of trajectories, and high-level concept selection. Additionally, main subsystems are sized: propulsion, communications, thermal control, attitude determination and control, command and data handling, payload and the main structure. The mission is found to be feasible within the provided constraints.

The assignment stipulates a few important constraints. The total mission duration shall be at most 25 years, the spacecraft must fit in a single launcher that has been used in other missions, and the gross cost is to be kept below USD 1.1 billion with a risk contingency of USD 0.3 billion. The main challenge of this mission, compared to previous spacecraft (New Horizons), is that Orpheus must orbit the Pluto Charon system for one year to fulfill the scientific objectives. Inserting the spacecraft into orbit from an interplanetary trajectory is found to be an extremely fuel-intensive manoeuvre, which demands an extensive search for optimal trajectories and multiple reiterations of the propulsion subsystem.

Trajectory to Pluto and Scientific Orbits

To design the interplanetary trajectory, a code is developed combining existing astrodynamics packages and newly developed modules. A genetic algorithm is used to optimise the launch date, sequence of gravity assists and propulsive manoeuvres for minimum fuel consumption. The analysis assumes impulsive thrust, therefore velocity changes occur instantly. This optimisation tool models the trajectory as a sequence of conic curves, commonly known as a patched conic approach. The results are verified using the mission analysis tool GMAT, freely distributed by NASA. GMAT simulates the spacecraft's path by integration of differential equations instead of patched conics, which are found using a Lambert solver. The former approach is orders of magnitude slower than the latter, therefore making it unsuitable for optimisation. Nonetheless, speed in GMAT is traded for a higher accuracy.

Hundreds of thousands of trajectories are analysed by the genetic algorithm, which evolved over time to select the sequences of manoeuvres that result in the most economical use of propellant. The use of the algorithm greatly reduced the computational time needed for this optimisation. The solution that is outputted has Orpheus depart Earth on *24th November 2027*, perform a gravity assist at Jupiter on *19th December 2029* and arrive at Pluto on *12th November 2051*. During these 24 years the spacecraft is inactive, with the exception of a burn during the gravity assist, minor trajectory adjustments along the way and a final 12.1-year-long burn of the ion engine to adjust the speed for the right arrival at Pluto. This low-thrust manoeuvre has not been included in the optimisation of the trajectory which assumes all burns to be impulsive, therefore further analysis is required to confirm the requirements are met. The complexity of this analysis is beyond the scope of the project, but an estimation is made on the impact on the travel time, which may increase by approximately one year. The complete mission phasing is shown in Figure 1.

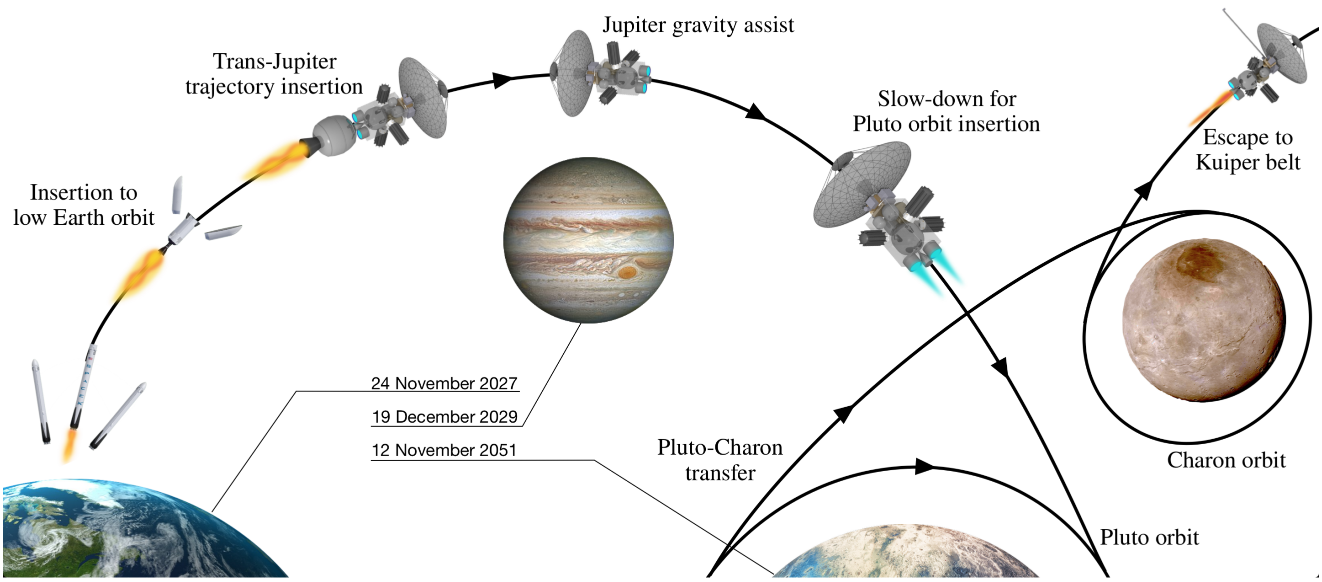

Figure 1: Overview of the Orpheus mission phases.

A thorough study is performed on the scientific orbits around Pluto and Charon. For each of the five Keplerian parameters that define the orbits, their effects on different mission aspects are studied to conclude with appropriate value ranges. These are used as inputs to GMAT for verification and final selection. The chosen orbits cover 98%

of Pluto's surface and 93% of Charon's, take only 15 days to map all visible areas with an overlap between groundtracks of 40%, have contact with Earth 100% of the time, and develop very small decay and precession over a period of 6 months which are corrected using a few short engine burns. The transfer from Pluto to Charon is also studied both analytically and numerically, linking its fuel usage to the choice of eccentricities for the two scientific orbits.

The spacecraft stays in the Pluto-Charon system for a total of one year, of which six months are spent on either Pluto or Charon. After this period, an escape burn is executed in order to enter an heliocentric trajectory. This serves two purposes: to prevent potential contamination of the planetary system and to explore other bodies of interest in the Kuiper belt.

Table 1 collects all the velocity increments (ΔV) for transitioning from different phases of the trajectory and for navigation and correction manoeuvres. This is used as input for designing the propulsion subsystem and sizing the propellant tanks. The ΔV to be provided by deep space manoeuvres, in total 7600 m/s, is by far the largest seen in history; the highest deep-space ΔV to date has been 1700 m/s, accomplished by Voyager 1 [25].

Table 1: Orpheus ΔV mission overview.

#	Manoeuvre	ΔV [m/s]	#	Manoeuvre	ΔV [m/s]
1	Interplanetary transfer (launcher)	4870	7	Pluto orbit & attitude control	12
2	Interplanetary transfer (kick stage)	1877	8	Charon transfer orbit injection	217
3	Earth-Jupiter transfer corrections	100	9	Pluto-Charon transfer corrections	20
4	Jupiter-Pluto transfer corrections	110	10	Charon insertion & circularising	167
5	Pluto insertion	6446	11	Charon orbit & attitude control	142
6	Pluto science orbit circularising	255	12	End of life disposal	131
	Total launch ΔV		: 6747 m/s		
	Total bi-propellant ΔV		: 770 m/s		
	Total mono-propellant ΔV		: 174 m/s		
	Total electric propellant ΔV		: 6656 m/s		
	Total mission ΔV		**: 14380 m/s**		

Propulsion

Given the extreme ΔV requirements for the Orpheus mission, the propulsion system design comprises a hybrid chemical-electric design. The electric stage consists of two NASA NEXT ion thrusters [54], each capable of providing a steady-state thrust of 26 mN at a specific impulse of 1410 s. The NEXT is the latest technology ion engine, which allows for multi-year long impulse duration. As 761 kg of xenon propellant is consumed for the slowdown, a substantial shift in centre of gravity is expected. Therefore, both NEXT thrusters are equipped with a thrust vector control mechanism, capable of steering the engine over a range of ±15° [54]. The ion propulsion system is used for manoeuvre 3 to 5 in Table 1.

As for the chaotic nature of Pluto and Charon, together with the short orbital period around both bodies, a high impulse chemical bi-propellant propulsion system is used for more short duration high thrust manoeuvring. The selected system is the Aerojet AMBR [38], which is the most efficient state-of-the-art storable space propulsion system, having a specific impulse of 333 s at a thrust of 623 N. The AMBR uses MON-3 and hydrazine propellants with a helium pressurant, and operates in a pressure-fed cycle. Helium leakage throughout the 25 year-long mission is no more than 5 L. Both commercial off-the-shelf propellant tanks are operated at a pressure of 20 bar, which allows for a MON-3 pressure drop of 2.1 bar and hydrazine pressure drop of 2.4 bar respectively. The bi-propellant system is reignited four times, for manoeuvres 6, 8, 10 and 12 in Table 1.

Orpheus is launched using the three-stage SpaceX Falcon Heavy in its expandable mode. To achieve sufficient ΔV to establish the Earth-Jupiter-Pluto transfer sequence, the Star 48B kick stage is used, which acts as a fourth stage of the launcher. The kick stage is fired directly after shutdown and separation of the third stage of the Falcon Heavy. An overview of the mission is depicted in Figure 1.

Other Spacecraft Subsystems

In the leg between Earth and Jupiter Orpheus is in hibernation for 2 years, throughout which it is spin-stabilised. The second 21 year-long leg is compromised of a full and partial hibernation, given the NEXT thruster is fired in the last 12.1 years of the journey. Here the spacecraft is spin-stabilised too by the attitude control system. Fine control of the attitude is obtained from four reaction wheels with an angular accuracy of 0.1 deg. For momentum dumping and spin/despin of the spacecraft, twelve 20 N hydrazine mono-propellant thrusters are used. This system operates in a blowdown configuration with a blowdown ratio of 3.27. Attitude determination is achieved using 2 fine sun sensors, a spinning sun sensor, 2 inertial measurement units and 2 star trackers, with a determination accuracy of 0.1 deg.

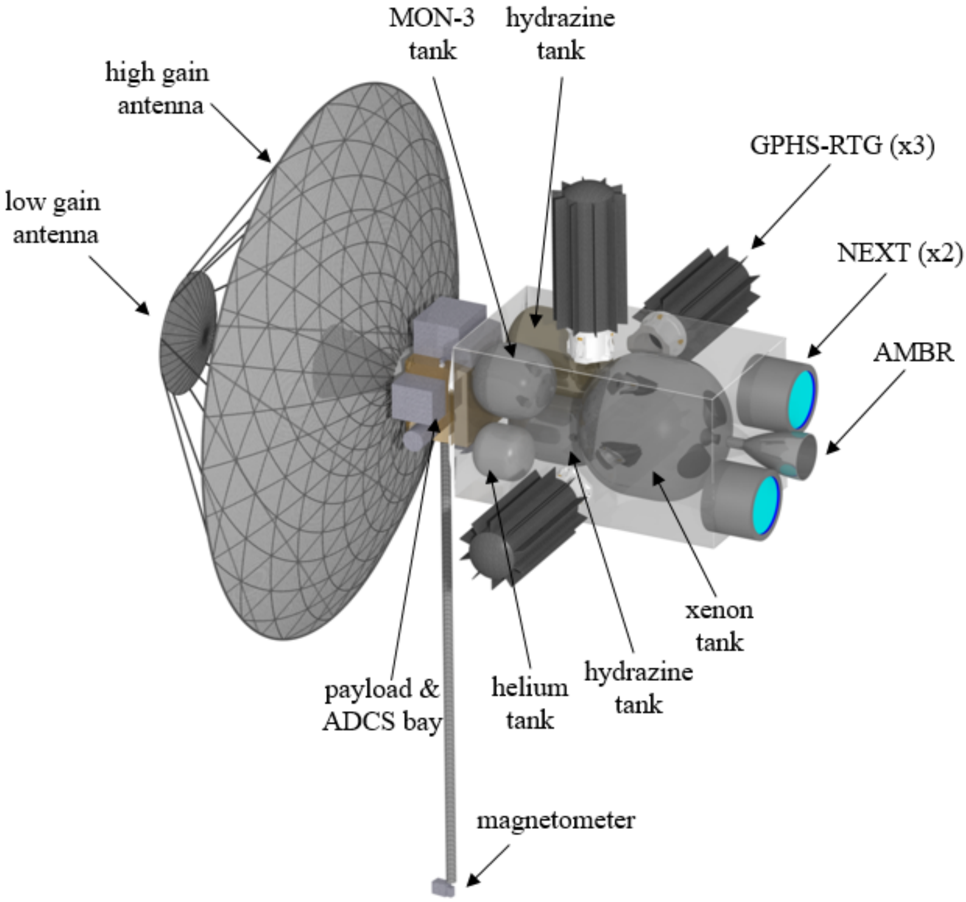

Figure 2: Overview of the Orpheus orbiter with most important elements labelled.

To power Orpheus, three United States General Purpose Heat Source Radioisotropic Thermoelectric Generators (GPHS-RTGs) are used, which rely on the decay of the isotope Plutonium-238 for power generation. At begin of life, these RTGs produce 900 W of electric power, from which 671 W is left at Pluto insertion.

All components in the spacecraft are kept at a temperature between -20 and 20 °C, by the thermal control system. This is achieved by a 34 m^2 skin of multi-layer insulation in combination with ten 0.16 m^2 louvers. Components that are very temperature sensitive, like the propellant tanks, are locally heated to above the freezing point using cartridge heaters and thermistors.

To transmit and receive data, a 4.5 m diameter carbon fibre high gain antenna is used, which allows for a data rate of 5.3 kbps at 43.6 AU (maximum expected distance during the mission). For redundancy a low gain 0.5 m diameter antenna is used that achieves a data rate of 22 bps. Command and data handling of the Orpheus spacecraft is achieved with the RUAG Next Generation computer [129], which has a storage of 2 × 50 GB and a processing memory of 537 MB. The computer runs on the Nucleus RTOS operating system.

The structure of Orpheus uses a combination between carbon fibre and aluminium 7075 T66, making it very lightweight (120 kg). The key design stress for the acceleration of the rocket is for carbon fibre in shear, which has a safety margin of 27%. Buckling is resisted with a safety margin of 7.8, meaning the structure can handle an acceleration 7.8 times larger than obtained from the Falcon Heavy. The lateral vibration mode is 10.6 Hz, which is 0.6 Hz higher than expected from the Falcon Heavy. The axial vibration mode yields 40.6 Hz which is significantly larger than the design minimum of 25 Hz from the launch manual.

To map at least 70% the surface of Pluto and Charon a ultra-violet, infra-red and visible light spectrometer are used. Additionally, the solar wind at Pluto is measured, as well as energetic particles. The radio science and gravity experiments determines the harmonics of the Pluto-Charon system. Lastly, for the first time in history, the magnetic field of Pluto is studied using a magnetometer. The 4 m long boom on which this sensor is attached has a lateral frequency of 13 Hz and longitudinal frequency greater than 25 Hz. An overview of important spacecraft components is shown in Figure 2.

The mass allocation for the different spacecraft components is shown in Table 2.

Table 2: Orpheus mass budget.

Dry mass contribution	Without margin	Margin	Total
Structure & Mechanisms	120 kg	20%	144 kg
Thermal Control	40 kg	10%	44 kg
Communications	32 kg	17.9%	38 kg
Command & Data Handling	7 kg	5%	7 kg
Attitude Determination and Control	14 kg	5%	14 kg
Propulsion	206 kg	7.8%	222 kg
Power source	168 kg	5%	176 kg
Power Management & Distribution	43 kg	20%	51 kg
Payload	36 kg	5%	37 kg
Others	5 kg	20%	6 kg
Total dry mass (excl. adapter)	669 kg		740 kg
System margin		20%	134 kg
Total dry mass with margin (excl. adapter)			874 kg

Wet mass contribution	Total
Xenon propellant	761 kg
Hydrazine propellant	243 kg
MON-3 propellant	133 kg
Helium pressurant	2 kg
Total wet mass (excl. adapter)	2013 kg
Kick stage	2134 kg
Adaptor mass (incl. separation mech.)	363 kg
Launch mass (incl. adapter)	**4510 kg**

Systems Engineering

As it is customary for space missions and any large scale project in general, a considerable part of the effort has also been directed in project management and systems engineering practices. Here, for all margins, European ESA standards have been adopted.

A statistical study is performed on several aspects of the mission. The results on reliability reveal an estimated 80% chance of successful operation after 25 years, which is comparable to that of the Cassini mission [37]. The availability is estimated at 20%. This is due to the 15 years of hibernation time and 12 years of electric engine operation, which leave insufficient power (< 10%) for continuous communication. Safety considerations have led to the establishment of the driving requirement to implement redundancy for the critical subsystems when this is a feasible within constraints. The long operation time also has called for the proposal of a maintenance procedure to periodically detect and correct anomalies.

A sustainability strategy has been drafted with the aim of abiding by international laws on the sustainable exploration of Space. This provides guidelines for the design of subsystems, trajectory planning and operations so as to avoid generating unnecessary pollution and protecting the pristine conditions of the planetary systems being approached during the mission.

After the detailed technical study presented in this work, the compliance with the complete list of requirements is assessed. The vast majority of requirements are met, with a few that are unknown to be fulfilled. There are no unmet requirements.

A high level cost breakdown of the USD 1.1 billion reserved for the mission is shown in Table 3. All individual total costs displayed readily include a margin (5-20%).

Table 3: Orpheus cost budget.

Contribution	Total Cost [million USD]
Spacecraft incl. integration, assembly and tests	586.9
Launch vehicle	157.5
Ground command and control	12.0
Systems engineering, project management & project assurance	25.2
Flight support operations & service	12.2
Aerospace ground equipment	18.0
Operations	188.4
10% system level margin	100.0
Total	**1100**

A study on risk is also performed on the development and production of the spacecraft as well as its operation. The most likely or catastrophic risks are identified, following with a proposal of mitigation strategies for those risks which pose the highest vulnerabilities. Approximately 130 events are included in the analysis.

List of Abbreviations

ADCS	Attitude Determination and Control Subsystem
AOP	Argument Of Periapsis
AU	Astronomical Unit
BOL	Begin Of Life
CG	Centre of Gravity
CP	Centre of Pressure
CBE	Current Best Estimate
C&DH	Command and Data Handling
CFRP	Carbon Fibre Reinforced Polymer
COI	Charon Orbit Injection
COM	Charon Orbit Maintenance
COPUOS	Committee on the Peaceful Uses of Outer Space (UN)
COPV	Composite Overwrapped Pressure Vessel
COTS	Commercial Off The Shelve
CSP	Constraint Satisfaction Problem
CV	Check Valve
DARE	Delft Aerospace Rocket Engineering
DHS	Data Handling System
DSN	Deep Space Network
DSE	Design Synthesis Exercise
DSS	Deep Space Simple
DSSS	Deep Space Simple (Short)
ECSS	European Cooperation for Space Standardisation
EJP	Earth Jupiter Pluto
EMC	Elastic Memory Composite
EOL	End Of Life
EPO	Earth-Parking Orbit
EPMD	Electrical Power Management Device
EPS	Electrical Power System
EPA	Energetic Particle Analyser
ESA	European Space Agency
ESTEC	European Space Research and Technology Centre
F	Filter
FDV	Fill/Drain Valve
FEM	Finite Element Method
FM	Flight Model
FOV	Field of View
GA	Genetic Algorithm
GHe	Gaseous Helium
GN_2	Gaseous Nitrogen
GMAT	General Mission Analysis Tool (NASA)
GPHS	General Purpose Heat Source
HDRM	Hold Down and Release Mechanism
HRC	High Resolution Camera
HW	Hardware
ICE	Integrated Concurrent Engineering
ICRF	International Celestial Reference Frame
IFOV	Instantaneous Field Of View
IMU	Inertial Measurement Unit
Inst.	Instrument
IPA	Isoprophylic Alcohol
IR	Infrared
IOT	In-orbit Testing
JD	Julian Date
JGA	Jupiter Gravity Assist
JPL	Jet Propulsion Laboratory (USA)
LEOP	Launch and Early Orbit Phase
LV	Latch Valve
LVA	Launch Vehicle Adaptor
MLI	Multi-Layer Insulation
MEOP	Mean Operating Pressure
MMH	Monomethylhydrazine, $CH_3(NH)NH_2$
MMRTG	Multi-Mission Radioisotope Thermoelectric Generator
MMOI	Mass Moment of Inertia
MON	Mixed Oxides of Nitrogen
NASA	National Aeronautics and Space Administration (USA)
NEXT	NASA Evolutionary Xenon Thruster
NC	Normally Closed
NO	Normally Open
N&T	Navigation & Targeting
NTO	Dinitrogen Tetroxide, N_2O_4
O	Orifice
O/F	Oxidiser to Fuel
ONS	On-board Navigation System
PCU	Power Control Unit
PDU	Power Distribution Unit
PL	Payload
PMD	Propellant Management Device
POM	Pluto Orbit Maintenance
PR	Pressure Regulator
PS	Pressure Sensor
PV	Pyrotechnic Valve
RAMS	Reliability, Availability, Maintainability and Safety
RCT	Reaction Control Thruster
RTG	Radioisotope Thermoelectric Generator
RW	Reaction Wheel
RWA	Reaction Wheel Array
S/C	Spacecraft
SCC	Standard Cubic Centimetre
SCCS	Standard Cubic Centimetre per Second
SOI	Sphere Of Influence
STEM	Storable Tubular Extendible Member
SIM	System Insertion Manoeuvre
SWI	Solar Wind Instrument
SW	Software
SWOT	Strengths, Weaknesses, Opportunities and Threats
TC	Thermocouple
TCM	Trajectory Correction Manoeuvre
Temp.	Temperature
TOF	Time Of Flight
TOI	Transfer Orbit Injection
TRL	Technology Readiness Level
UDMH	Unsymmetrical Dimethylhydrazine, $H_2NN(CH_3)_2$
UN	United Nations
USA	United States of America
UV	Ultra Violet
VL	Visible Light

List of Symbols

$\alpha_{1/2}$	$[deg]$	Signal half power beamwidth
γ	[°]	Precession angle
Δ	[-]	Wall roughness
$\bar{\Delta}$	[-]	Relative roughness
ΔP	[-]	Pressure drop
ΔV	[-]	Velocity increment
$\Delta V_{insertion}$	[-]	Velocity increment for insertion into a system
η	[-]	Antenna efficiency
θ	[deg]	Maximum deviation angle z-axis from local vertical
θ	[rad]	True Anomaly (only in chapter 7)
λ	[-]	Friction coefficient
λ_{Re}	[-]	Friction coeffient for a smooth pipe
λ_s	$[m]$	Signal wavelength
$\lambda_{1/2}$	$[m]$	Half life
μ	$[Nkg^{-2}m^2]$	Standard gravitational parameter (only in chapter 7 and chapter 15)
μ	$[Pa \cdot s]$	Dynamic viscosity (only in chapter 10)
ν	$[m^3/kg]$	Specific volume
ρ	[-]	Density
Φ	$[W\dot{m}^{-}2]$	Solar constant
ψ	$[rad]$	Swath angle
σ	[Pa]	Normal stress
σ_{bend}	[Pa]	Bending stress
σ_{tot}	[Pa]	Total stress
σ_{yield}	[Pa]	Yield stress
φ	[°]	Sun incidence angle
Ω	$[rad]$	Longitude of ascending node
ω	$[rad/s]$	Angular velocity
ω	$[rad]$	Argument of Perigee (only in chapter 7)
$\dot{\omega}$	$[rad/s^2]$	Angular acceleration
$\dot{m}$	[-]	Mass flow rate
ζ	[-]	Coefficient of fluid resistance

A	[m^2]	Area
$\AA$	[-]	Ångström, unit of length equal to 10^{-10} m
B	[-]	Blowdown ratio
D	$[m]$	Diameter
E	[Pa]	Young's modulus
F	$[N]$	Thrust (only in chapter 10)
F	$[rad]$	Mean hyperbolic anomaly (only in chapter 7)
H	[-]	Heliocentric
I	[-]	Moment of inertia
J	[-]	Jupiter-centric
L	$[m]$	Length
M	$[kg]$	Mass of larger body
OR	$[m]$	Orbit radius
P	$[Pa]$	Total pressure
Pu	$[Pa]$	Ullage pressure
Q	$[m^3/s]$	Volume flow rate
Q_h	$[J]$	Heat
R	$[J/K/kg]$	Specific gas constant
R_{orb}	$[km]$	Orbital radius
S	$[m]$	Maximum distance from Earth to Pluto during mission
$\mathbb{T}$	[-]	Rotation matrix
T	$[Nm]$	Torque
Tu	$[K]$	Ullage temperature
U	$[J]$	Internal energy
V_∞	[-]	Hyperbolic excess velocity
W	$[J]$	Work
VX	[-]	X component of velocity vector
VY	[-]	Y component of velocity vector
VZ	[-]	Z component of velocity vector
X	[-]	X component of position vector
Y	[-]	Y component of position vector
Z	[-]	Z component of position vector
a	[m]	Semi-major axis
c	$[m/s]$	Speed of light
c_p	$[J/K]$	Specific heat at constant pressure
cm	$[m]$	Centre of mass
cps	$[m]$	Centre of solar pressure
e	[-]	Eccentricity
f	$[GHz]$	Signal frequency
h	$[m]$	Altitude
i	[$^\circ$]	Inclination
k	$[J/K]$	Boltzmann constant
m	$[kg]$	Mass
m_{body}	$[kg]$	Mass of smaller body
q	[-]	Reflectance factor
r	$[m]$	Radius
s	[-]	Safety Factor
t	[s]	Time
v	$[m^3]$	Volume
A_s	$[m^2]$	Sunlit surface area
C_3	$[km^2/s^2]$	Characteristic energy
E_b/N_0	$[dB]$	Signal power to noise ratio
e_t	$[deg]$	Pointing accuracy
F_{dump}	$[N]$	Force to dump momentum
$f_{nat,lat}$	[Hz]	Natural lateral frequency
$f_{nat,lng}$	[Hz]	Natural longitudinal frequency
F_{thrust}	[N]	Thruster force
g_0	$[m/s^2]$	Gravitational acceleration at sea level
g_y	$[m/s^2]$	Acceleration in y-direction
g_z	$[m/s^2]$	Acceleration in z-direction
G_r	$[dB]$	Receiving antenna gain
G_t	$[dB]$	Transmitting antenna gain
h_p, lim	[km]	Lower limit of altitude
H_{rw}	$[Nms]$	angular momentum of reaction wheel
I_{sp}	$[s]$	Specific impulse
I_x	$[kgm^2]$	Mass moment of inertia over the x-axis
I_y	$[kgm^2]$	Mass moment of Inertia around y-axis
I_z	$[kgm^2]$	Mass moment of Inertia around z-axis
L_a	$[dB]$	Atmospheric loss
L_{pr}	$[dB]$	Pointing accuracy loss
L_r	$[dB]$	Overall system loss
L_s	$[dB]$	Space loss factor
M_h	$[rad]$	Mean hyperbolic motion
P^{He}	$[Pa]$	Helium propellant tank pressure
P_0	$[W]$	Initial power
P_t	$[W]$	Transmitted Power
P^V	$[Pa]$	Vapour pressure
R_0	$[mm]$	Bend radius
R_d	$[bps]$	Data rate
R_h	$[m]$	Pipe bend radius
R_{pl}	[km]	Planet radius
R_t	[m]	Distance of thruster to centre of gravity
R_{SOI}	[-]	Sphere If Influence radius
Re	$[-]$	Reynolds number
R_{outer}	$[m]$	Outer diameter
$r_{p,lim}$	$[km]$	Lower limit of periapsis radius
t_{dump}	$[s]$	time until momentum dump
t_i	$[s]$	Impulse duration
t_p	$[t]$	Time since passage of periapsis
T_c	$[K]$	Critical point
T_g	$[Nm]$	Gravity gradient disturbance torque
T_s	$[Nm]$	Solar radiation pressure disturbance torque
T_sys	$[K]$	System temperature
T_{tr}	$[K]$	Triple point
$\omega_{rw,max}$	$[rad/s^2]$	Maximum angular velocity of reaction wheel
$\omega_{rw,\dot{torque}}$	$[rad/s^2]$	Angular acceleration of reaction wheel due to disturbance torque

List of Subscripts

b	Branch pipeline (tee fitting)
c	Centre pipeline (tee fitting)
E	Earth
f	Fuel
o	Oxidiser
p	Pressurant (only in chapter 10)
p	Periapsis (only in chapter 7)
hyp	Hyperbolic
cap	Capture
P	Pluto
C	Charon
$char$	Property of Charon with respect to Pluto
esc	Escape
$target$	Relevant target orbit
J	Jupiter

List of Figures

List of Tables

Contents

1 Introduction

On January 19^{th} 2006, NASA's New Horizons spacecraft was launched. Travelling all the way to Pluto, its journey has almost been 32 times the distance between the Earth and the Sun. Being the first and, for now, the only spacecraft that has observed Pluto from close proximity, many facts about the Pluto-Charon system were revealed. Questions, such as whether Pluto and Charon have a magnetic field or what the origin of Pluto's internal oceans is, remain open. This leads to the need for a more extensive research mission to the Pluto-Charon system.

The American Institute of Aeronautics and Astronautics (AIAA) has set up a student design competition for undergraduate students to design a mission to this system [1]. This design challenge is accepted by the team and will be performed during the TU Delft spring Design Synthesis Exercise (DSE) 2018. The mission statement for this project is the following:

"Orbit the Pluto-Charon system to gather scientific data to unveil the secrets of this system, whilst extending humanity's capabilities of exploring the outer layers of the solar system."

The proposed mission is assumed to be a joint venture between NASA and ESA.

In line with the mission statement the name *Orpheus* is chosen for the spacecraft. It refers to the legendary musician who attempted to retrieve his wife from the underworld, where he encounters the god of the underworld, Pluto, and his ferryman, Charon.

The purpose of this report is to present the final design of the Orpheus spacecraft, with a detailed explanation on subsystem design choices and the systems' compliance with the requirements.
Firstly, Chapter 2 presents the overall mission concept and requirements that need to be fulfilled. Secondly, a market analysis is done in Chapter 3, where strengths and weaknesses of the current space market are assessed. Then, Chapter 4 provides the approach to the reliability, availability, maintainability and safety of the design, which is used throughout Orpheus' subsystems. Chapter 5 lists the general sustainability strategies used, as well as guidelines to keep space sustainable. After that, Chapter 6 elaborates in detailed the payload design for Orpheus, followed by Chapter 7 which explains the target orbit analysis and the interplanetary trajectory. A functional mission analysis of Orpheus' way to Pluto can be found in Chapter 8. Chapter 9 to Chapter 14 present each subsystem designs in detail. To conclude, the designs with the choice of launcher and kick stage are presented in Chapter 15, after which the structure of the entire spacecraft is described and analysed in Chapter 16. The system is finalised by elaborating on the cost, mass, power and ΔV budget in Chapter 17 and providing a system compliance analysis in Chapter 18. System Engineering aspects like the operations and logistics, the risks for the Orpheus mission as well as the further project design and development logic are explained in Chapters 19, 20 and 21, respectively. Lastly, overall conclusions and recommendations for the mission are given in Chapter 22.

[1] https://www.aiaa.org/2018UndergradTeamSpaceTransportation%E2%80%93PlutoOrbiter/ (April 25 2018)

2 Mission Description

Pluto, the infamous dwarf planet, orbits the sun in the far outer regions of the solar system. When the New Horizons spacecraft flew by in 2015, scientists were, for the first time, able to study the surface and atmosphere of both Pluto and Charon. However, far more can be revealed by going back. In this chapter, the Orpheus mission and its objectives are explained, a mission concept is presented.

2.1 Project and Mission Objectives

The findings of the New Horizons spacecraft gave scientists a detailed snapshot of the Pluto-Charon system. However, only one side of Pluto and Charon have been imaged during New Horizons' high-speed encounter, and other characteristics such as a magnetic field and core composition have yet to be determined [66]. The Pluto-Charon system still holds much information that is yet to be discovered. The main objective of this project is to propose an orbital exploration mission to the Pluto-Charon system by means of a spacecraft with the nominal instrument load of New Horizons.

From the project objective stem the mission objectives described in Table 2.1. These determine what the scientific goals are at Pluto and Charon. Group 1 (required) are objectives that must be met for the mission to be considered a success. If Group 2 (highly desired) objectives are not met, the mission is considered only a partial success. For Group 3 objectives (desired) no hardware is added, and are fulfilled when convenient with the chosen payload.

Table 2.1: Summary of scientific mission objectives.

Group	Identifier	Objective
Required	1.1	Map the geological surface composition of Pluto-Charon system.
	1.2	Determine gravitational harmonics of the Pluto-Charon system.
Highly desired	2.1	Characterise Pluto-Charon system magnetosphere.
	2.2	Determine time variability of Pluto's surface and atmosphere.
	2.3	Map the surface topography of Pluto and Charon bodies.
	2.4	Investigate the thermal properties (albedos, surface temperature) of Pluto and Charon.
Desired	3.1	Determine sub-surface compounds, density distribution and structure.
	3.2	Perform interplanetary observations not directly related to the Pluto-Charon system.
	3.3	Take measurements supplementary to those already made by New Horizons.

2.2 Requirements

User requirements are imposed on the mission, described in Table 2.2. These are the requirements that play the most instrumental role in the design process, and shape the mission from beginning to end. Requirements `R-MIS-070` and `R-MIS-090`, however, are killer requirements. They are adjusted accordingly, after deliberation with the project tutor and coaches, to the requirements in the second section of the table.

Table 2.2: Summary of scientific mission objectives

Identifier	Description
R-MIS-010	The exploration mission shall be an orbital exploration of the Pluto-Charon system.
R-MIS-020	The vehicle shall orbit the Pluto-Charon system for a minimum of one year.
R-MIS-030	The selected in-space propulsion system shall have TRL 6 or above.
R-MIS-040	The total launch mass of the Pluto orbiter mission (including in-space propulsion subsystem) shall not exceed the launching capability of the selected rocket.
R-MIS-050	The proposed exploration mission architecture and time-line is constrained by a single launch of a vehicle chosen by the team.
R-MIS-060	The minimum nominal instrumentation load shall be 401 kg.
~~R-MIS-070~~	The duration of the mission shall be no more than 15 years.
R-MIS-080	The selected launch vehicle shall have TRL 9.
~~R-MIS-090~~	The overall budget shall not exceed USD 700 million (2018).
R-MIS-071	The duration of the mission shall be no more than 25 years.
R-MIS-091	The overall budget shall not exceed USD 1.1 billion (2018) with a risk of no more than USD 300 million (2018).

2.3 Mission Concept

Although there have been probes that have reached the edges of our solar system ([43] [58] [89] [98] [37]), never has there been an orbiter mission farther than Saturn. To give an indication of the sheer distance Orpheus has to cross, Pluto lies approximately four and a half times as far from Earth as Saturn. The challenge of the mission, together with the requirements stated in Table 2.2 shapes the possible mission designs.

A selection of five concepts is first made. To determine which is most fitting, each concept is assessed in terms of characteristics that stem from the user requirements: potential scientific data, total cost, propulsion feasibility, Technology Readiness Level (TRL), and development time.

From the five proposed concepts, an orbiter is chosen as the most fitting proposal to explore the Pluto-Charon system. The main drivers for the choice are the TRL, cost, and propulsion feasibility. The high velocities needed to reach the Pluto-Charon system, as well as the deceleration needed to be captured into orbit within 25 years, presents a challenge for the propulsion subsystem [16]. The thermal system also has to account for the cold conditions, and the communication system has to be able to send the data back to Earth. These factors, coupled with the long mission duration of 25 years, push the mission proposal into territory that is at the forefront of what is technologically possible.

3 Market Analysis

Throughout the advancement of the mission, salient points with regard to market position and stakeholders involved in the project should be to maintain the scientific popularity of space exploration missions, and secure a constructive and positive relation with governmental bodies involved in the mission funding, as shown in the stakeholder map in Figure 3.1.

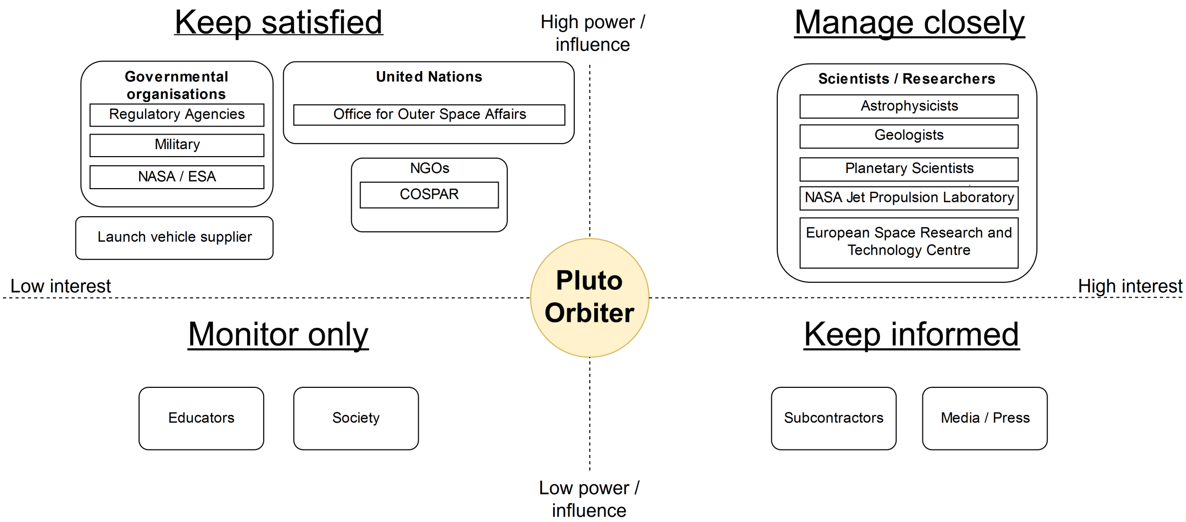

Figure 3.1: Stakeholder map of the Orpheus mission.

Furthermore, the Orpheus mission will have provide information for the "monitor only" and "keep informed" stakeholder groups for educational and informational purposes in order to help with the development of society while keeping the interest in deep space exploration high.

Scientists are a very important stakeholder for Orpheus, as they give the mission its goals. These need to be managed closely, as not fulfilling the demands of the scientific community would defeat the purpose of the whole operation.

An overview of the current space (exploration) market gives insight into the opportunities and challenges that the execution of the mission can encounter. A summarising overview of the market analysis is shown in Table 3.1 by means of a SWOT analysis: strengths, weaknesses, opportunities, and threats [81]. First, the internal market analysis is addressed by identifying the strengths and weaknesses. Next, the external market analysis is done by describing the opportunities and threats within the current market.

Table 3.1: SWOT analysis on the Orpheus mission in the current space market.

SWOT	
Strengths	Weaknesses
Revolutionary display of newest technologies Will supply scientifically valuable information about the Pluto-Charon system. 67% of the propellant is considered environmentally sustainable	Mission does not directly return any financial investment. Power system is not considered environmentally sustainable.
Opportunities	Threats
Can give a boost to outer space exploration missions popularity and development. Market has shown interest in future exploration of Pluto Can reopen debate or more funding for RTG development.	Privatising of the market focuses on profitable space projects. There is limited availability of resources. Unpredictable how public and political opinions will form coming 25 years.

To begin with, the power system is not considered to be environmentally sustainable, caused by the fact that the mission requires three Radioisotope Thermoelectric Generators (RTGs) to be used to ensure enough energy capacity. This is considered a weakness. Additionally, the limited availability of resources such as the absence of enough Plutonium-238 poses a major threat. Currently, NASA's Radioisotope power systems program aims to produce 400 grams per year by 2019, and increasing this rate to 1,500 grams per year by 2025 [51]. Nevertheless, about 67% of the propellant is considered environmentally sustainable, as xenon is used in an ion engine system.

Furthermore, the mission does not produce any direct return on financial investment, and is fully funded by governmental institutions. As the threats already indicate, the current market is shifting towards the privatisation of the space market [152]. These kind of companies will merely focus on profitable projects, and for now closer to Earth [26]. The lack of interest by private companies results in complete governmental dependency for receiving a green light for mission execution. Although current political views upon space travel can be identified properly, it is always unpredictable how political and public view will unfold over the duration of the mission. Timing and public opinion can be key once Orpheus reaches the Pluto-Charon system, and can greatly affect how the scientific progress details are received by the media and the public.

However, if the mission is carried out successfully, a possibility exists that the debate about RTG development policies can be revisited. This could give a huge boost to the possibilities of new (deep) space exploration, and can also encourage development of more space exploration mission proposals. Showing the scientific benefit of these types of missions is a crucial step, which is why the success of the mission is key for establishing a positive public and scientific opinion towards space exploration. As ESA ESTEC readily issued various proposals for mission to the Pluto-Charon system [123][132][10], the scientific community is assumed to be enthusiastic for more space exploration projects of similar scope.

4 RAMS Characteristics

Reliability, availability, maintainability and safety, or in short RAMS, are the fundamental elements for a successful mission. Before all the subsystems are fully designed and analysed, a general approach is presented for the integration of systems engineering into the mission design.

4.1 Reliability

In the midterm report, a method is presented for estimating the best and worst-case reliability of the spacecraft over the mission duration [27]. This estimation has been updated to the current mission plan, as visible in Figure 4.1. When entering hibernation, the degradation rate of the reliability becomes smaller, however, increases once the burn for slowing down is initiated. This is due to the fact that less wear out occurs of all the systems on-board.In the final year, when orbiting around the Pluto-Charon system, the reliability decreases by 4.7% for the best case and 6.9% for the worst case scenario. Fortunately, the best-case reliability after 25 years remains above 80%. Cassini, a mission comprising of 3 RTGs and a duration of 19 years, had a probability of failure of 6.7% median (4.2-11% range) for the planned 13 years [62]. Comparing these results to the graph at the same time, the Cassini mission ends up close to the upper limit of the reliability range. It should be redeemed possible for the current mission to stay close to the upper limit as well, under the condition that adequate measurements are taken to ensure the reliability rate.

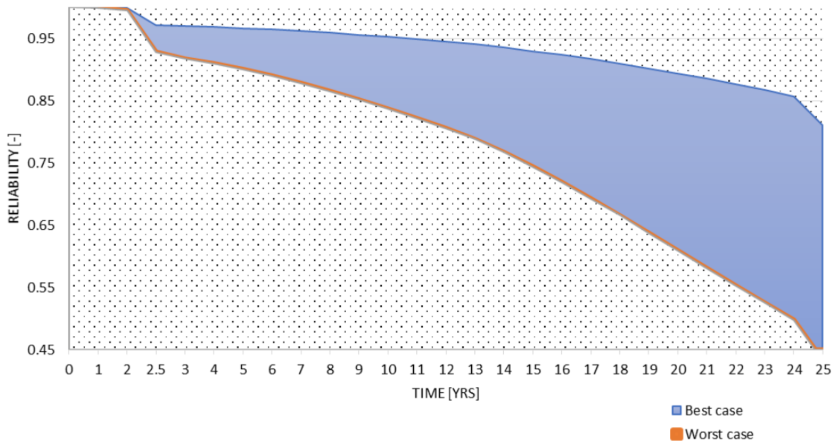

Figure 4.1: Reliability curve for the Orpheus mission.

Next to a total reliability estimation, an analysis of the most critical subsystems is made. Before being able to increase the reliability of the spacecraft, the most critical subsystem components need to be identified. Tafazoli presents the most critical components per subsystem that have been reported to cause most failures [135].

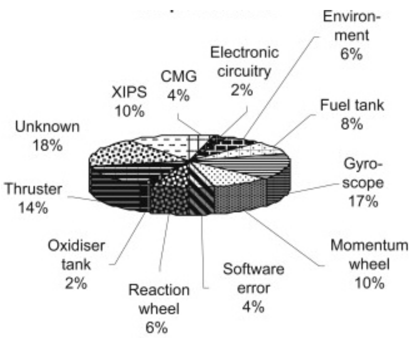

(a) ADCS.

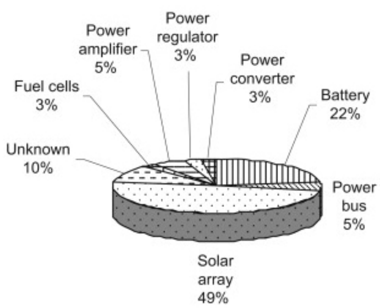

(b) Power.

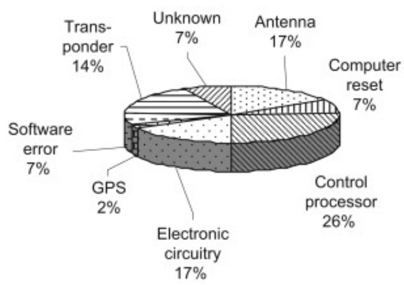

(c) Communications & C&DH.

Figure 4.2: Satellite failures (1980 - 2005) [135].

Note that the system described by Tafazoli [135] is applied to a spacecraft with a solar array for power source. As the current design is expected to use RTGs as a power source, the failure rate of the power source component could deviate from what is displayed in the figure. Proper handling of the power source will be key of increasing power subsystem reliability.

Additional to the systems described above, an identification of system failure of liquid propulsion has been identified. From Gill [79], it is known the most common failures for liquid-fuelled propulsion relevant for Orpheus are fuel feed and control (15%), oxidiser feed and control (7.5%), pressurisation (10%) and electrical control (8.3%). From this failures percentages the conclusion can be drawn that a high reliability of the feed and control of the fuel and the oxidiser, is critical for the reliability of the propulsion subsystem.

Figure 4.3 describes two possible methods for ensuring redundancy integration in a system. The first, conventional system redundancy ensures a second lifeline should the first malfunction. However, partitioned redundancy interlinks the second lifeline with the first one. Therefore, when parts of the first line malfunction, only those parts are taken over by the second lifeline. Therefore, multiple paths are possible for proper system functioning, opposed to only two. This method will be implemented into subsystem designing as much as possible.

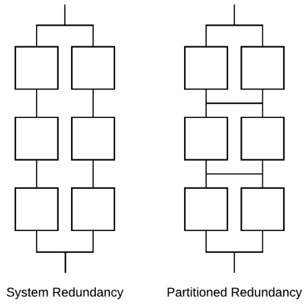

Figure 4.3: System redundancy methods [148].

Based on Figure 4.2, the most critical safety functions can be identified, listed below. If the failure of the component will result in mission failure, redundancy must always be applied in the design. If the failure of the component will result in mission degradation however, redundancy appliance is not a requirement, but highly desired.

- Antenna
- Battery
- On-board computer
- Control processor
- Payload instruments
- RTGs
- Thrusters
- Reaction wheels
- Electronic circuit
- Structure
- Propulsion control
- Pressurisation

4.2 Maintainability

As described in earlier maintenance proposals in the midterm report [27], subsystem specific duty cycles are used for spacecraft maintenance. The maintenance increases reliability and availability of the system, according to Tai et.al. [30] and Koutras et.al. [96]. Table 4.1 presents an overview of both scheduled and non-scheduled maintenance activities during the mission.

Table 4.1: Overview of Scheduled maintenance activities

Scheduled	
(Sub)sytem	Activitiy
Software	Software maintenance procedure
Hardware	Hardware maintenance procedure during assembly
Electrical system	Periodical electrical signalling
Non-scheduled	
(Sub)system	Activitiy
Main spacecraft	Autonomous hibernation software implementation hibernation
Main spacecraft	Autonomous hibernation software implementation burn mode
Communication	Connectivity check after mode switch
Command & Data Handling	System reboot
Software	Software update

The software maintenance procedure diagram is presented in Figure 4.4. When any software failures are found during the scheduled check-up, the measures as described in the flowchart are taken. When the software failures keep occurring, the ground control team should decide for the proper further actions to solve software problems.

The hardware maintenance procedure during assembly assures that the spacecraft will be stored and assembled in an open area, allowing high accessibility to all components [28]. As a result, storage is optimised and potential need for repair or replacement of parts can be readily performed.

Including a high degree of autonomy for the software regulation of the spacecraft is not only necessary due to the long communication distance, but also to ensure maintainability when in hibernation.

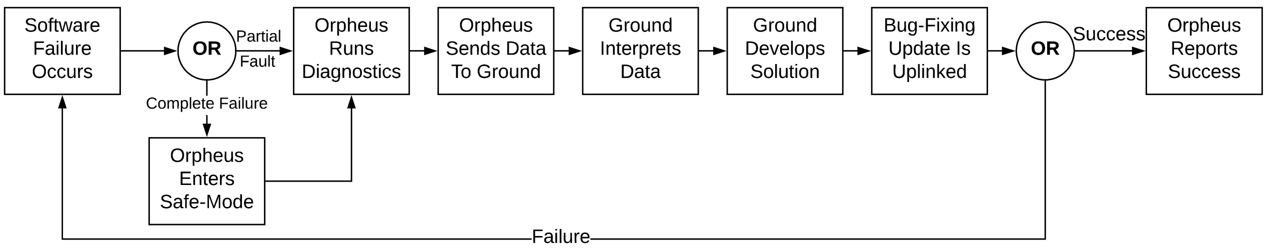

Figure 4.4: Software maintenance procedure [27]

4.3 Availability

Availability is the result of reliability and maintainability, and indicates the degree that a system will be ready or available when required [61]. Therefore, hibernation is not taken into account during the analysis. However, the burn should be taken into account. As well as the reliability estimation, the availability is updated as well. The availability estimation is given in Equation 4.1.

$$\text{Availability} = 1 - \frac{\text{Downtime}}{\text{Downtime} + \text{Uptime}} \tag{4.1}$$

Downtime is defined as the time when contact is desired/needed, but not possible. The uptime is the time when there is actual contact possible with the spacecraft. Subtracting the total hibernation time from the mission duration leaves 15 years, of which 12 are during the burn of the ion engine, calculated in chapter 10. As the ion engine requires over 90% of the power budget, proper communication with the spacecraft is not feasible, as seen in the power budget in chapter 17. Occasional system and trajectory check-ups are possible using the secondary communications system, however, is of little duration and therefore neglected in the computation. The downtime will thus be estimated to be 12 years.

During the final year of the mission, the spacecraft is orbiting the Pluto-Charon in a pre-calculated orbit. Therefore it is possible to select an orbit where communication is always possible and there is no occultation. The details of the orbit and the calculations can be found in section 7.3. During the two years preceding the hibernation the spacecraft is also assumed to be fully available, as it is still in the same plane as Earth. From this results an availability of 20%. Due to the low degree of availability, the spacecraft should be implemented with proper autonomy during hibernation and the ion engine burning phase.

4.4 Safety

Within this section, a general philosophy on implementing safety measurements is presented, and risks are identified that should be taken into account when making design choices. Final system sizing allows for inspecting not only the global, but also the subsystem reliability factors.

Throughout the design phase the main design philosophies are applied, as listed below:

- No single point of failure shall cause failure of the mission.
- Redundancy shall be applied wherever possible within the capacities of the mission.
- Margins should be applied accordingly to the expected reliability of a component.

These design philosophies have been implemented during the concurrent engineering design phase of the mission. The subsystem design chapters display the specific application per subsystem.

As safety is identified as the freedom from hazards to humans and equipment [61], the most safety-critical phase of the mission will be during launch. As the launcher is not designed by the design team, but merely selected amongst currently available launchers, a safety needs to be taken into account during selection.

Ensuring proper safety measurements will be elaborated on more thoroughly in chapter 20. There, the main critical functions per subsystem are discussed and risks mitigation possibilities are presented. A desired outcome of the risk analysis will be to maintain a reliability factor of the best-case scenario.

5 Sustainability Strategy

To make a space mission as sustainable as possible it is essential to have efficient sustainability strategies. The following chapter will provide an overview of strategies that are implemented in the Orpheus mission.

From the sustainability model introduced by Brennan et al. [12] the social, the techno-economical and the ecological facets of a product are harmonised. Once all three components are met a product can be considered to be sustainable. The Orpheus mission shall implement all three factors by the following goals.

Goal 1: Eco-centric concerns of waste and resources
With a large number of subcontractors, sustainability shall be traced down to the lowest supplier and monitored continuously by an assigned party.

- The majority of contracts shall meet and exceed federal mandates for acquiring products that are energy efficient, water efficient, bio-based, environmentally preferable, non-ozone depleting, recycled content or are non-toxic or less toxic alternatives.
- The delivered product shall meet or exceed environmental protection labels.
- Supply chain emissions shall be reduced by building on good communication in the company as well as setting intensive reduction targets (reducing emission per product).
- Used and faulty components shall be disposed responsibly at allocated locations, such as electric waste.

Goal 2: Techno-centric concerns towards design solutions
Innovative solutions that provide the most scientific value with the available resources shall be implemented in the following ways.

- New and innovative solutions that could lead to improved systems shall be received with an open mind.
- Proposals shall be subjected to a thorough and peer reviewed selection process.
- The engineers of the project shall develop their skills and knowledge continuously.

Goal 3: Socio-centric concerns encompassing academic opportunities and involvement
To enhance academic involvement in the project and keep society informed about latest discoveries, listed activities shall be done.

- Universities shall be involved in the design of the mission.
- A symposium shall be hosted to share results with the scientific community.
- Scientific data and related tools shall be open source.
- The Lambert-solver toolkit shall be made available for public use.

5.1 Keeping Space Sustainable

The following subsection explain how the Orpheus mission is keeping outer space sustainable by following certain guidelines. Each subsystem shall be designed such that the entire spacecraft and therefore the mission follows these guidelines. Especially a thorough analysis of the Earth Parking Orbit as well as a sufficient number of redundancies is needed in the design to comply with the rules.

According to the United Nations Committee on the Peaceful Uses of Outer Space (UN COPUOS), the Orpheus mission must follow the policy imposed by the Committee of Space Research [23]. This policy focuses on protecting celestial bodies from contamination.

Orpheus is considered to be a Category II mission, which means that the Pluto-Charon System is of large interest with respect to the process of chemical evolution and origin of life. Hence, the mission-specifics need to be analysed in detail to prevent sub-surface liquid contamination. Following the policy, an EOL ΔV of 125 m/s is required to place Orpheus into a heliocentric orbit, preventing planetary contamination of the Pluto-Charon system (discussed further in subsection 7.4.2.

The following measures are based on the planetary protection requirements as outlined by Debus[23].

- During assembly special care shall be taken to prevent contamination, this includes but is not limited to clean-room assembly and organic material control.
- Unplanned impact with Pluto or Charon shall be determined and recorded.
- A planetary protection plan shall be written and shall include:
    1. Brief description of the mission;
    2. Report of contamination prevention measures;
    3. Update of contamination prevention measures after launch;
    4. Update of planetary protection measures at start of operational phase;
    5. End of life report stating on the extend to which planetary protection requirements were met.

Besides protecting the celestial bodies from contamination, space debris shall be mitigated. The Orpheus mission shall follow the Space Debris Mitigation Guidelines imposed by the UN COPUOS [108]. The most important ones that apply to the proposed mission are listed below.

- Guideline 1: Limit debris release during normal operations.
- Guideline 2: Minimise potential break-ups during operational phase.
- Guideline 3: Limit the probability of accidental collision in orbit.
- Guideline 5: Minimise potential post-mission break-ups resulting from stored energy.

6 Payload

The following chapter presents the detailed design of the scientific payload carried by Orpheus. Seven instruments are chosen and their characteristics described. After establishing the subsystem's requirements from the payload on other systems, the spacecraft design, as well as the orbit design, is found to be sensitive to a change in payload. Lastly, verification and validation methods are discussed.

6.1 Payload Requirements

To confirm the payload choices made during the trade-off phase in the Midterm Report [27], it is determined throughout the chapter whether the instruments comply with the payload requirements shown in Table 6.1.

The following abbreviations are used throughout this chapter:

- UV: ultraviolet
- IR: infrared
- VL: visible light
- HRC: high resolution camera
- SWI: solar wind instrument
- MAG: magnetometer
- EPA: energetic particle analyser

Table 6.1: The payload requirements.

Identifier	Description	Traceability
R-PLD-010	The payload shall fit inside the spacecraft structure where necessary.	R-SYS-130
R-PLD-020	The payload mass shall be a maximum of 40 kg.	R-MIS-060
R-PLD-030	The payload shall be in use for a minimum of 1 year after reaching Pluto.	R-MIS-020
R-PLD-040	The payload shall contain a gravity experiment.	Goal 1.2
R-PLD-050	The payload shall contain a magnetometer.	R-SCI-080, R-SCI-090
R-PLD-060	The payload shall contain a radio science experiment.	R-SCI-100, R-SCI-110
R-PLD-070	The payload shall contain a visible and infrared imager/spectrometer.	R-SCI-030, R-SCI-040
R-PLD-080	The payload shall contain an ultraviolet imaging spectrometer.	R-SCI-010, R-SCI-020, R-SCI-160, R-SCI-170
R-PLD-090	The payload shall contain a telescopic camera.	R-SCI-050, R-SCI-060
R-PLD-100	The payload shall contain a solar wind and plasma spectrometer.	R-SCI-100, R-SCI-110
R-PLD-110	The payload shall not exceed a total costs of USD 21 million (2018).	R-MIS-091
R-PLD-120	The payload shall be functional for the duration of the entire mission.	R-MIS-020
R-PLD-130	The payload shall utilise a 0.8 code rate for data storage.	

6.2 System Characteristics

The characteristics of the instruments chosen for Orpheus can be found in Table 6.2. It should be noted, that each instrument is an exact copy of the one used on-board the associated spacecraft. For the total mass and power consumption of the payload, a 5% margin is added, according to ESA standards [76]. All instruments, with exception of the high resolution camera, are placed externally (on the outside of the spacecraft). The payload integration with the other spacecraft subsystems is shown in Figure 6.1.

Table 6.2: The payload aboard Orpheus.

Instrument	Spacecraft	Mass [kg]	Power [W]	Dimensions [cm]	Location on S/C	Source
UV spectrometer	LRO	6.1	4.5	55 x 16 x 12	External	[41]
IR and VL imaging spectrometer	New Horizons	10.7	6.7	49.5 x 40.6 x 29.5	External	[147]
Solar wind instrument	ACE	3.7	3.1	36 x 24 x 30	External	[35]
Energetic particle analyser	New Horizons	1.4	2.3	20 x 15 x 22	External	[147]
High resolution camera	New Horizons	8.6	5.1	23 (diameter) x 63	Internal	[147]
Radio science & gravity experiment	Bepicolombo	3.5	15.0	–	External	[93] [125]
Magnetometer	Messenger	1.5	2.0	sensor: 8.1 x 4.8 x 4.6 electronics: 13.0 x 10.4 x 8.6	External	[60] [9]
Total	—	35.5	38.7			
Total + 5% margin	—	37	41			

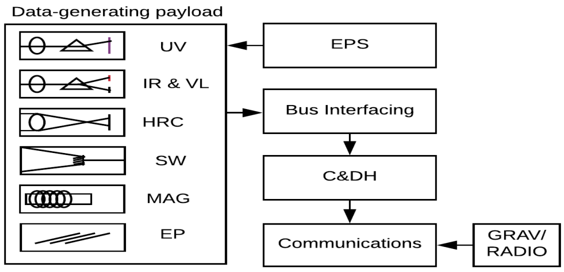

Figure 6.1: The payload architecture

In science mode, (mode 3 explained in Section 17.3), the total power consumed by the spacecraft is estimated to be 242.3 W, which is much below the maximum available power of 670 W provided by the RTGs. A duty cycle is therefore not necessary. However, the time variability instruments (solar wind instrument and energetic particle analyser) are switched on for 30 min, every hour for one Plutonian or Charonian day (153 hours) as specified by requirements `R-SCI-100` and `R-SCI-110`. This cycle is repeated every two Earth weeks. Therefore, Figure 6.2 displays the operations of each instrument for the 15 days that it takes to map 70% of Pluto or Charon.

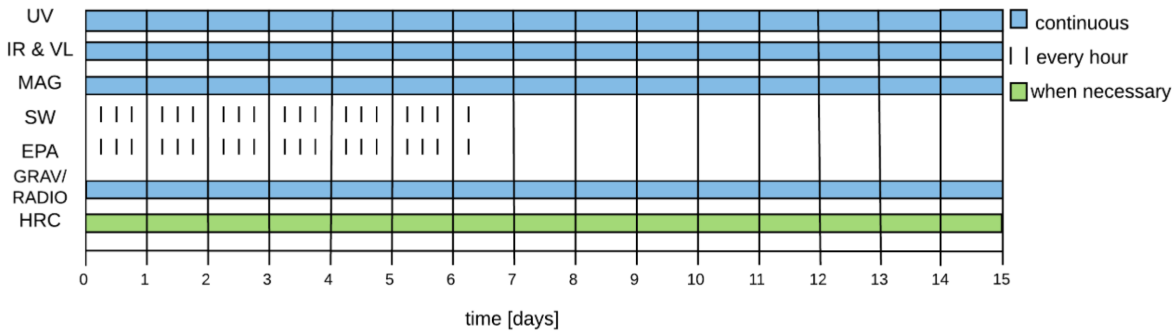

Figure 6.2: Payload duty cycle for Pluto and Charon.

The payload as presented here imposes several subsystem requirements on other spacecraft systems, such as the thermal control system as well as the power subsystem. All of these requirements, and whether they are met, can be found in the compliance matrix in section 18.2. The overall amount of data to be stored during the mission is about 63 Gbits.

6.3 Sensitivity of the Spacecraft w.r.t. Payload

The mission success is related to the payload, as the scientific data gathered by the instruments are the reason for the mission. Therefore if an instrument fails, it can jeopardize the mission. Figure 6.3 displays which mission goals, listed in Table 2.1, are still met when an instrument is taken out (a white box shows the objective is not met anymore). It can be seen that the infrared & visible light imaging spectrometer, the gravity/radio experiment and the magnetometer are critical to mission success. Figure 6.4 presents what percentage of scientific requirements are not met, should one instrument be taken out. The infrared & visible light imaging spectrometer is the most critical instrument. As no redundant instruments will be taken on the mission, it is critical that single points of failure are avoided within the instruments electronics to ensure complete mission success. For instance, additional small heaters are included in each instrument.

An increase in mass of the payload increases the total dry mass of the spacecraft by the same amount and with this the propellant needed. This leads to a higher cost of the mission. Any changes in the power consumption of the payload are negligible, as the total power budget for the spacecraft always lies below the 670 W the RTGs produce after the ion thruster burn as stated in Section 17.3.

Next to this, changes in volume of the payload affect the moment of inertia of the spacecraft, in turn affecting the ADCS subsystem. The spacecraft is designed to have equal moments of inertia about two of its axis in order to make the spin stabilisation simple. The magnetometer shall therefore only be deployed when in orbit around Pluto, as it would drastically change the moment of inertia and make it more difficult to spin stabilise the spacecraft during the hibernation phases.

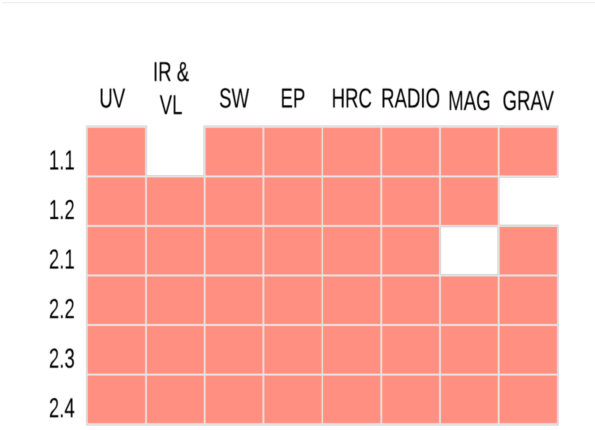

Figure 6.3: Mission objectives not met when an instrument is omitted.

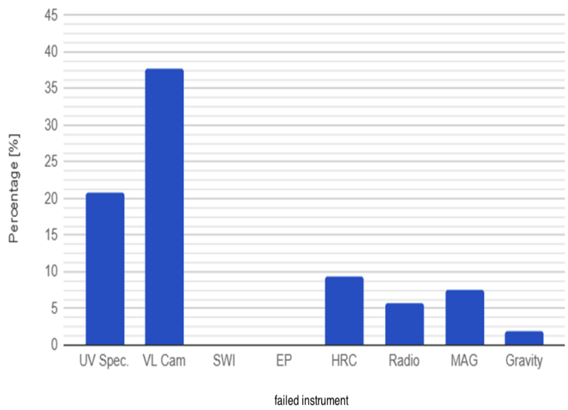

Figure 6.4: Percentage of non-met requirements per omitted instrument.

Concluding from the analysis above, the spacecraft as well as the entire mission is sensitive to certain changes in the payload. For instance, the success of the mission and fulfilment of scientific requirements is determined by how well the payload performs and how reliable it is. Therefore, in case of an instrument failure, the mission is considered unsuccessful.

6.4 Payload Verification and Validation

First of all, the payload also has to abide by the system requirements stated in the Baseline Report [28]. Each selected instrument is checked on whether it meets, for instance, the required range, resolution and accuracy. In addition to that, the instruments used by the New Horizons spacecraft are validated by similarity, since they have proven functional in Pluto's environment. Besides this, it is important for the mission success that the chosen payload meets all the previously stated requirements in Table 6.1.

Requirements `R-PLD-010` is verified, by placing most of the instrument on the outside of the spacecraft and designing the structure in a way that it is able to holds the necessary payload inside. This is further verified in section 16.2. This can however only be validated, when the entire system is assembled and ready to be launched.

From the system characteristics is it shown that the weight of the total payload is 37 kg (including a 5% margin), which complies with requirement `R-PLD-030`. Exact verification is done by determining the weight of each instrument by inspection of the instruments [80].

`R-PLD-040`, the operation of the payload for 1 year in orbit can be verified by a Monte-Carlo Simulation, under which all possible events of failures are randomly modelled and it is analysed how likely it is for the payload to comply with the requirement. Validation of the performance is only done once the spacecraft is actually in orbit around Pluto and operated according to plan.

`R-PLD-050` to `R-PLD-100` are met as can be seen from Table 6.2. During assembly of the spacecraft it can be inspected if all instruments are actually on-board the spacecraft, verifying the design.

Besides this, a vibration test shall be performed to ensure the instruments survive the high launch loads. This verifies the space segment requirement `R-SYS-120`. The instruments are already validated by experience, since all of them have flown on previous missions by the time Orpheus is launched.

To ensure the cost budget for the payload is met, inspection is done. The cost of all instruments needs to comply with `R-PLD-110`. `R-PLD-120` can only be verified by means of simulation. Same as mentioned for `R-PLD-040`, a Monte Carlo Simulation is done to predict the possibility of failure. The code rate requirement `R-PLD-130` can be verified through inspection as well, since the instruments are bought off the shelf.

In addition to the already proposed verification methods, tests in a thermal vacuum chamber, like the Phenix Thermal Vacuum Chamber used by ESA, are performed to show that the payload is able to operate in the required temperature ranges in vacuum [1]. In addition, it is necessary to make sure that the payload does not interfere with other systems of the spacecraft, Orpheus shall be tested for its electromagnetic compatibility ones assembled. This can be done in the Maxwell Test Chamber at ESA ESTEC in Noordwijk shown in Figure 6.5

[1] http://www.esa.int/Our_Activities/Space_Engineering_Technology/Test_centre/Phenix_Thermal_Vacuum_Chamber (June 2018)

[48]. This test is particularly important for the functionality of the magnetometer and its interference with the entire spacecraft.

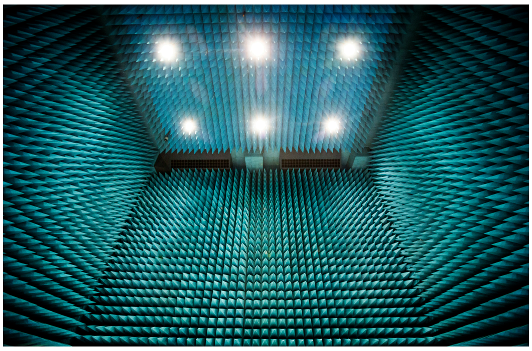

Figure 6.5: Maxwell Test Chamber at ESA [48].

Since the payload does not include any redundancy, it has a higher risk of failing than other systems. A failure in payload would make the mission unsuccessful as discussed in the sensitivity analysis above. However, since payload is considered to have a low failure rate, as shown in Chapter 4, it is unlikely that the mission fails due to an instrument's malfunction.

To make sure that the instruments comply with the sustainability strategies proposed in Chapter 5, organic cleaning methods shall be implemented when integrating the payload. In addition to that, parts shall be kept sterile by means of biocleaning with isoprophylic alcohol (IPA). With the presented payload, Goal 3 of the general sustainability strategies in Chapter 5 is can be fulfilled and the scientific data are used to enable further research of the Pluto-Charon System.

7 Mission Analysis

The journey to the Pluto-Charon system may be split in three main phases, namely: launching to Earth orbit, travelling to the proximity of Pluto and attaining the specific orbits for gathering and sending scientific data. In section 7.2 the reference frames for the rest of the section are introduced. In section 7.3 a study is done on the effect of the choice of orbital parameters at Pluto and Charon. In section 7.4 the target orbits are selected. A toolkit is developed in section 7.6 for the design of the trajectory from Earth to Pluto-Charon that uses genetic optimisation of gravity assists and impulsive manoeuvres for minimum fuel consumption. Finally, all the calculations performed in section 7.6 are verified in section 7.7.

7.1 The Method Of Patched Conics

Throughout the analysis conducted in this section, the method of patched conics is used to model the trajectory of the spacecraft through interplanetary space. A Keplerian (or two-body) orbit can be considered as a conic section with its focus at the attracting body. Due to the vast distances between planets and the sun in the solar system, the planet, and indeed its Sphere Of Influence (SOI), can be considered an infinitesimal point in the heliocentric frame; therefore the spacecraft can be considered to follow an unperturbed Keplerian orbit around the sun when the spacecraft is outside the SOI of a planet [86]. However, unlike in the heliocentric frame, the planet's SOI appears very large in the planet's reference frame, and can be considered to extend to infinity [86].

The SOI radius (r_{SOI}) can be calculated for any body with mass m_{body} at an orbital radius R_{orb} around a larger body of mass M using Equation 7.1. For example the SOI radius of the Earth is only 0.006AU, showing that a planet's SOI can indeed be considered infinitesimal in the heliocentric frame.

$$r_{SOI} = R_{orb} \left(\frac{m_{body}}{M}\right)^{2/5} \tag{7.1}$$

In order to analyse an interplanetary trajectory from planet 1 to planet 2, it is first necessary to determine the heliocentric trajectory (for example a Hohmann transfer could be used) intersecting the planets in their respective orbits (and therefore the SOI). At the SOIs, the heliocentric velocities determined by the transfer orbit can be used to determine the planet-centric velocities, and therefore the departure trajectory at planet 1 and the arrival trajectory at planet 2. It is in this way that we patch the 3 orbital conics, centred at the sun and the 2 planets.

7.2 Coordinate Systems

The multiple coordinate systems used for the distinct phases of the mission are defined in this section. These are split into those used within the Pluto-Charon system and those used for the interplanetary trajectory. When an epoch is associated to a vector it is often indicated in Julian date (JD). This is a standard date system in many packages that provide ephemerides (the position of astronomical objects in space and time).

7.2.1 Reference Frames within the Pluto-Charon System

This section defines five coordinate systems used during the orbit analysis in the Pluto-Charon system.

- The first system F_{orbit}, defined by $\boldsymbol{p}$ and $\boldsymbol{q}$ on the orbit plane as shown in Figure 7.1, facilitates the determination of the position along the orbit (true anomaly θ and radius r_{sc}).
- The second coordinate system F_{3d}, shown in Figure 7.2, has the x-axis pointing towards Charon's centre at epoch 1st January 2000 12:00:00.000 (JD 2451545.0), the z-axis pointing normal to Charon's orbit plane at that same epoch and the y-axis completing a right-handed orthonormal basis. It is used to compute the position of the spacecraft in 3 dimensions and for easy visualisation within the Pluto-Charon system. The angles indicate the argument of periapsis (ω), the inclination (i) and the longitude of the ascending node (Ω).
- The third reference F_{J2000} is the one adopted by the Jet Propulsion Laboratory (JPL) for all of their Solar System ephemerides: the J2000 standard, centred at Earth with the x-axis pointing towards mean equinox and the y-axis rotated 90° East about the mean equator at the same epoch that is chosen for F_{3d} [21].
- The last two reference frames are F_P and F_C, with F_P shown in Figure 7.3. They have the same orientation as F_{J2000} but are centred at Pluto and at Charon, respectively.

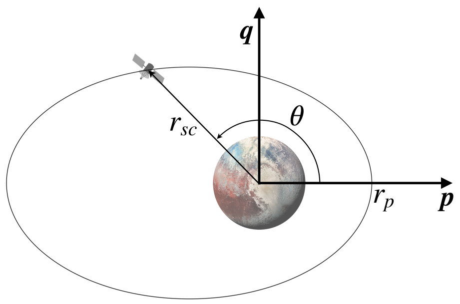

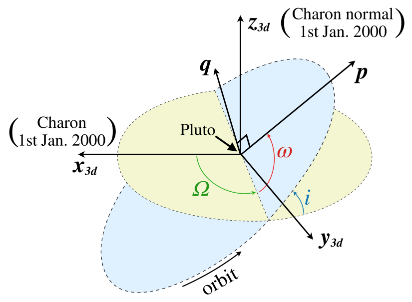

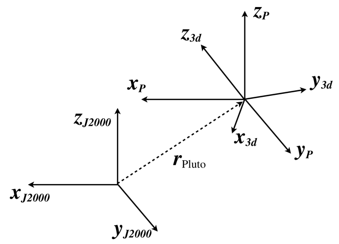

Figure 7.1: Orbital plane ref. system. Figure 7.2: 3D orbit ref. system Figure 7.3: J2000 ref. system.

The transformation from F_{orbit} to F_{3d} is done through three consecutive rotations ω, i, Ω and input coordinates $[p \;\; q \;\; 0]^T$. The transformation matrix $\mathbb{T}_{3d\leftarrow\text{orbit}}$ is shown in Equation 7.2.

$$\mathbb{T}_{3d\leftarrow\text{orbit}} = \mathbb{T}_z(\omega)\mathbb{T}_x(i)\mathbb{T}_z(\Omega) = \begin{bmatrix} \cos\omega & \sin\omega & 0 \\ -\sin\omega & \cos\omega & 0 \\ 0 & 0 & 1 \end{bmatrix} \begin{bmatrix} 1 & 0 & 0 \\ 0 & \cos i & \sin i \\ 0 & -\sin i & \cos i \end{bmatrix} \begin{bmatrix} \cos\Omega & \sin\Omega & 0 \\ -\sin\Omega & \cos\Omega & 0 \\ 0 & 0 & 1 \end{bmatrix} \tag{7.2}$$

For transforming from F_{3d} to F_P or F_C, first the basis vectors $\boldsymbol{x}_{3d}$, $\boldsymbol{y}_{3d}$ and $\boldsymbol{z}_{3d}$ are computed in F_{J2000} ($\hat{\boldsymbol{x}}|_{3d}^{J2000}$, $\hat{\boldsymbol{y}}|_{3d}^{J2000}$ and $\hat{\boldsymbol{z}}|_{3d}^{J2000}$) using Equations 7.3, 7.4 and 7.5. These employ the ephemerides by JPL (with `Python` module `jplephem`), which provide the positions of Pluto ($\boldsymbol{r}_{\text{Pluto}}$) and Charon ($\boldsymbol{r}_{\text{Charon}}$) both at the reference epoch and one day later ($\boldsymbol{r}_{\text{Pluto+1}}$ and $\boldsymbol{r}_{\text{Charon+1}}$). The next-day position is used to estimate the normal vector of Charon's orbital plane.

$$\hat{\boldsymbol{x}}|_{3d}^{J2000} = \frac{\boldsymbol{r}_{\text{Charon}} - \boldsymbol{r}_{\text{Pluto}}}{||\boldsymbol{r}_{\text{Charon}} - \boldsymbol{r}_{\text{Pluto}}||} \qquad \boldsymbol{r}_{\text{Charon}} \text{ and } \boldsymbol{r}_{\text{Pluto}} \text{ at epoch JD 2451545.0} \tag{7.3}$$

$$\hat{\boldsymbol{z}}|_{3d}^{J2000} = \frac{(\boldsymbol{r}_{\text{Charon}} - \boldsymbol{r}_{\text{Pluto}}) \times (\boldsymbol{r}_{\text{Charon+1}} - \boldsymbol{r}_{\text{Pluto+1}})}{||(\boldsymbol{r}_{\text{Charon}} - \boldsymbol{r}_{\text{Pluto}}) \times (\boldsymbol{r}_{\text{Charon+1}} - \boldsymbol{r}_{\text{Pluto+1}})||} \qquad \boldsymbol{r}_{\text{Charon+1}} \text{ and } \boldsymbol{r}_{\text{Pluto+1}} \text{ at JD 2451546.0} \tag{7.4}$$

$$\hat{\boldsymbol{y}}|_{3d}^{J2000} = \hat{\boldsymbol{z}}|_{3d}^{J2000} \times \hat{\boldsymbol{x}}|_{3d}^{J2000} \qquad . \tag{7.5}$$

These unit vectors directly provide the transformation $\mathbb{T}_{P/C\leftarrow 3d}$ from F_{3d} to F_P or F_C as shown in Equation 7.6.

$$\begin{aligned} \boldsymbol{x}|_{3d}^{3d} &= [1 \;\; 0 \;\; 0] \\ \boldsymbol{y}|_{3d}^{3d} &= [0 \;\; 1 \;\; 0] \\ \boldsymbol{z}|_{3d}^{3d} &= [0 \;\; 0 \;\; 1] \end{aligned} \qquad \begin{aligned} \hat{\boldsymbol{x}}|_{3d}^{J2000} &= [\;\;0.3489 \;\; 0.4488 \;\;\;\; 0.8227] \\ \hat{\boldsymbol{y}}|_{3d}^{J2000} &= [\;\;0.6469 \;\; 0.5198 \;\; -0.5570] \\ \hat{\boldsymbol{z}}|_{3d}^{J2000} &= [-0.6781 \;\; 0.7268 \;\; -0.1080] \end{aligned} \qquad \mathbb{T}_{P/C\leftarrow 3d} = \begin{bmatrix} \hat{\boldsymbol{x}}|_{3d}^{J2000} \\ \hat{\boldsymbol{y}}|_{3d}^{J2000} \\ \hat{\boldsymbol{z}}|_{3d}^{J2000} \end{bmatrix} \tag{7.6}$$

Finally, to transform a vector $\boldsymbol{r}|_{3d}^{3d}$ to F_{J2000} only a translation is required, as shown in Equation 7.7. This is a time-dependent transform, since the position of Pluto or Charon ($\boldsymbol{r}_{\text{Pluto/Charon}}|^{J2000}$) is time-dependent too.

$$\boldsymbol{r}|_{3d}^{J2000} = \mathbb{T}_{P/C\leftarrow 3d}\, \boldsymbol{r}|_{3d}^{3d} + \boldsymbol{r}_{\text{Pluto/Charon}}|^{J2000} \tag{7.7}$$

7.2.2 State vector to body centred-equatorial frame

This procedure follows the conversion of the state vector (position, $\mathbf{r}$ and velocity $\mathbf{V}$) of a spacecraft within the body-centred equatorial frame.

$$\hat{\mathbf{n}}_h = \frac{\mathbf{V}_{\infty,i} \times \mathbf{V}_{\infty,f}}{||\mathbf{V}_{\infty,i} \times \mathbf{V}_{\infty,f}||} \tag{7.8}$$

In Equation 7.8, $\mathbf{V}_{\infty,i}$ is the velocity on the incoming hyperbolic asymptote at infinity, and $\mathbf{V}_{\infty,f}$ is the outgoing velocity. The normal vector to the orbital plane ($\hat{\mathbf{n}}_h$) is determined using Equation 7.8.

$$\hat{\mathbf{V}}_p = \hat{\mathbf{V}}_{p,i} = \hat{\mathbf{V}}_{p,f} = \mathbb{T}_{\hat{n}_h}(\alpha_i/2)\frac{\mathbf{V}_{\infty,i}}{||\mathbf{V}_{\infty,i}||} \tag{7.9}$$

$$\mathbf{V}_{p,i} = V_{p,i} \cdot \hat{\mathbf{V}}_p \quad ; \quad \mathbf{V}_{p,f} = V_{p,f} \cdot \hat{\mathbf{V}}_p \tag{7.10}$$

Through the application of a rotation about $\hat{\mathbf{n}}_h$ by an angle of $\alpha_i/2$ to the unit vector $\hat{\mathbf{V}}_{\infty,i}$, the unit vector for the velocity at periapsis ($\hat{\mathbf{V}}_p$) is determined using Equation 7.9. This is derived from the geometry seen in Figure 7.24.The vector forms of $V_{p,i}$ and $V_{p,f}$ are found using Equation 7.10.

$$\hat{\mathbf{r}}_p = \mathbb{T}_{\hat{n}_h}(-\pi/2)\hat{\mathbf{V}}_p \quad (7.11) \qquad \mathbf{r}_p = \hat{\mathbf{r}}_p r_p \quad (7.12)$$

The location of the periapsis is found using the fact that $\hat{\mathbf{V}}_p$ is perpendicular to periapsis location unit vector ($\hat{\mathbf{r}}_p$). Therefore a rotation is applied about the z-axis ($\hat{\mathbf{Z}}$) as seen in Equation 7.11. This is then scaled to provide the position vector of the periapsis seen in Equation 7.12.

$$\mathbf{e}_i = \frac{\mathbf{V}_{p,i} \times (\mathbf{r}_p \times \mathbf{V}_{p,i})}{\mu} - \hat{\mathbf{r}}_p \quad (7.13) \qquad \mathbf{e}_f = \frac{\mathbf{V}_{p,f} \times (\mathbf{r}_p \times \mathbf{V}_{p,f})}{\mu} - \hat{\mathbf{r}}_p \quad (7.14)$$

The eccentricity vectors of the incoming ($\mathbf{e}_i$) and outgoing ($\mathbf{e}_f$) hyperbolic trajectories are then determined given the variables determined using the preceding equations, and is given by Equation 7.13 and Equation 7.14 [144].

$$\mathbf{n}_\Omega = \hat{\mathbf{K}} \times \mathbf{h} \quad (7.15) \qquad \mathbf{h} = \mathbf{r} \times \mathbf{V} \quad (7.16)$$

The vector defining the *line of nodes* is given using Equation 7.15 where $\mathbf{h}$ is defined in Equation 7.16. The following geometrical angles are described by Figure 7.4.

$$i = \arccos\left(\frac{\hat{K} \cdot \hat{n}_h}{||\hat{K}||\ ||\hat{n}_h||}\right) \tag{7.17}$$

The inclination (i) of the orbital plane is given by Equation 7.17 with no further conditional statements as i is always between 0 and π.

$$\Omega = \arccos\left(\frac{\hat{I} \cdot \mathbf{n}_\Omega}{||\hat{I}||\ ||\hat{n}_\Omega||}\right), \text{ If } (\mathbf{n}_{\Omega,j} < 0) \text{ then } \Omega = 2\pi - \Omega \tag{7.18}$$

The longitude ascension of ascending node (Ω) is calculated by the angle between the x-axis ($\hat{\mathbf{I}}$) and the line of nodes. If the y-component of $\mathbf{n}_{\Omega,j}$ is less than zero the ascending node occurs on the exit trajectory due to negative rotation around the y-axis, therefore Ω is subtracted from 2π.

$$\omega = \arccos\left(\frac{\mathbf{e} \cdot \mathbf{n}_\Omega}{||\mathbf{e}||\ ||\hat{n}_\Omega||}\right), \text{ If } (\mathbf{e}_k < 0) \text{ then } \omega = 2\pi - \omega \tag{7.19}$$

Similarly to the conditional statement seen for Ω, a similar correction is applied for negative rotations about $\hat{\mathbf{Z}}$ for the argument of perigee (ω) shown in Equation 7.19.

7.2.3 International Celestial Reference System (ICRS) coordinates of position on hyperbolic trajectory

This section deals with the methodology for calculating the entry ($\mathbf{r}_{entry}$) and exit ($\mathbf{r}_{exit}$) positions on the surface of the SOI given the Keplerian parameters defining the hyperbolic trajectory.

$$F = \ln\left[\frac{\sqrt{e+1} + \sqrt{e-1}\tan\theta/2}{\sqrt{e+1} - \sqrt{e-1}\tan\theta/2}\right] \quad (7.20) \qquad M_h = e\sinh F - F \quad (7.21) \qquad t_p = M_h\left[\frac{h^3}{\mu^2}\frac{1}{(e^2-1)^{(3/2)}}\right] \quad (7.22)$$

The true anomaly (θ) is calculated for the magnitude of the SOI for both entry and exit hyperbolic trajectories using Equation 7.24. Subsequently Equation 7.20 calculating the hyperbolic anomaly (F), Equation 7.21 for the mean hyperbolic motion (M_h) and Equation 7.22 in order of occurrence, the time since periapsis (t_p) can be calculated for the $\mathbf{r}_{entry}$ and $\mathbf{r}_{exit}$ on the surface of the SOI. These orbital parameters are then using the Poliastro[1] library for Python™. This results in values obtained for the coordinates of $\mathbf{r}_{entry}$ and $\mathbf{r}_{exit}$ in the bodies ICRS reference frame.

[1] Rodríguez, J. (2018). poliastro. Retrieved from https://pypi.org/project/poliastro/

7.3 Study on the orbital parameters and their effect on the mission

The scientific mission consists of two phases, one orbiting Pluto and one orbiting Charon. This section is a study on the effect of the target orbits on the fulfilment of the requirements and on time and fuel performance. For reference in the remaining of the section, the relevant entries of the mission requirements and design choices are listed in Table 7.1.

Table 7.1: Requirements relevant to the design of the scientific orbits.

Identifier	Description
R-MIS-020	The vehicle shall be in orbit in the Pluto-Charon system for a minimum of one year.
R-SCI-030-II	The system shall make a panchromatic map of the surface of Pluto at best resolution exceeding 0.5 km/pixel.
R-SCI-040-II	The system shall make a panchromatic map of the surface of Charon at best resolution exceeding 0.5 km/pixel.
R-SCI-120	The system shall perform topographic measurements of at least 70% of Pluto with a vertical resolution of at least 500 m (modified, previously 300 m).
R-SCI-130	The system shall perform topographic measurements of at least 70% of Charon with a vertical resolution of at least 500 m (modified, previously 300 m).
Camera	This instrument has a field of view of 5.7 degrees and an instantaneous field of view (per pixel) of 20μrad (see chapter 6)

An orbit is defined by the five atemporal Keplerian parameters shown in Figure 7.4 —namely, eccentricity (e), inclination (i), argument of periapsis (ω), longitude of ascending node (Ω) and radius of periapsis (r_p). Equations 7.23, 7.24 and 7.25 (the later one commonly referred to as vis-viva) are recurring relations in analytical astrodynamics, and therefore also in this work, to relate semi-major axis (a), magnitude of position vector (r), true anomaly (θ) and instantaneous velocity (V). Note that it is a particular property of the Pluto-Charon system that Charon's orbital plane coincides with Pluto's equatorial plane [67].

$$a = \frac{r_p}{1-e} \qquad (7.23)$$

$$r = \frac{a(1-e^2)}{1+e\cos(\theta)} \qquad (7.24)$$

$$V = \sqrt{\mu\left(\frac{2}{r}-\frac{1}{a}\right)} \qquad (7.25)$$

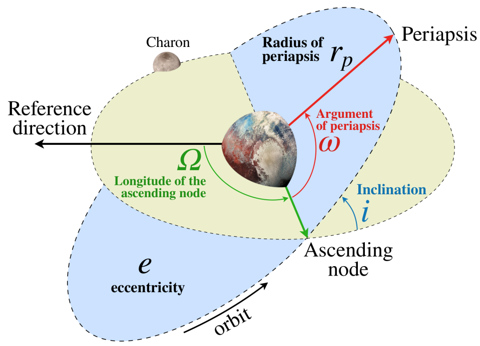

Figure 7.4: Orbital parameters

7.3.1 Argument of periapsis ω

The high cost of bringing fuel to the Pluto system, fuel efficiency is of utmost importance. From all possible trajectories between two bodies the most efficient are the Hohmann and the bi-elliptic transfers [5]. For this analysis, the Hohmann transfer is chosen due to its simplicity. It requires the periapsis of the original and target orbits to be aligned with the centres of Pluto and Charon. For this reason, and the fact that in the reference system F_{3d} Charon orbits on the x-y plane, the argument of periapsis must be zero. It is easy to infer this result by comparing Figures 7.4 and 7.5.

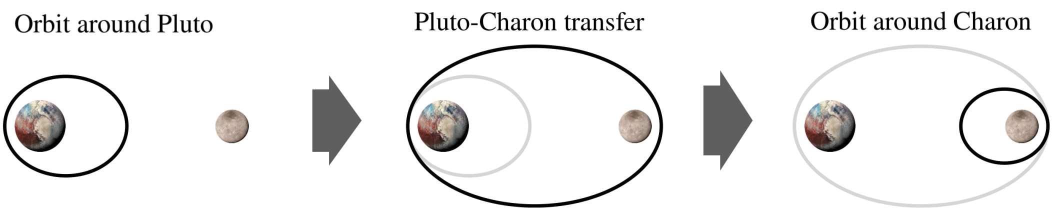

Figure 7.5: Hohmann transfer from Pluto to Charon.

7.3.2 Radius of Periapsis r_p

The radius at periapsis is the closest distance the spacecraft ever gets from the orbited body. A lower boundary may be chosen based on atmosphere thickness and orbital decay, while an upper boundary is set by the payload, in this particular case by the camera that records the map.

Lower boundary

Altitudes above 200 km at Pluto have a comparable atmospheric density to Earth orbits above 600 km (see Figure 7.6). The atmosphere is therefore not a large concern when setting a lower altitude limit. Too low altitudes may instead dangerously decay due to instability (see for instance Figure 7.14). No empirical relation has been derived, but simulations show decays of 30 km to 70 km at an apogee at 400 km altitude and eccentricities between 0.3 and 0.4 (higher eccentricities are unstable). Nonetheless, these decays may be corrected with propulsive maintenance as studied in section 7.4.

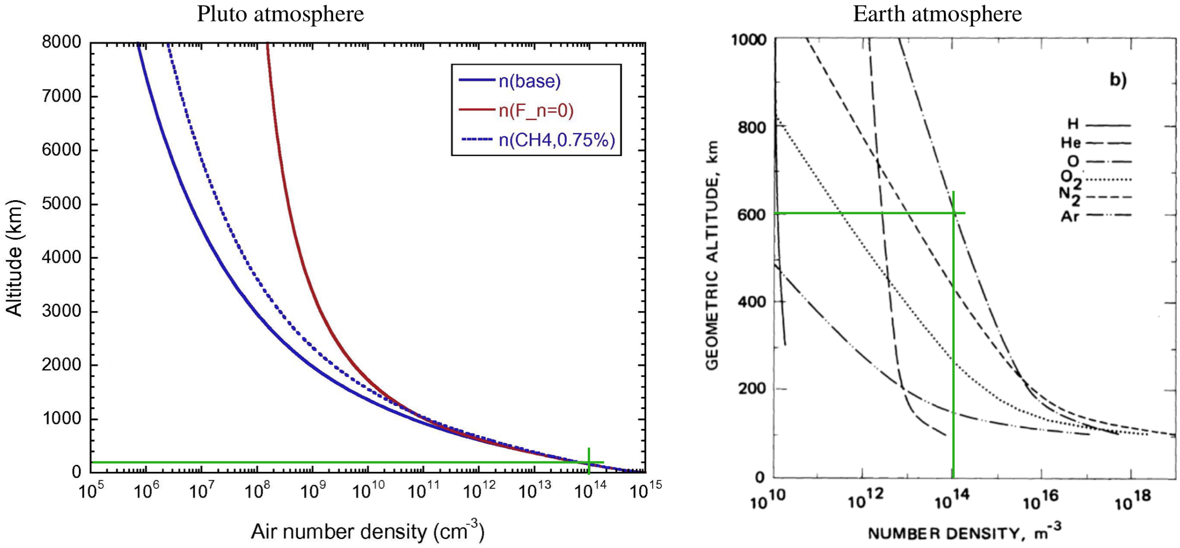

Figure 7.6: Number densities of the atmospheres of Pluto (left) [73] and Earth(right) [11].

Upper boundary

The upper boundary can be solved by applying requirements `R-SCI-030-II` and `R-SCI-040-II` (horizontal resolution (w_{max}) of at least 0.5 km for surface maps) or alternatively `R-SCI-120` and `R-SCI-130` (vertical resolution (dh_{max}) of at least 0.5 km for topographic maps). The first method constrains the maximum altitude ($h_{\max 1}$) to the results of Equation 7.26. The second method can be considered to put a constraint on altitude ($h_{\max 1}$) based on how much planet curvature is allowed within one image, in which case the constraint is given by Equation 7.28. Figures 7.7 and 7.8 and Equation 7.27 (the maximum planeto-centric swath angle ψ_{max}) are used for deriving the expressions of the constraint altitudes $h_{\max 1}$ and $h_{\max 2}$.

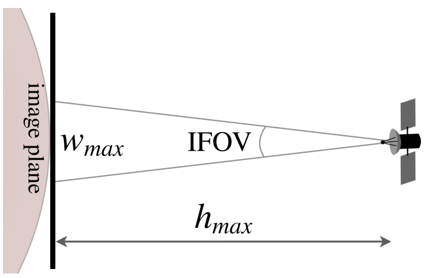

Figure 7.7: Geometry for finding $h_{\max 1}$

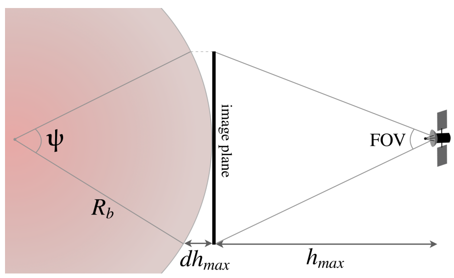

Figure 7.8: Geometry for finding $h_{\max 2}$

$$h_{\max 1} = \frac{w_{max}}{\tan\left(\mathrm{IFOV}/2\right)} \tag{7.26}$$

$$\psi_{max} = 2 \arccos\left(1 - \frac{dh_{max}}{R_b}\right) \tag{7.27}$$

$$h_{\max 2} = R_b \frac{\sin\left(\psi_{max}/2\right)}{\tan\left(\mathrm{FOV}/2\right)} \tag{7.28}$$

The results reveal that $h_{\max 2}$ is much more constraining and therefore the one used ($h_{\max 1}$=50000 km for both Pluto and Charon, $h_{\max 2,\ \mathrm{Pluto}}$=**692 km**, $h_{\max 2,\ \mathrm{Charon}}$=**494 km**).

For the analysis of the subsequent parameters, the periapsis is set at 400 km altitude for Pluto and 394 km for Charon. This choice is nonetheless arbitrary and other choices within a range of about 50 km above or below are probably valid too. This results in the following radii of periapsis:

$$r_{p\ \text{Pluto}} = 1588\,\text{km}\ , \qquad r_{p\ \text{Charon}} = 1000\,\text{km}$$

7.3.3 Eccentricity e and inclination i

For these two orbital parameters a tool has been developed to study their impact on the mapping time and total coverage. The mapping time is determined by how many orbital periods it takes to complete the map, while the coverage takes into account the area lost at the poles for non-polar orbits. The analysis also focuses on those orbits that have small but non-zero overlap so as to avoid repeating or missing regions.

The unmapped areas at the poles are determined by the inclination and the range angle (φ), which represents the segment of the orbit in which the spacecraft is closer to the surface than h_{max}. Some area is gained due to the maximum planeto-centric swath angle (ψ_{max}), which is computed earlier using Equation 7.27. The expression for φ (Equation 7.29) has been derived using Figure 7.10 and the standard Kepler relation between angular and radial coordinates. The radius of the body being orbited is R_b.

$$\left.\begin{aligned} r_s &= R_b + h_{max} \\ r_s &= \frac{r_p(1-e^2)}{(1-e)(1+e\cos(\theta))} \end{aligned}\right\} \quad \varphi = 2\theta_{max} = 2\arccos\left(\frac{1}{e}\left[\frac{r_p(1+e)}{h_{max}+R_b} - 1\right]\right) \tag{7.29}$$

The different cap areas (A_i, A_φ and $A_{\psi_{max}}$) are computed using Equations 7.30, 7.31 and 7.32, all derived using Figure 7.9. The total unmapped area (A_{unmapped}) is then found by Equation 7.33.

$$A_i = 2\pi R h_i = 2\pi R^2\left(1 - \sin i\right) \tag{7.30}$$

$$A_\varphi = 2\pi R h_\varphi = \begin{cases} 2\pi R^2\left(1-\sin\frac{\varphi}{2}\right)\sin i, & \text{if } \varphi<\pi \\ 0, & \text{if } \varphi \geq \pi \end{cases} \tag{7.31}$$

$$A_{\psi_{max}} = 2\pi R h_\psi = \begin{cases} 2\pi R^2\left[\sin\left(\frac{\psi_{max}}{2}+i\right) - \sin i\right], & \text{if } \frac{\psi_{max}}{2}+i<\frac{\pi}{2} \\ 2\pi R^2\left[1-\sin i\right], & \text{if } \frac{\psi_{max}}{2}+i \geq \frac{\pi}{2} \end{cases} \tag{7.32}$$

$$A_{\text{unmapped}} = 2\left(A_i + A_\varphi - A_{\psi_{max}}\right) \tag{7.33}$$

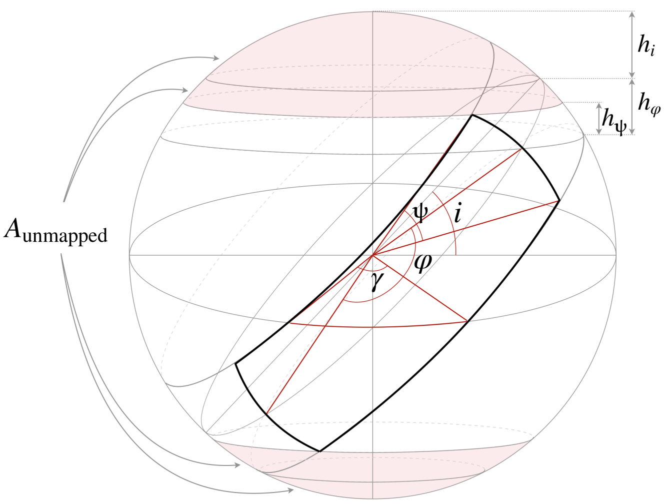

Figure 7.9: Geometry for finding unmapped areas

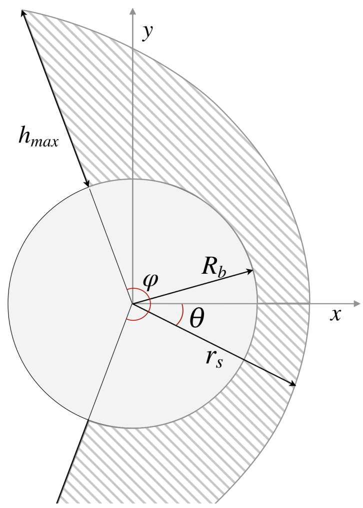

Figure 7.10: Geometry for finding range angle φ

For the mapping time the orbits with correct overlap must be found first. For this, the equatorial swath occurs at the equator and therefore the minimum planeto-centric swath (ψ_{min}) is used in this case, defined in Equation 7.34 where ϵ is the camera field of view. The equatorial swath (γ) and the equatorial shift of the ground-track ($\Delta\lambda$, see Figure 7.11) are calculated using Equations 7.35 and 7.36. The angular velocities of the spacecraft and of the celestial body are indicated as ω_s and ω_b, respectively, while the orbital period is indicated as T_s.

$$\psi_{min} = 2 \arcsin \left(\frac{r_p}{R_b} \tan(\epsilon/2) \right) \tag{7.34}$$

$$\gamma \approx \begin{cases} \psi_{min} / \sin i, & \text{if } \gamma < \varphi \\ \varphi, & \text{otherwise} \end{cases} \tag{7.35}$$

$$\begin{aligned} \Delta\lambda &= 2\pi - (\omega_s - \omega_b) T_s \\ &= 2\pi - (2\pi / T_s - \omega_b) T_s \end{aligned} \tag{7.36}$$

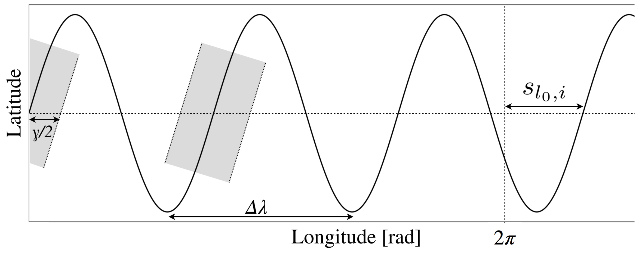

Figure 7.11: Geometry for ground-track overlap

The ground-track in Figure 7.11 does slightly more than two orbits until it passes again through the initial longitude l_0. Calling k the number of passes through l_0 that make a correctly overlapping track complete the map, defined in Equation 7.37 using the ceil operator $\lceil\ \rceil$, the shift from l_0 after each pass, $s_{l_0,i}$, is computed using Equation 7.38. Lastly, the shifts are sorted and the orbit is discarded if their differences after sorting are not within the allowed overlap.

$$k = \left\lceil \frac{\Delta\lambda}{\gamma} \right\rceil \tag{7.37}$$

$$s_{l_0,i} = \left\lceil \frac{2i\pi}{\Delta\lambda} \right\rceil \Delta\lambda - 2i\pi \qquad i = 1, \ldots, k \tag{7.38}$$

The results from this analysis are shown in Figures 7.12 and 7.13 for Pluto and Charon, respectively. Two limit contours have been marked, one at 70% mapping ratio according to requirements `R-SCI-120` and `R-SCI-130`, and one at the highest eccentricity at which the orbits are still stable. Only the orbits in the lower-right enclosed region may be selected.

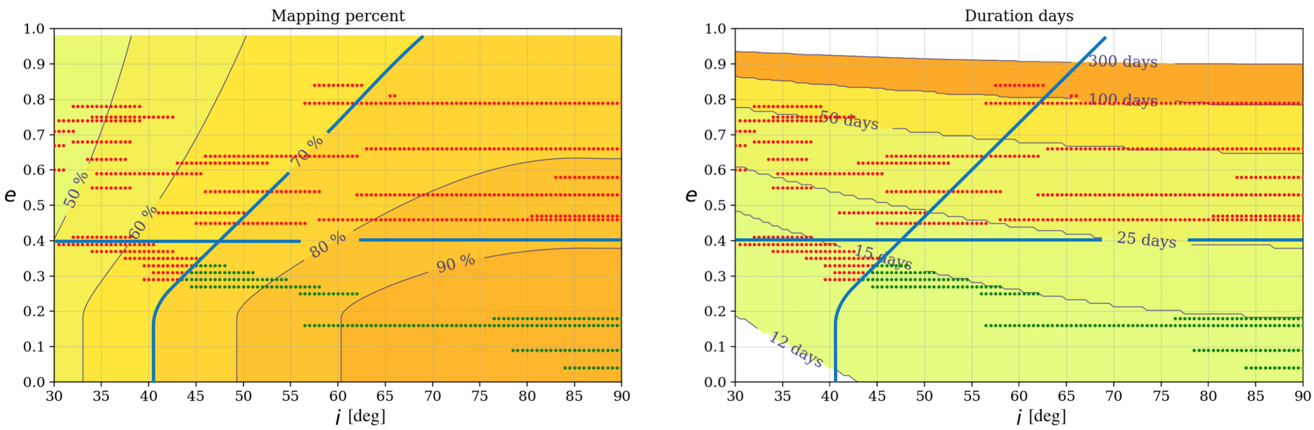

Figure 7.12: Mapping orbit analysis around **Pluto**. Dots represent acceptable orbits (overlap 3%-40%).

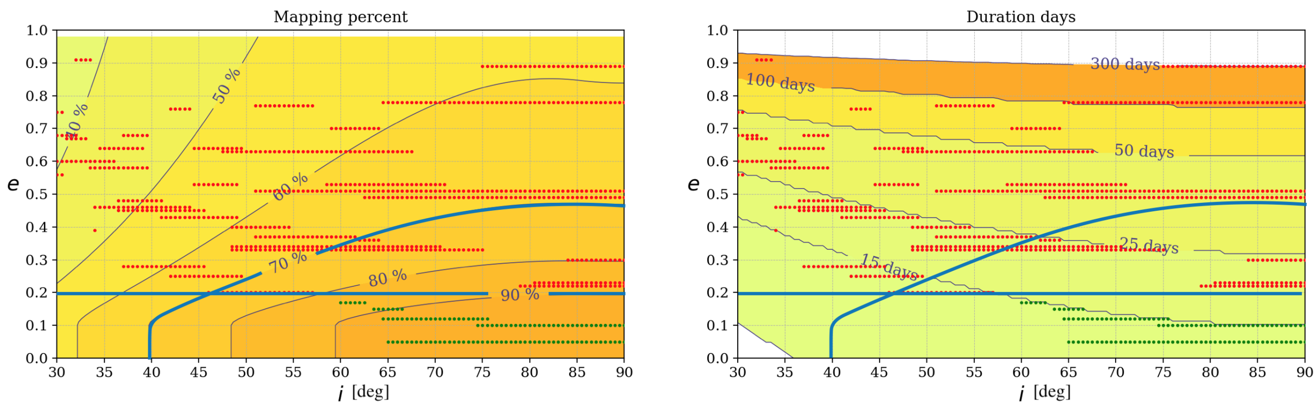

Figure 7.13: Mapping orbit analysis around **Charon**. Dots represent acceptable orbits (overlap 3%-40%).

When testing orbits using the high-fidelity propagator GMAT, it is quickly visible that orbits with high eccentricity become unstable after a few periods. This is due to the gravitational interaction of Charon when orbiting Pluto and, conversely, of Pluto when orbiting Charon. Figure 7.14 compares a stable and an unstable orbit. Through trial and error the limit eccentricities have been found for Pluto and for Charon where the periapsis decay after completing the map is within 70 km. These limits have been included in the plots of Figures 7.12 and 7.13.

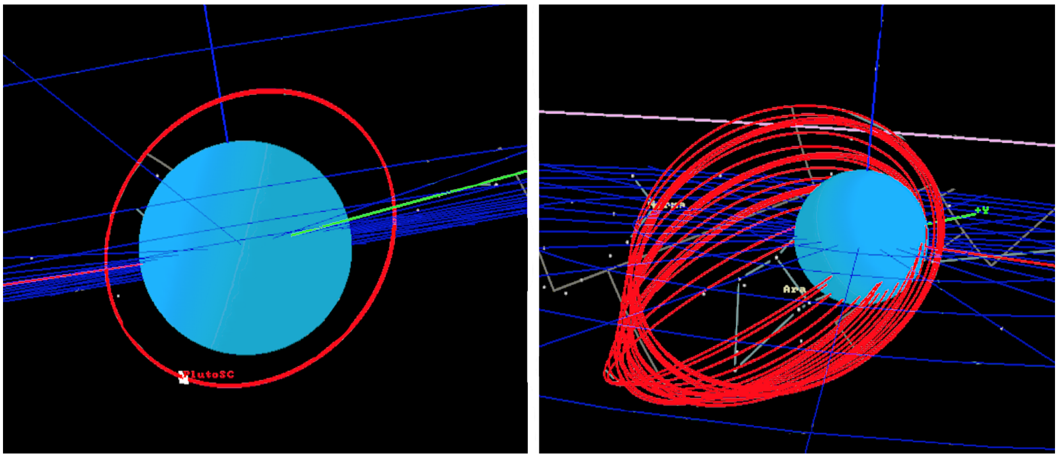

Figure 7.14: Orbit around Pluto with eccentricity 0.1 propagated for 15 days (left).
Orbit around Pluto with eccentricity 0.5 propagated for 10 days (right).

The eccentricity also has a large impact on the ΔV for transferring from Pluto to Charon. The transfer has been modelled similarly to a Hohmann transfer. The main difference is that the arrival into Charon's orbit is an hyperbolic capture instead of an elliptic orbit lowering. First, the apogee when orbiting Pluto is raised at the periapsis with ΔV_1 (computed using the vis-viva Equation 7.25). Next, the velocity V_{inf} of the spacecraft when entering the sphere of influence (SOI) of Charon is computed using also the vis-viva equation. The radius at the entry point is solved for by equating the radii r_1 (Equation 7.24) and r_2 (Equation 7.39, d_{P-C} is the distance between Pluto and Charon), defined in Figure 7.15. Finally, the difference between the velocity at the hyperbolic periapsis $V_{\text{p, hyp}}$ (Equation 7.40 [20]) and the target orbit periapsis yield the required ΔV_2 for capture.

$$r_2 = d_{P-C}\cos(\theta_2 + \pi) - \sqrt{R^2_{\text{SOI Charon}} - d^2_{P-C}\sin(\theta_2 + \pi)^2} \tag{7.39}$$

$$V_{\text{p, hyp}} = \sqrt{V_\infty^2 + 2\frac{\mu}{r_p}} \tag{7.40}$$

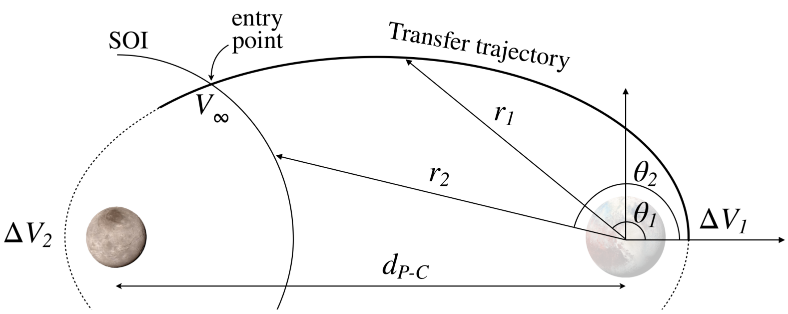

Figure 7.15: Geometry for finding the radius when entering the sphere of influence of Charon.

The sum $\Delta V_1 + \Delta V_2$ is plotted in Figure 7.16 as contours for all combinations of eccentricities around Pluto and Charon, also indicating the valid orbits identified earlier. This reveals a large penalty on fuel consumption for circular orbits with low eccentricity. The choice of eccentricity is therefore a trade-off between fuel burnt and map coverage. The compromise is studied in section 7.4.

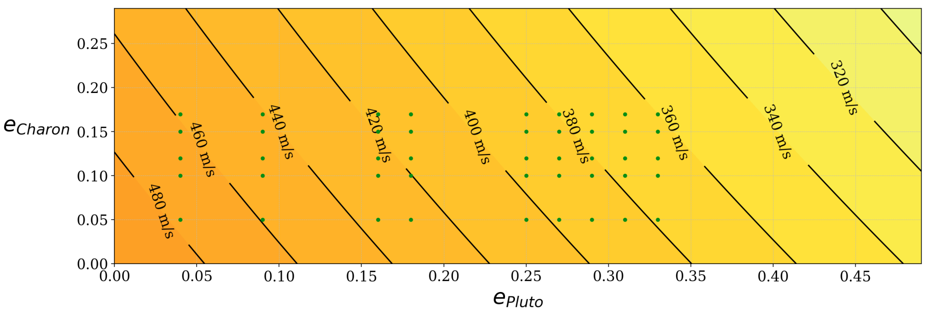

Figure 7.16: ΔV for orbital eccentricities at Pluto and Charon. Dots represent orbits with favourable ground-track.

7.3.4 Longitude of the Ascending Node Ω

This last orbital element has a large impact on the duration of the occultation from Earth or the Sun. The geometry for finding the occultation time is defined in Figure 7.17.

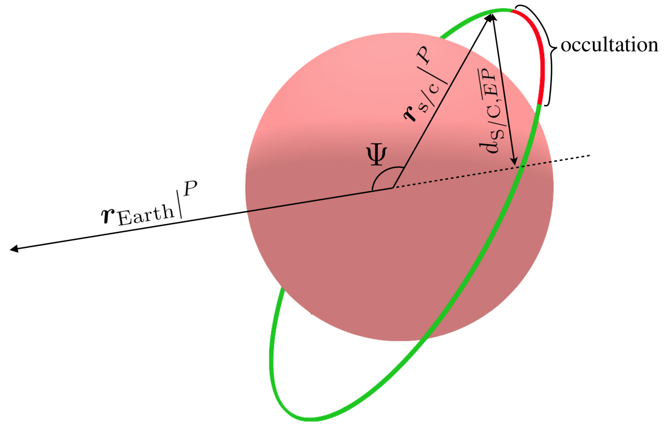

Figure 7.17: Geometry of the occultation problem.

The distance from the spacecraft to the line passing through the centres of Earth and Pluto ($d_{\mathrm{S/C},\overline{EP}}$) is computed for each position along the orbit, using Equation 7.41, as well as the angle between the Earth-Pluto and the Pluto-Spacecraft vectors (Ψ) using Equation 7.42.

$$d_{\mathrm{S/C},\overline{EP}} = \left\| \left. \boldsymbol{r}_{\mathrm{s/c}} \right|^P \times \left. \hat{\boldsymbol{r}}_{\mathrm{Earth}} \right|^P \right\| \tag{7.41}$$

$$\Psi = \arccos\left(\left. \hat{\boldsymbol{r}}_{\mathrm{Earth}} \right|^P \cdot \left. \boldsymbol{r}_{\mathrm{s/c}} \right|^P \right) \tag{7.42}$$

If $d_{\mathrm{S/C},\overline{EP}} < R_b$ and $\Psi > 90°$ then the spacecraft is in occultation. The same can be calculated for eclipse. Figures 7.18 and 7.19 show the percent of occultation per orbit around Pluto and Charon for the whole range of Ω. The transfer sequence to Charon requires the periapsis to be opposed to that of Pluto, as seen previously in Figure 7.5. Therefore, it is required that $\Omega_{\mathrm{Charon}} = \Omega_{\mathrm{Pluto}} + 180°$. This assumes no change of plane during the entire transfer, which is not entirely accurate since the attraction from Charon is out of plane. Therefore, the final longitude of ascending node may shift. This is further analysed in section 7.4.

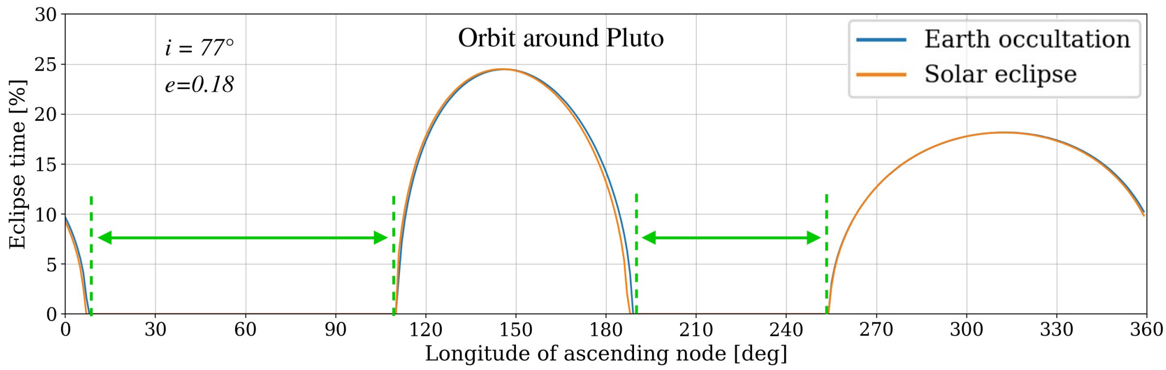

Figure 7.18: Occultation from Earth and the Sun at Pluto with respect to longitude of ascending node.

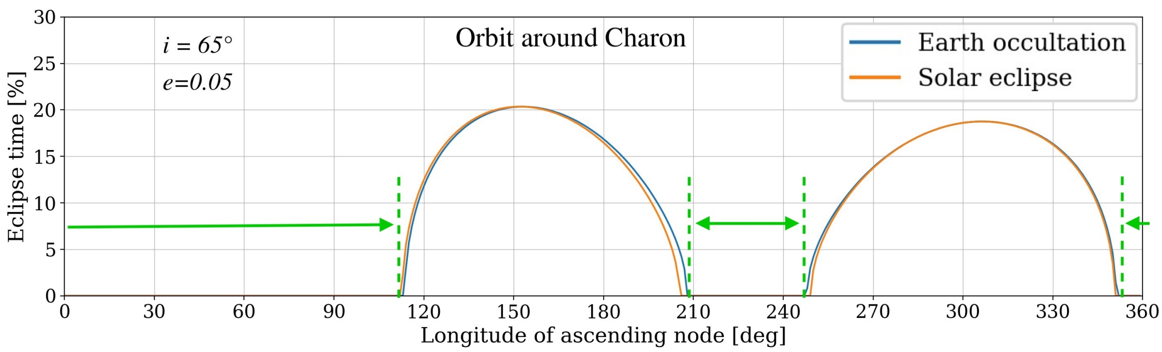

Figure 7.19: Occultation from Earth and the Sun at Charon with respect to longitude of ascending node.

Two ranges of values for both Ω_{Pluto} and Ω_{Charon} lead to no occultation in Figures 7.18 and 7.19. Recalling the requirement for a shift of approximately 180° between each, the two possible combinations are displayed in Table 7.2.

Table 7.2: Possible choices for longitude of ascending node at Pluto and at Charon.

	Ω_{Pluto} [deg]	Ω_{Charon} [deg]
Option 1	90 - 110	210 - 250
Option 2	190 - 250	350 - 110

7.3.5 Conclusions on Orbital Parameters

In summary from the above analysis, and recalling the definition of the orbital parameters in Figure 7.4, the following are the ranges of values that are recommended:

Argument of periapsis ω
Affects mainly: Fuel usage for transfer from Pluto to Charon.
Recommended values:
Pluto and Charon: As close to 0° as possible.

Radius of periapsis r_p
Affects mainly: Mapping time, map coverage, orbit stability.
Recommended values:
Pluto: 1588 km ± 50 km
Charon: 1000 km ± 50 km

Eccentricity e
Affects mainly: Mapping time, orbit stability, fuel usage for transfer.
Recommended values:
Pluto: only specific values between 0.0 and 0.4, see Figure 7.12
Charon: only specific values between 0.0 and 0.2, see Figure 7.13

Inclination i
Affects mainly: Map coverage
Recommended values:
Pluto: only specific values between ∼ 45° and 90°, see Figure 7.12
Charon: only specific values between ∼ 60° and 90°, see Figure 7.13

Longitude of ascending node Ω
Affects mainly: Earth occultation time and solar eclipse time
Recommended values:
Pluto: Either in the range (90° - 110°) or the range (210° - 250°)
Charon: Either in the range (190° - 250°) or the range (350° - 110°)
Common note: Ω_{Pluto} and Ω_{Charon} need to be shifted approximately 180° relative to each other.

7.4 Final Target Orbit Determination

Now that the ranges of possible orbital parameters have been defined, there are three main factors that must be considered to finalise the orbits: the total ΔV required for all manoeuvres involved with those orbits, the mapping percentage of each Pluto and Charon, and the occultation. The most pressing of these is the ΔV, since the propulsion system for this mission is on the edge of feasibility. Each component of ΔV is calculated, and the total ΔV for a selection of orbit configurations is presented.

7.4.1 Insertion to Pluto-Charon

In order to decide on the final target orbit around Pluto, it is helpful to know the effect that the target orbit has on the insertion ΔV; for this the method found in Curtis [85] for a planetary rendezvous with a hyperbolic orbit is used. Equation 7.43 can be used to find the insertion ΔV, where $v_{p,hyp}$ and $v_{p,cap}$ refer to the orbital velocity around Pluto for the hyperbolic and captured trajectories, respectively; the gravitational parameter of Pluto, μ_P, is a known constant, as is the periapsis radius r_p (since it was determined in subsection 7.3.2). The eccentricity e is the variable which determines the final orbit.

$$\Delta V_{insertion} = v_p,_{hyp} - v_p,_{cap} = \sqrt{V_\infty^2 + \frac{2\mu_P}{r_p}} - \sqrt{\frac{\mu_P(1+e)}{r_p}} \tag{7.43}$$

Therefore, the only term in the equation to be determined is the incoming hyperbolic excess velocity V_∞; this is done by simply finding the relative velocity of Pluto with respect to the spacecraft at the SOI given by the interplanetary trajectory, which gives the initial excess velocity $V_{\infty init}$ (for a more in depth explanation of SOI and the patched conic method, see section 7.1). From this, it is assumed that the electric propulsion system is able to reduce this velocity by 5.86 km/s, as can be found in chapter 10, which then provides the excess velocity to be used, V_∞. For this analysis it is assumed that the propulsion delivers the velocity increment impulsively. For an electric propulsion system this is, of course, not the case, however it still provides a reasonable estimate of what the incoming excess velocity would be; the finite nature of the burn can be modelled more accurately during later design phases.

Assuming an EJP (Earth-Jupiter-Pluto) transfer trajectory, the limiting capture cases for eccentricity 0 and 1 can be calculated, which give $\Delta V_{insertion,max} = 307$ m/s and $\Delta V_{insertion,min} = 0.3$ m/s respectively. If the intermediate eccentricities are also calculated, they approximate to a linear relationship with Equation 7.44.

$$\Delta V_{insertion} = -e * \Delta V_{insertion,max} + \Delta V_{insertion,max} \tag{7.44}$$

7.4.2 Escape From the Pluto-Charon System

In order to comply with the mission sustainability policy, the spacecraft will be ejected from the Pluto-Charon system at end of life (EOL). To do this, the technique used for insertion can also be applied using equations 7.45 and 7.46, but with one extra step to account for leaving Charon's SOI. It should be noted that the eccentricity of Charon around Pluto e_{char} is equal to 0, meaning the radius of Charon around Pluto r_{char} is equal to the semi-major axis a_C; in addition the excess velocity leaving the system $V_\infty,_P$ is equal to 0 (since the spacecraft is considered to just escape the system). Other parameters listed in the equations are as follows:

$\mathbf{\Delta V_{esc}}$: The velocity increment to be applied at Charon periapsis in order to escape the system
$\mathbf{V_{p,hyp,C}}$: The periapsis velocity of the hyperbolic orbit around Charo
$\mathbf{V_{p,target,C}}$: The periapsis velocity of the mission target orbit around Charon
$\mathbf{V_{\infty,C}}$: The excess velocity when leaving the SOI of Charon
$\mu_\mathbf{P}/\mu_C$: The standard gravitational parameter of Pluto/Charon
$\mathbf{r_{p,C}}$: The periapsis radius of the spacecraft around Charon
$\mathbf{e_C}$: The eccentricity of the spacecraft orbit around Charon
$\mathbf{V_{esc,P}}$: The velocity around Pluto needed to escape the system (at Charon altitude)
$\mathbf{V_C}$: The velocity of Charon around Pluto

$$\Delta V_{esc} = V_P,_{hyp},_C - V_P,_{target},_C = \sqrt{V_\infty,_C^2 + \frac{2\mu_C}{r_p,_C}} - \sqrt{\frac{\mu_C(1+e_C)}{r_p,_C}} \tag{7.45}$$

$$V_\infty,_C = V_{esc},_P - V_C = \sqrt{V_\infty,_P^2 + \frac{2\mu_P}{r_{char}}} - \sqrt{\frac{\mu_P(1+e_{char})}{r_{char}}} = \sqrt{\frac{2\mu_P}{a_C}} - \sqrt{\frac{\mu_P}{a_C}} \tag{7.46}$$

With these equations it is possible to calculate ΔV_{esc} for any target orbit around Charon, and will be done for a number of cases in subsection 7.4.5.

7.4.3 Orbit Maintenance Around Pluto and Charon

Due to the size and proximity of Charon to its parent body Pluto, a spacecraft orbiting around either Pluto or Charon is subject to significant perturbations that must be accounted for. A numerical model (GMAT) is used to simulate the perturbations. The reasoning for this is that using analytic techniques for a 3D orbit (i.e. inclined and eccentric) is significantly more difficult and time consuming to implement. For the orbit around Pluto and Charon, the Near Pluto and Near Charon propagators defined in Table 7.10 are used. An example of this using representative orbits is shown in Figure 7.20; it can be noted that the orbit degrades such that the spacecraft impacts Pluto and Charon over 6 months and 2 months respectively. The blue line represents the initial orbit (e = 0.18, i = 77°around Pluto, and e = 0.05, i = 65°around Charon) while the red line represents the perturbed orbit.

Figure 7.20: A simulation of orbits around Pluto (left) and Charon (right) without orbit maintenance using GMAT.

Maintenance Procedure

From the simulation without maintenance it can be seen that a number of orbital parameters are perturbed. Some of these perturbations do not need to be corrected, for instance the changes to inclination, argument of periapsis (ω) and longitude of the ascending node (Ω) are small enough to be ignored (see subsection 7.3.5). Therefore only the periapsis and apoapsis magnitudes are maintained.

The procedure in GMAT for this maintenance is as follows:

1. Propagate the spacecraft for 1 orbit of Charon around Pluto.
2. Propagate the spacecraft to periapsis.
3. Perform a manoeuvre directed along the spacecraft velocity vector, in the forward (prograde) or backward (retrograde) direction to correct apoapsis magnitude.
4. Propagate spacecraft to apoapsis.
5. Perform prograde or retrograde manoeuvre (in the order of 0.05 m/s and 1.5 m/s around each Pluto and Charon respectively) to correct periapsis magnitude.
6. Return to step 1.

It should be noted that the spacecraft is always propagated for one orbit of Charon before making any corrections. The reasoning for this comes from the fact that the perturbations on the spacecraft appear to partially cancel out over an orbital period of the perturbing body. Therefore making corrections more often than this would result in a higher ΔV cost for maintenance; this can be seen by performing corrections every orbit for Pluto orbit case P-4 (see Table 7.3) which results in a maintenance budget of 5.5 m/s per month, compared to only 1.19 m/s per month when corrections are made with a period of 1 Charon orbit. Corrections are also not made less often than this, in order to prevent the orbit from drifting by a significant amount.

Maintenance Test Orbits

A number of representative orbit options are shown in Table 7.3 with the ΔV budget for maintenance, all orbits considered have a mapping of at least 90% with the exception of the highlighted cells, which have a mapping of at least 70%. These options are taken from the possible mapping orbits outlined in subsection 7.3.5, with a range of combinations of eccentricity and inclinations. It can be clearly seen that the maintenance around Charon is much more severe than the maintenance required around Pluto.

7.4.4 Pluto-Charon Transfer Manoeuvres

Using the known possible target orbits, it is possible to calculate the transfer trajectory that links these orbits together. The starting configurations are chosen with the help of the results of subsection 7.3.3, and the final simulation can be done using GMAT. It should be noted that for this analysis the transfer time is not considered, since it is on the order of days and so would not affect the mission.

Since the orbits being considered are high inclination, it is not appropriate to assume a coplanar transfer; therefore GMAT can be used to numerically simulate and target the orbit required around Charon from a defined orbit around Pluto. There are two manoeuvres whose ΔV must be found: the Transfer Orbit Injection (TOI) which places the spacecraft on the transfer to Charon, as well as the Charon Orbit Insertion (COI) which places the spacecraft into the designated orbit around Charon. The procedure to determine these manoeuvres is as follows:

Table 7.3: Maintenance per month of a selection of orbits around Pluto and Charon.

Central Body	**Identifier**	**e**	**i [deg]**	**Maintenance ΔV per month [m/s]**
Pluto	P-2	0.16	60	0.93
Pluto	P-3	0.16	90	1.28
Pluto	P-4	0.18	77	1.19
Pluto	P-5	0.09	79	0.52
Pluto	P-6	0.09	90	0.61
Pluto	P-7	0.04	85	0.23
Pluto	P-8	0.31	45	1.67
Pluto	P-9	0.25	60	2.01
Charon	C-2	0.12	65	33.29
Charon	C-3	0.12	75	37.67
Charon	C-4	0.1	75	30.15
Charon	C-5	0.1	90	31.89
Charon	C-6	0.05	65	11.84
Charon	C-7	0.05	90	13.90

1. Set the propagator as Near Pluto, and determine rough TOI magnitude by raising the spacecraft apoapsis (with a prograde burn) around Pluto to the orbital radius of Charon.
2. Propagate until the correct manoeuvre epoch. This is necessary since the spacecraft is in an eccentric orbit, and so the when the spacecraft reaches apoapsis, its location should approximate that of Charon, as shown in Figure 7.21b.
3. Propagate to periapsis and use GMAT targeting routines to determine the refined 3-axis manoeuvre to place the spacecraft on a trajectory with the predefined periapsis and inclination around Charon, then perform the manoeuvre.
4. Propagate to the SOI of Charon, and switch to the Near Charon propagator. Then propagate to periapsis around Charon.
5. Calculate and perform the manoeuvre which achieves the predefined eccentricity of the spacecraft orbit around Charon.

For this process impulsive manoeuvres are assumed at TOI and COI, and therefore must be performed by the chemical propulsion system. Of course, it is possible to conduct this procedure for any configuration of orbits, however this would be very time consuming; therefore a representative selection of configurations is considered.

The major factor affecting transfer ΔV is the eccentricity of the chosen orbits, therefore for each Pluto and Charon one high eccentricity and one low eccentricity orbit is chosen which is able to map 90% of the body, as well as another orbit which is only able to map 70% of the body. It should be noted that all stable orbits around Charon are able to map 90% of the moon, therefore only two options are considered for Charon. The reasoning for considering the inclinations shown is that these correspond the the orbits with the lowest maintenance budget for their eccentricity,a few other inclination options were also chosen (namely PC-8, PC-9 and PC-10) in order to observe the affect of inclination on the transfer ΔV.

With these considerations the assessed Pluto orbits are P-4, P-7 and P-8, and the assessed Charon orbits are C-2 and C-6 (see Table 7.3 for the maintenance of these orbits). Transfer trajectories between any combination of these orbits is simulated, and the results are displayed in Table 7.4.

Table 7.4: Simulated transfer ΔV for a selection of representative orbit configurations.

Transfer	**Pluto Orbit Info**			**Charon Orbit Info**			**TOI**	**COI**	**Total Transfer**
Orbit ID	ID	e	i [°]	ID	e	i [°]	ΔV [m/s]	ΔV [m/s]	ΔV [m/s]
PC-2	P-4	0.18	77	C-2	0.12	65	203	148	351
PC-3	P-7	0.04	85	C-2	0.12	65	256	153	409
PC-4	P-8	0.31	45	C-2	0.12	65	188	167	355
PC-5	P-4	0.18	77	C-6	0.05	65	203	159	362
PC-6	P-7	0.04	85	C-6	0.05	65	256	164	420
PC-7	P-8	0.31	45	C-6	0.05	65	188	155	343
PC-8	P-2	0.16	60	C-2	0.12	65	232	175	406
PC-9	P-3	0.16	90	C-2	0.12	65	221	156	377
PC-10	P-4	0.18	77	C-7	0.05	90	223	161	384

Once again, the highlighted cells represent options in which the mapping percentage is only 70%, so these options should be discarded if possible. It can be clearly seen that the eccentricity of the Pluto orbit makes a significant difference to the transfer ΔV (e.g. PC-2 and PC-3), whereas a similar change in eccentricity on the Charon orbit has a much smaller impact (e.g. PC-2 and PC-5). An example of one of these transfers can be seen in Figure 7.21, in which the blue line represents the initial orbit around Pluto, the black line represents the transfer trajectory,

Table 7.5: Total ΔV required for all considered combinations of target orbits, with the two most important options highlighted in green and orange.

Transfer Orbit Identifier	SIM ΔV [m/s]	Transfer ΔV [m/s]	Escape ΔV [m/s]	POM [m/s]	COM [m/s]	Total ΔV [m/s]
PC-2	243	351	97	7	200	898
PC-3	292	409	97	1	200	999
PC-4	200	355	97	10	200	862
PC-5	243	362	125	7	71	808
PC-6	292	420	125	1	71	909
PC-7	200	343	125	10	71	749
PC-8	250	406	97	6	200	958
PC-9	250	377	97	8	200	931
PC-10	243	384	125	7	83	842

the red line represents the trajectory inside Charon's SOI, the green line represents the final orbit of the spacecraft around Charon.

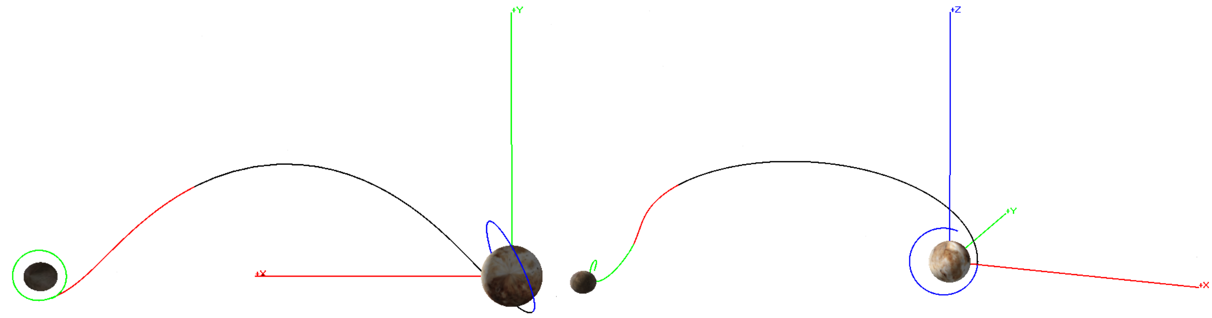

(a) Transfer trajectory simulation visualised in the Pluto-Charon rotating reference frame.

(b) Transfer trajectory simulation visualised in the Pluto frame of reference.

Figure 7.21: GMAT visualisation of an example transfer trajectory (PC-5).

It should be noted that the visualisation used in Figure 7.21a is one fixed at Pluto and rotates with Charon's orbital motion; this visualisation provides a useful view of the final orbit around Charon and Pluto (i.e. the green and blue lines), but the transfer itself may appear distorted. In contrast, Figure 7.21b is centred on Pluto, but shows an inertial reference frame, so the orbit in Pluto's SOI (i.e. the blue and black lines) are representative, but the orbit around Charon appears distorted.

7.4.5 Final Target Orbit Selection

In the previous sections, sufficient calculations were made to trade-off a number of final orbit options. The parameter used to determine the chosen orbits is the total ΔV, since the propulsion system is heavily dependent on it. The process for this analysis is for each orbit configuration to sum the ΔV components of: the System Insertion Manoeuvre, SIM (using the relation found in subsection 7.4.1); the maintenance manoeuvres (see subsection 7.4.3) using a 6 month orbit around each Pluto and Charon; and finally the transfer ΔV. The results of these calculations are summarised in Table 7.5 where POM and COM stand for Pluto Orbit Maintenance and Charon Orbit Maintenance respectively.

After inspecting these results, there are two clear options to take: the lowest ΔV option is PC-7, however in this case only 70% of Pluto is mapped. Therefore PC-5 will be taken as the nominal configuration (since it is the lowest configuration with 90% mappings of both bodies), with PC-7 being recorded as a contingency option in the case of unforeseen changes to the design or mission.

At this stage there are only two orbital parameters left to be determined for each target orbit, namely longitude of ascending node Ω and the argument of periapsis (ω). To decide these, the ranges calculated in subsection 7.3.5 can be used; ω must be approximately 0°, whereas ranges of values (shown in subsection 7.3.5) are available for Ω. Determining a specific Ω shall be done in a later design phase, when the overall trajectory is better defined. To summarise, the target orbits for the mission are shown in Table 7.6, in which type I and type II refer to the fact that there are two distinct complementary ranges available for Ω.

Table 7.6: Summary of final chosen target orbit parameters

Keplerian Parameters	**Unit**	**Pluto**	**Charon**
Semi-major axis	km	1936.6	1052.6
Eccentricity	-	0.18	0.05
Inclination	deg	77	65
Argument of Periapsis	deg	0	0
Longitude of ascending node (type I)	deg	190 - 250	10 - 70
Longitude of ascending node (type II)	deg	30 - 65	210
Orbital Period	hours	5.04	5.79

7.5 Sensitivity Analysis of Final Target Orbit

An important aspect to consider after choosing this orbit is its sensitivity to small changes in the chosen parameters. In this case only the affect on ΔV is considered, as the occultation is insensitive to changes due to the large range of possible values; in addition the chosen orbit is within the requirement for mapping, so a sensitivity analysis is not required (all possible configurations that can be chosen map a sufficient % of the surface).

The process for this sensitivity analysis is as follows: the eccentricity and inclination of orbits around both Pluto and Charon are incrementally adjusted by $\pm 20\%$, with increments of 5%; the affects of this on the different components of ΔV are then calculated, and added together to give a total ΔV value. The most extreme cases of the sensitivity analysis are shown in Table 7.7, in which the ID reads as "Body - change sign %" where an "e" and "i" change represent eccentricity and inclination respectively; for example "P-iP20" represents a 20% increase in the inclination of the orbit around Pluto.

Table 7.7: Sample of Sensitivity Analysis Variations

Orbit ID	**e**	**i [°]**	**POM [m/s]**	**COM [m/s]**	**ΔV insertion [m/s]**	**ΔV Escape [m/s]**	**Total ΔV [m/s]**	**ΔV Difference from Nominal [m/s]**	**% Difference from Nominal**
P-iP20	0.180	92.4	9.10	71.0	243	125	809	2	0.24
P-iM20	0.180	61.6	4.64	71.0	243	125	805	-2	-0.31
P-eP20	0.216	77.0	9.68	71.0	231	125	798	-10	-1.19
P-eM20	0.144	77.0	5.11	71.0	255	125	818	10	1.28
C-iP20	0.050	78.0	7.14	80.5	243	125	817	9	1.17
C-iM20	0.050	52.0	7.14	55.4	243	125	792	-16	-1.93
C-eM20	0.040	65.0	7.14	54.4	243	121	787	-21	-2.55

After completing the sensitivity analysis, it was found that all of the studied relationships are approximately linear for the range of observed values. Furthermore, the maximum increase in ΔV is 1.28%, equivalent to a 10 m/s increase overall (found for case P-eM20); similarly, the maximum decrease in ΔV is -2.55%, equivalent to a 21 m/s decrease overall (found for case C-eM20). The analysis shows that the ΔV budget is very insensitive to both changes in inclination and eccentricity, and so targeting accuracy may not need to be a significant concern.

7.6 Interplanetary Trajectory

This section deals with the mission analysis pertaining to the analysis of interplanetary trajectories within the heliocentric frame from Earth departure to Pluto rendezvous. First, the problem statement with the provided mission constraints is formulated. Subsequently, the theory used for planetary interactions are defined in subsection 7.6.2, subsection 7.6.3, subsection 7.6.4 and subsection 7.6.5. A preliminary analysis is then performed in subsection 7.6.6 to provide a baseline for the rest of the section. The methodology for optimisation is then discussed and a genetic algorithm is used as the optimisation technique. Finally, a sensitivity analysis is performed on the genetic algorithm's convergent behaviour in subsection 7.6.10, with the final optimised solution described in subsection 7.6.11.

7.6.1 Problem Statement

There are numerous degrees of freedom to consider, in order to explore the search space for an interplanetary trajectory that meets the requirements of an Earth departure to Pluto rendezvous mission. Many of these freedoms in the design space are constrained according to set requirements during the early design stages.

Table 7.8: Guiding requirements for the interplanetary trajectory computation.

Identifier	Requirement
R-MIS-020	The vehicle shall be in orbit in the Pluto-Charon system for a minimum of one year.
R-MIS-071	The duration of the mission shall be no more than 25 years.
R-MIS-170	The mission shall adhere to the space agency launch windows.
R-MIS-180	The mission shall adhere to regulations set in place by regulatory agencies of the governments involved.
R-MIS-200	The mission shall adhere to planetary protection class II regulations.
R-MIS-230	Press release kits shall be made available for the media at key mission milestones.
R-MIS-091	The overall budget shall not exceed USD 1.1 billion (2018) with a risk of no more than USD 300 million (2018).
R-MIS-010	The exploration mission shall be an orbital exploration of the Pluto-Charon system.
Propulsion	Both an ion engine and mono-propellant thrusters are available.

The requirements determined through the design process must be related to the constraining of the degrees of freedom within the context of an interplanetary trajectory. This refines the design space of the possible mission trajectories.

Interplanetary Trajectory Constraints

- **Launch Date:** The launch determines the start of the operational phase of the mission. These must abide by launch windows set forth by government agencies, which regulate the country administrating the launch sites. (`R-MIS-170`)
- **Launch Inclination:** Regulations constrain the available range for the launch inclinations from the launch location latitude (`R-MIS-180`). For example, launches from the Kennedy Space Center (KSC) in Florida, USA are restricted to inclinations between 29°and 57°[149].
- **Powered Gravity Assist(s):** The number of powered gravity assists defines the trajectory, quantity of interplanetary legs and opportunities to transfer a relatively small amount of a celestial bodies momentum into kinetic energy imparted on the spacecraft within the heliocentric frame. This minimises the ΔV to be delivered by the propulsion system, reducing cost and weight (`R-MIS-091`) [133]
- **Target Orbit:** Target orbit for planetary rendezvous has been established, and constrained according to the analysis and verification performed in subsection 7.4.5.

7.6.2 Lambert's Problem

Lambert's problem is widely known within the field of orbital mechanics as an orbital boundary value problem with the objective of calculating trajectories, usually interplanetary, between two known positions with a given time of flight (TOF) [94]. It can be described as such: $(\mathbf{v}_0, \mathbf{v}_1) = f(\mathbf{r}_0, \mathbf{r}_1, TOF)$, where $\mathbf{v}_0$ and $\mathbf{v}_1$ are the orbital boundary value solutions of velocity associated with $\mathbf{r}_0$ and $\mathbf{r}_1$ respectively.

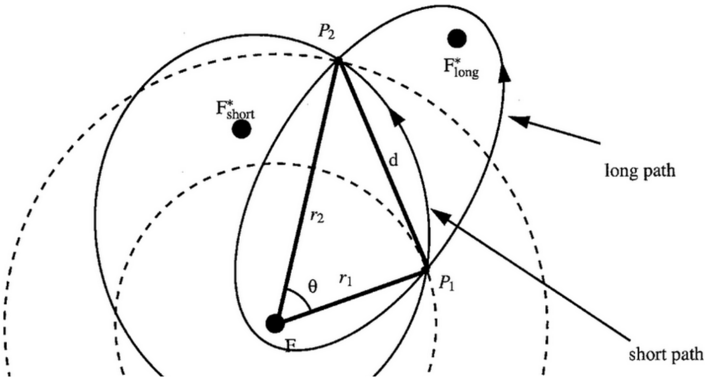

Figure 7.22: Geometrical representation of Lambert's problem and the boundary conditions [68].

Figure 7.22 shows the geometrical representation of Lambert's problem. Given two points in space P_1 and P_2, assumed position time-invariant $\mathbf{r_1}$ and $\mathbf{r_2}$, a preliminary orbit is to be determined. The problem depicted is not constrained due to the numerous elliptical orbits which could be formed using the focus F. For example, the two paths shown, one of longer duration formed with the empty focus F^*_{long} and one of short duration formed with empty focus F^*_{short}. In the case of solving an interplanetary trajectory, the TOF of the solution affects the position of the arrival body due to the bodies change in position, given a fixed departure epoch.

7.6.3 Planetary Departure

Planetary departure is concerned when a spacecraft is situated in a near-circular parking orbit around a body and subsequently provides an impulsive manoeuvre to establish a hyperbolic trajectory ($e > 1$). The Keplerian parameters are desired in order to analyse the geometry of the complete interplanetary trajectory. The desired parameters for a *basic analysis* are the eccentricity (e) and the velocity required at the periapsis (V_p).

The orbital parameters are determined using the equations derived by D. Curtis [86]. These scalar parameters allow for complete description of the perifocal coordinate system (PQW), otherwise known as the *natural frame* of an orbit [86].

$$e = 1 + \frac{r_p \cdot V_\infty^2}{\mu} \tag{7.47}$$

$$v_c = \sqrt{\frac{\mu}{r_p}} \tag{7.48}$$

Given the v_∞ required for the interplanetary leg following departure, Equation 7.47 is used to calculated the eccentricity which gives full geometrical description of the orbital conic shape with r_p having been set by the parking orbit altitude.

$$\Delta V = V_{p,hyp} - V_c \tag{7.49}$$

Where $V_{p,hyp}$ is defined in Equation 7.40. V_c, the orbital velocity of a circular orbit, the ΔV required at periapsis to provide v_∞ at infinity can be calculated as shown in Equation 7.49.

7.6.4 Powered Trailing-side Planetary Flyby

In order to allow for alternative sources of kinetic energy to supplement the spacecraft for the purpose of reducing the amount of ΔV required, trailing-side powered flybys are considered for the interplanetary legs between Earth and Pluto. The theory and geometrical description discussed initially is constrained by the following coanditions:

1. $v_{\infty,i} = v_{\infty,f}$, which states matching between the arrival and departure velocity at infinity.
2. $\alpha \leq \alpha_{max}$, which states that the required bending angle for the flyby should be less than the maximum, so that the $r_{p,min}$ is not exceeded.

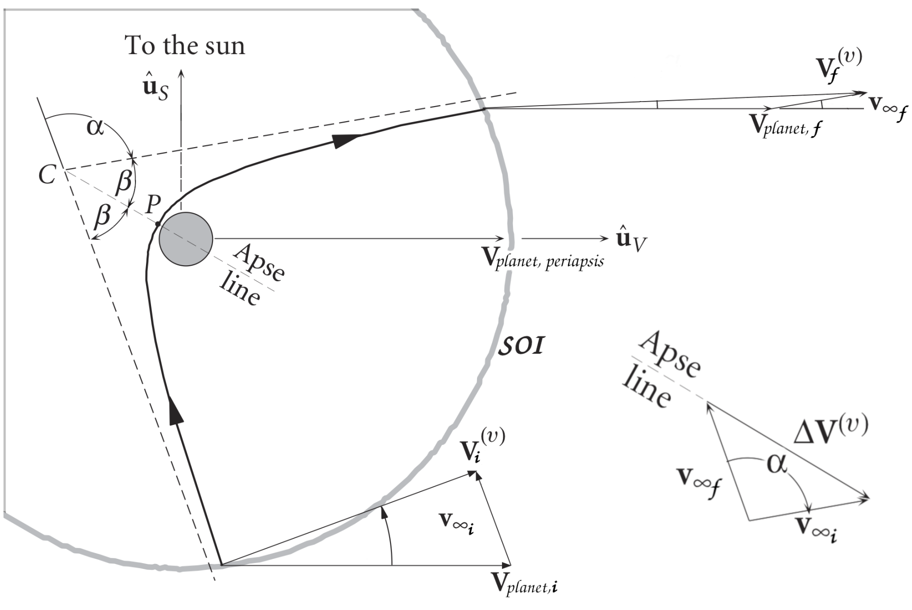

Figure 7.23: Illustration of trailing-side flyby trajectory ($v_{\infty,i} = v_{\infty,f}$) of a spacecraft about planet P [86].

Figure 7.23 shows the geometry of the flyby manoeuvre around planet P. The spacecraft enters and exits the SOI at two positions ($\mathbf{r}_i$ and $\mathbf{r}_f$) separated in time by the duration of the hyperbolic orbit within the SOI. There is therefore a distinct boundary that links the planetary flyby velocities to connect interplanetary legs in the heliocentric frame.

$$V_{\infty_i} = V_i^{(v)} - V_{planet,i} \quad (7.50) \qquad V_{\infty_f} = V_f^{(v)} - V_{planet,f} \quad (7.51)$$

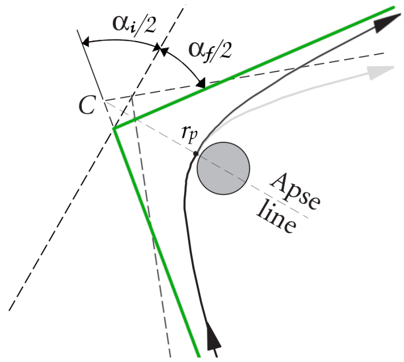

Figure 7.24: Powered flyby showing the bending angle of incoming (α_i) and outgoing (α_f) hyperbole ($v_{\infty,i} < v_{\infty,f}$).

Considering the case of a powered flyby, as seen in Figure 7.24, the maximum achievable bending angle (α_{max}) is defined by the lower limit of the radius of periapsis ($r_{p,min}$) and expressed as follows:

$$\alpha_{max} = \frac{\alpha_i}{2} + \frac{\alpha_f}{2} = \arcsin\left(\frac{1}{1 + \frac{r_{p,min} V_{\infty,i}^2}{\mu_t}}\right) + \arcsin\left(\frac{1}{1 + \frac{r_{p,min} V_{\infty,f}^2}{\mu_t}}\right) \quad (7.52)$$

The two hyperbolic trajectories incoming and outgoing are related by Equation 7.53 as the retrograde manoeuvre is applied at the periapsis.

$$r_p = a_i(1 - e_i) = a_f(1 - e_f) \quad (7.53)$$

The first orbital parameter, the semi-major axis (a) is obtained given $V_{\infty,i}$ and $V_{\infty,f}$ from the Lambert solutions using Equation 7.54 which is the definition of a for a hyperbolic trajectory [86].

$$a_i = -\frac{\mu_t}{v_{\infty,i}^2} \quad ; \quad a_f = -\frac{\mu_t}{v_{\infty,f}^2} \quad (7.54)$$

The problem of matching the incoming hyperbolic trajectory to the outgoing is known as *vis-viva matching* as stated in [100] with the vis-visa equation in Equation 7.25. An iterative method using a Newton-Rhapson root finder is chosen [105].

$$e_{i,n+1} = e_{i,n} - \frac{f(e_{i,n})}{f'(e_{i,n})} \quad (7.55)$$

Using the following formulation of the root finding problem, $e_{i,n}$ of the incoming hyperbole can be found, where $f'(e_{i,n})$ is simply the derivative of Equation 7.56, where the initial guess of $e_{i,0}$ can arbitrarily be set to 1.01 as it is known that it represents a hyperbolic orbit ($e_i > 1$).

$$f(e_{i,n}) = \arcsin\left(\frac{1}{e_{i,n}}\right) + \arcsin\left(\frac{1}{1 - \frac{a_i}{a_f}(1 - e_{i,n})}\right) - \alpha \quad (7.56)$$

Following the solution of e_i and e_f from Equation 7.55 and Equation 7.54, the velocity at periapsis before and after the application of the impulse is calculated using Equation 7.57 which provides the ΔV required for the desired trajectory using Equation 7.58.

$$V_{p,i}^2 = V_{\infty,i}^2 \left(\frac{e_i + 1}{e_i - 1}\right) \quad ; \quad v_{p,f}^2 = v_{\infty,f}^2 \left(\frac{e_f + 1}{e_f - 1}\right) \quad (7.57)$$

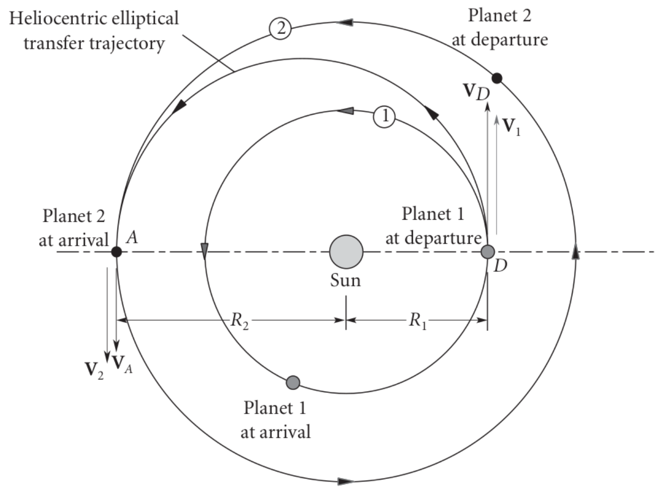

Figure 7.25: Hohmann transfer from planet 1 (Earth) to out planet 2 (Pluto) [86].

$$\Delta V_1 = |V_{p,f} - V_{p,i}| \tag{7.58}$$

Imposed Periapsis Radius Limits

When designing a gravity assist, certain limits on the periapsis radius must be imposed, for instance the spacecraft should not impact the surface of the planet. For larger bodies such as Jupiter, one must also account for the environment of the planet, where the spacecraft may experience unwanted atmospheric drag, severe radiation, or magnetospheric effects. As a baseline, the smallest swing-by distances of previous missions are used to define the smallest allowable periapsis distances. Table 7.9 outlines the defined limits, which are taken from Schlijper [124], with the exception of the Mars swing-by, which comes from ESA (2006b)[2].

Table 7.9: Periapsis distance limits for solar system planets expressed in terms of their radius [124]

Planet	R_{pl} [km]	$r_{p,lim}$ [R_{pl}]	$h_{p,lim}$ [km]	Mission
Mercury	2440	1.082	200	Messenger
Venus	6052	1.047	284	Cassini
Earth	6378	1.048	306	Galileo
Mars	3397	1.076	257	Rosetta
Jupiter	71492	1.60	42895	Pioneer 11
Saturn	60268	1.342	20612	Pioneer 11
Uranus	25559	4.190	81533	Voyager 2
Neptune	24764	1.181	4482	Voyager 2

7.6.5 Planetary Rendezvous

The evaluation of the planetary rendezvous ΔV for the final component of the total ΔV follows from the same process defined in subsection 7.4.1. The chosen capture orbit parameters, for use in this procedure, during the basic analysis of possible mission sequences are assumed to be $e = 0.25$ and $r_p = 1588\,\text{km}$ in Equation 7.43.

7.6.6 Preliminary Analysis

An initial foundation to the quantitative assessment of the ΔV requirements for an interplanetary trajectory to the Pluto-Charon system using an interplanetary Hohmann transfer analysis, the most energy efficient two-impulse orbital maneuver for two co-planar circular orbits sharing a common focus [86]. This was previously discussed, however it is detailed upon in the following section.

Figure 7.25 depicts an interplanetary transfer using the low energy method of Hohmann. The spacecraft departs from planet 1 at point D and arrives at point A, planet 2's position, using an elliptical transfer. The analysis itself is only within the heliocentric frame which disregards ΔV for departure or capture within the two planet's

[2]Rosetta, Science and Technology http://www.esa.int/Our_Activities/Space_Engineering_Technology/Test_centre/Phenix_Thermal_Vacuum_Chamber (June 2018)

SOI's. Due to the constraints on the mission, namely the resources of time, capital and mass allocations of the mission. Maximized ΔV requirements causes undesirable effects on the design, at it increases fuel or technology requirements leading to increased structural mass in a process that must be iterated.

$$\Delta V_A = V_2 - V_A = \sqrt{\frac{\mu_{sun}}{R_2}}\left(1 - \sqrt{\frac{2R_1}{R_1 + R_2}}\right) \quad (7.59) \qquad \Delta V_D = V_D - V_1 = \sqrt{\frac{\mu_{sun}}{R_1}}\left(\sqrt{\frac{2R_2}{R_1 + R_2}} - 1\right) \quad (7.60)$$

Equation 7.59 and Equation 7.60 provide the required ΔV for the heliocentric injection and insertion into the Pluto-Charon system for a Hohmann transfer [86].

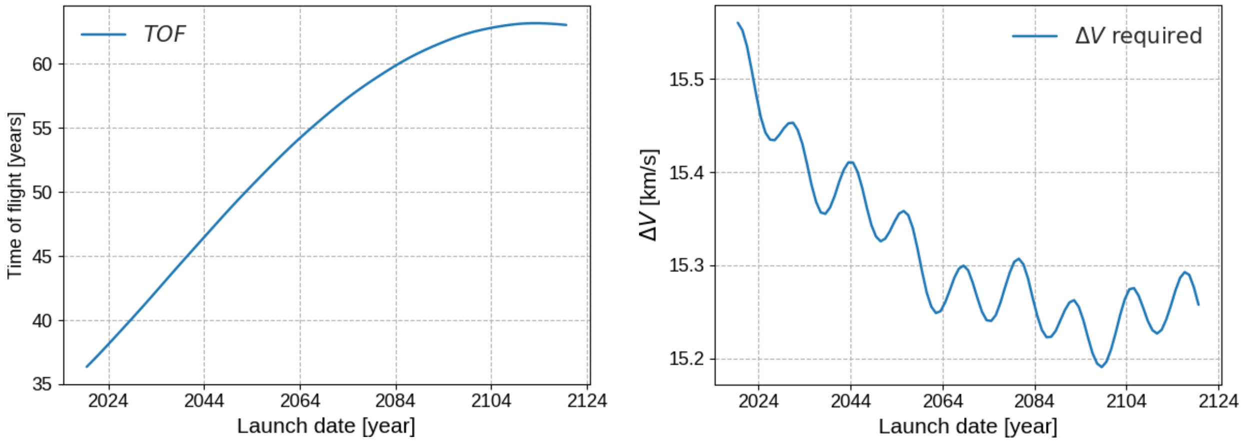

(a) Time of flight (TOF) versus launch date. (b) ΔV versus launch date.

Figure 7.26: Preliminary analysis results of Hohmann transfer from Earth to Pluto.

The preliminary analysis performed indicates a minimum time of flight of 36 years, as shown in Figure 7.26a. This exceeds the maximum mission duration 25 years stated by requirement `R-MIS-071`. Hence, a more complex trajectory involving a gravity assist is researched.

7.6.7 Mathematical Description

Following the formulation of the problem statement defined in terms of engineering design constraints and requirements, the problem must be translated into a mathematical description of the search space. This is done in order to provide the ability to perform a simulated search for an optimal solution. Constraint satisfaction problems (CSP) are widely known within the field of artificial intelligence and are phrased in order to provide a solution that meets defined constraints, which is the case for the interplanetary trajectory [4]. A CSP composes of three main components, namely a set of variables (X), a set of domains (D) for each variable and a set of constraints (C) that specify the allowable combination of values [122]. The complete CSP formulation for the Earth-Pluto interplanetary trajectory can be found in Appendix A and is omitted due to the extensive nature of CSP definitions.

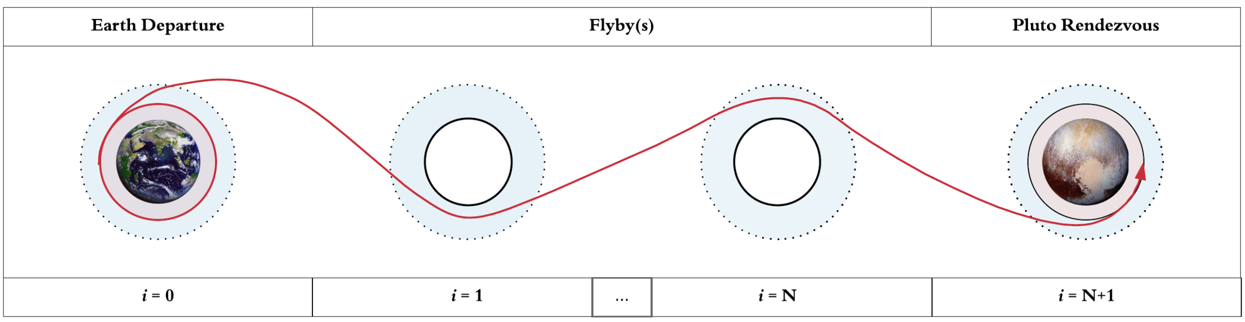

Figure 7.27: Mathematical representation of interplanetary trajectory problem.

A general disingenuous visual for description of the interplanetary trajectory in terms of $N + 1$ planetary nodes is seen in Figure 7.27 around which the spacecraft exhibits predominant gravitational interactions. Dotted circles represent the SOI of each body. The Earth parking orbit (EPO) and capture orbit are depicted as solid lines around the departure and rendezvous bodies respectively. An example of a top level variable of the CSP are the *planetary nodes* (P) of the mission trajectory. P is an ordered set representing the planetary bodies from Earth departure to Pluto rendezvous which is as follows in Equation 7.61. The *planetary nodes* domain (D_p) is therefore intuitively a set of all the planets within the Solar System excluding Pluto seen in Equation 7.62 (since Pluto is the destination). Examples of constraints such as no repeated flybys of the same bodies and no use of Earth as the first powered flyby assist is implied by Equation 7.63.

$$P = \{p_0, p_1, ..., p_N, p_{N+1} \mid N \in \mathbb{Z},\ N > 0\} \tag{7.61}$$

$$D_p = \{Mercury, Venus, Earth, Mars, Jupiter, Saturn, Uranus, Neptune\} \tag{7.62}$$

$$C_p =< P,\ p_i \neq p_{i+1},\ p_1 \neq Earth > \tag{7.63}$$

The CSP formulation can now be used to structure the machine learning approach of a genetic algorithm (GA). Usually CSP is not a prerequisite for the use of GA's although it reduces the computational intensity by ignoring regions of the *search space* which are known to violate the constraints of the search problem.

7.6.8 Genetic Algorithm (GA) Search

Genetic algorithms are a form of local search methods which involve small changes being made to competing solutions until a termination condition is met, usually resulting in an optimal solution [4]. This technique is heavily inspired by biological evolution described by Charles Darwin: *"One general law, leading to the advancement of all organic beings, namely, multiply, vary, let the strongest live and the weakest die."* [22] This biological mimicry has been achieved by structuring the process with specific processes or elements that are designed according to the specific problem. The design specific to this problem are described here and results are seen in subsection 7.6.11.

1. *Representation*: The full trajectory solution is represented by the chosen chromosome design as shown in Figure 7.28. It is segmented into four separate gene sequences:

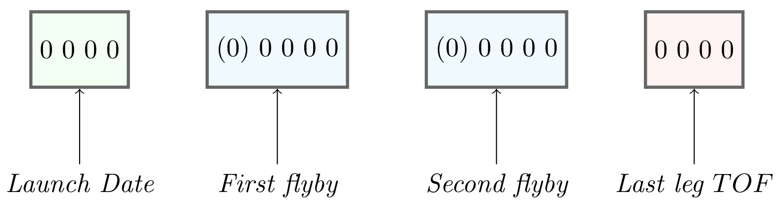

Figure 7.28: Chromosome representation of potential solutions.

(1) The *launch date* is represented by an integer value of days following the first of January 2025. This defines the launch date search space into the closed interval [2025-01-01 - 2052-05-18]. (2) The *first flyby*, which is required according to the CSP formulation in subsection 7.6.7, has two variables represented, namely the flyby planetary node (**0** 0 0 0 0) and the integer value of days for the first leg following launch (0 **0 0 0 0**). (3) The *second flyby* may or may not exist within the search space and follows from (2). (4) The *last leg TOF* represents the integer value of days for the last leg which could be from the first or second flyby depending on the number of flybys.

2. *Fitness*: The fitness function of the chromosomes, f(C), is evaluated based on their total required ΔV. The function used is as follows:

$$f(C) = 15.0 - \Delta V_{total} \quad \text{[km/s]} \tag{7.64}$$

As the standard is to maximise the concept of 'fitness' in genetic algorithms, the inverse relation was chosen. The offset value was chosen so as to eliminate uninteresting results with a ΔV of more than 15.0 km/s which was the estimate of a direct Hohmann transfer in subsection 7.6.6.

3. *Crossover*: The reproduction of chromosomes to form new ones inheriting genes from both 'parent' chromosomes constitute the definition crossover points within the chromosome. The illustration of a crossover between parent Y_1 and Y_2 to form children Z_1 and Z_2 is seen below.

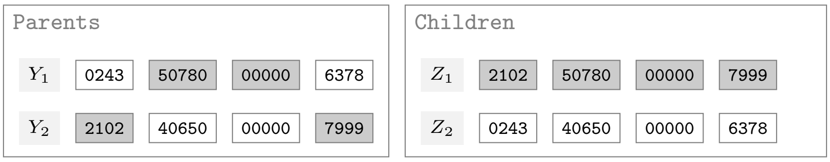

Figure 7.29: Crossover example between two chromosomes representing a Saturn flyby and a Jupiter flyby.

The method of crossover is simply the choice of a sequence of genes (represented by each box) from either parent Y_1 or Y_2 to be inherited by child Z_1 (represented by shaded boxes). All gene sequences not chosen are inherited by child Z_2. The choice is made simply by the cumulative of a uniform distribution function, F(x) where $x \in [0, 1]$, if $F(x_s) >= 0.5$ then the sequence is chosen from Y_1.

4. *Mutation*: The mutation is arbitrary defined to be a swap of one of the integers to any other value within its respective constraint. This is evaluated based on probability, where if $F(x_g) >= 0.5$, then a randomised swap occurs.

5. *Termination Criteria*: There is no explicit definition of the termination criteria due to no knowledge of the optimal solution, therefore termination occurs when stagnation has taken place for an arbitrarily defined number of generations. *Stagnation* occurs when the population loses diversity with very similar genetic sequences in all the chromosomes resulting in no variation in maximum fitness levels. The convergence accuracy was set such that no changes in fitness occurred over the evolution of 20 subsequent generations following a change.

7.6.9 Trajectory Optimisation Flowchart

Figure 7.30 shows a planetary flyby linked to the entire mission trajectory at its SOI by interplanetary legs determined by the Lambert's problem, as discussed in subsection 7.6.2. There exist three fixed boundaries describing the linked flyby, namely: E_0 and $\mathbf{r}_0$ at the start of the first leg, E_p and $\mathbf{r}_p$ defining the periapsis of the flyby and finally E_2 and $\mathbf{r}_2$ defining the aiming location and time following the flyby.

In order to solve the iterative linkage of the flyby with the Lambert's solutions discussed in subsection 7.6.4, the solution to the boundary conditions for the previous and following Lambert's solutions on the surface of the SOI, must be calculated using subsection 7.2.2 and subsection 7.2.3 using the epoch at the periapsis of the planetary flyby body and position of the centre of mass of the body for the first guess value.
$V_{planet,i}$ and $V_{planet,f}$ are defined by P's velocities at the entry position ($\mathbf{r}_i$) and exit position ($\mathbf{r}_f$) which are traversed at the entry (E_i) and and exit epochs (E_f) respectively. These velocities although are not accurate for the first guess due to the mismatch with the position on the surface of the SOI. Therefore the velocities for the Lambert solutions are assumed to be at the epoch of periapsis for the first guess.

Following the initial guess, the first iteration of the entry and exit positions on the SOI ($\mathbf{r}_i$ and $\mathbf{r}_f$) are known. These are then used to calculate the time since passage of periapsis (t_p) along with the orbital parameters determined from conversion of the state-vector using subsection 7.2.2. This is then repeated until the tolerance of error for the boundary conditions in terms of position and velocity are below one cm error.

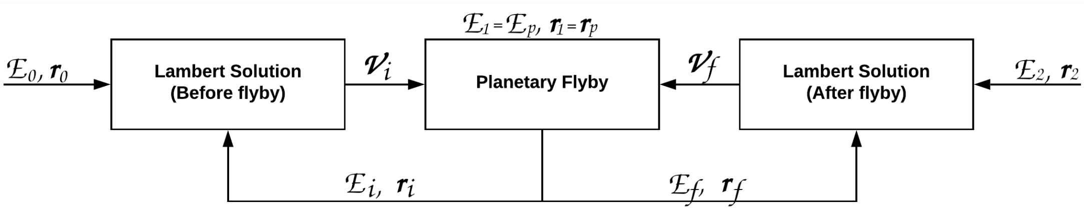

Figure 7.30: Flow-chart showing the inter-dependency between the boundary conditions at the planet P's SOI.

7.6.10 Trajectory Sensitivity Analysis

In order to investigate and evaluate the sensitivity and variability of the genetic algorithm's dependency on the defined evolution characteristics, three different settings are chosen: varied population sizes (P) and varied mutation rates (M) are chosen with the other kept constant. Each configuration is used to perform an evolution of 50 generations to provide insight into the convergence characteristics.

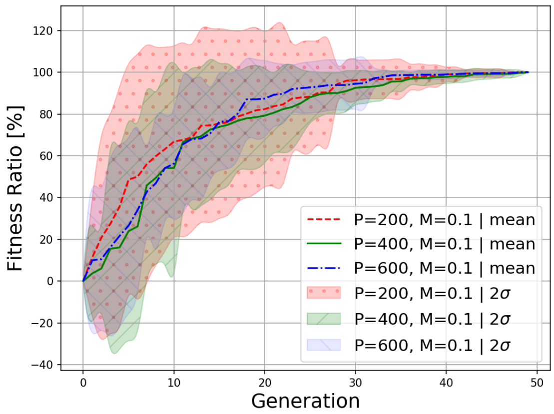

(a) Convergence characteristics for varied P.

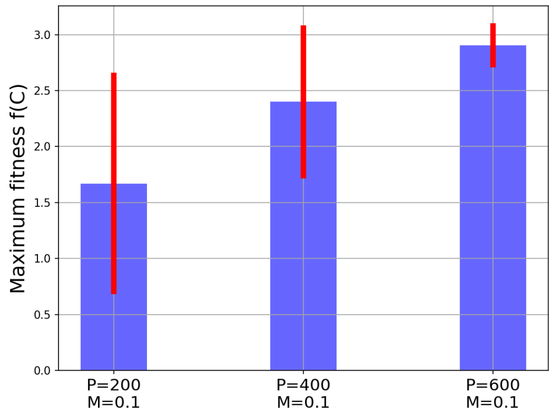

(b) Converged maximum fitness for varied P.

Figure 7.31: Performance of genetic algorithm for varied population sizes (P) after 50 generations.

Figure 7.31a depicts the normalised convergence over 50 generations. The normalisation is simply the percentage of the final converged fitness level following the evolution, where zero indicates the initial. This provides the basis of comparison for highly stochastic initial fitness levels. It can be seen that population has a distinct effect on the variability of the convergence to the final value. As the population size increases, the variability per generation series is seen to decrease with decreasing effect resembling that of a logarithmic relation. Due to the high variance, no supported hypothesis can be made on the mean line. Figure 7.31b shows a clear logarithmic relation to the final converged value over a quantity of generations, similarly the 2σ (standard deviation) interval exhibits and identical relation.

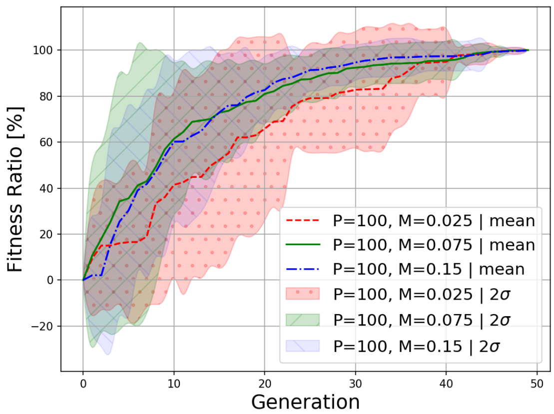

(a) Convergence characteristics for varied M.

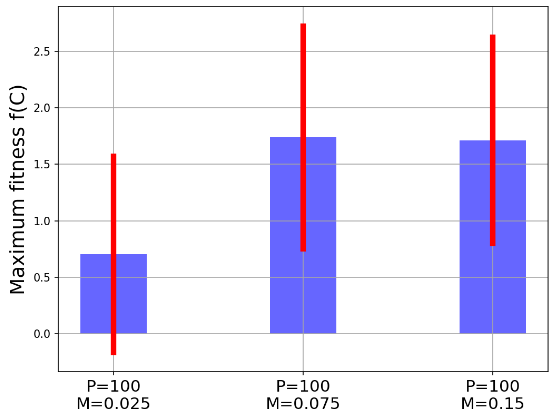

(b) Converged maximum fitness for varied M.

Figure 7.32: Performance of genetic algorithm for varied mutation rates (M) after 50 generations.

Figure 7.32a shows a high level of 2σ spread for all mutation rates chosen for the analysis. It is indistinguishable whether this is a result of introduction of high variability due to low population size of 100 as shown in Figure 7.31. Although, Figure 7.32a does show one distinguishable feature, namely the predominantly lower rate of convergence for the mutation rate of 2.5% over 50 generations. Figure 7.32 shows no distinct difference between the mutation rates of 7.5% and 15% which is potentially due to the noise, as mentioned, presented by the low population quantity. The final converged fitness does indicate that a higher level of mutation rate is desired, supported by the previous analysis of the convergence characteristics.

7.6.11 Optimised Interplanetary Itinerary

Following the optimal converged solution derived from the genetic algorithim discussed in subsection 7.6.8 using a population (P) of 600 and mutation rate (M) of 0.025, the chromosome derived is: `1057 50756 00000 7998`.

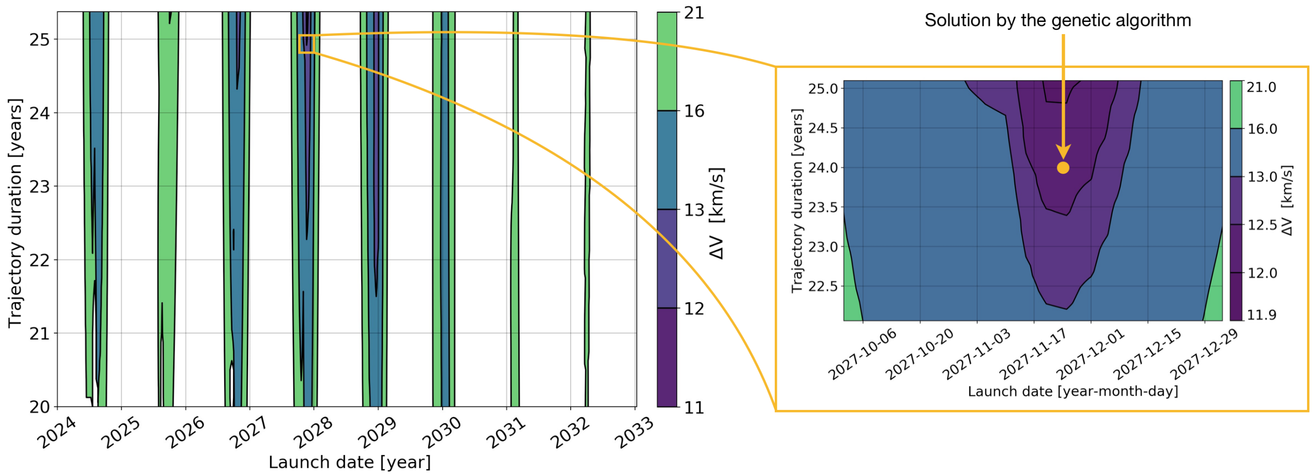

Figure 7.33: Pork-chop plot for the possible Earth-Jupiter-Pluto (EJP) trajectories.

Figure 7.33 shows the possible EJP solutions for the Orpheus mission providing a basis of evaluation for the final decided trajectory. `1057 50756 00000 7998` derived from the genetic algorithm is highlighted on the plot. Given the mission trajectory duration constraint of 24 years, it is seen that the final trajectory is optimal.

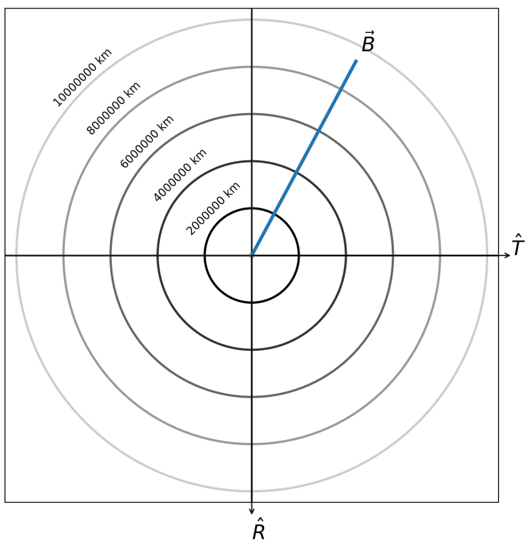

(a) B-plane targeting flyby assist.

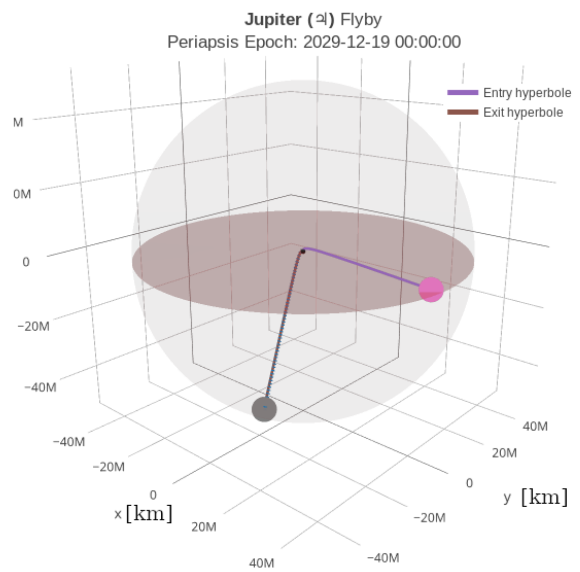

(b) Powered flyby assist within the Jovian ICRS inertial frame.

Figure 7.34: Interplanetary trajectory Jupiter powered flyby assist.

Figure 7.34a shows the B-plane targeting for the flyby gravity assist around Jupiter. The B-plane itself is a plane perpendicular to the spacecraft orbital plane. The B-vector is defined to be on this plane and shows the location of aiming on approach of the planet to achieve the desired flyby. This position is the intersection of the approach asymptote with the plane perpendicular to the asymptote itself. $\hat{T}$ is arbitrarily set to intersect with the equatorial plane. The following is a summarising conclusion of the itinerary parameters defining the interplanetary trajectory.

Earth departure

Earth departure is set for the 24th of November, 2027. The position of entry into the heliocentric frame is provided as used by the Lambert's solution.

$E_f = 2027 - 11 - 24 \;\; 07:02:24$ TDB
$\mathbf{r}_f = \{71556108\,\vec{i} + 118147193\,\vec{j} + 5122214\,\vec{k}\}$ km

---

Jupiter flyby

The boundary conditions for the entry and exit of the Jupiter SOI are provided. Additionally the orbital plane is defined fully.

Entry

$E_i = 2029 - 10 - 08 \quad 23:44:49$ TDB
$\mathbf{r}_i = \{-609448483\,\vec{i} - 447240345\,\vec{j} - 172983080\,\vec{k}\}$ km
$a_i = -2466140$ km
$e_i = 1.279$

Exit

$E_f = 2030 - 02 - 27 \;\; 07:02:24$ TDB
$\mathbf{r}_f = \{-551243940\,\vec{i} - 569140739\,\vec{j} - 263796285\,\vec{k}\}$ km
$a_i = -2404079$ km
$e_i = 1.287$

Orbital Plane

$i = 61.76$ deg
$\Omega = 354.20$ deg
$\omega = 139.97$ deg

Pluto rendezvous

Finally the boundary condition for the entry of Pluto's SOI is provided.

$E_i = 2051 - 11 - 12 \;\; 00:00:00$ TDB
$\mathbf{r}_i = \{5740445392\,\vec{i} - 1305648920\,\vec{j} - 2137022937\,\vec{k}\}$ km

7.7 Verification of Interplanetary Trajectory Analysis

After completing the calculations it is of course now necessary to verify and validate those results; this will be done primarily with the use of GMAT. Each module of the toolbox, made up of the Lambert's solver and the gravity assist module, will be individually verified, followed by a full trajectory verification and validation.

Throughout the verification procedure, various GMAT propagators are used depending on the accuracy and speed of propagation required. These propagators are outlined in Table 7.10. It should be noted that per GMAT documentation recommendations, the integration scheme used throughout is “PrinceDormand78”, the minimum step size is 0, and the accuracy is determined on a case by case experimentation basis [138].

Table 7.10: Propagation parameters for each GMAT propagator used in the verification procedure.

Propagator	Max step size [s]	Accuracy	Central body	Point masses
Deep Space	864000	10^{-12}	Sun	Sun, Jupiter, Saturn, Uranus, Neptune
Deep Space Simple	864000	10^{-12}	Sun	Sun
Deep Space Simple (Short)	86400	10^{-12}	Sun	Sun
Near Jupiter	2700	10^{-11}	Body	Jupiter, Europa, Ganymede, Callisto, Io
Near Jupiter Simple	86400	10^{-11}	Body	Jupiter
Near Pluto	86400	10^{-11}	Pluto	Pluto, Charon, Sun
Near Charon	86400	10^{-11}	Charon	Pluto, Charon, Sun

7.7.1 Lambert's Solver Verification

In order to verify the Lambert's solver module, a relatively simple case is taken in which only the Sun is considered an attractor: namely an Earth-Jupiter-Pluto itinerary with chromosome 1057 50756 00000 7998. The verification procedure is as follows:

1. The initial state vector for the first leg from the Lambert's solution is used to instantiate the Orpheus spacecraft in GMAT; from this point the spacecraft is propagated using the Deep Space Simple (DSS) propagator.
2. Once the spacecraft reaches Jupiter's SOI, it is then propagated to the closest approach to Jupiter, at which point the velocity vector of the spacecraft is manually changed to impose the velocity vector needed for the second leg of the Lambert's solution. During this, the propagator is switched from DSS to DSSS; this reduces the maximum step size such that the spacecraft does not overshoot the closest approach to Jupiter.

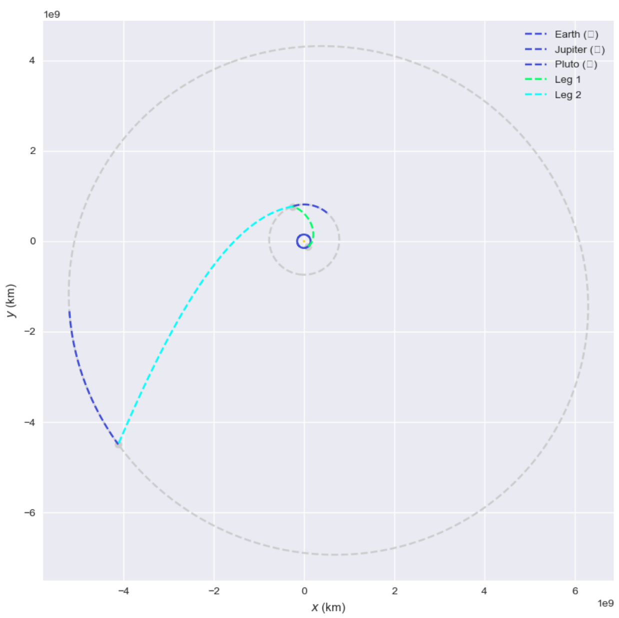

(a) Calculated Full Trajectory

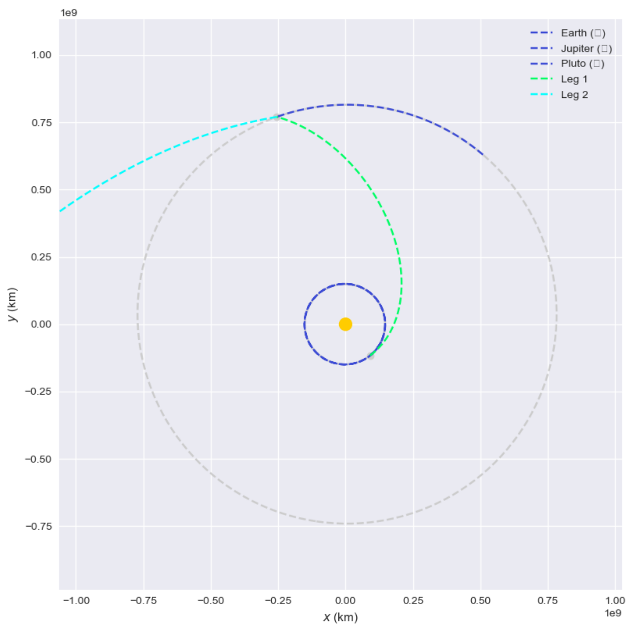

(b) Calculated Earth to Jupiter Trajectory

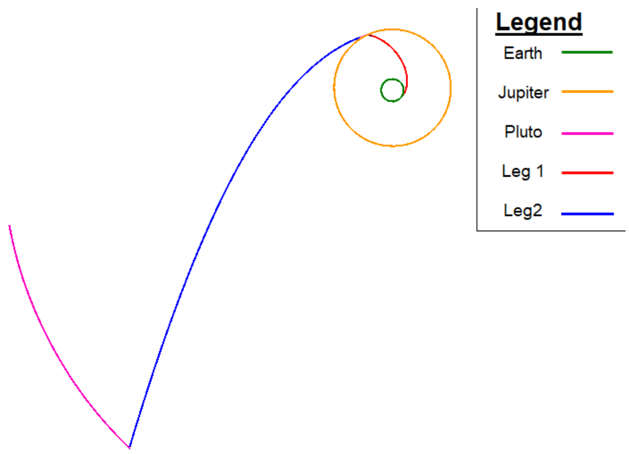

(c) Simulated Full Trajectory

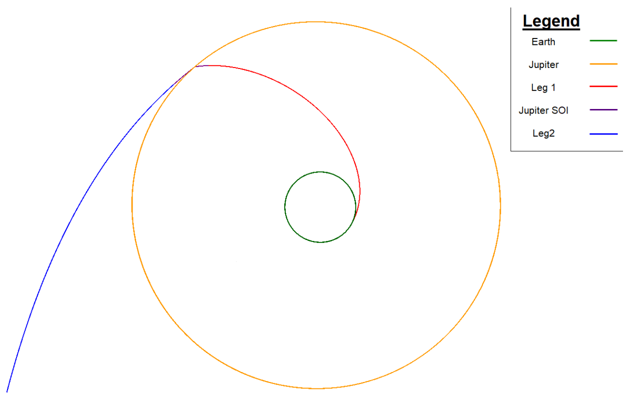

(d) Simulated Earth to Jupiter Trajectory

Figure 7.35: Verification of Lambert's Solution

3. The propagator is then switched back to DSS, and the spacecraft is propagated to the closest approach to Pluto.

Shown in Figure 7.35 are the calculated Lambert's solutions alongside the GMAT simulation; promisingly the plots appear identical, however it is also necessary to inspect the numerical similarity of the simulation. For this the closest approach and arrival times to both Jupiter and Pluto are analysed. The simulated closest approach to the location of Jupiter (if Jupiter were not there), $r_{p,J}$ is 520km, which is within the radius of the planet and can be considered to coincide with the centre of the planet, therefore the first leg is verified. The closest approach to Pluto, $r_{p,P}$ is 269,000km, which is $0.085R_{SOI_P}$, where R_{SOI_P} is the sphere of influence of Pluto; since the spacecraft is found to be well within the SOI of the Pluto-Charon system, the second leg can also be considered verified.

The date of arrival to Jupiter and Pluto found in the simulation are 19 Dec 2029 00:00:37 and 09 Nov 2051 09:50:28 respectively; whereas the calculated arrival dates are 19 Dec 2029 00:00:00 and 12 Nov 2051 00:00:00. Clearly the arrival time to Jupiter is not a problem (the difference is only 37s); additionally the difference of around 3 days at Pluto can be justified by considering that this is only a difference of 0.04% of the total Jupiter-Pluto leg. Upon completing the script for the Lambert's solver, it passed the verification test first time, and so no further correction and re-verification is required.

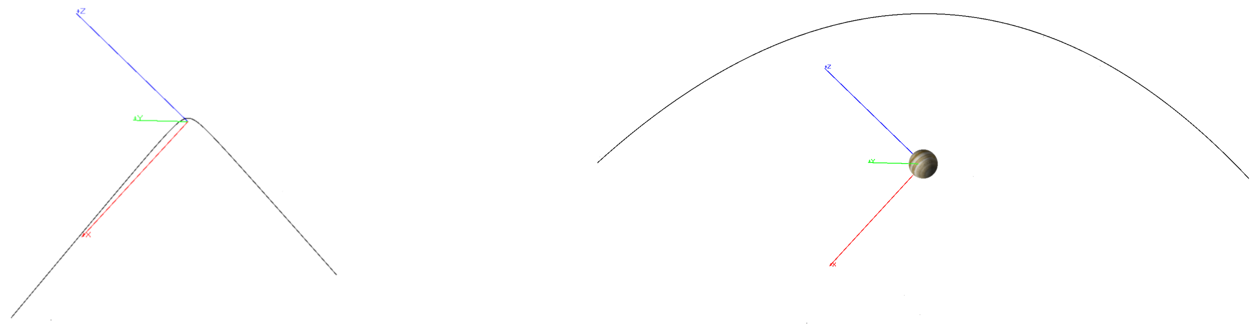

(a) Visualisation of gravity assist used for verification (b) Close-up visualisation of gravity assist used for verification

Figure 7.36: GMAT visualisation of the gravity assist derived from chromosome 1057 50756 00000 7998.

7.7.2 Gravity Assist Verification

The next module to be verified is the gravity assist module, which will again be verified in GMAT, using the output of the refined analysis shown in subsection 7.6.11. The procedure for this module test is as follows, with the Near Jupiter propagator used throughout:

1. The initial state of Orpheus is taken to be on entry to the SOI of Jupiter, this can be defined in GMAT either in Cartesian vector format, or by Keplerian elements of the hyperbolic orbit around Jupiter (both of which are defined in subsection 7.6.11).
2. Orpheus is then propagated to Jupiter periapsis, at which point the achieved periapsis radius (among other things) can be compared with the calculated value. At this point the correction manoeuvre defined in subsection 7.6.4 can also be applied.
3. Finally, Orpheus can then be propagated to the SOI exit point, where the state vector and Keplerian parameters can be compared to the calculated ones.

Figure 7.36 shows a visualisation of the gravity assist verification process, in which the spacecraft trajectory is shown in black (the coordinate system used is an International Celestial Reference Frame (ICRF) system centred on Jupiter). Figure 7.36a is an overview of the assist, and clearly shows the hyperbolic orbit and its asymptotes. Figure 7.36b is a view of the trajectory as seen closer to Jupiter itself, and it shows the spacecraft to indeed be passing at an appropriate altitude.

For a more concrete verification of the assist module, one should refer to Table 7.11, in which the calculated results (from subsection 7.6.11) and the GMAT simulated results are shown along with the % difference between them (defined as the difference in values divided by the calculated value). When referring to the reference frame column, H stands for Heliocentric, while J stands for Jupiter; also X, Y, Z and VX, VY, VZ represent the positional coordinates and velocity components respectively. It can be seen that the majority of variables are within a few % of each other, showing that the module is sufficiently accurate . The exception to this is the semi-major axis (a) of the orbit, which has a discrepancy of over 10%; this can be justified since for a hyperbolic orbit, a is incredibly sensitive [86], so a 10% difference is acceptable.

It should be noted that some parameters shown have a difference of 0, this is because those parameters are used to instantiate the spacecraft.

7.7.3 Full Trajectory Verification

With the individual modules of the tool independently verified, it is now possible to begin verification of the entire mission trajectory in GMAT, using the results of subsection 7.6.11. The procedure for the verification is as follows:

1. Orpheus is instantiated in GMAT with a heliocentric state vector, as it leaves the SOI of Earth. From here the spacecraft is propagated to Jupiter's SOI (using Deep Space Simple, DSS, propagator).
2. At this point the propagator is switched over to Near Jupiter, and the spacecraft is propagated to periapsis, at which point the relevant correction manoeuvre is performed.
3. Orpheus is then propagated to the edge if Jupiter's SOI, where the propagator is changed back to the DSS propagator.
4. Finally, the spacecraft is propagated to Pluto's closest approach, where the distance from Pluto and time of flight can be recorded for analysis.

Table 7.11: Numerical Results of the Gravity Assist Verification

Parameter	**Symbol**	**Unit**	**Reference Frame**	**Calculated**	**Simulated**	**%Difference**
Jupiter Periapsis						
VX	-	km/s	J-ICRF	-13.86	-13.39	3.36
VY	-	km/s	J-ICRF	-6.06	-6.38	5.28
VZ	-	km/s	J-ICRF	-13.84	-13.81	0.23
Radius of Periapsis	-	km	H-ICRF	689,000	698,000	1.31
Jupiter Exit						
X	-	km	H-ICRF	-551,000,000	-547,000,000	0.70
Y	-	km	H-ICRF	-569,000,000	-571,000,000	0.29
Z	-	km	H-ICRF	-264,000,000	-262,000,000	0.59
VX	-	km/s	H-ICRF	10.37	10.72	3.37
VY	-	km/s	H-ICRF	-11.11	-11.20	0.76
VZ	-	km/s	H-ICRF	-9.77	-9.66	1.12
Keplerian Parameters						
Semi-Major axis	a	km	J-ICRF	-2,400,000	-2,650,000	10.37
Argument of Periapsis	ω	$^\circ$	J-ICRF	140	141	0.91
Inclination	i	$^\circ$	J-ICRF	61.8	60.8	1.52
Longitude of Ascending Node	Ω	$^\circ$	J-ICRF	354	354	0.00
Eccentricity	e	-	J-ICRF	1.287	1.263	1.83
Radius of Periapsis	rp	km	J-ICRF	689,000	698,000	1.31
Arrival Epoch	-	days	-	08/10/2029 23:44	8/10/2029 23:44	0.00
Departure Epoch	-	days	-	27/02/2030 07:02	2/3/2030 00:43	0.01
Assist Duration	-	days	-	141	144	1.94

Figure 7.37 shows a visualisation of the total trajectory, in which a sun-centres ICRF coordinate system is used. Figure 7.37a shows a close-up of the first leg of the trajectory, showing the spacecraft (red) leaving Earth's orbit (green) towards Jupiter's orbit (orange); the small blue section represents the region where the spacecraft is inside Jupiter's SOI before continuing it's journey. Figure 7.37b shows the remainder of the trajectory to Pluto (pink), and it can be clearly seen that Orpheus does indeed have a close approach with Pluto.

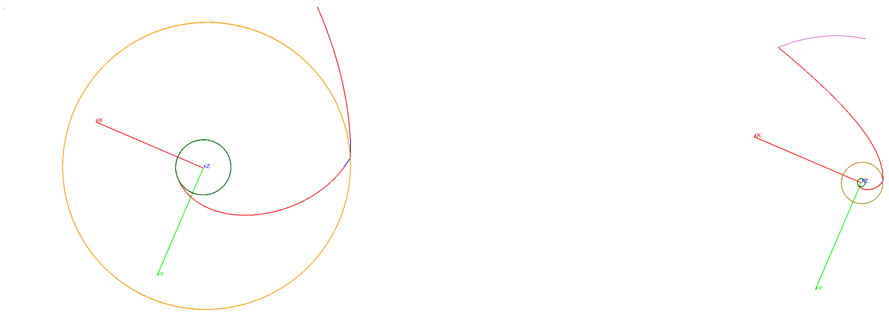

(a) Visualisation of the full trajectory, with a close-up of the Earth-Jupiter leg

(b) Visualisation of the full trajectory

Figure 7.37: GMAT visualisations of the entire trajectory of Orpheus defined by chromosome 50756 00000 7998.

For a more numerical representation of the trajectory verification, refer to Table 7.12, which compares the calculated results of the mission (shown in subsection 7.6.11) with the results simulated in GMAT for various stages of the trajectory. It can be seen that the majority of parameters are within a few % of each other, proving the calculated solution to be sufficiently accurate. There are however a few exceptions to this, outlined as follows: VX for Jupiter entry: the difference here is 15%, which appears considerably higher than the the other velocity components. however the magnitude of the error is approximately equal ($\approx$ 0.05 km/s). The higher % can therefore be attributed to the lower overall magnitude of VX being significantly less than VY or VZ. In addition the semi-major axis (a) around Jupiter also has a large error of over 11%, this can be justified in a similar manner as the discrepancy also found in subsection 7.7.2.

In the simulation, the closest approach to Pluto is 35934633 km (which is equal to 0.24AU, or 11 Pluto SOI radii); this may seems substantially high although it is only 0.16% of the distance from the Sun to Pluto, so it is indeed a very close approach, which can be easily finalised in later design phases.

In addition the arrival epoch in the simulation is 09 Dec 2050, again this may seem a lot compared to the calculated value of 12 Nov 2051. However compared to the total mission time is only a discrepancy of 4%, in addition the

Table 7.12: Numerical Results of the Trajectory Verification

Parameter	Symbol	Unit	Reference Frame	Calculated	Simulated	%Difference
Jupiter Entry						
X	-	km	H-ICRF	-609,000,000	-609,000,000	0.02
Y	-	km	H-ICRF	-447,000,000	-450,000,000	0.56
Z	-	km	H-ICRF	-173,000,000	-174,000,000	0.69
VX	-	km/s	H-ICRF	0.36	0.41	14.55
VY	-	km/s	H-ICRF	-8.31	-8.27	0.46
VZ	-	km/s	H-ICRF	-3.94	-3.92	0.38
Jupiter Periapsis						
VX	-	km/s	J-ICRF	-13.86	-13.34	3.75
VY	-	km/s	J-ICRF	-6.06	-6.43	6.20
VZ	-	km/s	J-ICRF	-13.84	-13.46	2.76
Radius of Periapsis	rp	km	J-ICRF	689,000	718,000	4.15
Jupiter Exit						
X		km	H-ICRF	-551,000,000	-548,000,000	0.61
Y		km	H-ICRF	-569,000,000	-571,000,000	0.41
Z		km	H-ICRF	-264,000,000	-262,000,000	0.66
VX		km/s	H-ICRF	10.37	10.62	2.42
VY		km/s	H-ICRF	-11.11	-11.27	1.42
VZ		km/s	H-ICRF	-9.77	-9.62	1.60
Departure epoch		days	-	32,560	32,560	0.01
Assist Duration		days	-	141	140	0.37
Keplerian Parameters						
Semi-Major axis	a	km	J-ICRF	-2,470,000	-2,740,000	11.30
Argument of Periapsis	ω	°	J-ICRF	140	141	0.64
Inclination	i	°	J-ICRF	61.8	60.1	2.79
Longitude of Ascending Node	Ω	°	J-ICRF	354	354	0.01
Eccentricity	e	-	J-ICRF	1.28	1.26	1.40
Radius of Periapsis	rp	km	J-ICRF	689,000	718,000	4.15
Arrival Epoch	-	days	-	32,420	32,420	0.01

difference is such that the true arrival time is sooner than the calculated one, which means the calculation tool produces a conservative estimate.

8 Mission Functional Analysis

This chapter presents the mission functional analysis performed, incorporating design decisions taken in previous and present project phases. The first section contains the functional flow block diagram, while the second presents the functional breakdown structure. The functional analysis serves to provide insight on the mission and is the basis for the design process.

8.1 Functional Flow Diagram

The functional flow block diagram presented in the Baseline Report [28] is updated and made more specific to the Orpheus mission. The resulting diagram is presented in two parts, in Figure 8.2 and Figure 8.3. The legend of the functional flow block diagram can be found in Figure 8.1.

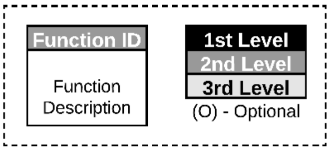

Figure 8.1: Functional flow block diagram - Legend

In order to maintain a relatively low complexity, repeated actions were only detailed upon once. For example, 4.12 is representative of all manoeuvres performed throughout the mission. There are also several optional functions that depend on the situation at hand, like 5.16 and 7.7, which can only be performed if the insertion trajectory passes by a moon of Pluto.

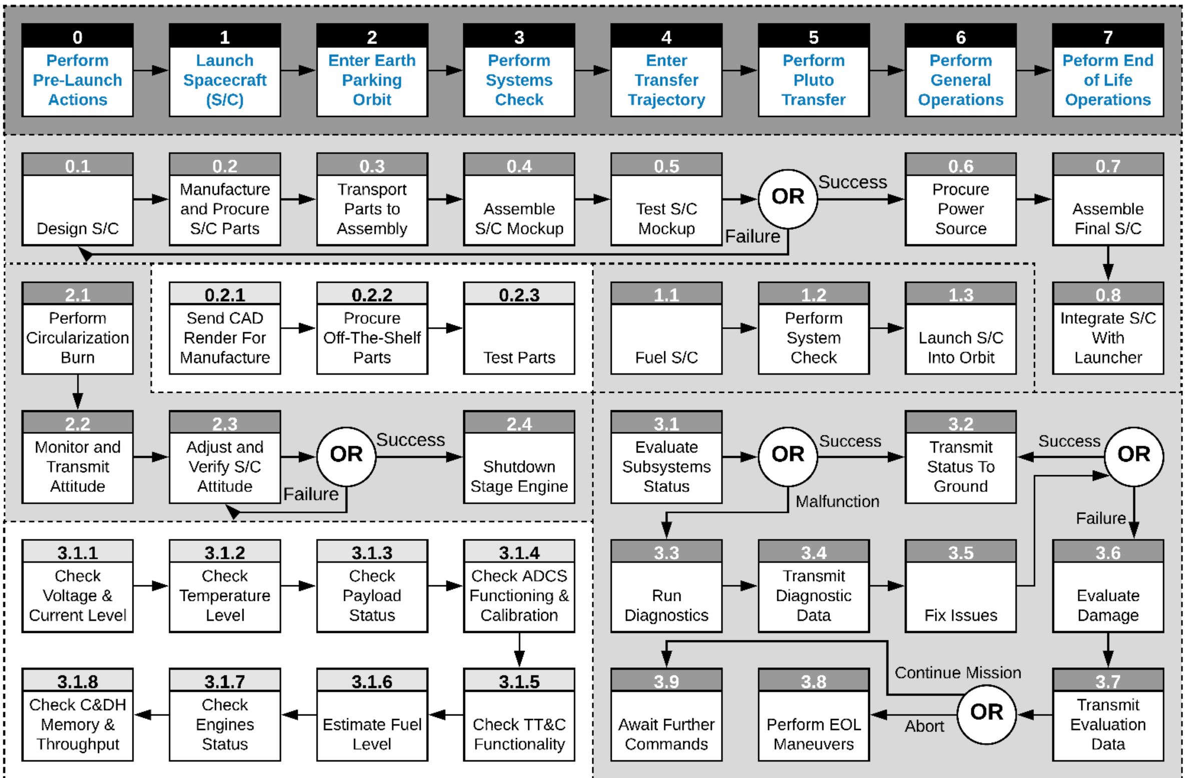

Figure 8.2: Functional flow block diagram - Part 1.

8.2 Functional Breakdown Structure

Since the functional flow diagram is already defined, a functional breakdown structure diagram is made and can be found in Figure 8.4. As already mentioned in the Baseline Report [28], the break down structure presents lower level activities that need to be accomplished before the top level is satisfied. Hence, the mission is only successful when each of the presented actions is fulfilled. As can be seen in the diagram, the transfer trajectory phase involves many separate activities and the operations shall be clearly defined before the launch.

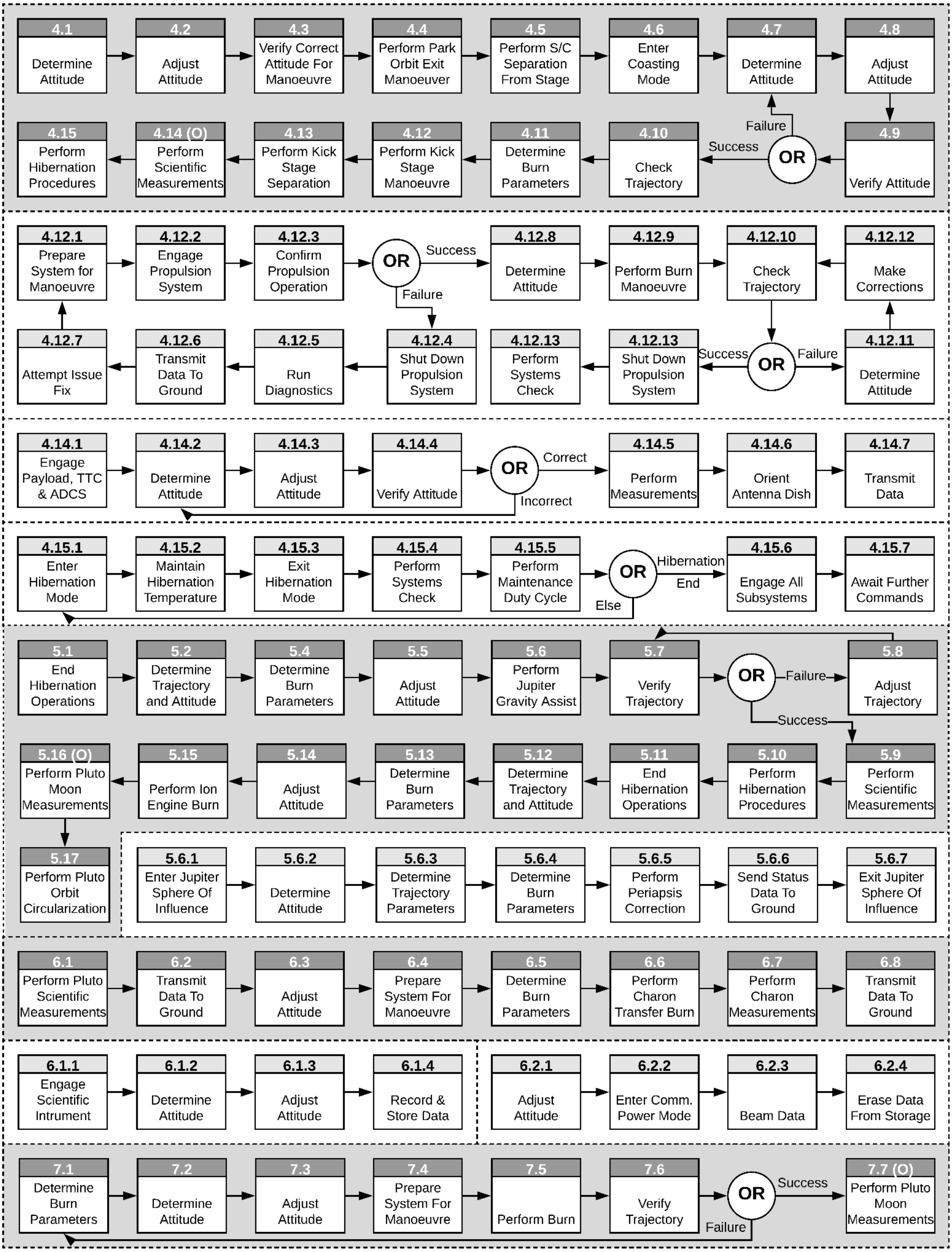

Figure 8.3: Functional flow block diagram - Part 2.

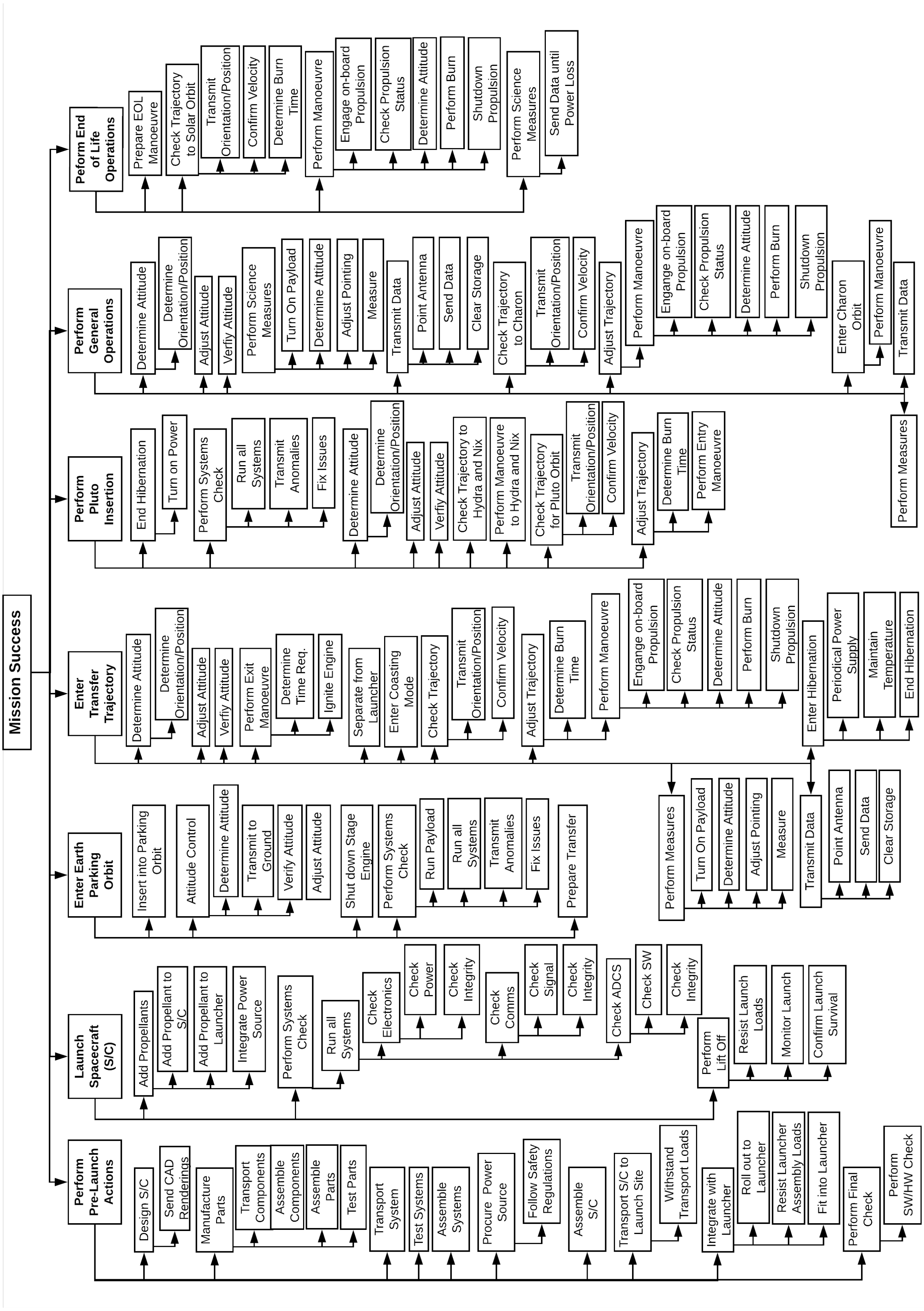

Figure 8.4: Functional Breakdown Structure

9 Power

This chapter analyses the Orpheus power system, which is comprised of 3 General Purpose Heat Sources (GPHS)-Radioisotope Thermal Generator (RTG). The second option using a Fission reactor is deemed unfeasible and impractical. This is due to its low level of development and the time, which will be required to qualify(both technical and non technical) this design for a space mission(Internal discussion with Dr. Angelo Cervone). The power source selection is explained and reasoned, the Electrical Power System (EPS) architecture is designed and presented. The design is based on the architecture of New Horizons, and this existing system design is used and altered only to account for the additional systems, which New Horizons did not have. This is done as the New Horizons EPS is a tried and tested configuration, and thus verified.

9.1 EPS Requirements

The EPS subsystem requirements are stated in Table 9.1. The EPS subsystem design took into account all requirements and ensured all are verified in section 9.5.

Table 9.1: EPS Requirements

Identifier	Requirement	Traceability
R-EPS-010	The EPS module shall be able to provide a minimum peak power of 670 W until the end of the electrical manoeuvre (24 years).	R-MIS-071
R-EPS-020	The EPS module shall have a mass of no more than 220 kg.	R-MIS-010
R-EPS-030	The EPS module shall not cost more than USD 353 million (2018).	R-MIS-091
R-EPS-040	The EPS module shall be able to dissipate excess heat power.	R-MIS-010
R-EPS-050	The EPS module shall contain a hibernation mode.	R-MIS-010
R-EPS-060	The EPS shall not pollute the Pluto or Charon environment.	R-MIS-160

The 670 W until the end of the electrical manoeuvre (24 years), is calculated based on the power needed by the Ion engines (630 W) [54] and the other active systems during the burn.

The 220 kg arises based on the mass distributions of the spacecraft and payload capabilities of the launcher.

9.2 Power Source Selection

The GPHS-RTG uses Plutonium-238 to generate thermal energy, which is then converted into electric energy [146]. This heat source is extensively used in previous space missions such as New Horizons and Cassini [15] [113]. This type of RTG produces approximately 300 Watts of power at the beginning of life (BOL) and has a mass of 56 kg [44]. The half life ($\lambda_{1/2}$) of plutonium-238 is 89 years [114], the power degradation of the RTGs is calculated using Equation 9.1. P_0 is the initial power, and t is the time [153].

$$P = P_0 \exp\left(\frac{-0.693t}{\lambda_{1/2}}\right) \tag{9.1}$$

The NASA NEXT ion thruster requires 630 W from the EPS throughout the burn [54]. Since other spacecraft systems are not fully operational during the ion thruster burn, they do not require substantial power. A contingency of 20%, as set by ESA standards, is applied to the power delivery capabilities of the RTGs, and as such, 4 RTGs are necessary. The power that the RTGs are able to deliver at the end of the electrical propulsion burn (24 years) is 667 W (including marging) using Equation 9.1.

However 796 W is far more power than needed for the spacecraft operations, as seen in chapter 17. If the power contingency is lowered from 20% to 10%, using 3 RTGs becomes a feasible option. This results in 670 Watts of power available at the end of the ion thruster burn. This reduction is reasoned with the fact that the majority of subsystems power budgets are known in detail and are likely to not increase increase throughout the future spacecrafts design. Using 3 RTGs leads to a reduction in over 117 million USD and 56 kg, therefore it is clear using 3 RTGs is the optimum configuration.

9.3 EPS Architecture

The EPS architecture can be seen in Figure 9.1. The arrows indicate the direction of the data flow between the subsystems.

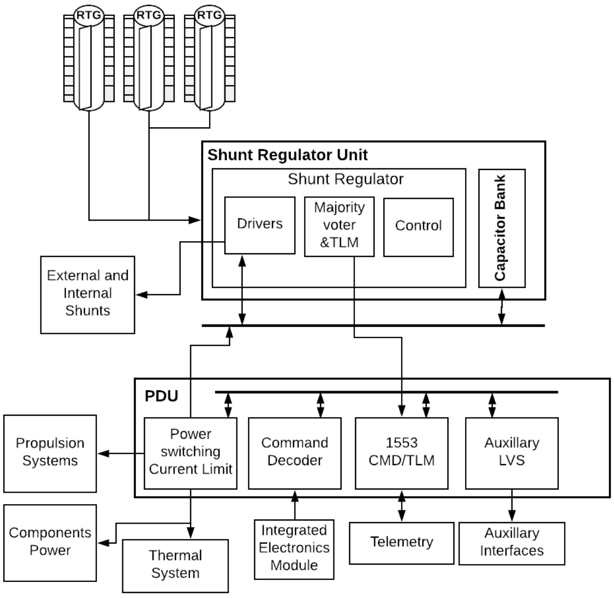

Figure 9.1: EPS Architecture

The power management and distribution system is sub divided into two main blocks, the shunt regulator unit and the Power Distributor Unit (PDU). The shunt regulator functions to control and regulate the power output of the RTGs to the PDU. The PDU governs the transmission of the power to the spacecraft subsystems, as well as monitoring these subsystems. As mentioned before, this system is taken from the New Horizons spacecraft.

The major components used in the EPS are explained below (Personal conversation B.S. Maurits van Heijningen (DARE)):

Capacitor bank: Used to ensure a stable output power, in case the RTG output varies. If this occurs, the capacitor can discharge some of its power and guarantee the output power does not vary.
Control: Used to control which drivers are active, the regulators and capacitor banks.
The Majority Voter & TLM: Determines if a certain amount of requirements are met and if so it will allow the shunt regulator to perform a command.
The Drivers: The actual hardware that performs the actions when a signal is received.
The Command Decoder: Receives signals from the integrated electronics module, and transmits signals to the other components informing them what function to perform.
Power Switching Current limit: Used to power on and off the subsystems of the spacecraft. In case of an electronic fault the power switches off to minimise any damage.
The 1553 CMD/TLM: Used to interface with the telemetry to ensure it is powered when needed.
External and Internal Shunts: Used to dissipate extra heat away from the system, when power is not needed[34].
The Auxiliary Low Voltage System: Is used to control the auxiliary interfaces, which are minor.

9.4 Power Management and Distribution System

The power management and distribution system controls, regulates and distributes all the power from the RTGs to the subsystems. The electrical distribution system (harness) of a satellite consists of all cabling and connectors, which are used to connect components and systems together [40]. This also includes the insulation which is required to prevent electromagnetic disturbances. The New Horizons spacecraft had a power distribution system mass of 4.3 % of the total spacecraft mass, which is 20.5 kg. In the case of the Orpheus spacecraft, the mass slightly increases due to extra valves needed, the additional ion system and higher power consumption. The final harness mass is sized based on the ESA standards [76]. Using these standards the harness mass is 5 % of the nominal dry mass, resulting in a mass of 38.8 kg. Since the harness does not include the Power Control Unit (PCU) an estimate is needed for this unit, this is calculated using Equation 9.2 [153].

$$M_{PCU} = 0.0045 P_{BOL} \tag{9.2}$$

M_{PCU} is the mass of the PCU and P_{BOL} is the power of the spacecraft at the beginning of life. A resulting PCU mass of 3.7 kg is determined. The total power management and distribution system mass is therefore 42.7 kg.

This being the preliminary mass, a contingency of 20 % is applied to account for growth, in accordance with ESA standards [76].

9.5 EPS Verification and Validation

This section discusses the verification and validation of the EPS design. Many of the components used in the EPS are flight proven parts. These parts are bought off-the-shelf from a manufacturer and thus much less verification is needed. Integration of components does require a complete verification, additionally verification of the parts ordered are verified once again to ensure a high reliability. Table 9.1 contains all EPS requirements and their relevant tracer.

The GPHS-RTGs uses an already existing design, which has been used on many missions, therefore it has been verified and largely validated by the manufacturer. As previously mentioned, the power output of the RTG deteriorates according to Equation 9.1. Using this equation it is calculated that the 3 RTGs provide 272 Watts of power at the end of 24 years, thus meeting requirement `R-EPS-010`. In order to verify this requirement, a simulation of the degradation is performed to model the power output decrease.

Each GPHS-RTG costs 117 million USD [50]. Thus in total the cost of 3 RTGs is 351 million USD, which is within the the allocated budget of 353 million USD, meeting requirement `R-EPS-030`.

The EPS has external and internal shunts, used to dissipate any excess heat created from the RTGs, to ensure the system does not overheat. This fulfils requirement `R-EPS-040`. This additional heat occurs as high amounts of power are required for the ion propulsion system. However, after the ion engines are shut down, there is an excess of power available from the RTGs. Verification is done by means of simulating the heat dissipated, and later by a test in a vacuum chamber such as the Large Space Simulator (LSS) [106].

The EPS module contains a hibernation mode, which powers down non-essential systems. This occurs after the Jupiter gravity assist, as the payloads and other systems will not be fully operational during the transfer from Jupiter to Pluto. By implementing the hibernation mode, requirement `R-EPS-050` is fulfilled. This mode is simulated, to verify if the hardware functions as intended.

The EPS system shall not contaminate the Pluto-Charon system. Therefore 3 RTGs are not staged and remain attached to the spacecraft for the entire mission life. No part or by-product of the EPS will come into contact with Pluto or Charon, hence meeting the requirement `R-EPS-060`. In order to verify if the EPS module can withstand the launcher lateral and longitudinal loads, an acceleration test will be required to simulate the launch loads and to inspect if the system can withstand the loads. This will be done by means of a centrifuge. This will satisfy requirement `R-SYS-120`. However its is not possible to place the RTGs in a centrifuge, the smaller components will be placed.

The EPS module is subjected to a vibration test to ensure it can handle both the lateral and longitudinal vibrations. The RTGs are also tested as done to the RTGs used upon the New Horizons mission [84]. The test verifies that the EPS meets requirement `R-SYS-130`.

The subsystem components is subjected to a vacuum test, where the entirety of the system is placed within a vacuum chamber, to investigate how its performance changes. By doing so, requirement `R-SYS-130` is fulfilled. The EPS module is also be subjected to acoustic loads in the Large European Acoustic Facility [131], to verify it complies with `R-SYS-100`.

The overall EPS will only be able to be validated once the mission has been completed. The EPS will power the spacecraft for the entire 25 year mission duration. After which it may be validated. However, it will likely continue powering the spacecraft after the 25 year period, as the GPHS-RTGs will be able to operate for longer than this.

section 18.5 Includes further system verifications test of the EPS.

9.6 EPS Sustainability

Since the design of Orpheus includes a radioactive power source, it is important to consider the possible environmental consequences. Proposed safety features to the RTG, to mitigate the impact on the environment on Earth and in space, can be found below [99].

- Modularity: the RTG disassembles in case of a launch failure, minimising the terminal velocity and thus the impact.
- Aeroshell module: is composed of a carbon-carbon Fine Weaved Pierced Fabric to strengthen it curing re-entry.
- Iridium Fuelled Clads: has a melting temperature of 2245 °C and provides even more strength to the module during impact.
- PuO_2 fuel: shatters into none-respirable pieces upon impact and is insoluble in water.

The RTGs will not be staged at any point during the mission to ensure no contamination of any celestial bodies.

10 Propulsion Design

This chapter elaborates on the propulsion subsystem. This system is designed based on the ΔV budget which is simulated in chapter 7 and listed in Table 17.4. First propulsion requirements and design philosophy are presented. Second the bi-propellant, mono-propellant and electrical propulsion system are designed. Third a sensitivity analysis is performed after which the design requirements are verified and validated.

10.1 Propulsion Requirements

The propulsion subsystem requirements are stated in Table 10.1. The design of the propulsion subsystem took into account all requirements, which are all verified in section 10.8.

Table 10.1: Propulsion Requirements

Identifier	Requirement	Traceability
R-PRP-010	The propulsion subsystem shall adhere to ESA margin standards (SRE-PA/2011.097/).	R-SYS-090
R-PRP-020	The selected in-space propulsion subsystem shall have TRL 6 or above.	R-MIS-030
R-PRP-030	The electrical propulsion subsystem shall require a maximum peak power of below 640 watts at EOL.	R-MIS-010
R-PRP-040	The propulsion subsystem shall have total dimensions not exceeding 4 x 1.5 x 1.5 m.	R-MIS-080
R-PRP-050	The electrical subsystem shall be able to provide thrust for minimum 12.1 years.	R-MIS-071
R-PRP-060	The chemical subsystem shall be re-ignitable for a minimum of 5 times.	R-MIS-020
R-PRP-070	The electrical subsystem shall provide minimum 6060 m/s .	R-MIS-071
R-PRP-080	The bi-propellant subsystem shall provide minimum 986 m/s.	R-MIS-071
R-PRP-090	The mono-propellant propulsion subsystem shall provide minimum 150 m/s.	R-MIS-020
R-PRP-100	The fuel tanks shall be compatible with hydrazine.	R-MIS-030
R-PRP-110	The oxidiser tank shall be compatible with Mon-3.	R-MIS-030
R-PRP-120	The electrical ion thruster shall have a thrust vectoring system.	R-MIS-071
R-PRP-130	The propulsion subsystem shall not exceed a total cost of USD 50 million (2018).	R-MIS-091
R-PRP-140	The propulsion subsystem shall be a maximum of 215 kg	R-MIS-060

10.2 Design Philosophy

After conceptual sizing of the propulsion subsystem in the Midterm Report [27] it is clear that with the current technology and the single-launch requirement it is impossible to fulfil the mission with a single chemical propulsion stage, such as Cassini or New Horizons [121]. In this case, the propellant mass would be more than 8 tons, requiring in-orbit refuelling or multiple launches, which does not comply with `R-MIS-050`. Therefore, a hybrid chemical-electric design is proposed with the following propulsion subsystems:

- *Ion propulsion*: For the slowdown at Pluto-Charon. This propulsion system is very efficient (high specific impulse) and sustainable (non-toxic). However this comes at the cost of a low thrust.
- *Bi-propellant:* For the manoeuvres within the Pluto-Charon system. Bi-propellant systems offer a high thrust at the cost of a lower efficiency and sustainability.
- *Mono-propellant:* For the small orbit maintenance and attitude manoeuvres. Mono-propellant systems are the least efficient from all aforementioned, however they are the least complex.

Parallel to the design of these three propulsion subsystems, launcher configuration are iterated in chapter 15, as well as the mass budget in chapter 17. Key inputs of the propulsion subsystem design are the ΔV requirements and dry mass, and important outputs the propellant mass, which is in term used to obtain the wet mass of Orpheus. Undertaken steps are shown in Figure 10.1 where all dotted lines indicate iteration loops. Key inputs of the propulsion design are shown in the grey bold-face boxes. The different propulsion subsystems are shown in distinct highlighted areas.

First, the bi-propellant system is designed, as this system has to provide the end of life (EOL) manoeuvre, hence having the highest impact on the mass budget (given that multiple different propulsion systems are used). The propellant mass in box 1.1 is found using the Tsiolkovsky equation [149]:

$$m_{initial} = m_{final} \exp\left(\frac{\Delta V}{g_0 I_{sp}}\right) \tag{10.1}$$

where g_0 indicates the gravitation acceleration at sea level, I_{sp} is a measure of the system efficiency and relates directly to the propellant quantity required and m the mass. The propellant mass is obtained from Equation 10.1 as the difference between the initial and final mass. For all manoeuvres, the required propellant mass is shown in

Table 17.4, together with the specific impulse of the different propulsion systems. Steps 1.2 to 1.16 in Figure 10.1 and are discussed in section 10.3.

The second concept designed is the mono-propellant. Key inputs are the orbital maintenance ΔV budget and attitude control propellant budget. Using Equation 10.1, thruster performance parameters in box 2.0 (Figure 10.1) are converted to propellant mass requirements in step 2.1. Steps 2.2 to 2.9 are elaborated in section 10.4.

Third the electric propulsion subsystem is designed. Key inputs are the ΔV for the interplanetary manoeuvres and the Pluto-Charon insertion. From the engine specifications in step 3.0, propellant mass is obtained in 3.1 using Equation 10.1. Given the low thrust level of the ion engine, and the limited lifetime of the thruster, the impulse duration t_i in step 3.2 is evaluated by Equation 10.2.

$$t_i = \frac{m \cdot I_{sp} \cdot g_0}{F} \tag{10.2}$$

Here m specifies the propellant mass from step 3.1 and F the thrust of the engine, obtained in step 3.0. Values for the specific impulse of the different propulsion systems together with the impuls duration are shown in Table 17.4. If the impulse duration is found to be incompatible with the selected engine, the concept is reevaluated and (possibly) a different engine is chosen. Steps 3.3 to 3.6 are further discussed in section 10.5.

The last undertaken step is the selection and design of the launcher stage as this has no direct impact on the spacecraft mass. Given the performance of the SpaceX Falcon Heavy, and mass of Orpheus, it was checked if the rocket can put the spacecraft on the right trajectory to Jupiter (step 4.2). If not, a kick stage was selected and iterated, as shown in steps 4.3 and 4.4. An elaboration on this design is provided in chapter 15.

10.3 Bi-Propellant System Design

This section elaborates on the design of the bi-propellant system, and how the conclusion is reached that the Orpheus spacecraft is using the AMBR 623 N bi-propellant engine.

10.3.1 Chemical Bi-propellant Engine Selection

Given the dynamics of the celestial bodies present in the Pluto-Charon system, short impulse duration manoeuvres are required, which implies the use of a bi-propellant propulsion subsystem. It is needed to perform a short duration high thrust manoeuvre to transfer from Pluto to Charon. This is due to the low orbital period of the spacecraft, as shown in Table 7.6.

For the selection of the space propulsion subsystem, two options are considered: the in-house development of a new system or using an off-the-shelf system. Based on an analysis of market possibilities, shown in chapter 3, it was found out many market options are available and suitable for the mission. Additionally, buying off-the-shelf systems limits high development costs and verification/validation of the system.

Table 10.2 shows a list of potential engines(all having a TRL 6 or above) and their performance characteristics which could be used for the spacecraft.

Table 10.2: Possible Liquid Bi-propellant Engines, all having TRL 6 or above

Engine	**Manufacturer**	**Fuel**	**Oxidiser**	**Nominal Thrust* [N]**	I_{sp}* [s]	**Mass [kg]**	**O/F ratio [-]**	**Max firing time [s]**	**TRL**
Leros 1b	MOOG-I_{sp}	N_2H_4	MON	635	317	4.5	0.90	2520	9
Leros 2b	MOOG-I_{sp}	MMH	MON	407	318	5.0	1.65	4000	9
400N Bi-Prop Apogee Motor	Ariane Group	MMH	NTO / MON	425	321	4.3	1.65	6660	9
TR-308	Northrop Grumman	N_2H_4	NTO	472	322	4.8	1.00	3000	9
Leros 1c	MOOG-I_{sp}	N_2H_4	MON	458	324	4.3	0.89	5800	9
HIPAT 445N	Aerojet	N_2H_4	MON-3	445	329	5.4	0.85	1800	8
TR-312-100YN	Northrop Grumman	N_2H_4	NTO	556	330	6.0	1.06	3000	7
AMBR [38]	Aerojet	N_2H_4	MON-3	623	333	5.4	1.10	2700	6

* at defined Oxidizer to Fuel(O/F) ratio.

Based on the engine data as seen in Table 10.2 it is concluded that the AMBR engine by Aerojet Rocketdyne is the best engine for the Orpheus mission. The AMBR engine has the highest I_{sp} of all engines which is crucial

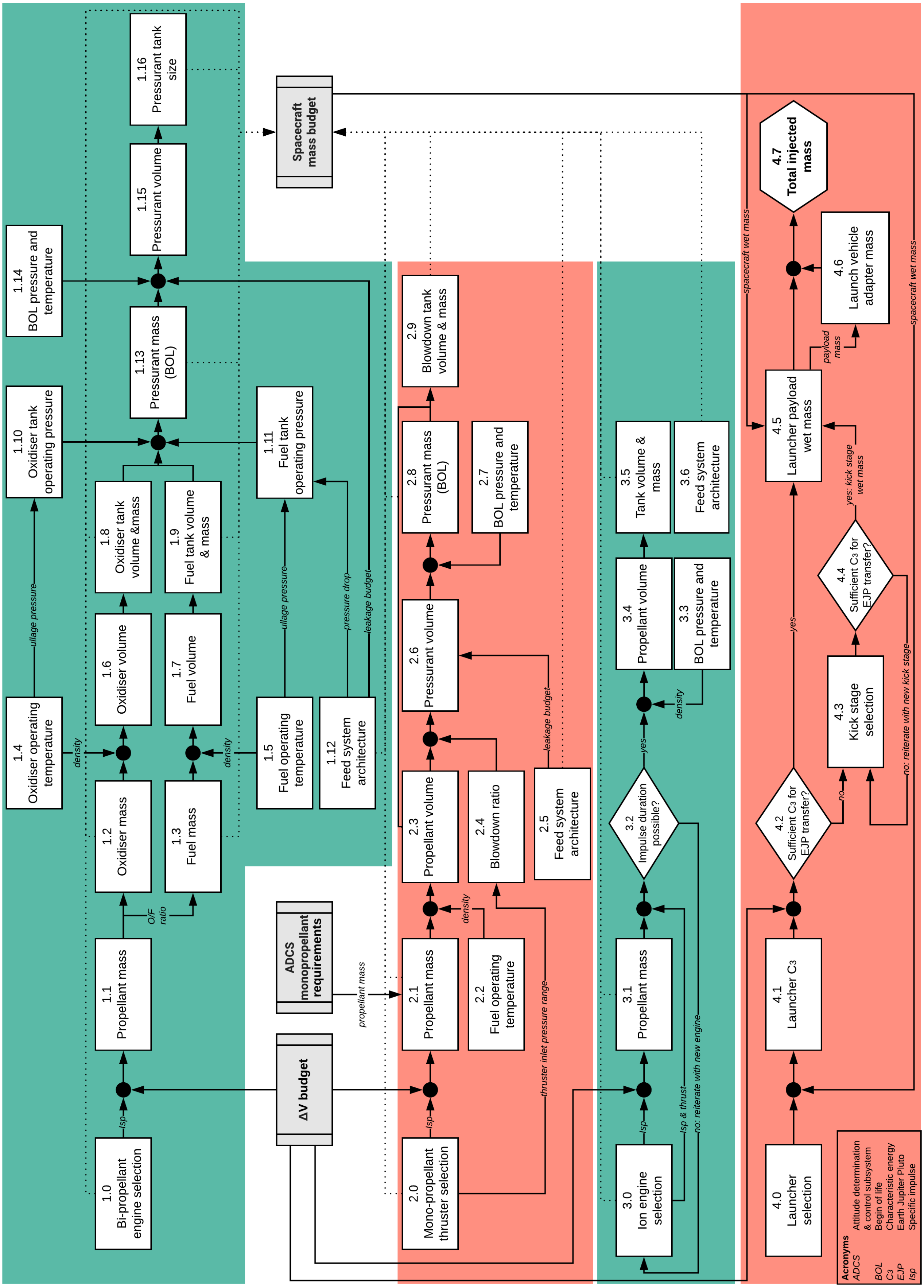

Figure 10.1: Schematic overview of the design philosophy of the propulsion subsystem and launcher selection. Dotted lines indicate the mass budget iterations performed.

to minimise the propellant mass. Its maximum firing time allows it such that the engine can burn for the entire expected duration without needing to shut down and the mass of the engine is in the medium range.

To select the optimal propulsion subsystem, the propellant blend, O/F ratio and I_{sp} are considered. The thruster is required to have a high I_{sp}, to minimise the amount of propellant needed. O/F ratio and propellant blend relate to the density of the propellants used. Low volumes are beneficial to keep the tank dry mass as low as possible. As the AMBR engine uses hydrazine as a fuel and the density of hydrazine is relatively low (1010 kg/m^3) in comparison to the commonly used oxidisers [119]. Thus as hydrazine is used a high O/F ratio is preferred to reduce the propellant mass.

The AMBR engine can operate in a specific range of possible pressures, O/F ratios and thrust levels. This can be seen in Figure 10.2. An analysis of the operating points concludes that the optimum operating point is at a fuel pressure of 17.6 bar (250 psia), oxidiser pressure 17.9 bar (260 psia) and an O/F ratio of 1.1. This was decided upon as it is the the design point which has the lowest oxidiser and fuel pressures within the 332.5 s I_{sp} region. Using lower pressures results in less pressurant being needed, and lighter tanks. However if the I_{sp} was lowered, it would result in a mass increase, exceeding the mass saved by the propellant tanks. The mass flow of the AMBR engine is 204 g/s.

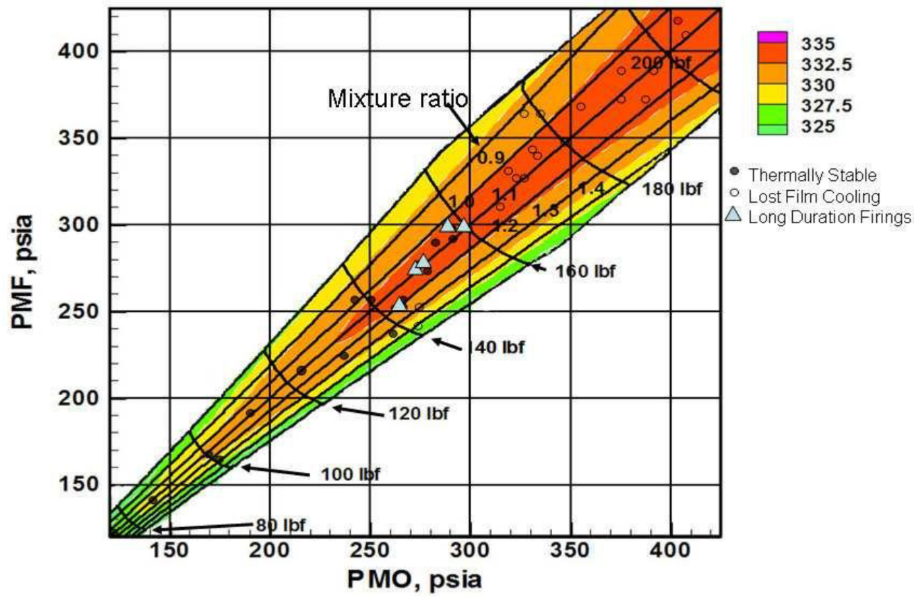

Figure 10.2: Thrust, mixture ratio, specific impulse (legend top left), oxidiser feed pressure and fuel feed pressure for the Aerojet AMBR engine [38].

10.3.2 Chemical Propellant Feed System Architecture and Valve Selection

A full feed system is designed for the Orpheus spacecraft as depicted in Figure 10.3. This section will analyse the design of the propellant management, specifically of the feed system architecture. The design is based upon that of previous missions such as Cassini-Huygens [55] and guarantees that no single line of failure exists. This ensures a high reliability system. All components in the feed system are selected from established commercial off-the-shelf (COTS) aerospace manufacturers, like Ariane Group (Germany), Vacco (United States), Omnidea-RTG (Germany) and MOOG (United States).

Due to the long mission duration and type of propulsion subsystem it is decided to isolate the helium pressurant lines as much as possible. This approach guarantees a minimal leakage, this is key to ensure the propellants tanks do not become pressurised before the needed time. The bi-propellant tanks will only become fully pressurised once in the Pluto-Charon system. The mono-propellant system, however, will be pressurised earlier for ADCS (Attitude Determination and Control Subsystem) reasons. This also increases the level of safety, as it reduces the risk that the mono-propellant can travel upstream and react with the oxidiser, resulting in a catastrophic failure [55]. Additionally, burst discs are put in place to further ensure no helium pressurant reaches the bi-propellant tanks.
The bi-propellant system functions in a pressure regulated mode, due to the high performance needed for the transfer manoeuvre. The mono-propellant thrusters are not required to be high performance, thus it is decided to use a blowdown system. These thrusters are solely used for ADCS purposes. The mono-propellant tank is pressurised on the launch pad, this is done to remove the need of a mono-propellant helium pressurant tank. This results in a spacecraft mass reduction.

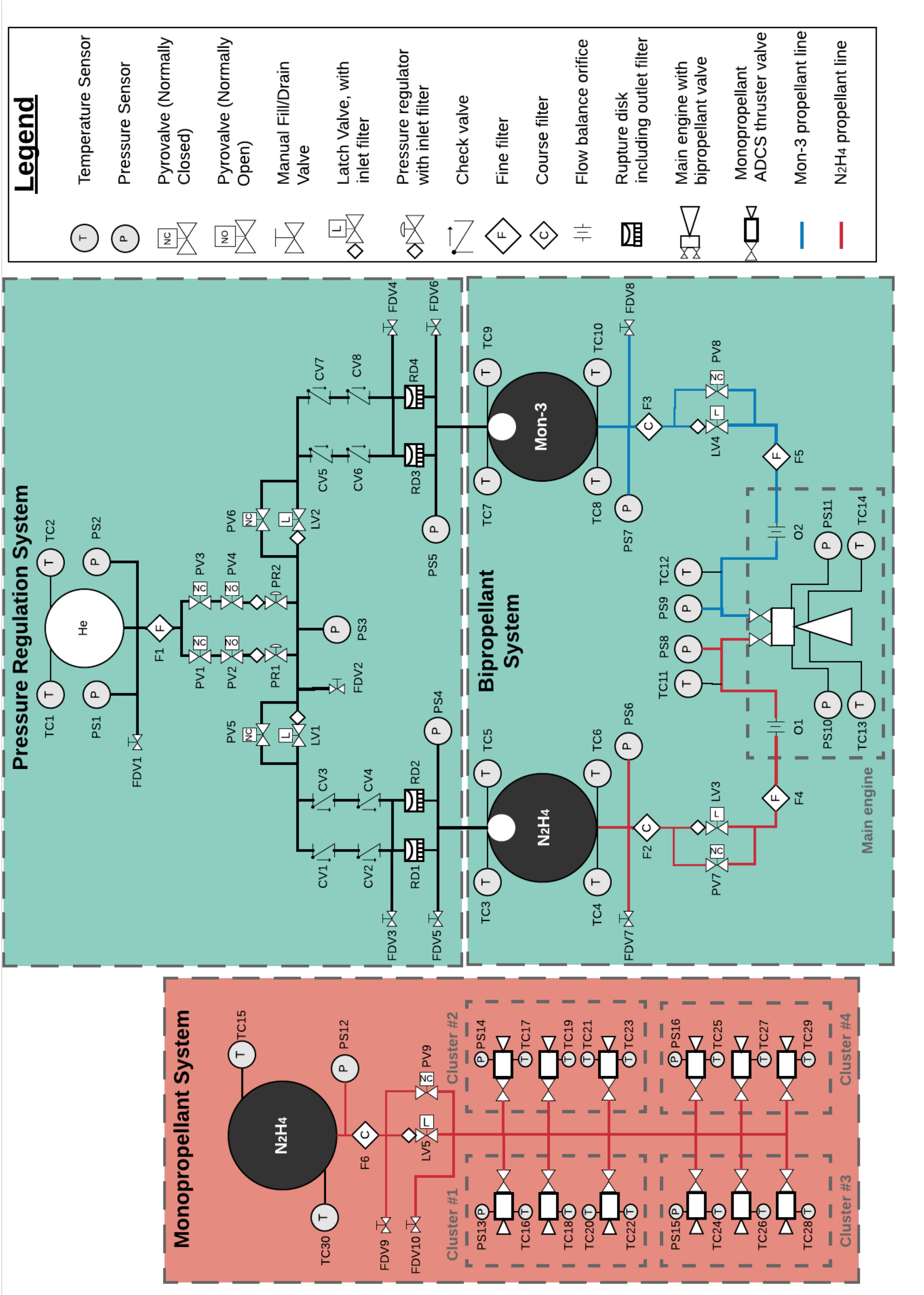

Figure 10.3: Chemical feed system diagram.

Manual fill/drain valves (FDV) are used in order to create a vacuum in the feed system after which propellants can be loaded through these valves. Given latch and check valves only permit flow in one direction, a FDV is needed downstream of the valve to allow for the upstream system to become a vacuum. FDVs are only used for ground operations and are not operated in space (however, these valves do introduce significant pressurant leakage over time). For the FDV, the Vacco V1D10855-01 are selected, which has a low mass of only 10 g whilst still having a 3/8" connection and being compatible with hydrazine, NTO and helium. Technical specifications of this valve are shown in Table 10.3 (Vacco fill and drain valves catalogue).

Table 10.3: Technical specifications of the Vacco V1D10855-01 fill drain valve.

Parameter	Value	Unit
Mass	10	g
Mean operating pressure	462	bar
Helium internal leakage	1×10^{-6}	sccs
Helium external leakage	1×10^{-6}	sccs
Life cycle	50	-
Operating temperature range	283.2-303.2	K

Table 10.4: Technical specifications of the MOOG Mini Pressure Transducer

Parameter	Value	Unit
Mass	125	g
Operating pressure	0-320	bar
Helium internal leakage	1×10^{-8}	sccs
Helium external leakage	1×10^{-8}	sccs
Life cycle	1000000	-
Power supply	< 300	mW

Pressure sensors: Ensure the propellants are stored at the correct conditions, and to detect if any anomalies occur. Pressure sensors provide feedback to the spacecraft systems such as the pressurant system. The selected pressure sensor is shown on Table 10.4 (MOOG Pressure Transducer Catalogue).

Filters: Used to capture impurities and contaminants, from continuing in the system. A coarse filter will be used to stop large contaminants and a finer filter will be used further downstream to capture any smaller contaminants which have passed through.

Flow balance orifices: Used to ensure a specific pressure drop across a line. This pressure drop compensates for different hose lengths and configurations, which if left unaltered would lead to uneven mass flows [91].

Check valves ensure that no back flow of the propellants in the pressurisation system can occur. Given the hypergolic nature of MON-3 and hydrazine, mixing of the propellants within the feedsystem would result in an explosion with catastrophic results for the spacecraft. It is highly preferred to minimise the amount of oxidiser vapour in the system as accumulated oxidiser vapour poses a significant threat. It is corrosive, can combine with the fuel to form a sludge [55]. The selected check valve is the Vacco V1D10856-02, specifications can be found in Table 10.5 (Vacco check valve catalogue).

Table 10.5: Specifications of the Vacco V1D10856-02 check valve.

Parameter	Value	Unit
Mass	20	g
Mean operating pressure	38	bar
Helium internal leakage	$<2.8 \times 10^{-2}$	sccs
Helium external leakage	$<1 \times 10^{-6}$	sccs
Life cycle	5000	-
Operating temperature range	103.2-318.2	K

Table 10.6: Specifications of the Vacco V1E10453-01 latch valve with 40μ inlet filter.

Parameter	Value	Unit
Mass	725	g
Mean operating pressure	20.7	bar
Helium internal leakage	2.8×10^{-3}	sccs
Helium external leakage	$<1 \times 10^{-6}$	sccs
Life cycle	150000	-
Operating temperature	277.6 - 322.0	K

Latch valves: Solenoid actuated bi-state valves, which can be easily opened and closed multiple times [148]. The selected latch valve is the Vacco V1E10453-01 which can be used for helium, hydrazine and NTO. Specifications of this valve are listed in Table 10.6(Vacco latch valves catalogue).

Pressure regulators: Used in order to reduce the pressure of the helium to the desired value. This is needed in order to allow for tank pressurisation at a specific pressure. The pressure regulator selected is the Omnidea-RTG P/N PR1&PR2. Specifications are show in Table 10.7.

Table 10.7: Technical specifications of the Omnidea-RTG P/N PR1&PR2 pressure regulator [111].

Parameter	Value	Unit
Mass	1100	g
Mean operating pressure	350	bar
Helium internal leakage	1.4×10^{-4}	sccs
Helium external leakage	1×10^{-6}	sccs
Life cycle	1000000	-
Regulated pressure	16-21	bar
Max flow rate	1.8	g/s
Inlet filter	2	μ

Pyrovalves: One-time-use valves, which can be normally open or normally closed. This valve type is commonly used as isolation valves and are placed in parallel with latch valves. The advantages of pyrovalves are the lower leak rates, smaller steady state pressure drops, lower mass and high reliability [148].

Rupture discs: Used to minimise the amount of oxidiser vapour available in the system. These have the lowest leak rate compared to other valves, however they can only be used once. A potential supplier for the pyrovalves was found in Ariane Group, of which the specifications are listed in Table 10.8.

Table 10.8: Specifications of the Ariane Space Normally Open & Normally Closed Pyrovalve.

Parameter	Value	Unit
Mass	<160	g
Mean operating pressure	310	bar
Helium internal leakage	$<1 \times 10^{-6}$	sccs
Helium external leakage	$<1 \times 10^{-6}$	sccs
Life cycle	1 (2 pyrocharges)	-
Operating temperature	183.2 - 373.2	K

Filters: the selected filters in the propellant lines (downstream of tanks), are the Omnidea-RTG P/N PF2 is selected. This filter has a mesh size of 2 microns and has a mass of 110 g [111]. In the pressurant lines, the Omnidea-RTG PN/ PF1 can be used, the technical specifications are specified in Table 10.9 and Table 10.10.

Table 10.9: Technical specifications of the Omnidea-RTG PF1 filter [111].

Parameter	Value	Unit
Mass	76	g
Mean operating pressure	350	bar
Helium internal leakage	0	sccs
Helium external leakage	0	sccs
Life cycle	1*	-
Filter mesh size	2	μm

Table 10.10: Technical specifications of the Omnidea-RTG PF2 filter [111].

Parameter	Value	Unit
Mass	110	g
Mean operating pressure	350	bar
Helium internal leakage	0	sccs
Helium external leakage	0	sccs
Life cycle	1*	-
Filter mesh size	2	μm

10.3.3 Propellant Storage Tank Selection

The Aerojet AMBR consumes NTO (MON-3) and hydrazine (N_2H_4) propellant. The purpose of this section is to describe the characteristics of these propellants and decide on the operating conditions. This in turn allows for sizing of the tanks.

Key parameters regarding the boiling and freezing point of the propellants are shown in Table 10.11. The main conclusion is that both hydrazine and MON-3 have a high freezing point, hence proper insulation and heaters are required to keep the propellants at their operating temperatures. Han and Choi [87] report freezing of the MON-3 or hydrazine propellant has catastrophic consequences for the spacecraft which will lead to mission failure. Both MON-3 and hydrazine shall be operated at a temperature of 285 K ± 1 K, which is obtained by active thermal control with heaters. The small temperature range is required to avoid thermal stratification. Given the vapour pressure at the operation point is less than 1 bar for both propellants, it is assumed to be negligible w.r.t. the 20 bar pressure required in the tanks at engine operations.

Table 10.11: Properties of AMBR engine propellants.

Parameter	Condition	NTO (MON-3)	Hydrazine	Source
Boiling point [K]	1 bar	294.3	387.4	[109]
Freezing point [K]	1 bar	261.9	274.7	[109]
Density [km/m^3]	298 K, 1 bar	1433	1004	[109]
Vapour pressure [Pa]	285 K	65428	825	[39] [102]
Viscosity [Pa s]	285 K	4.6×10^{-4}	1.1×10^{-3}	[1] [2]

To size the propellant tanks for the bi-propellant propulsion system, the fuel m_f and oxidiser m_o mass are calculated. From the ΔV budget displayed in Table 17.4, it is concluded the bi-propellant propulsion system is required to deliver a total ΔV of 770 m/s spread over four different burns, which is equivalent to a propellant mass of 253 kg. Using Equation 10.3 and Equation 10.4, together with the design O/F ratio of 1.1 for the Aerojet AMBR, the oxidiser and fuel masses are computed and found to be 133 kg and 121 kg, respectively.

$$m_f = \frac{m}{O/F + 1} \tag{10.3}$$

$$m_o = \frac{O/F \cdot m}{1 + O/F} \tag{10.4}$$

From the aforementioned masses, the MON-3 and hydrazine volumes can be calculated by dividing the mass by the propellant densities. Using the NTO (MON-3) and hydrazine density listed in Table 10.11, the obtained volumes are 93 L and 120 L respectively. To these volumes a margin of 10% is added to allow for propellant growth and ullage volume, as described in ESA standard `R-M2-9` [76]. Thus the total required oxidiser tank volume is 102 L and fuel tank volume 132 L.

One of the disadvantages of chemical bi-propellant tanks is the centre of gravity (CG) shifts: when Orpheus is in space, the propellant floats around in the tank. This is a significant problem for any liquid engine, as only hydrazine and MON-3 are allowed to enter the combustion chamber, not the pressurant. It is decided to use surface tension propellant management devices (PMD) inside the tanks, as this is the lightest possible PMD configuration (at the cost of a reduced control of the CG). Surface tension tanks consist of traps, liners and vanes inside the tank [154].

Table 10.12: Comparison of different suitable PMD bi-propellant tanks.

Tank	**Manufacturer**	**Volume [L]**	**Diamete [mm]**	**Length [mm]**	**MEOP [bar]**	**Mass [kg]**
PTP-124	MT Aerospace	124	605	695	24.0	9.8
E3000 Family - 124L	MT Aerospace	124	603	695	20.0	9.8
21.49" DIA x 44.2"	Keystone Engineering	156	546	1123	27.6	11.1
PTP-166	MT Aerospace	166	603	856	20.0	10.8
80334-1[71]	Nortrop Grumman (ATK)	175	584	838	17.6	12.9

As tank development is very expensive [154], commercial off-the-shelf (COTS) tanks were selected. Suitable tanks for Orpheus are shown in Table 10.12. For the MON-3 (102 L required) the MT Aerospace (Germany) PTP-124 tank is selected, given this is the lightest possible option to store the propellant and has the required volume. For the hydrazine (132 L required), the MT Aerospace PTP-166 tank is selected, which is also the lightest possible solution for the given volume.

Both selected propellant tanks have a polar mounting (mounting on top of the tank). Moreover, the tanks are made out of titanium (Ti6Al4V) which is compatible with both NTO (MON-3) and hydrazine [141]. To ensure only propellants are fed to the engine, the hydrazine and MON-3 shall be pushed to the bottom of the tanks by accelerating the spacecraft slightly, by firing the mono-propellant thrusters just before the start of the AMBR engine.

10.3.4 Pressurant Tank Selection and Leakage Budget

The purpose of this section is to size the propellant feeding mechanism and define the required pressurant mass. The function of the pressurant feeding mechanism is to distribute the propellants to the engine. Their are three common ways to feed the propellant to the engine:

- *Blowdown*: The tanks are pressurised at launch with a gas which pushes the propellant to the engine. When propellant is consumed, the gas expands, resulting in a gradual decrease of the pressure in the tank, and thus a decrease in AMBR injector feed pressure. This concept is shown in Figure 10.4 on the left.
- *Pressure fed*: A separate pressurant tank with a gas is present, which is connected to the propellant tanks with a gas regulator. This way, the pressure in the tanks can be kept constant, which also allows for a constant AMBR injector feed pressure. This concept is shown in Figure 10.4 on the right.
- *Turbo/electric pump*: A pump is driven by a gas turbine or electric motor to feed the propellants to the combustion chamber. Additionally the propellant tanks needs to be pressurised (at a lower pressure than pressure fed/blowdown) to prevent the pump from stalling. This concept allows for a constant injector feed pressure and high mass flow rates.

It is decided to use a pressure fed system is the best choice for Orpheus. The blowdown system is unfavourable due to its non-constant engine feed pressure which might introduce instabilities of the AMBR. Turbo/electric pumps have never been used in interplanetary deep space missions and are not practical for the low mass flow rate of the AMBR engine.

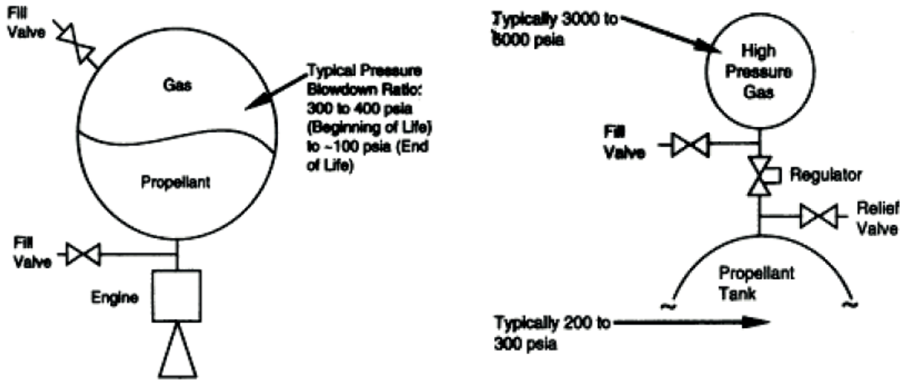

Figure 10.4: Schematic overview of blowdown cycle (left) and pressure fed cycle (right) [149].

Sutton and Biblarz [134] and Hermsen [90] report the required pressurant mass m_p can be calculated with Equation 10.5. Here Pu represents the ullage pressure in the propellant tanks, v the propellant tank volume, γ_p the specific heat ratio of the pressurant and R_p the specific gas constant of the pressurant. $T_{p,BOL}$, $P_{p,BOL}$ and $P_{p,EOL}$ represent the temperature and pressure of the pressurant, at begin of life (BOL) and end of life (EOL).

$$m_p = \frac{\gamma_p \cdot (Pu_o \cdot v_o + Pu_f \cdot v_f)}{R_p \cdot T_{p,BOL} \cdot \left(1 - \frac{P_{p,EOL}}{P_{p,BOL}}\right)} \tag{10.5}$$

Two common pressurants used in spacecraft are helium and nitrogen [148]. Key characteristics of these gases influencing Equation 10.5 are:

- *Helium*: $R_p = 2077.1$ J/kgK and $\gamma_p = 1.67$ [134]. Hence $\gamma_p/R_p = 8.0 \times 10^{-4}$ kgK/J.
- *Nitrogen*: $R_p = 296.8$ J/kgK and $\gamma_p = 1.40$ [134]. Hence $\gamma_p/R_p = 4.7 \times 10^{-3}$ kgK/J.

Clearly, the ratio γ_p/R_p is more than 5 times higher for nitrogen w.r.t. helium. As $m_p \propto \gamma_p/R_p$, using nitrogen would result in a pressurant mass more than 5 times higher! Therefore, it is decided to use helium as the pressurant.

Using Equation 10.5 with a design ullage pressure of 20 bar, BOL helium pressure of 300 bar, EOL pressure of 22 bar, BOL helium temperature of 293 K and propellant tank volumes as specified in subsection 10.3.3, a required helium mass of 1.7 kg is obtained. This translates to a pressurant volume v_p of 35 L, which is obtained by using Equation 10.6.

$$v_p = \frac{m_p \cdot R_p \cdot T_{p,BOL}}{P_{p,BOL}} \tag{10.6}$$

Given no valve/component used in the feed system has a 'perfect' sealing, it is known that some of the helium leaks away over time. For short duration missions this leakage is often negligible, however for a 25 year mission, like Orpheus, helium leakages must be taken into account. Two different types of leaks can be distinguished: internal and external. As illustrated in Figure 10.5 internal leakage acts from one side of the valve (A) to the other side (B). Valves are often designed for internal leakage to reduce friction of the metal valves parts. Note that internal leaks stay within the system (except for fill drain valves). External leaks, on the other hand, cause helium to leak outside the system into space. These leaks should be monitored carefully, as they could potentially cause an attitude disturbance for the spacecraft if the leakage rate is too high.

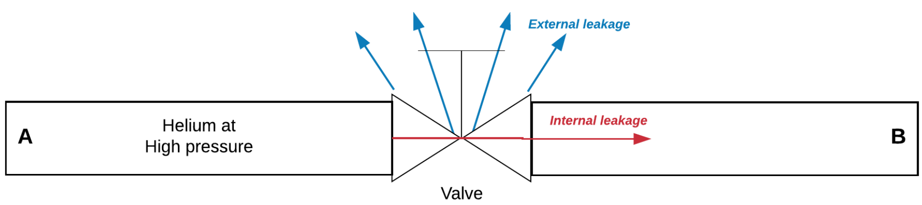

Figure 10.5: Schematic overview of internal and external leakage.

As every valve and connection is expected to leak, the part of the feed system pressurised with helium should be kept at a minimum, to avoid major leakages over the 25-year mission. The proposed solution is to fire pyrotechnic valves PV1 and PV2, in Figure 10.3 upon Pluto arrival. This way, all feed system downstream of these valves is pressurised, meaning helium leakage in this part can be neglected. Two cases are considered in the leakage budget:

- *Interplanetary coast:* This takes 24 years. In this time frame, the feed system (Figure 10.3) is only pressurised up to PV1 and PV2.
- *Pluto-Charon operations:* This takes no more than 1 year. During this phase of the mission, all feed system components up to the propellant tanks are expected to leak.

Based on these two operation modes, a leakage budget is constructed as shown in Table 10.13 and Table 10.14, using the following assumptions:

- All connections in the feed system are welded and are 'perfect'. Hence, leakage of connections is not taken into account. The effect of this assumption is that the leakage rate might be underestimated.
- All valves or other components in the feed system leak at a constant rate independent of the pressure. This assumption is made as no expression for the leakage rate as a function of pressure is available from manufacturers (only maximum leakage rate). The effect of this assumption is a possible underestimation of the leakage rate.
- All valves and other feed system components leak at the maximum leakage rate. This assumption is made because no expression for leakage rate versus pressure was available. The result of this assumption is that it might overestimate the leakage rate.

Note that in the leakage budget, only helium leaving the system is considered (external leakage). For the fill drain valve though, internal leakage is taken into account (as internal leaks here leave the system). Leakage rates in Table 10.13 and Table 10.14 are given in sccs (standard cubic centimetre per second).

Table 10.13: Orpheus helium leakage budget for 24 years interplanetary coast.

Element	**Leakage rate per element [sccs]**	**Total leakage rate [sccs]**	**Total leakage [scc]**
PS1, PS2	1×10^{-8}	2×10^{-8}	15
F1	1×10^{-6}	1×10^{-6}	757
FDV1 (internal)	1×10^{-6}	1×10^{-6}	757
FDV1 (external)	1×10^{-6}	1×10^{-6}	757
PV1, PV2	1×10^{-6}	2×10^{-6}	1515
Total			3802

Table 10.14: Orpheus helium leakage budget for 1 year of Pluto-Charon operations.

Element	**Leakage rate per element [sccs]**	**Total leakage rate [sccs]**	**Total leakage [scc]**
PS1, PS2, PS3, PS4, PS10	1×10^{-8}	5×10^{-8}	2
F1	1×10^{-6}	1×10^{-6}	32
FDV1, FDV2, FDV3, FDV4, FDV7, FDV8 (internal)	1×10^{-6}	6×10^{-6}	189
FDV1, FDV2, FDV3, FDV4, FDV7, FDV8 (external)	1×10^{-6}	6×10^{-6}	189
PV1, PV2, PV3, PV4, PV5, PV6	1×10^{-6}	6×10^{-6}	189
PR1, PR2	1×10^{-6}	2×10^{-6}	63
LV1, LV2	1×10^{-6}	2×10^{-6}	63
CV1, CV2, CV3, CV4, CV5 CV6, CV7, CV8	1×10^{-6}	8×10^{-6}	252
RD1, RD2, RD3, RD4	1×10^{-6}	4×10^{-6}	126
Total			853

From Table 10.13 and Table 10.14 it is concluded that the total leakage is of $3802 + 853 = 4655$ scc. As connector leaks are not taken into account, this leakage rate is rounded up to 5 L. Therefore, the total required helium volume is 40 L.

To keep equipment cost as low as possible a COTS pressure vessel is preferred. As depicted in Table 10.15, three different options are considered from established aerospace manufacturers.

Table 10.15: Commercial off-the-shelf suitable pressurant tanks.

Tank	**Manufacturer**	**Volume [L]**	**Diameter [mm]**	**Length [mm]**	**MEOP [bar]**	**Mass [kg]**
PVG Family 40-75L	MT Aerospace	40	432	467	310	8.5
PVG-50	MT Aerospace	50	432	673	310	9.5
80412-1[71]	Nortrop Grumman (ATK)	50	335	681	150	7.0

It is decided to use the PVG-40 from MT Aerospace. This tank allows the pressurant to be stored at the required pressure of 300 bar at the lowest possible mass. Although 80412-1 is lighter, it is not suitable for the mission as it would require the helium to be stored at a significantly lower pressure.

The PVG-40 is a carbon over-wrapped pressure vessel, which consists of a thin titanium TI6Al4V liner with a carbon-fibre wrap around the liner for increased strength. It is compatible with helium and has a polar mounting.

10.3.5 Pressure Drop Analysis

Over all feed system piping, valves and other feed system elements in Figure 10.3, a pressure drop (ΔP) will be present. Given this drop can be in the order of multiple bars, an analysis is required to ensure the propellants are fed to the engine at the right pressure to obtain the desired performance. Only the main MON-3 and hydrazine lines are analysed, since the pipeline of the mono-propellant system is not designed yet. Global assumptions made for the analysis of the pressure drop are:

- *All pipes have a uniform roughness.* This assumption allows the use of empirical expressions for rough pipes. The effect of this assumption is a possible local change in total pressure on places where the local roughness is different.
- *Pressure drops due to welded connections are negligible.* All components of the feed system are welded connections, which very likely also deforms the inside of the pipe, increasing the pressure drop. Neglecting these effects leads to a possible underestimation of ΔP.
- *Density and viscosity of the fluids in the pipelines are constant.* This assumption significantly simplifies the calculations. This is only true if the changes in temperature and pressure of the fluids in the pipes are small (which is achieved by insulation/heating of the feed system and design for a low pressure drop). The impact of this assumption is a possible miscalculation of the Reynolds number which in term results in a possible underestimated or overestimated pressure drop

Straight Pipes

For a straight pipe, the coefficient of fluid resistance due to friction (ζ_f) is given by Equation 10.7. Here λ represents the friction factor, L the hydraulic length of the pipe and D the inner diameter of the pipe.

$$\zeta_f = \lambda \cdot \left(\frac{L}{D}\right) \qquad (10.7)$$

$$\bar{\Delta} = \frac{\Delta}{D} \qquad (10.8)$$

The friction factor is a function of the relative roughness of the pipe ($\bar{\Delta}$), which is related to the pipe roughness Δ using Equation 10.8. For new or old welded steel pipes, Richter and Schmidt [120] report typical pipe roughness values of 0.04-0.1. It is assumed these values are also valid for stainless steel pipes, which are used for the Orpheus mission. Additionally, the friction factor is dependant on the Reynolds number of the flow, defined as:

$$Re = \frac{\rho \cdot V \cdot D}{\mu} = \frac{4\dot{m}}{D \cdot \pi \cdot \mu} \qquad (10.9)$$

where μ represents the viscosity of the fluid, ρ the fluid density, V the flow velocity and $\dot{m}$ the mass flow rate (see section 10.3). Input and outputs of Equation 10.9 are shown in Table 10.16. With the Reynolds number and relative pipe roughness, the friction factor is found by using a Moody diagram, as depicted in Figure 10.6.

To see how the pressure drop develops for different feed system diameters, it is evaluated for two common tube sizes, 1/4" and 3/8". Huzel and Huang [134] state for stainless steel piping with maximum working pressure of 1500 psi (103 bar), the wall thickness of 1/4" tube is 0.02" and for 3/8" tube 0.028". Hence, the inner diameter of the pipes are 0.319" (8.1 mm) for 3/8" pipe and 0.21" (5.3 mm) for 1/4" pipe.

Using Equation 10.7 to Equation 10.9, the coefficient of fluid resistance is evaluated for two different pipe sizes, 1/4" and 3/8" in Table 10.16. Based on a preliminary routing for both the oxidiser and fuel line is shown in Figure 10.7 and bend radius of 11 m for 1/4" pipe and 17 mm for 3/8" pipe (ca. twice the inner diameter), the straight length is evaluated. For 1/4" pipe this yields 1773 mm and for 3/8" pipe 1749 mm.

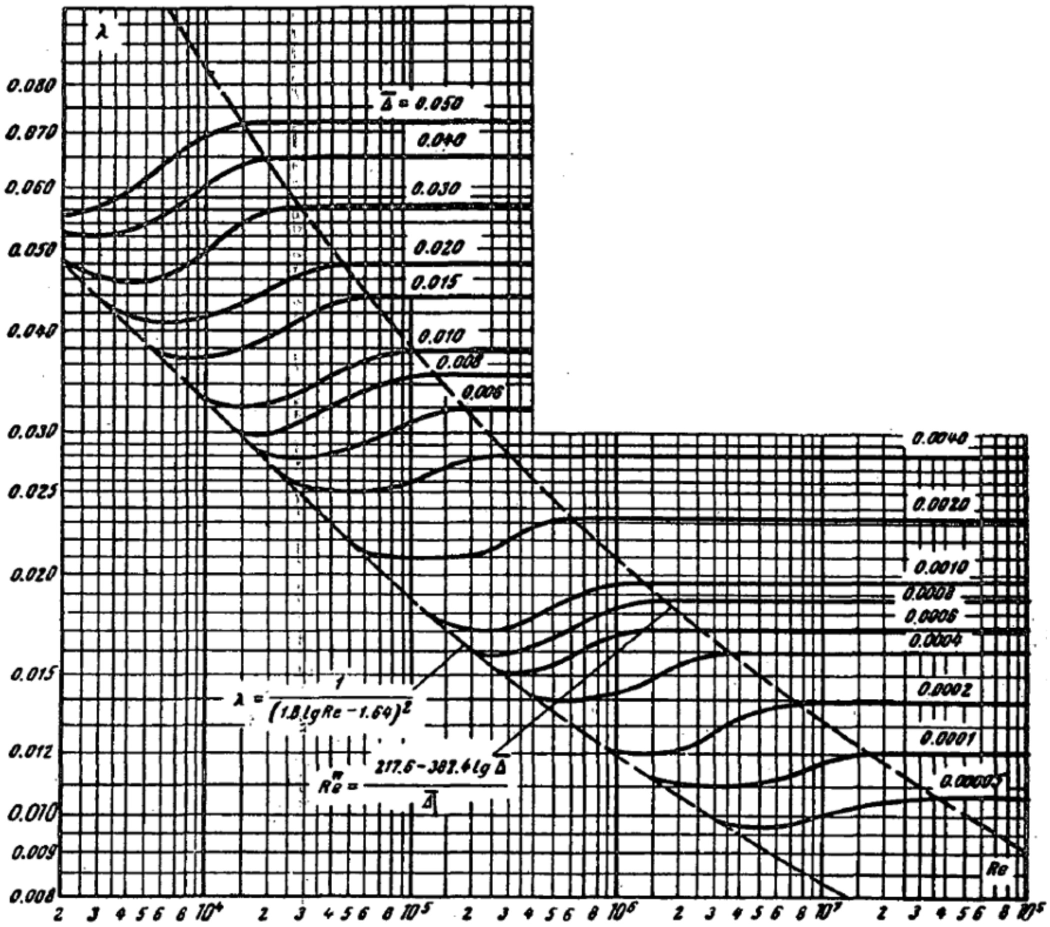

Figure 10.6: Moody diagram indicating the pipe friction coefficient (λ) as a function of Reynolds number (Re) and relative roughness ($\bar{\Delta}$) [92].

Table 10.16: Coefficient of fluid resistance due to friction for 1/4" and 3/8 straight pipe.

Para-meter	Unit	MON-3 1/4" pipe	3/8" pipe	Hydrazine 1/4" pipe	3/8" pipe	Rationale
μ	Pas	4.6×10^{-4}	4.6×10^{-4}	1.1×10^{-3}	1.1×10^{-3}	From Table 10.11.
$\dot{m}$	g/s	100	100	91	91	From section 10.3.
Re	-	5.5×10^4	3.6×10^4	2.0×10^4	1.3×10^4	From Equation 10.9.
$\bar{\Delta}$	mm^{-1}	0.019	0.012	0.019	0.012	From Equation 10.8, with Δ=0.1.
λ	-	0.048	0.037	0.044	0.034	From Figure 10.6.
ζ_f	-	16.1	8.0	14.7	7.3	From Equation 10.7.

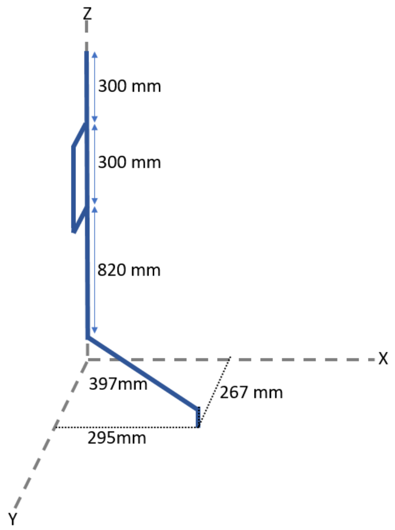

Figure 10.7: Preliminary feed system routing for the MON-3 and hydrazine line.

Elbows

For rough elbows (90 degree pipeline bends), Idelchik and Fried [92] report the coefficient of fluid resistance as expressed in Equation 10.10, where R_0 represents the bending radius. The Reynolds range in which this expression is valid is dependant on the selected values for empirical constants k_Δ and k_{Re}:

- k_Δ equals 1 in the flow regime $3 \times 10^3 < Re < 4 \times 10^4$ or 2 in the flow regime $4 \times 10^4 < Re < 2 \times 10^5$ (obtained from Table 6-6 in Idelchik and Fried [92]).
- k_{Re} equals $64\lambda_{Re}$ in the flow regime $3 \times 10^3 < Re < 2 \times 10^5$, where λ_{Re} is the friction coefficient for a smooth pipe, obtained from empirical expression $\lambda_{Re} = \frac{0.3164}{Re^{0.25}}$ [92] (obtained from Table 6-6 in Idelchik and Fried [92]).

$$\zeta = k_\Delta \cdot k_{Re} \cdot \left(\frac{0.21}{\sqrt{\frac{R_0}{D}}} \right) + \zeta_f \tag{10.10}$$

Note the first term in Equation 10.10 expresses the increased fluid resistance due to the curvature of the pipe, and the second term implies the friction loss, given in Equation 10.7.

The coefficient of fluid resistance over a 1/4" and 3/8" elbow is shown in Table 10.17. Key to remark is the much lower pressure loss over the corner than the straight pipe. It is expected this is caused by the fact the straight pipes are much longer than the corner section, introducing a large reduction in pressure.

Table 10.17: Coefficient of fluid resistance for 1/4" and 3/8 elbows.

Para-meter	Unit	MON-3 1/4" pipe	3/8" pipe	Hydrazine 1/4" pipe	3/8" pipe	Rationale
k_Δ	-	2.0	1.0	1.0	1.0	
k_{Re}	-	1.32	1.47	1.7	1.9	
R_0	mm	11	17	11	17	Ca. 2x inner diameter.
ζ	-	0.30	0.27	0.29	0.26	From Equation 10.10.

T-Junctions
For symmetrical, 90 degree T-junctions, Idelchik and Fried [92] provide an expression for the flow resistance coefficient as given in Equation 10.11, without partition.

$$\zeta = 1 + \left(\frac{A_c}{A_b}\right)^2 + 3\left(\frac{A_c}{A_b}\right)^2 \left[\left(\frac{Q_b}{Q_c}\right)^2 - \left(\frac{Q_b}{Q_c}\right)\right] \tag{10.11}$$

Here, A represents the internal area of the pipe and Q the volume flow rate. Subscripts c and b indicate the flow in the centre pipeline and branch respectively. Given all feed system branches downstream of the propellant tanks have the same internal diameter, all area-ratios in Equation 10.11 are equal to 1. Moreover, in nominal state, PV7 and PV8 in Figure 10.3 are closed. Therefore, it is assumed the volume flow in the branch (where the pyrovalves are located) is zero, which cancels out the second term in Equation 10.11. Hence, for the T-junctions in the feed system (2 per line), the fluid resistance coefficient is 2.

The total fluid resistance factor over the pipeline system is shown in Table 10.18. Here, the total pressure drop is obtained from multiplying the resistance factor with the dynamic pressure:

$$\Delta P 0.5 \cdot \zeta \cdot \rho \cdot V^2. \tag{10.12}$$

Table 10.18: Fluid resistance factor and total pressure drop for the feed system excluding valves and filters.

Section	**MON-3** 1/4" pipe	3/8" pipe	**Hydrazine** 1/4" pipe	3/8" pipe
Straight pipe	16.1	8.0	14.7	7.3
Elbows (x2)	0.60	0.54	0.58	0.52
Tees (x2)	4	4	4.0	4.0
Total (resistance factor, ζ)	20.7	12.5	19.3	11.8
Total (pressure loss, ΔP)	1.49 bar	0.17 bar	1.64 bar	0.18 bar

As expected, the pressure loss of a 1/4" piping system is much higher than over a 3/8" piping system. Nevertheless, it is decided to use 1/4", as this would result in a 45% decrease in tubing mass. Moreover, this pressure drop is still within allowable range.

Latch Valve and Filters
In both the fuel and oxidiser system, during nominal operations where PV7 and PV8 are closed, the fluids encounter filters (F2, F3, F4, F5), latch valves (LV3, LV4) and balancing orifices (O1, O2). For the latch valves, a characteristic pressure drop curve is obtained from Vacco and shown in Figure 10.8. The MON-3 and hydrazine flow rate are converted to a water flow rate, which is used in Figure 10.8, using Equation 10.13. Here, $\dot{m}$ and ρ indicate the propellant (MON-3/hydrazine) mass flow rate and density.

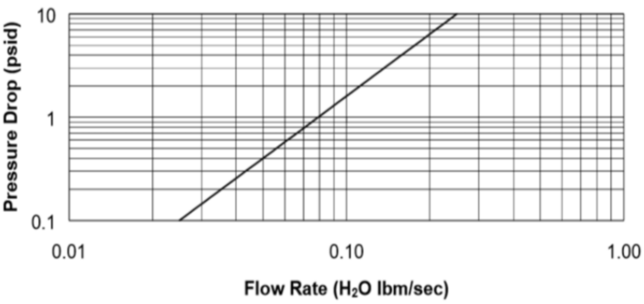

Figure 10.8: Pressure drop for the Vacco V1E10453-01 latch valve [143].

$$\dot{m}_{water} = \dot{m}\left(\frac{\rho_{water}}{\rho}\right) \tag{10.13}$$

Using the propellant properties defined in Table 10.11, a hydrazine pressure drop of 0.45 bar is found, together with a MON-3 pressure drop of 0.20 bar.

The second element in the flow path are the filters, for which the Omnidea-RTG P/N PF2 is selected. In the data sheet of this filter, a pressure drop of 102 mbar at 89 g/s (water flow rate) is reported [111]. As this is very close to the corresponding propellant flow rates and no additional data is available, it is assumed this pressure drop is valid for the flow conditions in the feed system.

Concluding, for 1/4” pipe, the total pressure drop over the MON-3 line is 1.89 bar and for the hydrazine line 2.29 bar.

Flow Balancing Orifice

Both propellant tanks are operated at a pressure of 20 bar. To ensure the oxidiser and fuel are fed to the AMBR engine at a pressure of 17.9 bar and 17.6 bar respectively, a flow balance orifice is added in the line. Assuming the upstream flow area is much larger than the orifice area, the pressure drop over the orifice is described by Equation 10.14.

$$A_o \cdot C_d = \frac{\dot{m}}{\sqrt{2 \cdot \rho \cdot \Delta P}} \tag{10.14}$$

Here, A_o is the orifice area and C_d the non-dimensional discharge coefficient. The discharge coefficient is the ratio between the actual flow rate through the orifice and the theoretical flow rate. This coefficient is typically obtained from computational fluid analysis or actual discharge tests.

To allow for the correct MON-3 feed pressure, an additional pressure drop of 0.21 bar is required, meaning the required value $A_o \cdot C_d$ equals 12.9 mm^2. For hydrazine, this value follows from Equation 10.14 to be 19.7 mm^2.

10.4 Mono-Propellant System Design

To allow for orbit maintenance and attitude control, a mono-propellant propulsion system is required. Mono-propellant thrusters only require a fuel, like hydrazine, which is fed to the engine in which is decomposes exothermic and produces thrust. From `R-ADCS-100` it is known that the thrust produced by the thruster at BOL shall be at least 20 N. Based on this requirement, a range of COTS thrusters are considered, listed in Table 10.19. The Ariane Group (Germany) 20 N mono-propellant thruster is selected since it has the lowest mass.

Table 10.19: Possible Mono-propellant Thrusters, all having TRL 6 or above and running on hydrazine.

Engine	Manufacturer	Nominal Thrust [N]	Nominal inlet pressure [bar]	Inlet pressure range [bar]	I_{sp} [s]	Mass [kg]
Monarc-22-6	MOOG-ISP	22	20.0	4.8-27.6	229.5	0.72
Monarc-22-12	MOOG-ISP	22	13.1	4.8-27.6	228.1	0.69
MRE-5.0	Norhrop Grumman	28	19.0	4.8-32.8	232.0	1.50
20N Mono-propellant	Ariane Group	25	24.0	5.5-24.6	230.0	0.65

To keep the system complexity as low as possible and to allow the least amount of feed system to be pressurised with helium, a blowdown concept was selected to pressurise the hydrazine tank. This way, the bi-propellant and mono-propellant feed system are in no way connect to each other, as visualised in Figure 10.3.

From the design of the ADCS, it is known that 23 kg of hydrazine is necessary for all manoeuvres. According to ESA standard `R-DV-1` [76] a 100% margin shall be added to attitude control and angular momentum manoeuvres, which brings the total required mass to 46 kg. Next to attitude control, Orpheus needs to maintain its correct science orbit around Pluto and Charon. From Table 17.4 it is concluded that 76 kg of propellant is required for these manoeuvres. This already includes a 100% margin from ESA standard `R-DV-1` [76]. Hence, the total hydrazine mass needed for the mono-propellant system is 122 kg, or 122 L.

Given the use of a blowdown cycle, the feed pressure to the thrusters gradually decreases over time as the helium in the hydrazine tank expands. Larson and Wertz [149] reports an important design criteria for a blowdown system is the blowdown ratio B which is given by:

$$B = \frac{v_{pf}}{v_{pi}} \approx \frac{v_{pi} + v}{v_{pi}} \tag{10.15}$$

Here v_{pi} and v_{pf} indicate the initial and final pressurant volume and v the hydrazine fuel volume. The value for the blowdown ratio is a function of the thruster inlet pressure range. It is assumed there is no temperature change when the gas expands and no heat is added to the gas during expulsion. In this case, from the first law of thermodynamics stating that $\partial U = \partial Q_h - \partial W = c_p \cdot \partial T$, the term ∂Q_h cancels out (no heat added). Additionally, in the vacuum of space, there is no work performed by the helium (as no force is required to push the propellants out, given a vacuum). Therefore, ∂W cancels out as well, meaning $c_p \cdot \partial T$ is zero, hence there is no temperature change. For a tank with no temperature change (isothermal), Brown [13] states the pressure over time can be calculated as shown in Equation 10.16.

$$P_p(t) = P_{pi} \left(\frac{v_{pi}}{\frac{m_f(t)}{\rho_f} + v_{gi}} \right) \tag{10.16}$$

Where $P_p(t)$ indicates the instantaneous pressurant pressure, P_{pi} the initial pressure, $m_f(t)$ the instantaneous hydrazine mass and ρ_f the hydrazine density. Using Equation 10.15, the EOL pressure is plotted as a function of the blowdown ratio. Dashed lines indicate the inlet pressure range, of the Ariane Group 20 N thruster. To account for possible pressure drops in the system, an initial 20% margin is added on the EOL pressure, indicated with the red line. Hence, the blowdown ratio shall be no higher than 3.57 for a correct operation of the thruster. Note from Equation 10.15 a high blowdown ratio implies a smaller helium volume at the cost of a lower EOL pressure thus a lower specific impulse and thrust.

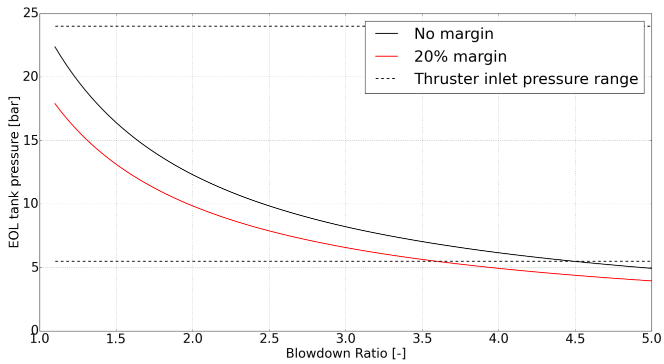

Figure 10.9: Mono-propellant system EOL tank pressure for different blowdown ratios assuming isothermal expansion.

For the mono-propellant system, a diaphragm tank is used, since it is impractical to use a PMD (surface tension) tank. The mono-propellant thrusters are fired to push the propellants of the main bi-propellant system to the bottom of the tanks before pressurisation of the bi-propellant system, to avoid helium being fed to the AMBR engine. For the mono-propellant thrusters the same holds in case a PMD tank is used; however in this case there is no extra propulsion system available which can push the propellants to the bottom of the tank. Possible COTS tanks with the required volume that have a diaphragm are listed in Table 10.20.

Table 10.20: Suitable off-the-shelf diaphragm/bladder mono-propellant tanks.

Tank	**Manufacturer**	**Volume [L]**	**Diameter [mm]**	**Length [mm]**	**MEOP [bar]**	**Mass [kg]**
PTD-177	MT Aerospace	177	655	827	240	15.5
Model DT190	Ariane Group	180	623	907	35.6	21.0
PTD-222	MT Aerospace	222	608	1027	24.5	17.1

The PTD-177 is selected given it low mass. This tank is made out of titanium T16Al4V which is compatible with hydrazine according to Uney and Fester [141]. The diaphragm is made out of an EPDM (Ethylene Propylene Diene Monome) rubber. Additionally, Li et al. [56] show that the properties of EPDM are not affected by hydrazine, making this tank usable in the configuration of Orpheus. With the volume of the PTD-177, a blowdown ratio of 3.27 is taken, which is equivalent to a helium volume of 54 L, excluding leaks. At the helium side of the tank, only one fill drain valve is present, Vacco V1D10855-01 (Table 10.3), which has an internal and external leakage rate of 1×10^{-6} sccs. Over a mission duration of 25 years (788923149 s), this results in a total leakage of 789 scc, or 0.8 L. This is added tot the required helium volume of 54 L, which brings the total helium volume to 55 L.

Using Equation 10.15 in combination with the ideal gas law, the diaphgragm tank pressure over the life is obtained, as depicted in Figure 10.10. With the assumption that the decrease in thrust is proportional to the decrease in tank pressure, an EOL thrust of 8 N is found.

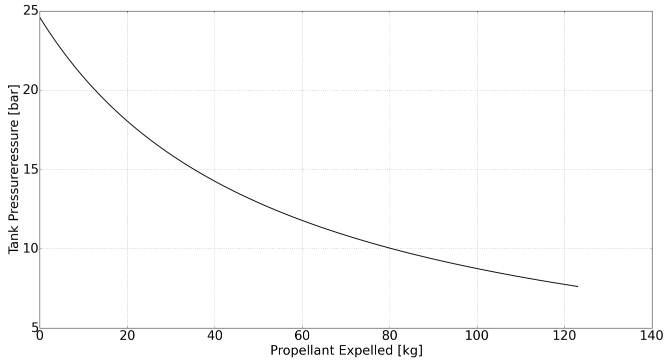

Figure 10.10: Blowdown tank pressure as a function of the expelled hydrazine mass.

Lastly, Brown [13] provides and expression for the decrease in specific impulse as a function of the blowdown ratio for hydrazine mono-propellant thrusters:

$$\frac{I_{sp,EOL}}{I_{sp,BOL}} = 1 - 0.005B \tag{10.17}$$

Based on the selected blowdown ratio, 3.27, a decrease in the specific impulse of 1.6% is expected at EOL. The extra propellant required for this decrease in efficiency is included in the 100% contingency added for attitude and orbit control.

10.5 Electric Propulsion System Design

It is concluded that an ion propulsion system is required in combination to the chemical propulsion system, as explained in the Midterm Report [27]. This electrical system is used to slow down the spacecraft after the Jupiter assist.

Ion engines in the past have not been able to burn for longer than 1 year [148]. However, NASA is intensively researching and developing the NEXT ion thruster, which is revolutionary due to its ability to burn for > 5 years [54]. Due to the high ΔV required (5.86 km/s) and low thrust which the ion engine can deliver, the ion thruster will be required to burn for over 6 years. The NASA NEXT ion thruster will be used aboard the Orpheus spacecraft. This section will discuss the selection of ion propulsion system and put forward the final design.

10.5.1 Thruster Selection

The electrical thruster is selected from the list of available thrusters which have a TRL level of 6 or above. The power available for the thruster is limited to approximately 600-640 watts. This was calculated using the half life of plutonium and 3 GPHS RTGs. This cancelled out a large portion of the possible options. It is observed that if the thrust of the ion thruster is lowered, the burn time required begins to increase drastically as seen below. This results in unfeasible thruster options.

Table 10.21: Electrical Thrusters Compilation

Name	Manufacturer	Type	Power [W]	I_{sp}[s]	Thrust [mN]	P/T*[W/N]	Burn Time [Years]
BHT-200	Busek	Hall-effect	200	1375	13	15385	23.8
BHT-600	Busek	Hall-effect	600	1500	39	15385	7.9
BHT-1500	Busek	Hall-effect	1800	1820	103	17476	3
Tile 200k	Accion	Ion	280	1500	10	28000	30.9
BPT-2000	Aerojet	Hall-effect	2200	1765	123	17886	2.5
BPT-4000	Aerojet	Hall-effect	2000	1676	132	15152	2.3
RIT 10 EVO	Arianespace	Ion	760	3200	25	30400	12.4
NSTAR	NASA	Ion	2300	3185	62	37097	5
NEXT	NASA	Ion	630-7240	4190	25.6 -236	29237	7.7
T6	Qinetiq	Ion	4500	4300	143	31469	2.2

*Power/Thrust

It is observed that none of the engines can burn for durations of longer than a year, with the exception of the NEXT ion thruster [54]. Due to this it was decided to use the NASA NEXT ion thruster. A possibility is to cluster ion engines and stage the engines after their life time, however this approach has an elevated risk and is quite costly. As such this approach was not followed.

The NEXT thruster has a wide thrust range. It is selected to use the lowest thrust possible, which is 25.6 mN when consuming 630 W. This is mainly due to the available power, which can be provided by the GPHS-RTGs. The thruster's mass including current harness is 13.5 kg [54]. Two NEXT thrusters will be required in order to meet the required burn time of 12.1 years. 12.1 years was determined based upon the required ΔV to insert the spacecraft into orbit around Pluto, calculated in chapter 7. The ΔV, in combination with the performance of the thruster, results in a burn time of 12.1 years.

10.5.2 Electrical Propellant and Tank Sizing

The NEXT thruster uses xenon gas as its propellant. The tank which is used to house the xenon is the L-XTA/ 600-900 Family 1 from MT Aerospace(MT Aerospace, Spacecraft Tank Catalogue).

The mass of xenon propellant is calculated using the large ΔV script as explained in section 10.2. This script was the basis of all propulsion calculations both chemical and electrical. In total 720 kg of Xenon propellant will be required, which results in 434 L, assuming a BOL operating pressure of 310 bar. Based on this volume and propellant type, an investigation into possible tanks is performed. Table 10.22 contains a list of potential tanks which could be used aboard the Orpheus spacecraft.

Table 10.22: Specifications of different main xenon propellant tanks

Tank	**Manufacturer**	**Volume [L]**	**Diamete [mm]**	**Length [mm]**	**MEOP [bar]**	**Mass [kg]**
L-XTA / 300-500 Family 2	MT Aerospace	300-500	907	802-1163	187	40-60
Xenon propellant tank	COBHAM	268	907	673	187	22
PVG-65 2	MT Aerospace	65	432	788	310	12
S-XTA-60	MT Aerospace	60	440	790	187	11.7
L-XTA / 600-900 Family 1	MT Aerospace	600-900	1144	979–1306	187	68-85

After reviewing the compilation of different xenon tanks, it is clear that the only tank which can withstand such high pressures is the PVG-65 2. However it can only hold 65 L, thus 7 tanks would be required resulting in a total mass of 84 kg. As such the BOL pressure of the xenon propellants will be required to be reduced. The next highest pressure option is 187 bars, which results in a Xenon volume of 700 L. Based on this the only feasible and practical tank to be used is the L-XTA/ 600-900, from MT Aerospace. Using this tanks results in an approximate Xenon tank mass of 75 kg.

10.5.3 Electrical Propulsion Architecture

Figure 10.11 contains the architecture of the Orpheus ion thruster; the architecture is based upon that of the NEXT thruster [52]. This system uses a single large xenon tank to house all the propellant. The proportional flow control valve allows for a variable outlet pressure and mass flow. This system allows for mass and cost reductions as it no longer requires plenum tanks as used in the DAWN mission [52] and other previously launched ion-propelled spacecraft. This improvement allows for mass reductions in the design.

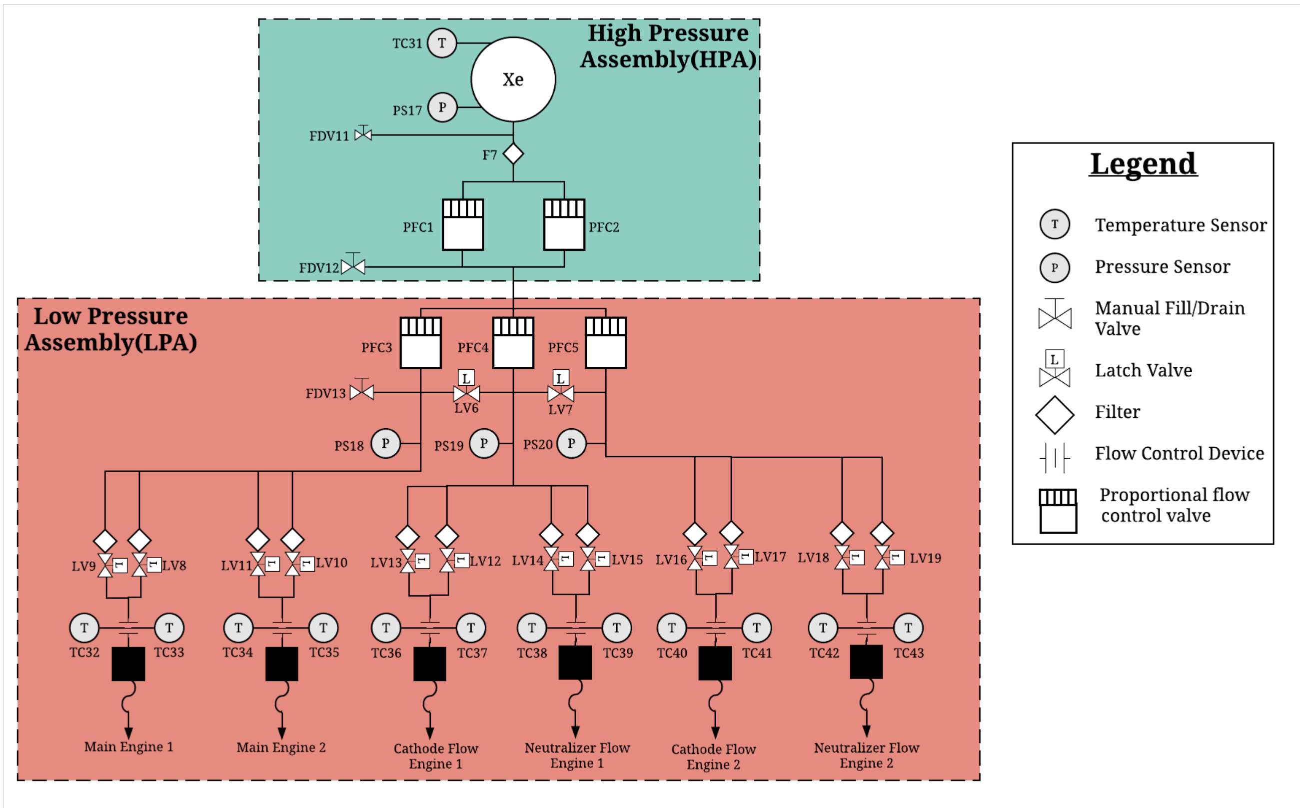

Figure 10.11: Ion propulsion feedsystem architecture

10.5.4 Gimbal System

As the Orpheus spacecraft is a single body structure with no stages, a gimbal system is required for the electrical propulsion system. This is due to the fact that the larger main bi-propellant engine is centred on the spacecraft, to ensure a gimbal system is not required for this bi-propellant engine, due to its high thrust. The high thrust would result in a much larger and heavier system. As two ion thrusters are used each requires its own gimbal system to ensure the thrust is always kept through the centre of gravity of the spacecraft. A gimbal system has already been designed by Swales Aerospace for the NEXT thruster. This system has a mass of less than 6 kg [145]. Figure 10.12 shows the gimbal system which was designed for the NEXT thruster.

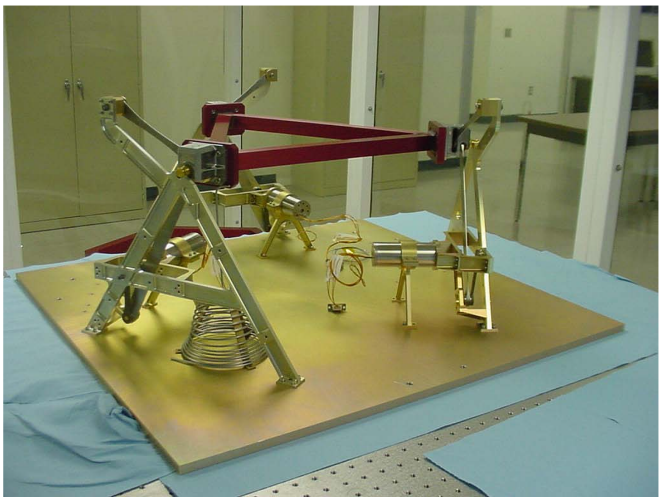

Figure 10.12: NEXT thruster gimbal assembly [145].

Table 10.23: Propulsion subystem component mass distribution.

Component	**No.**	**Total Mass [kg]**	**Mass margin [%]**	**Mass + margin [kg]**
Aerojet AMBR bi-propellant engine	1	5.4	5%	5.7
Ariane Group mono-propellent thruster	12	7.8	5%	8.2
MT Aerospace PTP-124 tank	1	9.8	5%	10.3
MT Aerospace PTP-166 tank	1	10.8	5%	11.3
MT Aerospace PVG family 40-75L tank	1	8.5	5%	8.9
MT Aerospace PTD-177 tank	1	15.5	5%	16.3
Ariane Group Pyrovalve NO	2	0.3	5%	0.3
Ariane Group Pyrovalve NC	6	1.0	5%	1.0
Vacco latch valve	5	3.6	5%	3.8
Vacco fill drain valve	10	0.1	5%	0.1
Vacco check valve	8	0.2	5%	0.2
Omnidea-RTG pressure regulator	2	2.2	5%	2.3
Omnidea-RTG high pressure filter	2	0.1	5%	0.1
Omnidea-RTG low pressure filter	5	0.6	5%	0.5
Burst disks	4	1.0	5%	1.1
MOOG pressure transducer	20	2.5	10%	2.8
NASA NEXT ion thruster	2	27.0	5%	28.4
NASA NEXT Feed System including valves	1	9.0	5%	9.5
Xenon Tank	1	84.0	10%	92.4
Electric Propulsion Gimbal	2	12.0	10%	13.2
Feed system piping and fittings	1	5.0	20%	6.0
Total		**206.4**	**7.8%**	**222.4**

10.5.5 Ion Propulsion Mass

The ion propulsion system is comprised of multiple components. The feedsystem for the NEXT thruster was designed for a single thruster, and as the Orpheus spacecraft has 2, a small amount of extra valves and piping is necessary. In total 9 extra latch valves are added. The MOOG 1/4' latching valve is used for the electrical propulsion system due to its low mass of 340 g (MOOG Isolation Valves Catalogue). The gimbal system has a maximum mass of 6 kg. The tank used has an approximate mass of 80 kg. The total mass of ion propulsion system can be found in Table 10.23.

10.6 Propulsion Subsystem Mass Budget

To allow for an accurate mass estimation of the propulsion subsystem, the mass of different components in the propulsion system are considered, as listed in Table 10.23. Margins are added based on ESA standard `R-M2-4` [76], which implies 5% margin for COTS, 10% for COTS with minor modifications and 20% for a complete new design. Based on Table 10.23 it is found that the total contingency on the propulsion subsystem equals 7.8%, which is in term used in the mass budget in Table 17.5.

10.7 Sensitivity Analysis

For the sensitivity analysis of the propulsion system, it is considered how the propellant mass changes for different design cases. From Equation 10.1, it is known the mass, ΔV and engine performance (I_{sp}) have the largest effect on the propellant mass. In this report, four cases are presented which have the highest sensitivity:

- Effect of change in spacecraft dry mass.
- Effect of change in I_{sp} bi-propellant system.
- Effect of change in orbit around Charon.
- Effect of change in orbit around Pluto.

All sensitivity analyses are made non-dimensional, by considering the percentage change w.r.t. the design value (i.e. the design values imply 0% change).

Firstly, the sensitivity of the dry mass of the spacecraft is examined, with the help of Figure 10.13. The upper boundary (ca. +2%) is constrained by the maximum launch mass of the Falcon Heavy plus kick stage (for all sensitivity analyses). Clearly a dry mass growth above 1.1% requires a reiteration of the launcher or kick stage. Figure 10.14 shows a maximum decrease of 4.4% in specific impulse is allowed to stay within launchable mass. The upper boundary for the specific impulse is set by the maximum performance of the AMBR engine, shown in Figure 10.2.

Second, the effect of a change in orbit around Pluto is considered. When only eccentricity is considered, the Pluto circularisation ΔV is directly related to the maintenance budget (a low circularisation ΔV implies a more eccentric

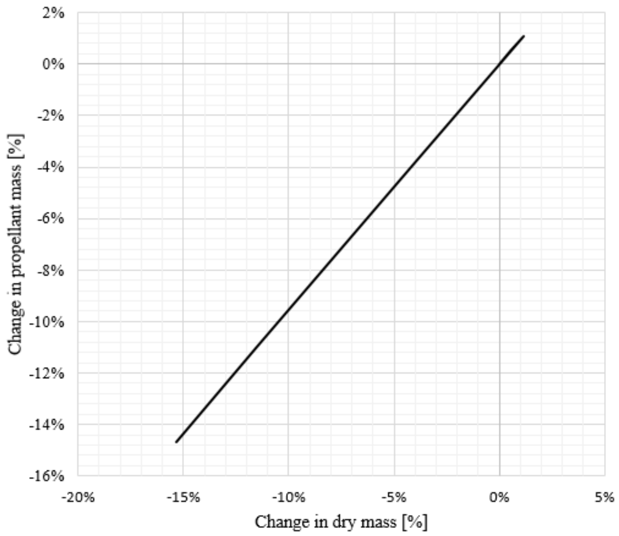

Figure 10.13: Percentage change in total propellant mass for different dry masses.

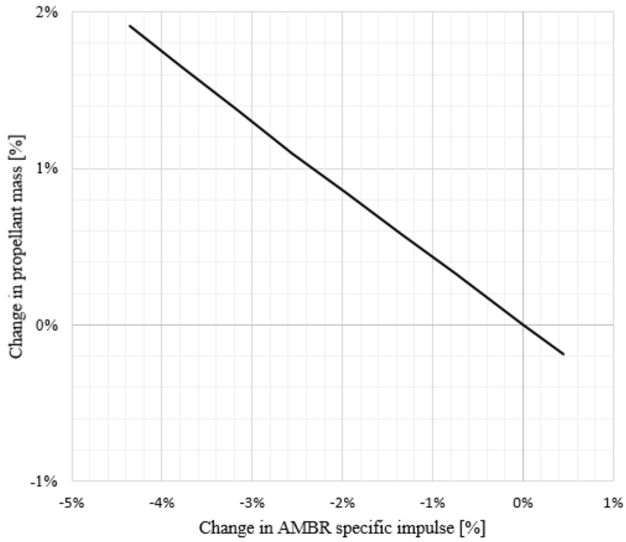

Figure 10.14: Change in total propellant mass for different AMBR specific impulses.

orbit, hence more maintenance is required). The sensitivity of the maintenance and circularisation ΔV is shown in contour Figure 10.15, where the lines in the coloured area indicate the change in propellant mass. Note that the white area on the right corner indicates the no-go zone: here the propellant mass grow out of proportion, making the spacecraft too heavy to launch without changing the launcher configuration (see also chapter 15).

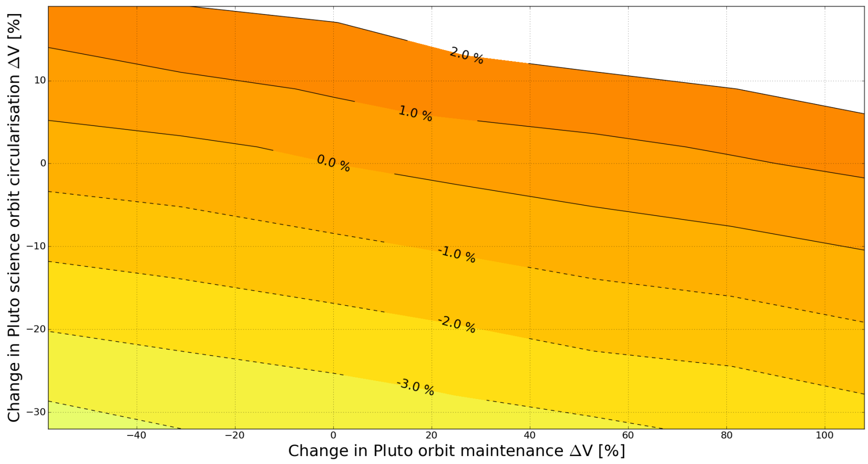

Figure 10.15: Percentage change in Orpheus total propellant mass for different Pluto orbit configurations.

To check the sensitivity on the ΔV for the Charon orbit, a similar approach is followed as for the Pluto orbit sensitivity. Results are shown in the surface plot in Figure 10.16.

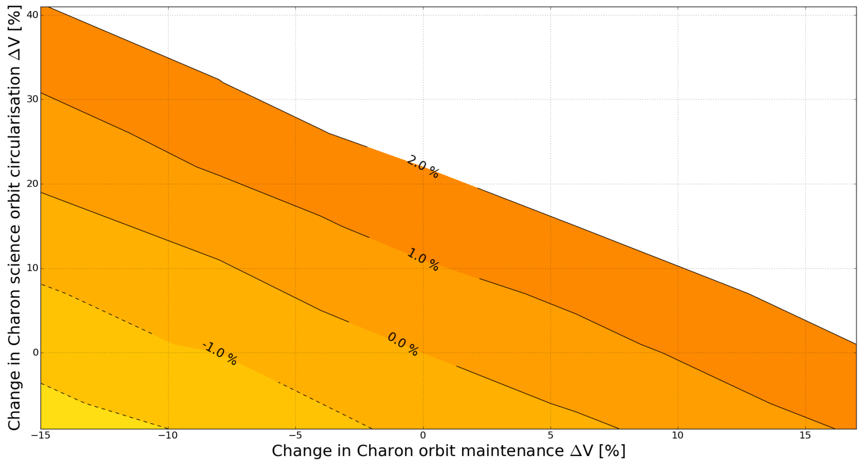

Figure 10.16: Percentage change in Orpheus total propellant mass for a different Charon orbit configurations.

10.8 Propulsion Verification & Validation

In this section the verification and validation methods for the design and the requirements of the propulsion system are discussed. Table 10.1 contains all propulsion subsystem requirements and their tracer.

As many of the propulsion components are acquired off the shelf, integration tests of the parts together is crucial to ensure the functionality of the spacecraft and maintain a high reliability.

Both the chemical and electrical propulsion subsystems have been tested on the ground. The NEXT engine has been fired over 5 times and has been fired for just over 5 years by NASA [54]. The AMBR engine has also been fired over 40 times by Aerojet [65], as such both systems have a TRL level of 6, thus meeting requirement `R-PRP-020`. The electrical propulsion subsystem will be fired for a full burn duration (6.1 years), in order to validate the design can function for that duration (Personal conversation with Dr. Angelo Cervone, TU Delft). This is required to ensure a high reliability, as the burn time specified by the NEXT engineers is currently only theoretical [54].

The electrical propulsion subsystem consumes a maximum power amount below 640 Watts. This power level corresponds to the lowest thrust level of the NEXT thruster [54]. Thus, requirement `R-PRP-030` is met.

The propulsion system is limited to a vertical height of 4 meters and a horizontal distance of 1.5 meters. This is verified by means of Catia V5 R21. Hence requirement `R-PRP-040` is met.

The propulsion subsystem is tested on acoustic loads in the Large European Acoustic Facility [131], to verify it complies with with `R-PRP-050`.

It is required that the ion subsystem operates for 12.1 years. However, the NEXT engine can not operate for this long duration. Therefore two NEXT engines are used, each with a gimbal system, thus requirement `R-PRP-050` is fulfilled. A single NEXT thruster can burn for a theoretical maximum time of 7.77 years [54]. However this is a theoretical value and as such a verification test is required, where the NEXT thruster is placed in a vacuum chamber and operated for 7.77 years. If the thruster can is unable to operate for the full 7.77 years, this is not an issue as it will only need to operate for 6.1 years abord the Orpheus spacecraft.

As previously stated the chemical propulsion subsystem is the AMBR engine from Aerojet. This engine uses a hypergolic propellant combination, thus the engine may be ignited far more than 5 times if needed, thus requirement `R-PRP-060` is fulfilled. [1]. This is verified by means of performing ground tests, where the engine is placed within a vacuum and reignited for a minimum of 5 times.

The ion thrusters are required to deliver a total ΔV of 6060 m/s. This is excluding all margins, for the electrical system a 10% margin was included, thus requirement `R-PRP-070` is met. The margins allow for future spacecraft growth and/or thrusting inaccuracies. This is verified by a static fire test, to ensure the correct ΔV is delivered.

The bi-propellant subsystem is designed to deliver 986 m/s, excluding the 5% margin. This system is designed to fulfil requirement `R-PRP-080`. The margin further guarantees this requirement is met. The mono-propellant system is designed to deliver 150 m/s as per requirement `R-PRP-090`, additionally a margin of 100% is added

[1] http://www.rocket.com/files/aerojet/documents/Capabilities/PDFs/Bi-propellant%20Data%20Sheets.pdf (21-06-2018)

according to ESA standards [76]. This will be verified by a static fire test, to analyse the engine burn and ensure the correct ΔV is delivered.

The oxidiser and fuel tanks, which have been selected, are built and designed by MT Aerospace to be compatible with MON-3 and hydrazine. This is done by an exterior company, as such it doe not need to be verified once again. Due to this requirements `R-PRP-100` and `R-PRP-110` are fulfilled.

As two thrusters are needed, they will be orientated through the CG of the spacecraft, which varies over time. Without a thrust vectoring system the electrical thrusters would propel the spacecraft off course. A gimbal system is included to ensure the thruster orientation is variable. This gimbal is verified by ground testing during a static fire to guarantee its functionality, precision and accuracy. Thus ensuring requirement `R-PRP-120` is fulfilled.

The propulsion system mass is calculated to be 206.4 kg, thus requirement `R-PRP-140` is fulfilled. This will be verified by inspection by measuring the mass of all components and lastly by measuring the mass of the assembled subsystem.

The entirety of the propulsion subsystem is required to function in space. In order to verify this requirement, the subsystem is placed within a vacuum chamber and tested. This will assures requirement `R-SYS-100` is met.

The propulsion subsystem is required to handle a 2 g lateral acceleration and a 6 g longitudinal acceleration. The propellant management devices are designed to handle these loads, and the tanks are also capable as well. The thrusters and other components will be put under vigorous testing to ensure they can handle these loads. This is done to guarantee requirements `R-SYS-130` is met.

The propulsion subsystem is subjected to a vibration test to ensure it can handle both the lateral and longitudinal vibrations of the launch, in order to guarantee compliance with requirement `R-SYS-130`.

The overall system will only be validated after the the mission is completed. The propulsion system will operate for one of the longest space missions. The electric propulsion system will be validated after it has completed the 12.1 year burn, whilst the chemical propulsion system will only be fully validated at the EOL manoeuvre when the bi-propellant system is ignited for the last time to place the spacecraft in a heliocentric orbit.

10.9 Sustainability Analysis

The propulsion subsystem of Orpheus is designed by keeping sustainability in mind, in particular by minimising the use of toxic propellants like hydrazine or NTO (MON-3). Orpheus carries 243 kg of hydrazine and 133 kg MON-3. Although green propellants have been looked at, at this moment there are no available bi-propellant system running on ecological friendly propellants. For the mono-propellant thrusters, sustainable propellants like AF-M315E [59] were considered, however much more propellant mass would be required given the decrease specific impulse obtained from thruster running on AF-M315E. Additionally, there is very limited to no flight heritage of these green propulsion subsystems, significantly increasing the risk of the design. Therefore, the Orpheus design team strongly recommends research institutes to investigate more in the use of green propellants, so that in the future substances like hydrazine or NTO can be completely banned from space.

Although Orpheus consumes toxic propellants, it also gives a lot back to society. As the mission is assumed to be a joint venture between ESA and NASA, propulsion subsystem products were outsourced to both European and American subcontractors. This way, Orpheus gives something back to both nations by providing employment opportunities.

11 Attitude Determination and Control

This chapter addresses the design process of the ADCS (Attitude Determination and Control Subsystem). The determination sensors are sun sensors, inertial measurement units and star trackers. The control actuators are made up of a combination of reaction wheels and thrusters, to allow for various levels of control. A sensitivity analysis and verification and validation of the ADCS is then presented.

11.1 Design Properties and Requirements

The ADCS shall adhere to the requirements displayed in Table 11.1. The following chapter explores the design choices made to ensure the requirements are met.

Table 11.1: ADCS requirements

Identifier	Description	Traceability
R-ADCS-010	The ADCS shall have a safe mode.	R-SYS-100
R-ADCS-020	The ADCS shall fit inside the spacecraft structure.	R-SYS-130
R-ADCS-030	The ADCS mass shall be a maximum of 28 kg.	R-SYS-010
R-ADCS-040	The ADCS shall be functional for the duration of the mission.	R-MIS-091
R-ADCS-050	The ADCS shall have a minimum pointing accuracy of 0.1 degrees.	R-GND-010
R-ADCS-060	The ADCS shall be able to rotate the spacecraft 180° over any of the three axes within 1 hour.	R-SYS-030
R-ADCS-070	The ADCS shall provide a minimum orientation accuracy of 0.1 degrees.	R-GND-010
R-ADCS-080	The ADCS shall be able to spin stabilise the spacecraft at an angular rate of at least 3 rpm.	R-CDH-030
R-ADCS-090	The ADCS shall not exceed a total costs of USD 13 million (2018).	R-SYS-050
R-ADCS-100	The ADCS thrusters shall provide a minimum of 20N per thruster at BOL.	R-ADCS-060
R-ADCS-110	The ADCS shall achieve the spin stabilisation spin rate within 1 hour.	R-ADCS-080
R-ADCS-120	The ADCS shall counter the anticipated disturbance torques.	R-SYS-030

In the Midterm Report [27], the sensor and actuators were selected. The attitude sensing composes of 4 different sensor types, namely two star trackers, two Inertial Measurement Units (IMU), two fine sun sensors, and one sun pulse sensor.

Actuation is comprised of reaction wheels in combination with thrusters, selected in chapter 10. All the chosen instruments for the ADCS can be found in Table 11.2, with the exception of the thrusters, which are detailed in chapter 10. The combination of attitude determination instruments ensures `R-ADCS-070` is met, and the total mass of 24.3 kg, as found in Table 11.2, meets `R-ADCS-030`. Redundancy is implemented for each instrument to lower risk.

The layout of the subsystem will follow the structure displayed in Figure 11.1 [17]. A feedback loop will ensure that the actuation of the attitude is checked by the sensors to achieve an attitude as close as possible to the desired attitude.

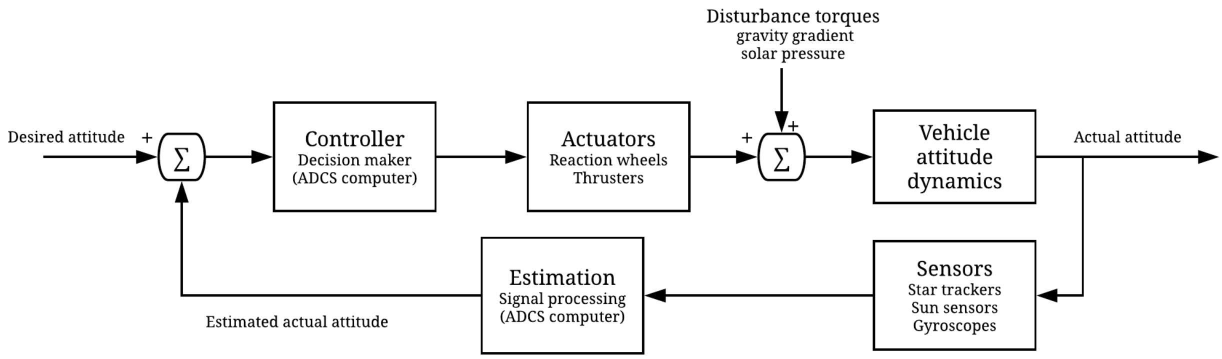

Figure 11.1: Attitude determination and control system diagram [17].

Table 11.2: System Characteristics Attitude Determination and Control subsystem

Instrument	Manufacturer	Angular Accuracy[°]	Mass [kg]	Power [W]	Size [mm^3]	Temp range [K]
Fine sun sensor (x2)	Newspace systems	0.01	0.07	2.6	2x(34x32x21)	248 to 323
Spinning sun sensor	Adcole	0.1	1.50	0.4	2x(66x33x25)	NA
Star tracker (x2)	Jenaoptronik	1	4.00	12.0	2x(274x178 diam)	243 to 333
IMU (x2)	Northrop Grumman	0.1	1.50	24.0	2x(85x89 diam)	219 to 357
Reaction wheel (x4)	Blue Canyon Tech	0.1	16.0	32.0	4x(70x170x170)	NA
Total		**0.1**	**23.1**	**91.0**		**248 to 323**
Total + Margin (5%)			**24.3**	**95.6**		

Due to the range of scenarios the spacecraft must account for, ADCS modes are identified, described in Table 11.3. The addition of a safe mode fulfils `R-ADCS-010`. The actuators used per mode are also given (RCT= Reaction Control Thruster, RWA = Reaction Wheel Array). Within the four modes, submodes are recognised, related to the different phases of the mission, also described in Table 11.3.

The interaction between the modes is shown in Figure 11.2. The spacecraft may only switch between modes independently when entering safe mode from 3-axis and active spin mode. In hibernation mode the spacecraft makes no autonomous decisions. The spacecraft can, however, switch between submodes autonomously, with the exception of the initiation of the burn and TCM (Trajectory Correction Manoeuvre) submodes. To enter a burn/TCM phase, ground control must give the command.

The configuration and placement of the RCT and RWA can be seen in Figure 11.3 and Figure 11.4, respectively. The thrusters are placed so that two thrusters are available in each direction per axis, in case one thruster fails. The fourth reaction wheel (not on an axis) is also placed so that it will produce torque over any axis, should any of the other reaction wheels fail. The spacecraft is assumed to be designed (using strategic tank placements) so that the MMOI over the x-axis and y-axis is equal.

Mode	Description	Actuator
3-Axis	This mode allows the spacecraft to be at a fixed attitude, at a high degree of accuracy.	RWA
Active Spin	The active spin mode monitors and maintains the rotational speed of the spacecraft.	RCT
Safe	When the spacecraft encounters a critical fault, the safe mode is initialised. It breaks out of either active spin or 3-axis mode to point to Earth and send an emergency signal.	RCT
Hibernation	Component-saving mode throughout a section of the trajectory. Hibernation mode shuts down all subsystems with the exception of the thermal and EPS cannot be shut down. Weekly check-ups are performed for health [43]. ADCS is only activated when correction manoeuvres are necessary.	None
Submode	**Description**	
Up/Downlink	Communication and data transfer	
Science	Scientific measurements at Pluto/Charon	
TCM	Trajectory correction manoeuvre for small corrections	
Coast	Mode throughout a section of the trajectory where checks can be run and the spacecraft is monitored	
Burn	Perform transfer burns and manoeuvres	
Find-Earth	Establish communication with Earth in case of a critical fault	
Find-Sun	If no contact with Earth can be established, emergency Find-Sun mode is initiated	

Table 11.3: The modes and submodes of the ADCS system

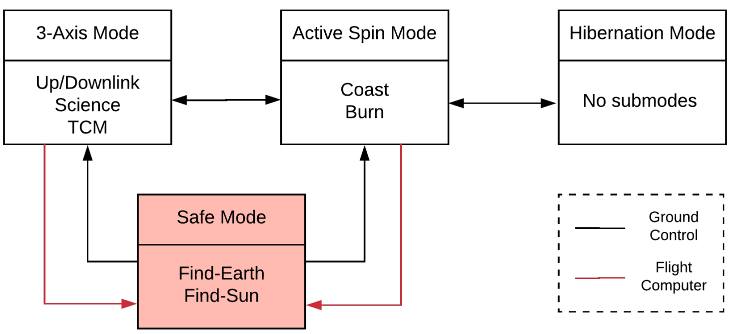

Figure 11.2: The interaction between the ADCS modes

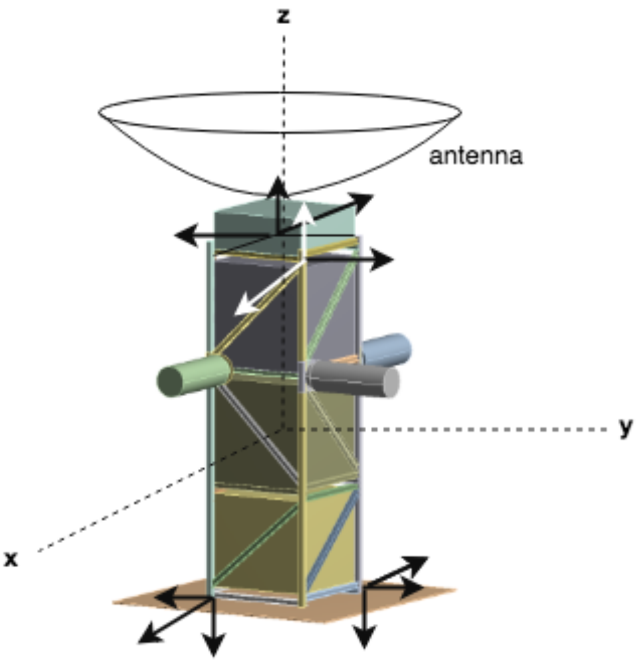

Figure 11.3: The configuration of the RCT.

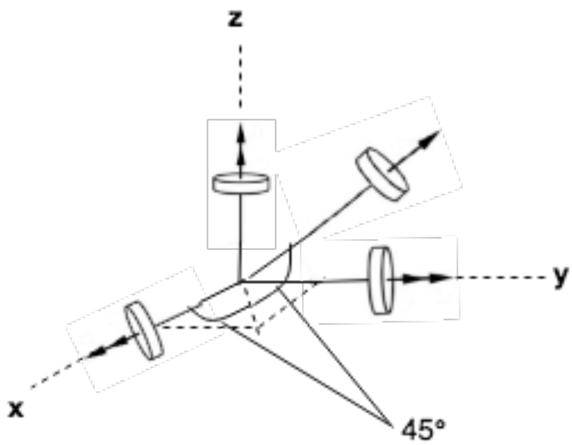

Figure 11.4: The configuration of the RWA [74].

11.1.1 Thrusters

Thrusters are selected in chapter 10 for the active spin mode, safe mode, and to correct the spacecraft trajectory. The thrusters have to be able to orient the spacecraft for trajectory burns (`R-ADCS-060`), handle the spin-up and de-spin manoeuvres (`R-ADCS-80`, `R-ADCS-110`) and dump the momentum accumulated in the reaction wheels `R-ADCS-120`.

Two thrusters are available to produce torque over a single axis, as seen in Figure 11.3. For *rest-to-rest* manoeuvres, they operate using the sequence shown in Figure 11.5.

The Mass Moment of Inertia (MMOI) decreases throughout the mission, hereby also affecting the thruster effectiveness to induce a rotation. In Figure 11.6, the performance of the thrusters when inducing a rotation over the x-axis is studied at different points in the mission: at Earth when the kick stage is still attached, approaching Jupiter before the gravity assist (approximately the same as when the spacecraft is to be rotated for ion thrusting before Pluto), at Pluto before the transfer to Charon, and before the End Of Life (EOL) burn. The MMOI over the x-axis and y-axis is highest, and therefore assessed. The thruster firing time is 1 second, and the mass taken as constant throughout the burn.

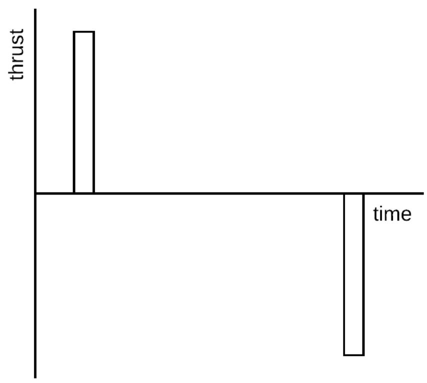

Figure 11.5: Bang-bang thruster configuration.

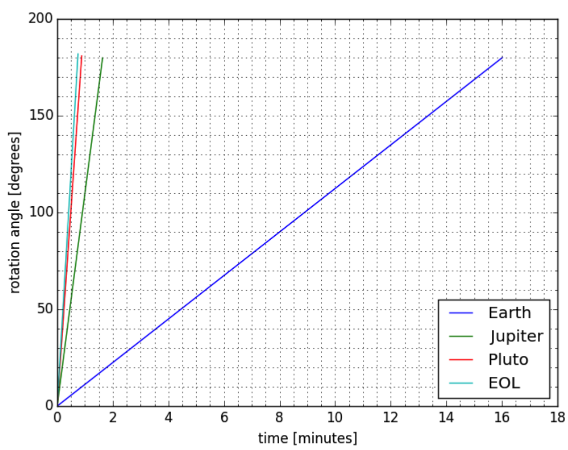

Figure 11.6: The rotation rate of the spacecraft over the x-axis.

R-ADCS-110 has been met, thus no further actions are necessary in this regard.

The thrusters also must be capable of dumping the momentum built up in the reaction wheels. Each reaction wheel has a maximum momentum storage (H_{rw}) of 4 Nms. At an EOL thrust level of 8 N (F) and a distance of 0.65 m from the centre of mass (smallest distance, R_t), a thruster pair must fire for 0.14 seconds to dump the momentum (t_i). This is calculated using Equation 11.1.

$$t_i = \frac{H_{rw}}{F \cdot R_t} \tag{11.1}$$

11.1.2 Reaction Wheels

Reaction wheels were selected for the 3-axis mode, and to counter the disturbance torque generated in the Pluto-Charon system. There are four main sources to take into account: the magnetic field, the gravity gradient, the solar radiation pressure and the atmospheric drag torque. When calculating the atmospheric density disturbance torque following the SMAD [148] method, a torque with magnitude 10^{-26} is reached, making it negligible in the torque estimation. As the magnetic field has not been measured beforehand, it is not possible to estimate a disturbance torque for it. Nevertheless, a margin on the total estimated disturbance torque will be implemented to account for unknown torques as stated in 11.4.

Equation 11.2 [148] displays the formula for obtaining the gravity gradient disturbance torque, T_g. μ represents the gravitational constant, and OR the orbit radius. Two cases are considered for computing the maximum gravity gradient disturbance torque: orbiting Pluto while being as close as possible to Charon, and orbiting Charon, while being as close as possible to Pluto. The sine of twice the angle between local vertical and z principal axis, θ, is taken, with a maximum value of 1. I_x and I_z represent the MMOI. The case with the maximum disturbance torque is selected.

Equation 11.3 [148] describes the solar radiation pressure torque, T_s. Here, Φ is the solar constant, for which the mean value of Pluto's orbit around the sun is taken. With a value of 0.878 $W \cdot m^{-2}$, the constant is about 1560 times smaller than for the Earth's orbit, c is the speed of light, and A_s is the sunlit surface area of the spacecraft exterior. As the final layout is still sensitive to changes, a simplified version of the spacecraft structure is taken as estimation, for which at most half of the surface can be lit. Next, q describes the reflectance factor, which ranges between 0 and 1. To ensure contingency and allowing the material design to be interchangeable, the factor is set at 1. In ideal configuration, the centre of gravity (CG) will lie on the x-axis of the spacecraft, along the middle of the rectangular structure. Therefore, the centre of pressure (CP) can never exceed the outer bounds of the cuboid, 1.84 metres diagonally, which will be set as a limit to this parameter. Last is the cosine of the sun incidence angle.

$$T_g = \frac{3\mu}{2OR}|I_z - I_y| \sin(2\theta) \tag{11.2}$$

$$T_s = \frac{\Phi}{c} A_s(1+q)(CP - CG)\cos(\varphi) \tag{11.3}$$

Using the factors described above, a worst-case estimation of the disturbance torque is made, visible in Table 11.4. There are, however, inaccuracies to account for, which require a margin on the maximum disturbance torque. A moderate margin of 10% is therefore chosen.

Table 11.4: Disturbance torque values.

Torque	Value [Nm]
Solar radiation	8.33×10^{-7}
Gravity Gradient	1.63×10^{-4}
Total	1.64×10^{-4}
+ 10% Margin	1.80×10^{-4}

$$I_{sc}\dot{\omega}_{sc} = I_{rw}\dot{\omega}_{rw} \tag{11.4}$$

$$T = I\dot{\omega} \tag{11.5}$$

The reaction wheels must be sized to account for a 1.800×10^{-4} Nm of torque. Using Equation 11.4 and Equation 11.5 (I = MMOI, rw = reaction wheel, sc = spacecraft, T = torque, $\dot{\omega}$ = angular acceleration), the acceleration of the reaction wheels can be calculated. It is found that every 58.7 hours (211228 seconds), a thruster pair must fire to dump the momentum. This, combined with the thrusters, verifies R-ADCS-120.

Other disturbances can occur due to the unmeasured magnetic field, wheel friction torques, propellant slosh, thruster misalignment and instruments in operation causing torque [148]. These all are identified as internal torque disturbances. Another external disturbance to take into account is leakage of the helium of the propulsion system to the exterior. This is not only problematic as a disturbance, but on a sustainable level as well. Appropriate helium and propellant handling is integrated in the propulsion system, as described in chapter 10.

The spacecraft must be able to orient itself at Pluto and Charon, which is next assessed. It is necessary that the accuracy is at least 0.1° (R-ADCS-050). A simplified Simulink model, based on Figure 11.1 is therefore made to assess the spacecraft's capabilities to do so, shown in Figure 11.7. Theta represents angular displacement. The model assumes a constant mass, and only applies to motion in one axis. The reaction wheel and spacecraft blocks are explained below the figure.

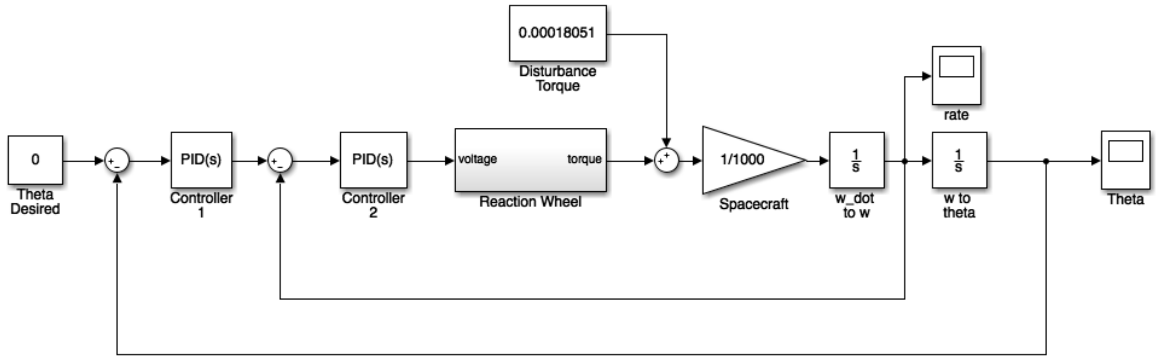

Figure 11.7: The Simulink model of the reaction wheels.

Reaction wheel: Transforms the input voltage to torque on the spacecraft, capping the acceleration at 0.3 Nm (given by the manufacturer).

Spacecraft: Transforms the input torque to angular acceleration of the spacecraft. The value '1000' represents the MMOI, and is altered accordingly.

The PID controllers (Proportional, Integral, Differential) must be tuned so that a range of MMOIs can be controlled. The lowest and highest MMOI are assessed: beginning of operations at Pluto and before EOL burn. Figure 11.8 shows the spacecraft's response to an input command to turn to 1 radian (57°), with no initial angular displacement or angular velocity. As can be seen, the responses do not vary much. The response is tuned using the two controllers to be slow, as this results in the least overshoot. Both cases settle at 1 radian within 2000 seconds (33.3 minutes).

Figure 11.9 shows the spacecraft's response to an input command to turn to 0 radians with an initial angular displacement of 0.52 radians (30°), and angular velocity of 0.01 rad/s (0.57° /s). Again, the spacecraft is capable of orienting itself for both MMOIs within 2000 seconds, fulfilling R-ADCS-060. Upon closer inspection of the graph, both scenarios converge at <0.1° of the target theta, fulfilling R-ADCS-070.

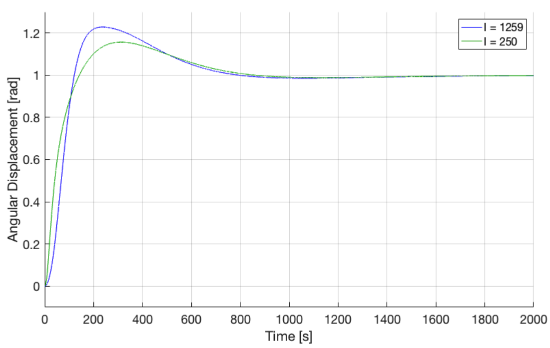

Figure 11.8: Spacecraft angular displacement response to a command to turn to 1 radian.

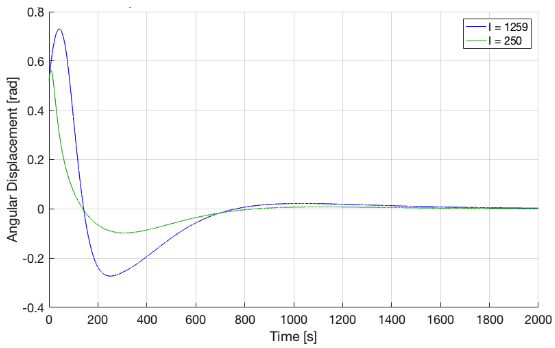

Figure 11.9: Spacecraft angular displacement response to a command to turn to 0 radians.

11.1.3 Spin Stabilisation

In active spin mode and hibernation mode, the spacecraft is spin-stabilised. It will spin about its z-axis, so that the antenna points towards Earth. The z-axis also has the lowest MMOI, requiring the least torque from the thrusters for the spin-up and de-spin manoeuvres. However, due to external torques, spin-stabilised spacecraft precess after some time. This is shown in Figure 11.10. Disturbance torques induce accelerations about the x- and y-axes, causing the axis of rotation to move in a circular motion at angle of γ about the z-axis. As the ADCS will be shut down throughout hibernation phase, except for necessary trajectory correction manoeuvres, the hibernation phase is the case that will be designed for.

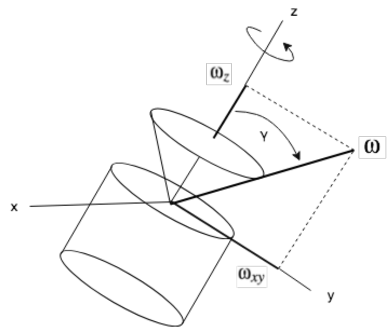

Figure 11.10: The precession of spacecraft.

Using literature from B. Wie and M. M. Peet [150] [116], Euler's equations are first set up in matrix format, as seen in Equation 11.6. I represents the MMOI over its subscript's axis, ω represents angular velocity. ω_z is considered constant, therefore $\dot{\omega}_z$ goes to 0, due to the spacecrafts configuration $I_x = I_y$. Rewriting the ODEs, the relationship in Equation 11.7 is found, which is used to determine the angular velocity vectors. λ is given by Equation 11.8, and $\omega_x(0)$ and $\omega_y(0)$ are determined by Equation 11.5. From the angular velocity vectors, the precession angle γ is calculated using Equation 11.9.

$$\begin{bmatrix} 0 \\ 0 \\ 0 \end{bmatrix} = \begin{bmatrix} I_x\dot{\omega}_x + \omega_y\omega_z(I_z - I_y) \\ I_y\dot{\omega}_y + \omega_x\omega_z(I_x - I_z) \\ I_z\dot{\omega}_z + \omega_x\omega_y(I_y - I_x) \end{bmatrix} \tag{11.6}$$

$$\begin{bmatrix} \omega_x(t) \\ \omega_y(t) \\ \omega_z(t) \end{bmatrix} = \begin{bmatrix} cos(\lambda t) & -sin(\lambda t) & 0 \\ sin(\lambda t) & cos(\lambda t) & 0 \\ 0 & 0 & 1 \end{bmatrix} \begin{bmatrix} \omega_x(0) \\ \omega_y(0) \\ \omega_z(0) \end{bmatrix} \tag{11.7}$$

$$\lambda = \left(\frac{I_z - I_x}{I_x}\right)\omega_z \tag{11.8}$$

$$\tan(\gamma) = \frac{\sqrt{\omega_x^2 + \omega_y^2}}{\omega_z} \tag{11.9}$$

First, the stability characteristics for various spin rates are determined. This is done by applying a torque of 0.1 mNm for 1 second over the x- and y-axis for different spacecraft spin rates, and assessing the consequential precession angle. 0.1 mNm is 10 times the solar radiation torque at Jupiter (calculated using Equation 11.3), and therefore a large disturbance torque.

In Figure 11.11 the precession angles are shown for different spin rates. The spin rate should make the spacecraft as insensitive to disturbance torques as possible, whilst minimising the fuel needed for the spin-up and de-spin manoeuvres, and must be above 3 rpm (`R-ADCS-080`). Figure 11.12 displays how much the precession angle is reduced when increasing the rpm. As can be seen, between 4 and 6 rpm there is only a marginal decrease in precession angle. A spin rate of 5 rpm is therefore chosen, fulfilling `R-ADCS-080`. Both New Horizons and Juno are spin stabilised at 5 rpm, supporting the choice [69] [63].

As solar pressure constantly induces torques on the spacecraft, the precession angle will also increase over time. With the selected spin rate of 5 rpm, the precession rate can be calculated. The solar radiation pressure torque at Jupiter and Pluto was assessed (calculated using Equation 11.3), with its corresponding MMOI. Using the same equations (11.5, 11.6, 11.7, 11.8, 11.9) the precession rate is calculated. This can be seen in Figure 11.13. If left unattended, the total precession angle over a year is 19.0° at Jupiter, and 2.8° at Pluto.

The ADCS must also be able to reach the 5 rpm spin rate within one hour, as stated by `R-ADCS-110`. The thrusters are capable of doing this within 93 seconds with full thrust capabilities (20 N), and at an EOL thrust of 5 N it takes 369 seconds (4.5 minutes), fulfilling the requirement.

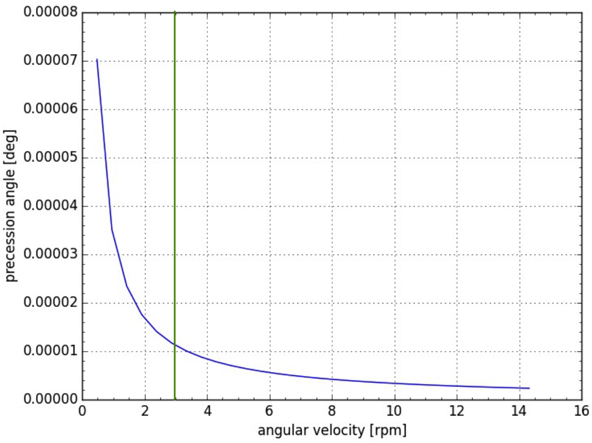

Figure 11.11: The precession angle at different spin rates.

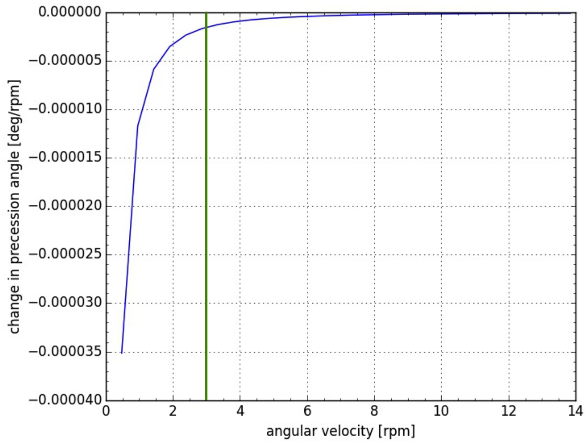

Figure 11.12: The precession minimisation per spin rate.

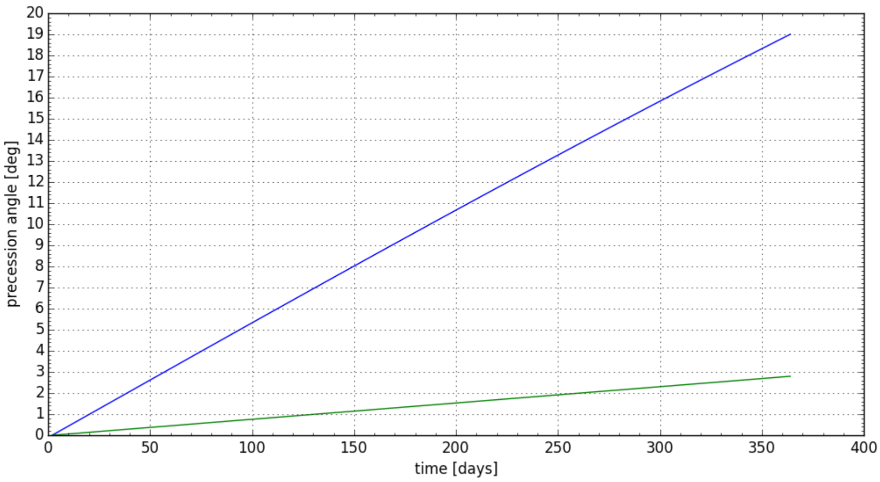

Figure 11.13: The precession angle over time.

11.2 Sensitivity Analysis and Iteration

In Figure 11.14, a different reaction wheel is chosen from Blue Canyon (RW1), with a lower torque and momentum storage capability (0.1 Nm, and 1.5 Nms, respectively). The time to turn to 1 radian from 0 initial displacement or velocity is very similar for both MMOI cases, and both fulfil the 0.1° accuracy requirement `R-ADCS-050`. The lower mass of the reaction wheel means that momentum dumping must take place every 22 hours as opposed to 57; however, the thruster firing time to dump is shorter (0.05 s instead of 0.14), and therefore the total fuel mass needed is equal. RW1 is opted to be the chosen reaction wheel, instead of the RW4, saving 9.6 kg of mass (0.2%).

In Figure 11.15 the I_x and I_y are varied by $\pm$ 100 kg m^2 (for changes in I_z there is no change in precession angle). As in Figure 11.13, 0.0001 Nm is applied over the x- and y-axis. For the chosen rate of 5 rpm, there is very little change in precession angle when either increasing or decreasing I_x or I_y, making it a robust choice.

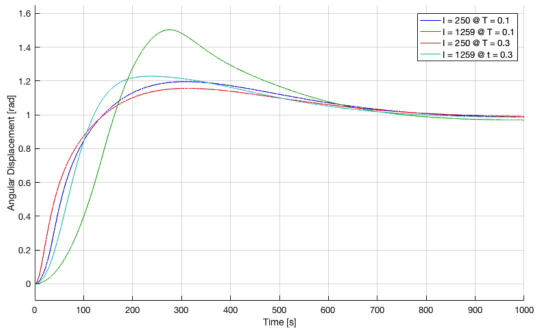

Figure 11.14: The spacecraft response to turn 1 radian for two reaction wheels

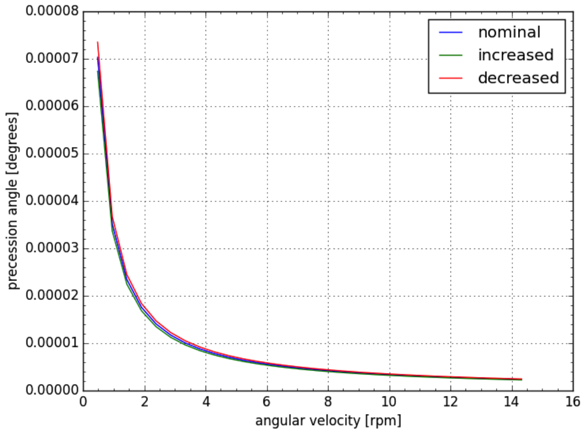

Figure 11.15: The spacecraft precession angles for different MMOIs

11.3 Verification and Validation

Before the subsystem is ready to be used on the spacecraft, several components need to be individually tested before (sub)assemblies can be verified. A general test will be necessary if all equipment is mounted on the spacecraft. The full system testing procedures are discussed in chapter 18 and chapter 21 describes the schedule and testing flow.

To begin with, bench tests can be supplied by the manufacturers of the sensors, as well as other off-the-shelf components of the control system. Thus, all instruments displayed in Table 11.2 have to be thoroughly bench tested by the manufacturers before being integrated into the design. Once these tests have been properly carried out and the instruments have been approved, system verification can take place.

Further testing of the reaction wheels is performed through a thermal-vacuum test, where the compliance of the reaction wheel with the thermal range can be verified [80]. Other possibilities are interference tests to check whether the induced vibrations are not interfering with the measurements of the gyroscopes. For thruster verification, static grounds test are performed within vacuum chambers to simulate the space environment and verify the thrusters performance.

Last, the on-board navigation system (ONS) verification procedure comprises of five steps that need to be followed [80]:

- **Phase I** Test ONS software with simulation environment in Simulink
- **Phase II** Software integration into on-board computer, establish ONS interface
- **Phase III** Integration of sensor hardware for interface testing
- **Phase IV** Full functional integration of sensor software and hardware
- **Phase V** Full functional integration of sensor software and hardware and inputs from other subsystems

The final validation of the ADCS can unfortunately only be done once the mission has propagated, in particular during the end of the mission. Here, the reaction wheels will be used for the first time to ensure enough accuracy for the payload to take measurements correctly. Only after the measurements have been completed, a final review and validation can be done about the full performance of the ADCS.

To ensure the ADCS subsystem follows the sustainability strategies outlined in Chapter 5, parts shall be kept sterile by means of biocleaning with isoprophylic alcohol (IPA). In addition to that, organic cleaning method shall be used. By adding redundancy in the design, the probability of in-orbit break up is decreased and with this guideline 2, explained in section 5.1, is met.

12 Thermal Control Subsystem

This chapter discusses the heat balance of the entire spacecraft, as well as the required temperature range per subsystem, and how it is achieved. The chapter starts by stating the requirements, after which the theory relevant to thermal control is discussed. Next, the system design approach and the design choices are presented. The chapter ends with executed and proposed verification and validation techniques.

12.1 Thermal Subsystem Requirements

Table 12.1 presents the subsystem requirements developed for the thermal control subsystem, traced to mission and segment requirements presented in the baseline report [28].

Table 12.1: Thermal control subsystem requirements.

Identifier	**Requirement**	**Traceability**
R-TCS-010	The TCS shall maintain the temperature of the payload between -40°C and 40°C	R-SYS-100
R-TCS-020	The TCS shall maintain the temperature of the magnetometer between -40°C and 20°C	R-SYS-100
R-TCS-030	The TCS shall maintain the temperature of the energetic particle instrument between 0°C and 40°C	R-SYS-100
R-TCS-040	The TCS shall maintain the temperature of the solar wind analyser between 0°C and -20°C	R-SYS-100
R-TCS-050	The TCS shall maintain the temperature of the energetic particle instrument between 0°C and 40°C	R-SYS-100
R-TCS-050	The TCS shall maintain the temperature of the visible light/IR camera at 25°C	R-SYS-100
R-TCS-060	The TCS shall maintain the temperature of the hydrazine propellant between 2.5°C and 12.5°C	R-SYS-100
R-TCS-060	The TCS shall maintain the temperature of the MON-3 propellant between -6.3°C and 3.7°C	R-SYS-100
R-TCS-070	The TCS shall fit inside the spacecraft structure	R-SYS-130
R-TCS-080	The TCS mass shall be no more than 40 kg	R-SYS-010
R-TCS-090	The active TCS shall be in use for the full duration of the scientific mission	R-SYS-100
R-TCS-100	The TCS shall keep the spacecraft bus at a temperature between -20 and 20 °C	R-SYS-100
R-TCS-110	The TCS shall not exceed a total costs of USD 1.4 million (2018)	R-SYS-050
R-TCS-120	The active TCS shall not consume more than 41 W	R-EPS-010

12.2 Theory for Thermal Control

There are three types of heat transfer: radiation, conduction and convection. As Orpheus will operate in a vacuum, convection is not considered for the thermal control subsystem. All interaction with the space environment is through emitted and absorbed radiation, which will be discussed in more detail in subsection 12.2.1. Internally, heat is assumed to be transferred between subsystems through both radiation and conduction [151], the latter is discussed in subsection 12.2.3. Finally, the RTGs and electronic components of the spacecraft generate heat. Figure 12.1 gives a schematic overview of the heat flows considered for this design phase. Note the difference between internal radiation and external radiation.

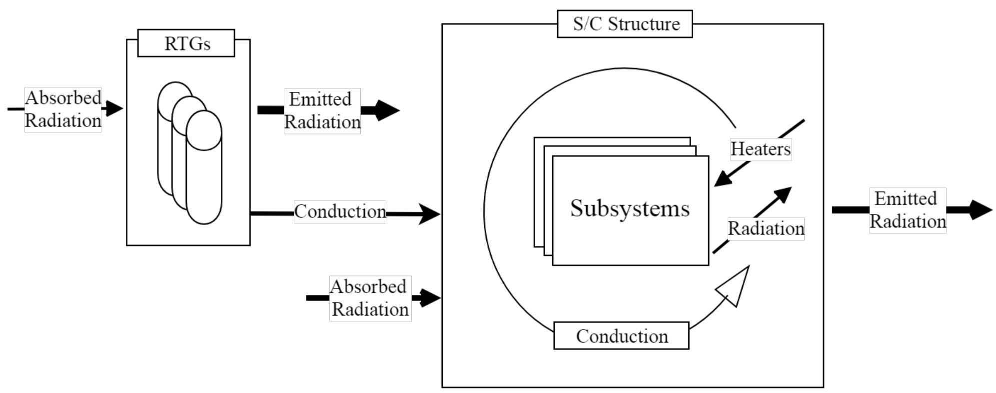

Figure 12.1: Schematic overview of the thermal subsystem.

12.2.1 Radiation Equations

Radiation is both responsible for absorption of and emittance of heat within the spacecraft, subsequently referred to as $\dot{Q}_{absorbed}$ and $\dot{Q}_{emitted}$. The amount of heat transferred is described by equations 12.1 and 12.2, respectively. α_{sc} is the spectral absorption ratio and ϵ_{IR} is the infrared absorption and emission ratio for the infrared spectrum.

Both are discussed in more detail in subsection 12.3.2. The J terms represent flux intensities exposed to a specific area A, indicated with the same subscript. Three fluxes are considered: Solar (subscript s), planet albedo (subscript a) and planet thermal radiation (subscript IR). A_{sc} is the total area of the spacecraft and T_{sc} is the temperature of the emitting surface. σ is the Stefan-Boltzmann constant, which is equal to $5.67 \times 10^{-8} W m^{-2} k^{-4}$.

The albedo flux, estimated by Equation 12.3, is dependent on the albedo of the planet a, given in Table 12.2 and the visibility factor F, discussed in subsection 12.2.2. Planet thermal radiation, Equation 12.4, is a function of the planet temperature T_{IR}, given by Table 12.2 and the Stefan-Boltzmann constant.[153]

$$\dot{Q}_{absorbed} = \alpha_{sc} \cdot J_s \cdot A_s + \alpha_s \cdot J_a \cdot A_a + \epsilon_{IR} \cdot J_{IR} \cdot A_{IR} \quad (12.1)$$

$$\dot{Q}_{emitted} = \epsilon_{IR} \sigma \cdot A_{sc} \cdot T_{sc}^4 \quad (12.2)$$

$$J_a = a \cdot J_s \cdot F \quad (12.3)$$

$$J_{IR} = \sigma {T_{IR}}^4 \quad (12.4)$$

Table 12.2: Thermal characteristics planets on trajectory.

Symbol	Unit	Description	Earth	Jupiter	Pluto	Source
a	[-]	Planet albedo	0.30	0.52	0.16	[153]
T_{IR}	[K]	Absolute planet temperature	255	109	43	[82]
J_s	$[W/m^2]$	Solar flux	1367	51	1.22	[82]
J_a	$[W/m^2]$	Albedo flux	128.74	23.10	0.01	Eq. 12.3
J_{IR}	$[W/m^2]$	Planet flux	239.74	8.15	0.19	Eq. 12.4

12.2.2 Calculation of Visibility Factor

Relevant for the radiation is the area of the spacecraft that absorbs radiation. This is a function of the attitude of the spacecraft, displayed by Figure 12.2. The visibility factor is calculated as the area normal to the direction of the radiation. Figure 12.3 gives this area as a percentage of the total spacecraft surface area for different attitude angles. Varying the three angles shown in Figure 12.2 gives all possible visibility factors. The black dots each represent a certain attitude of the spacecraft. The maximum and minimum visibility are shown by the beginning and end of the black bars. As displayed in the figure, between 4.9% and 32.3% of the spacecraft can be seen. This model does not take into account the spacecraft being in complete eclipse of the planet. As the passive thermal control system is designed for worst case scenarios, the largest visibility is taken for Earth, the warmest part of the mission.. At Pluto, it is assumed the spacecraft is in complete eclipse as this is the coldest part of the mission.

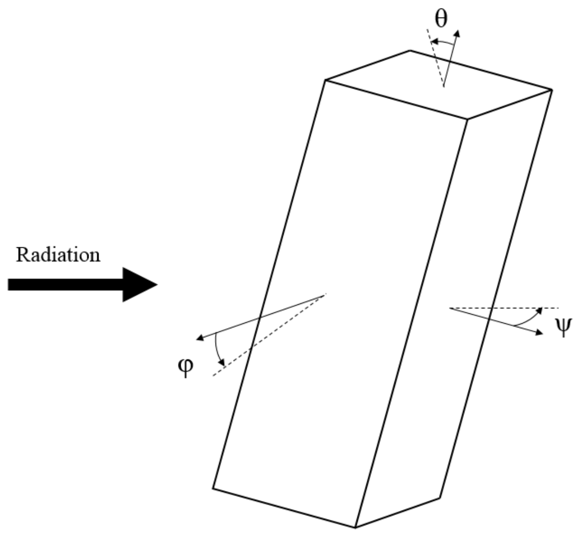

Figure 12.2: Attitude of spacecraft with respect to radiation.

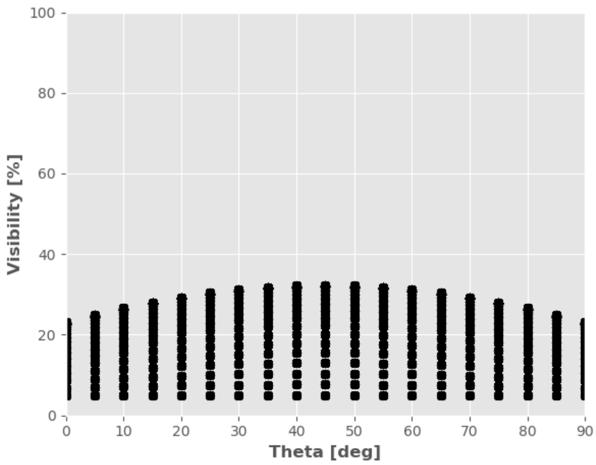

Figure 12.3: Visibility of spacecraft as a function of attitude angle θ.

12.2.3 Conduction Within the Spacecraft

The heat transfer from conduction is given by Equation 12.5 [82]. There are three important variables for conduction. The heat transfer coefficient h_c, which depends on the materials used and the connection, the area of the conduction interface A_c, and ΔT, the difference in temperature between the two parts. It is assumed that all parts are connected to the spacecraft structure.

$$\dot{Q}_{conduction} = h_c \cdot A_c \cdot \Delta T \tag{12.5}$$

12.3 System Design Method

The entire system was modelled using a thermal network in Simulink. The thermal network considers all subsystems to be nodes, interacting with the spacecraft structure through conduction and radiation. The spacecraft itself is split into two main components: spacecraft (S/C) bus and RTGs. The model assumes that these components emit and absorb radiation independently.

12.3.1 Transfer Function Thermal Subsystem

The temperature of the spacecraft is defined by Equation 12.6. Q_{sc} is the total heat in the spacecraft system in Joule, K_{sc} is the heat capacity of the spacecraft. Since the emitted heat is a function of the spacecraft temperature, a transfer function can be derived. The transfer function is given in Equation 12.7. P_{diss} is the heat generated by the spacecraft bus itself, either due to subsystem inefficiencies or from heat conducted by the RTGs.

$$T_{sc} = \frac{Q_{sc}}{K_{sc}} \tag{12.6}$$

$$T_{sc} = \frac{1}{K_{sc}} \int_0^t \dot{Q}_{absorbed} + P_{diss} + \epsilon_{IR}\sigma A_e T_{sc}^4 dt \tag{12.7}$$

12.3.2 Multilayer Insulation - Passive Thermal Subsystem

Multilayer insulation (MLI) is a broadly-used method to achieve an extremely low effective emissivity and absorptivity of radiation [153]. It consists of a number of insulating layers with minimal mutual conduction. The theoretical emissivity of MLI is given by Equation 12.8. However, because of a complex interaction between the layers it is often better to find the actual emissivity experimentally. Several historical MLIs have been collected by Gilmore (2002) and given in Figure 12.4. Here, ϵ_{eff} and ϵ_{IR} are the effective emissivity and the emissivity of one layer respectively. N is the number of layers in the MLI.[82]

In general Equation 12.9 holds, which means the ratio between absorptivity and emissivity is constant for any number of layers [95].

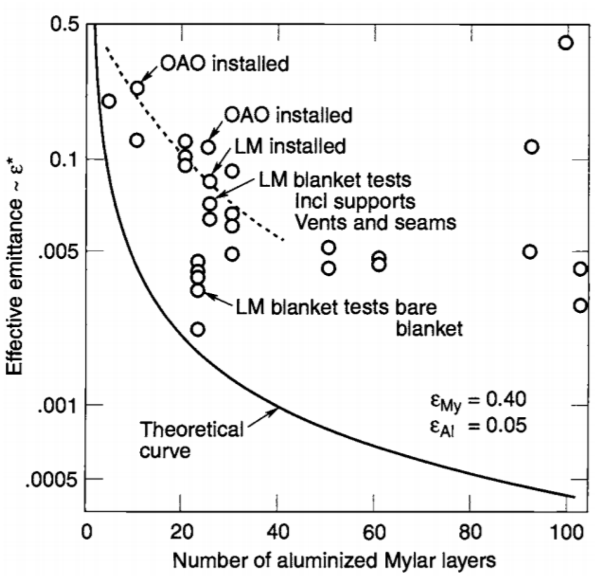

Figure 12.4: Effective emittance versus number of MLI layers [82]

$$\epsilon_{eff} = \epsilon_{IR} \cdot \left(\frac{1}{N+1}\right) \tag{12.8}$$

$$\frac{\epsilon_{IR}}{\epsilon_{eff}} = \frac{\alpha_s}{\alpha_{eff}} \tag{12.9}$$

In Simulink the MLI is programmed using a variable input for the visibility and the planet characteristics. Depending on the location of Orpheus in the solar system these variables are changed. Also relevant is a feedback loop from the spacecraft temperature to the emitted heat, as described by Equation 12.2. Figure 12.5 shows the Simulink model of the radiation. It shows the three types of absorbed radiation described by equations

12.1, 12.3, and 12.4, as well as the emitted heat from Equation 12.2. All heat is assumed to flow directly into the structure.

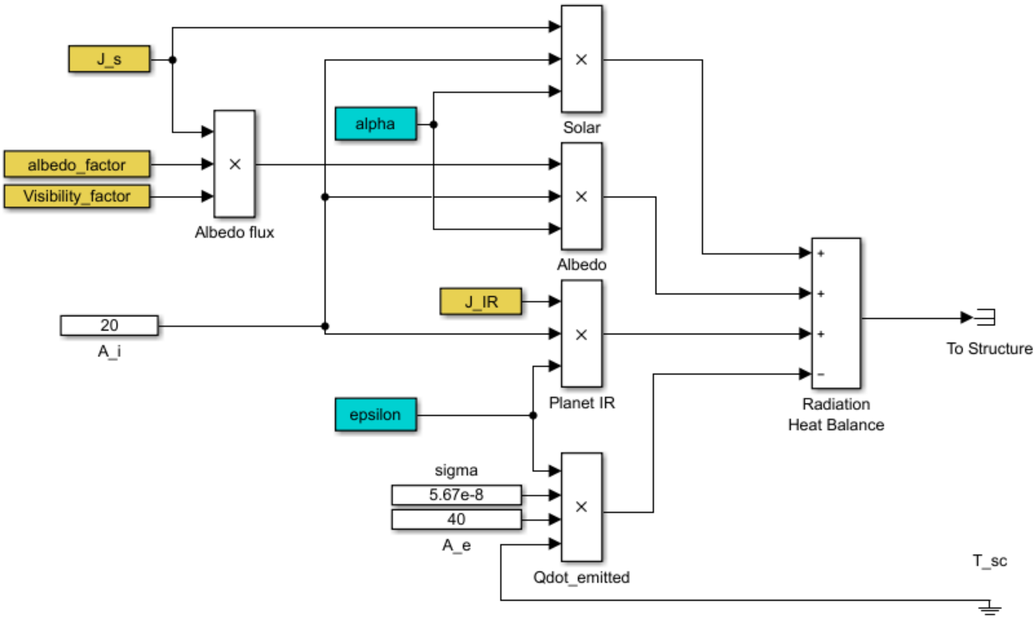

Figure 12.5: Part of the Simulink model showing the radiation absorbed and emitted by the spacecraft.

Using the radiation equations from section 12.2, one can find the equilibrium temperature where the same amount of heat is emitted as absorbed and dissipated by the subsystems. The equilibrium temperature is calculated at both Earth and Pluto, which are considered the warmest and the coldest parts of the mission. Only temperatures between 273 and 303 Kelvin are shown in Figure 12.6, as these are considered viable temperatures for most subsystems. The line at Earth is much more horizontal since there is much more solar radiation at Earth and thus absorptivity plays a much bigger role in the thermal equilibrium. It can be concluded that especially at Pluto the emissivity is extremely sensitive. Also, it is easy to overheat at Earth with the emissivity required to stay warm at Pluto.

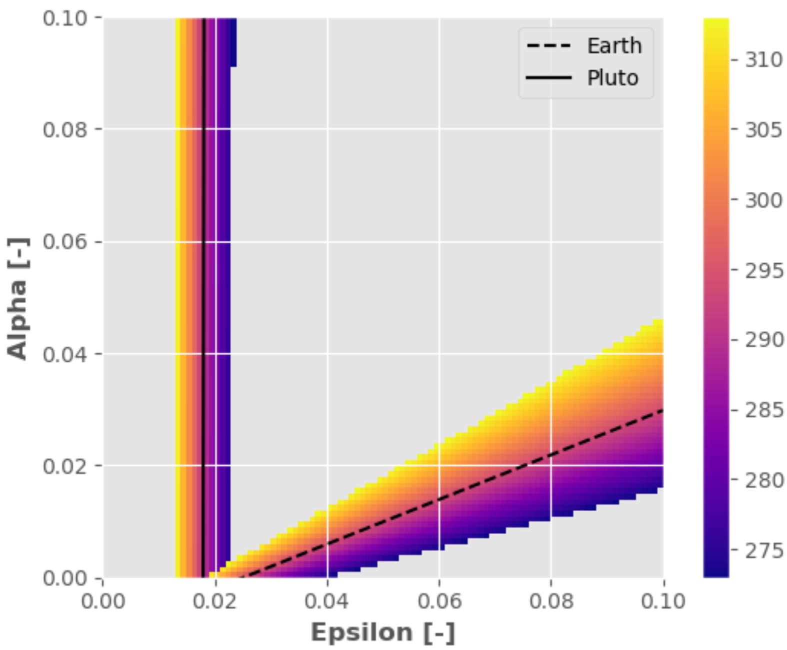

Figure 12.6: Equilibrium spacecraft temperature in Kelvin at Earth and at Pluto. The black lines represent 293°C.

12.3.3 Louvers - Passive Thermal Subsystem

To account for the problem posed by Figure 12.6, louvers are placed on the exterior of the spacecraft. The louvers interrupt the MLI and have a variable ϵ_{IR}. Because of the sensitivity of the spacecraft temperature to ϵ_{IR}, opening and closing the louvers has a large impact and is thus perfect for controlling the spacecraft temperature. This is demonstrated by Figure 12.7, both at Earth and at Pluto the louvers can be used to control the spacecraft temperature. An MLI ϵ of 1.5% and a louver ϵ of 74% is assumed. As can be seen, the marginal effectivity decreases as the louver size increases.

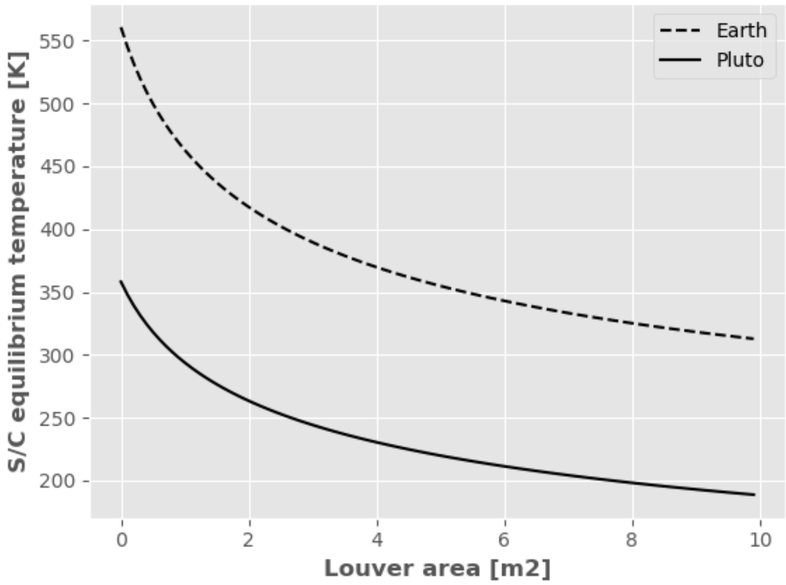

Figure 12.7: Spacecraft equilibrium temperature in response to varying area of louvers opening.

Passive louvers open over a range of temperatures and thereby emit part of the spacecraft heat. They do not use electricity for this as the blades open as a result of thermal expansion. Figure 12.8 shows the part of the Simulink model that account for the louvers. Simulink takes the structure's temperature as an input, along with the desired temperature and louver characteristics. Important to note is a maximum emissivity value when the louvers are completely open, and a minimum emissivity when the louvers are entirely closed.

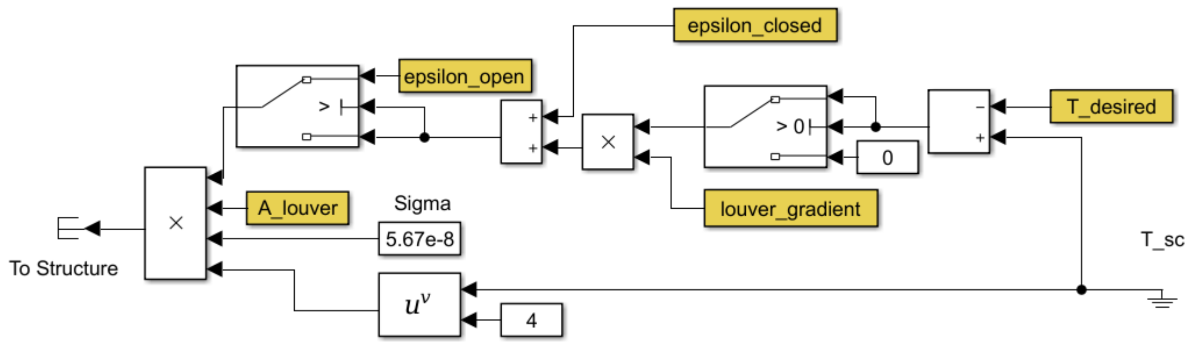

Figure 12.8: Simulink model of louvers, input is structures temperature, output is heat to structures.

12.3.4 Heaters

Heaters are used to apply heat wherever necessary. The extent to which this is required is dependent on the conduction from and to the part and the difference in temperature between the part and the structure. As Orpheus is designed to require minimum power, in most cases the conduction from and to the part is tuned such that no heater is required during operation hours of a subsystem. If the subsystem is then shut off, heat may be applied to maintain the part within an acceptable temperature range. Figure 12.9 gives the Simulink representation of a subsystem heater. Input is the spacecraft temperature T_{sc}, output is the heat from or to the structure of the spacecraft bus.

Figure 12.10 gives a sensitivity analysis of the temperature of the payload subsystem as a function of heat added by a heater. The figure assumes a spacecraft temperature of 266 K and a conductivity of 2 $W/°C$. There is a clear

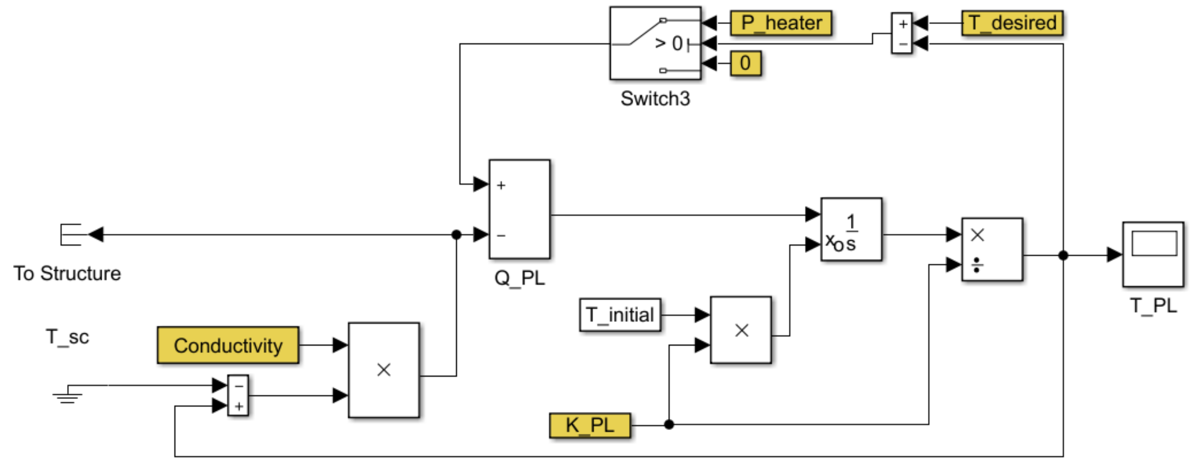

Figure 12.9: Simulink model of a heater for the payload subsystem.

linear relation, which can be explained by a linear increase in conducted energy as a result of an increasing ΔT between the payload and the rest of the spacecraft. Using this information, it is easy to determine the required heater power for each subsystem.

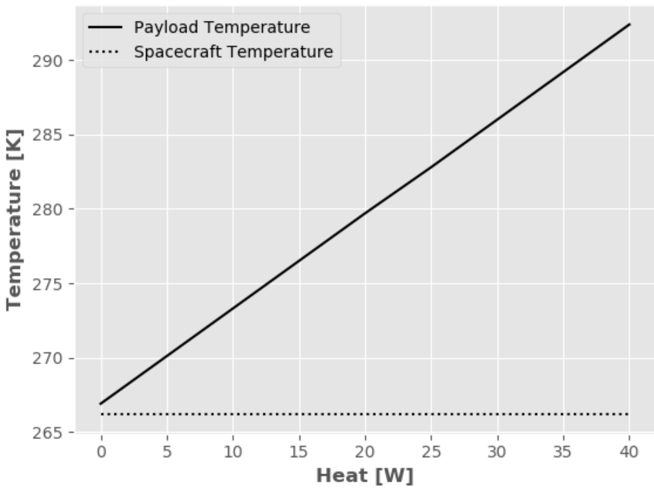

Figure 12.10: Sensitivity analysis of heat added to Payload subsystem.

12.4 Mission Thermal Characteristics

Table 12.3 gives an overview of the spacecraft variables that influence the temperature range, which is used in the selection of hardware in section 12.5. Also relevant is an estimation of the heat capacity of the major components, given by Table 12.4.

Table 12.3: Spacecraft thermal characteristics.

Parameter	Unit	Explanation	Based on	Estimation
T_s	[K]	S/C temperature	Determined in section 12.5	TBD
A_e	[m^2]	Area emitting heat	Surface area designed in architecture (section 16.2)	34
A_i	[m^2]	Area facing sun/planet	A_e times the visibility factor	7.7-10.8
P_{RTG}	[W]	Heat generated by RTGs	Efficiency of RTG (5%)	12000
ϵ_{IR}	[-]	Emissivity spacecraft	Determined in section 12.5	TBD
α_s	[-]	Absorptivity spacecraft	Determined in section 12.5	TBD

Table 12.4: Specific heat capacity for subsystems.

	Mass [kg]	Dominant material [-]	Specific Heat Capacity [J/kg K]	Total Heat Capacity [J/K]	Source
Structure	132	Carbon fibre	1130	149160	
Thermal Control	48	Kapton	1090	52320	
Communications	41.36	Carbon fibre	1130	46736.8	
C&DH	6.825	Silicon	710	4845.75	
ADCS	33.6	Aluminium	910	30576	
Propulsion	525	Aluminium	910	477750	
Power & harness	107.5	Copper	390	41925	
Payload	37	Aluminium	910	33670	
Propellant	979	Hydrazine	3078	3013362	
Total S/C bus	1912	-	-	3852211.05	
RTG	50	Aluminium	910	45500	

12.5 Hardware Selection

The selection of hardware can be split into internal and external components. The external, or passive, components should ensure the spacecraft bus remains between -20°C and 20°C (`R-TCS-110`). The internal hardware ensures the more specific temperature requirements (`R-TCS-010` to `R-TCS-060`).

Using Figure 12.4 and Figure 12.6 an MLI with an emittance of 0.02 is selected. This is achieved by using 20 layers of aluminized kapton.

Passive louvers are used to emit any redundant heat into space. Sierra Nevada Corporation provides louvers which open linearly over a range of 14°C. They have an emissivity of 14% when closed and 74% when opened. Figure 12.11 shows the variant with 20 blades and a surface area of $0.16m^2$. A total of 1.6 m^2 is needed to account for the difference in heat absorbed and emitted between Earth and Pluto. 10 louvers are to be used.

Cartridge heaters can be inserted into a component to distribute the heat over all its elements. They are selected such that they produce the amount of heat that would otherwise be generated by the payload itself. The difference between science mode and communication mode is 29.4 W, assuming an efficiency of 30%, that means heaters need to compensate 20.6 W. The tanks have to be kept very close to 0°C (`R-TCS-070` and `R-TCS-080`). This is done using patch heaters on the tank making up the difference between -20°C and 0°C. Using the appropriate tank insulation this is achieved with 20W. For reliability issues, every required heater has a redundant one added to it [82]. Also, every heater has an accompanying thermistor and redundant copy to measure the local temperature.

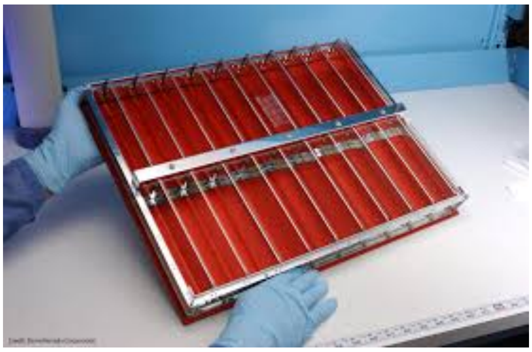

Figure 12.11: Passive Thermal Louvers [19]

Table 12.5: Thermal control subsystem hardware.

Element	Quantity	Total mass	Total power	Source
MLI outer layer	34 m^2	1.87 kg	-	[82]
MLI inner layer	34 m^2	1.7 kg	-	[82]
MLI seperator layers	680	28.56 kg	-	[82]
Louvers (0.16 m2)	10	12.9	-	Sierra Nevada Corp.
Thermistor	-	<1kg	2.0	muRata Thermistors
Cartridge Heaters	-	<1kg	20.6	Table 17.3, THERMOCOAX
Patch Heaters	-	<1kg	15	Table 17.3, THERMOCOAX
Total	-	34.13-37	37.6	-

Figure 12.12 gives a schematic overview of all active components in the thermal subsystem in relation to the rest of the spacecraft.

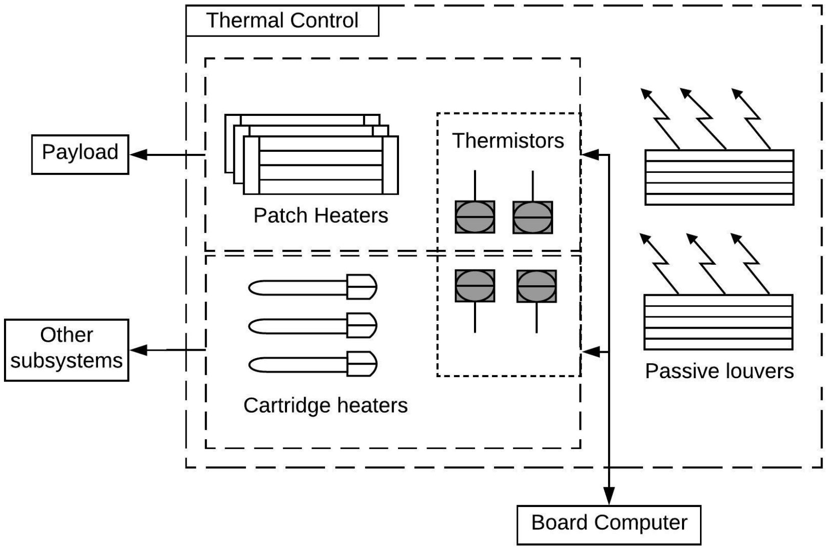

Figure 12.12: Overview of Thermal Subsystem

12.5.1 Sustainability and Reliability

To comply with the sustainability strategies proposed in Chapter 5, organic cleaning methods shall be implemented during assembly of the thermal control system. In addition to that, parts shall be kept sterile by means of biocleaning with isoprophylic alcohol (IPA). Besides this, during the use of insulation foils and anti-radiation coatings, maximum effort will be spent on preventing the contamination of the environment. A big risk for the MLI is the degradation and darkening of the layers. This increases the absorptivity and emissivity over the lifetime of Orpheus. To minimize this, the MLI is made out of carefully selected materials and protected with an optical coating which decreases the effect of UV on the MLI [47]. All active components of the thermal control subsystem are fully parallel redundant. Which means the termistor can cooperate with both heaters and the heater can cooperate with both thermistors.

12.6 Verification and Validation

Verification and validation of the thermal control subsystem is an integral part of the design phase. The full system testing procedures are discussed in chapter 18 and chapter 21 describes the schedule and testing flow.

To verify the design process unit tests are performed on the Simulink model. By isolating elements of the model, like those presented earlier in this chapter, and placing them in a different environment, their correctness is verified. The entire model is verified using available data from existing spacecraft, by altering the input parameters to those from an actual spacecraft and seeing whether the model predicts the spacecraft to function as it did in reality, the Simulink model can be validated.

Validation of the multilayer-insulation is crucial because the exact properties of MLI are hard to predict. The first stage of validation can be done analytically, after that a physical test setup is required, for which A vacuum chamber is essential to filter out any convection effects [53].

All off-the-shelf products (louvers, thermistors, and heaters) must be bench tested by the manufacturers. All instruments displayed in Table 12.5 should comply with the requirements before buying them from the suppliers. After the individual components have been verified the system can be tested.

Validation of the power usage and mass is easily performed by testing the system once assembled. The final validation of the entire system is performed in a boundary condition thermal vacuum chamber [107]. Results from the tests are used to alter the input values of the Simulink model.

13 Communications Subsystem

The following chapter presents the final design concept for the communication subsystem, which links the Orpheus spacecraft with the Deep Space Network (DSN). Firstly, the design concept is presented, with the required components and system characteristics. The design and iteration process is then described, and the system characteristics are generated. Finally, verification and validation procedures for this subsystem are proposed.

13.1 Initial Design Concept

In the Midterm Report [27], a trade-off was made for the communication subsystem on which type of antenna shall be used. It was concluded that, due to its high gain, a parabolic antenna would be the most appropriate for the Orpheus mission.

Due to the launcher size constraints, the antenna cannot be larger than 4.5 meters in diameter. Therefore, a preliminary link budget was developed to verify the concept choice. The main output values of this analysis are the following: the antenna diameter is 4.5 meters for a required input power of 80 W; the obtained data rate is 3.6 kbps. The following sections present a more detailed re-iteration of the design based on these initial parameters.

13.2 Communication Subsystem Requirements

The following section presents the subsystem requirements developed for the communication subsystem, traced to mission and segment requirements presented in the Baseline Report [28].

Table 13.1: Communication subsystem requirements.

Identifier	Requirement	Traceability
R-COM-010	The communications array shall consume 50% of the available power or less.	R-SYS-050
R-COM-020	Science data shall be downlinked by the spacecraft in X-band.	R-GND-010
R-COM-030	The maximum bit error rate during data downlink shall be equal or lower than 10^{-5}.	R-MIS-260
R-COM-040	The communication subsystem shall not cost more than USD 9 million (2018).	R-SYS-050
R-COM-050	The communication subsystem shall not weigh more than 44 kg.	R-SYS-010
R-COM-060	The spacecraft shall downlink to Earth with a data rate of more than 1 kbps.	R-GND-010
R-COM-070	The spacecraft shall have a downlink frequency of 8.4 GHz	R-GND-010
R-COM-080	The spacecraft shall have an uplink frequency of 7.145 GHz	R-GND-020
R-COM-090	The antenna shall have a diameter equal or less than 4.5 m.	R-SYS-130
R-COM-100	The communication subsystem shall have no single points of failure.	R-SYS-080
R-COM-110	The communication subsystem shall operate within the temperature range 15-45° C .	R-SYS-100

Requirement `R-COM-020`, `R-COM-070` and `R-COM-080` are given by the capability of the DSN, as its 70 m diameter antennas only function in the X-band [136]. Requirement `R-COM-030` is an industry standard [78] for deep space missions. Requirement `R-COM-040` comes as a result of the cost budget breakdown presented in the Midterm Report [27].

Taking the capabilities and specifications of the New Horizons communication subsystem [32], requirements `R-COM-050` and `R-COM-060` are made in order to ensure the improvement of the system compared to the first Pluto mission, by improving on the data rate New Horizons achieved. Requirement `R-COM-090` is given by the selected launcher, the Falcon Heavy payload diameter [130]. Finally, `R-COM-110` is the most narrow temperature range in which all the components of the communication subsystem can normally operate in.

13.3 Design Process

The communication subsystem must provide a reliable link between the spacecraft and the ground station. In order to achieve this, the architecture presented in Figure 13.1 is required, based on the New Horizons mission [32].

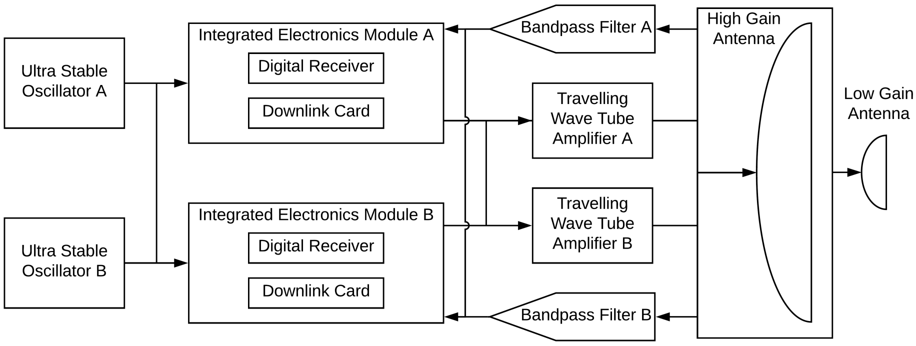

Figure 13.1: Communication subsystem block diagram, based on New Horizons architecture.

Redundancy is implemented in the system by implementing two duplicate branches: A and B. Each component is also connected to both branches, increasing the reliability of the subsystem. The following components can be identified:

- **High gain antenna:** As determined previously, a high gain parabolic antenna is required to close the link budget.
- **Low gain antenna:** This component is required for redundancy, in case the high gain antenna fails. It obtains a lower data rate than the high gain antenna.
- **Bandpass filter:** A bandpass filter is needed to minimise the impact of noise on received data. Frequencies outside the transmitted bandwidth are diminished, while the needed frequencies are amplified [32].
- **Integrated electronics module:** Contains the receiver and the downlink card. Modulates data to the carrier signal [32].
- **Ultra stable oscillator:** Produces the carrier signal [32].
- **Travelling wave tube amplifier:** Amplifies the carrier signal before it is transmitted by the antenna [32].

An important part of the design is the downlink budget, which is iterated by implementing actual component characteristics rather than statistical or analytic values. Therefore, by considering the initial link budget, the components presented in Table 13.2 are selected, based on the New Horizons architecture.

Table 13.2: Communication subsystem components.

Name	Amount	Mass Per Piece (Margin)	Size	Source
Boeing 601 Antenna	1	18 kg (5%)	4.5 m diameter	[140]
Thales TH4704 TWT	2	2.35 kg (5%)	TWT: 381x80x55 mm EPC: 177x67x113 mm	[126]
Low Gain Antenna	1	2 kg (20%)	0.5 m diameter	[140]
JPL/APL Ultra Stable Oscillator	2	0.5 kg (5%)	50.8x50.8x38 mm	[42] [75]
Integrated Electronics Module	2	0.5 kg (5%)	150x230x20 mm	[88]
Other Components	-	10 kg (10%)	-	[32]
Total		39.1 (9.6%)		

The relative margin of the total mass is obtained by adding the margins set on all components in comparison with the total mass of the subsystem. Therefore, by taking into consideration the characteristics given by the component selection, the link budgets presented in Table 13.4 and Table 13.5.

13.4 System Characteristics

Considering the design process presented above, the resulting system characteristics are explained in this section. For redundancy, two antennas are used: the 4.5 m diameter high gain antenna used on the Boeing 601 bus, and a 0.5 m diameter downscaled version of the same model, placed at the focal point of the main one, acting as a reflector. Therefore, the system characteristics shown in Table 13.3 can be determined.

Table 13.3: Communication subsystem characteristics for each antenna.

Name	Value	Source	Name	Value	Source
High Gain Antenna			Low Gain Antenna		
Diameter	4.5 m		Diameter	0.5 m	
Efficiency	0.57	[139]	Efficiency	0.57	[139]
Required Pointing Accuracy	0.1 deg		Required Pointing Accuracy	3 deg	
Input Power	160 W		Input Power	160 W	
Obtained Data Rate	5.3 kbps		Obtained Data Rate	22 bps	

A maximum data rate of 5.3 kbps is obtained using the high gain antenna with an input power of 160 W, requiring a pointing accuracy of 0.1° from the attitude control subsystem. The low gain antenna provides a data rate of 22 bps with a required pointing accuracy of 3°. This is optimal for safe mode and low rate communication with the ground, in case the high gain antenna is unavailable.

The data rates are computed for a distance of approximately 44 AU, which is the sum of the distance from the Sun to Pluto in 2055, one year after the latest arrival, and one astronomical unit to account from when the Earth is at its furthest distance with respect to Pluto. The power is limited to 160 W due to the limited capability of the Thales TH4704 TWT amplifiers, and due to dry mass restrictions. A link budget is also used to confirm that the Deep Space Network is able to provide data rates of up to 1 Mbps, however, as it does not pose any constraint to the design, it is not included in this report.

To ensure that the system complies with the sustainability strategies proposed in Chapter 5, organic cleaning methods shall be implemented when integrating the communication system. In addition to that, parts shall be kept sterile by means of biocleaning with isoprophylic alcohol (IPA). Since the antenna is made out of carbon fibres, during manufacturing care shall be taken to protect the health of workers and the environment, as described in chapter 5. Therefore, subcontractors would have to implement extra safety measures in order to avoid potential health hazards, or electronic component breakdowns due to the conductive nature of carbon.

13.5 Verification and Validation

In case of the communication subsystem, verification is done by developing a link budget, as shown in Table 13.4 for the high gain antenna, and Table 13.5 for the low gain antenna, and a sensitivity analysis, presented in Figure 13.2. The link closes with the required margin, therefore the design is verified.

The following equations, also described in the Midterm Report [27], are used to determine the link budget. The signal to noise ratio is given by the following equation [149]:

$$\frac{E_b}{N_0} = \frac{P_t \cdot G_t \cdot L_a \cdot G_r \cdot L_s \cdot L_{pr} \cdot L_r}{R_d \cdot k \cdot T_{sys}} \tag{13.1}$$

Where E_b/N_0 is the signal power to noise ratio, P_t is system the input power, G_t is the gain of the transmitting antenna (Equation 13.2), L_a is the loss factor due to atmospheric conditions, G_r is the receiving antenna gain, L_s is the loss factor due to free space propagation (Equation 13.4), L_{pr} is the loss due to pointing accuracy (Equation 13.3), L_r is the overall system loss, R_d is the data rate, k is Boltzmann constant, and T_{sys} is the system temperature.

The gain of a parabolic antenna can be estimated using the following equation [148],

$$G_t = \frac{\pi^2 D^2}{\lambda_s^2} \cdot \eta \tag{13.2}$$

where D is the antenna diameter, λ_s is the transmitted signal wavelength, and η is the antenna efficiency.

The pointing loss of an antenna in decibels is estimated by Equation 13.3 [149]:

$$L_{pr} = -12 \cdot \left(\frac{e_t}{\alpha_{1/2}}\right)^2 \tag{13.3}$$

where e_t is pointing accuracy, and $\alpha_{1/2}$ is the half power beamwidth angle.

The free space loss is given by Equation 13.4 [149]. Furthermore, Equation 13.5 [148] estimates the half power angle of a parabolic antenna. In the equations below, S is the transmission distance, and f is the signal frequency.

$$L_s = \left(\frac{\lambda_s}{4\pi S}\right)^2 \tag{13.4}$$

$$\alpha_{1/2} = \frac{21}{f \cdot D} \tag{13.5}$$

Another element required for the link budget is the theoretical channel capacity. The Shannon-Hartley theorem [117] can be used to determine the theoretical data rate as a function of the bandwidth and signal power to noise ratio. The law resulting from this theorem is presented in Equation 13.6:

$$C = B \cdot \log_2\left(1 + \frac{E_b}{N_0}\right) \tag{13.6}$$

where C is the theoretical channel capacity and B is the signal bandwidth. Therefore, using the equations presented, the link budgets can be summarized with the values shown in Table 13.4 and Table 13.5.

Table 13.4: High gain antenna link budget for the Orpheus mission.

Parameter	Value	Unit	dB	Source
ORPHEUS Antenna Gain	-	-	49.52	[139]
ORPHEUS System Temperature	150	K	-21.76	[46]
ORPHEUS System Loss		-	-1.7	[37]
ORPHEUS Transmission Power	160	W	22.04	
Space loss		-	-307.22	
Atmospheric loss	-	-	-0.05	[148]
DSN Antena Gain	-	-	74.6	[136]
Frequency	8400	MHz	-	[136]
Pointing Loss	-	-	-0.39	[149]
Boltzmann	1.38E-23	J/K	228.6	
Data Rate	5.3	kbps	-37.24	
Bandwidth	6	MHz	-67.78	[127]
Eb/No	4.36	-	6.40	
CNR			-24.14	
Theoretical Data Rate	14537	kbps		[117]
Half Power Beamwidth	0.56	deg		[148]
Required Eb/No			3.4	[148]
Required margin			3	[148]
Final margin surplus			0.00	

Table 13.5: Low gain antenna link budget for the Orpheus Mission

Parameter	Value	Unit	dB	Source
ORPHEUS Antenna Gain	-	-	30.43	[139]
ORPHEUS System Temperature	150	K	-21.76	[46]
ORPHEUS System Loss		-	-1.7	[37]
ORPHEUS Transmission Power	160	W	22.04	
Space loss		-	-307.2	
Atmospheric loss	-	-	-0.05	[148]
DSN Antena Gain	-	-	74.6	[136]
Frequency	8400	MHz	-	[136]
Pointing Loss	-	-	-5.015	[149]
Boltzmann	1.38E-23	J/K	228.6	
Data Rate	22	bps	-13.42	
Bandwidth	6	MHz	-67.78	[127]
SNR	4.47	-	6.50	
CNR			-47.85	
Theoretical Data Rate	14712	kbps		[117]
Half Power Beamwidth	5.88	deg		[148]
Required SNR			3.4	[148]
Required margin			3	[148]
Final margin surplus			0.10	

In order to verify the robustness of the proposed design, a sensitivity analysis is developed, presented in Figure 13.2. Both sub-figures present the effect of a change in data rate (Figure 13.2a) or input power (Figure 13.2b) on the link margin, which determines if the budget closes or not, and therefore if the communications subsystem works in an optimal mode. The initial value is shown in both cases, together with the slopes at that point. From the equation of the slope in Figure 13.2a, the high sensitivity of the link margin to a change in data rate can be observed, as the slope is approximately 0.8. This means that a 1% change in the amount of information sent per second changes the link margin by 0.04 dB, which is a considerable amount.

On the other hand, the local sensitivity of the link margin to a change in input power is lower, as it can be seen from the slope of the derivative (0.0271 as opposed to -0.71). However, a 1% change in power has the same effect as the data rate, as the same multiplication factor is used in Equation 13.1.

Furthermore, tests are performed using conditions predicted during the mission to structurally and functionally test the system. The components are placed in vacuum to verify the effects of low pressurisation on their properties and performance. This can be tested using the IV10 Vacuum Chamber of the University of Pisa in Italy, as the vacuum chamber has a diameter of 6 m, enough to fit the high gain antenna [79].

Furthermore, the data rate is tested on a small scale and compared to simulated results. The distance upon which the test is performed can be of low magnitude, and then up-scaled to simulate the distance to Pluto. The data obtained would have to be highly accurate, and the conditions need to be controlled thoroughly.

The subsystem cannot be fully validated before the launch, as the 50 AU distance between Pluto and Earth cannot be replicated on ground. Therefore, the simulations and tests need to be thoroughly verified in order to minimise the risk of low data rates. Furthermore, the effects of the long mission time cannot be replicated either, therefore the subsystem cannot be validated from this point of view. The expected reliability of the mission must therefore

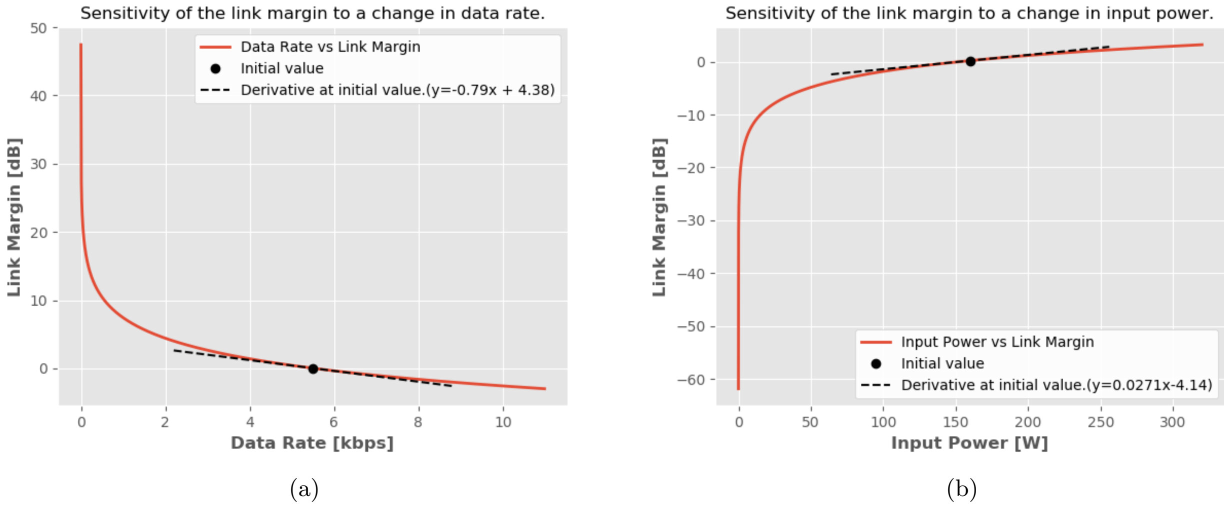

Figure 13.2: The sensitivity of the link margin to a change in data rate (a) and power (b) for the high gain antenna.

be investigated using past data, and simulations must be run in order to ensure that the probability that the subsystem will fail during the mission life is minimised.

13.6 Communication Flow Diagram

The purpose of the communication subsystem is to achieve connection with the ground. The communication flow diagram presented in Figure 13.3 shows the path that the data need to take in order to reach the end user. This diagram is an update with respect to the one presented in the Midterm Report [27].

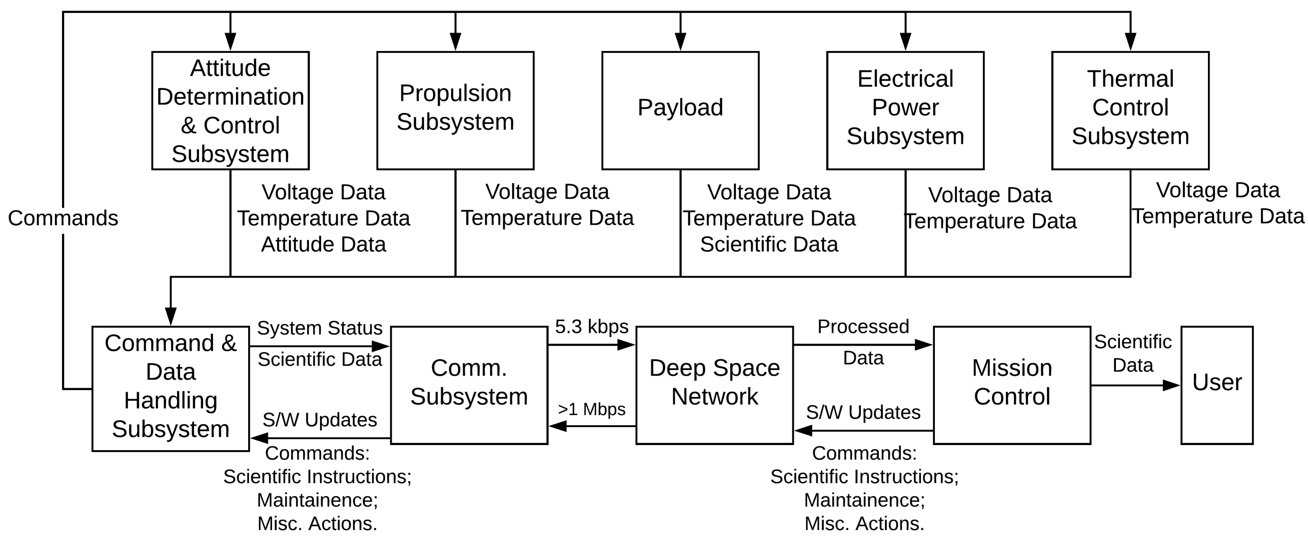

Figure 13.3: Communication flow diagram.

Subsystems receive instructions from the command & data handling subsystem (C&DH), and output status parameters (voltage, temperature). Other data received by the C&DH subsystem include spacecraft attitude and scientific data. This data is then processed, and transmitted by the communications subsystem to the Deep Space Network, and then it reaches its final destination (the scientific community).

14 Command & Data Handling Subsystem

The following chapter presents the detailed design process and results for the Command and Data Handling subsystem (C&DH). Firstly, the initial design concept is presented, which is used as a baseline for the design. Then, subsystem requirements are stated, which are then used to select an on-board computer. Finally, software considerations are discussed, and verification and validation procedures are explained.

14.1 Initial Design Concept

It was decided in the Midterm Report [27] that the operating system used for the mission will be Nucleus RTOS from Mentor, due to its low price and wide hardware support. Furthermore, it was predicted that the storage required for the mission will be larger than that of New Horizons, therefore more than 16 Gigabytes.

As the payload data rate is defined in the section 6.2, an on-board data processing unit can be chosen for the Orpheus mission. The interface of the C&DH subsystem with the other subsystems and components of the spacecraft is then developed upon.

14.2 Command & Data Handling Subsystem Requirements

Subsystem requirements were developed in order to serve as guidelines for the design of the on-board computer, presented in Table 14.1

Table 14.1: C&DH subsystem requirements traced to segment or mission requirements.

Identifier	Requirement	Traceability
R-CDH-010	The software shall be updateable from ground.	R-SYS-030
R-CDH-020	The spacecraft shall send a confirmation signal if a command was executed or failed.	R-SYS-030
R-CDH-030	The C&DH subsystem shall implement system hibernation.	R-SYS-110
R-CDH-040	The C&DH subsystem shall implement system safe mode.	R-SYS-100
R-CDH-050	The C&DH subsystem shall contain more than 16 Gigabytes of storage.	R-MIS-260
R-CDH-060	The C&DH subsystem shall transmit a periodic status update during hibernation.	R-SYS-110
R-CDH-070	The real-time data system shall be able to monitor the spacecraft operational status.	R-SYS-100
R-CDH-080	The C&DH subsystem shall be available a minimum of 99% of the mission time.	R-MIS-091
R-CDH-090	The C&DH subsystem shall have a reliability of 0.99 or above.	R-MIS-091
R-CDH-100	The C&DH subsystem shall have a mass of 10 kg or less.	R-MIS-060
R-CDH-110	The C&DH subsystem shall use 30 W or less input power.	R-MIS-260
R-CDH-120	The C&DH subsystem shall comply with size requirements set by the launcher.	R-SYS-130
R-CDH-130	The C&DH subsystem shall not have any single points of failure.	R-MIS-091

Requirements `R-CDH-010`, `R-CDH-020` and `R-CDH-070` stem from the required maintainability level of the spacecraft, described in Chapter 4. The software will be maintained through updates uplinked using the DSN. Furthermore, Orpheus will also have to be monitored constantly during the mission to ensure compliant availability and reliability. `R-CDH-030`, `R-CDH-040` and `R-CDH-060` are produced by the need to have a hibernation and safe mode to increase the reliability and availability of the system, explained in more detail in section 14.5.

The size of the storage is determined by requirement `R-CDH-050`, as it was concluded in the previous project phase that the memory would have to be greater than that of New Horizons. `R-CDH-080`, `R-CDH-090` and `R-CDH-130` stem from the need for the Orpheus components to be highly reliable, due to the large mission time. Finally, `R-CDH-100` to `R-CDH-120` are produced by the budget requirements for the system (mass, power and size), described in Chapter 17.

14.3 On Board Computer

Functions of the C&DH subsystem include command management, science and engineering data management and transmission, and general system maintenance. The most important part of C&DH is the on board computer. The RUAG Next Generation On Board Computer was selected for its long guaranteed lifetime, its architecture presented in Figure 14.1 [129]. The diagram also presents the data interface between the other spacecraft components and the C&DH subsystem.

The most important characteristics are given in Table 14.2 [129]. Another important aspect is that of software-hardware compatibility. In this case, the SPARC V8 Processor is supported by Nucleus RTOS (according to the compatibility database created by Mentor, the developer of Nucleus[1].

[1])

The on board computer is designed to be parallel redundant. If the processing unit, the input/output interface or memory processing fails, the redundant half can cover the function individually. Another safety feature included in the computer is a programmable reconfiguration sequence. This functions as a watchdog timer (detects computer malfunctions) and resets the computer periodically.

Table 14.2: Characteristics RUAG Next Generation On Board Computer.

Parameter	Value	Unit	Rationale
Mass	6.5	kg	
Power	<23	W	
Reliability	0.99	-	for 20 years
Processing Memory	537	MB	
Processing Power	110 DMIPS	-	@87.5Hz
Data Storage	2x50	GB	
Size	208x242x278	mm	

All data is generated by the subsystems and science instruments, as depicted in Figure 14.1. It enters the on board computer via the input ports of the instrument and subsystem interface. There it is processed and stored in long term memory, while concurrently the processor manages the data: generated bits are compressed, encrypted and prepared for downlinking. The subsystem data is evaluated and subsystem commands are outputted, if required. The RUAG Next Generation On Board Computer also holds two memory storage units of 50 Gigabytes. This far exceeds the 16 Gigabytes as prescribed by requirement `R-CDH-050`. The memory provides redundancy by having both units connected to both processors.

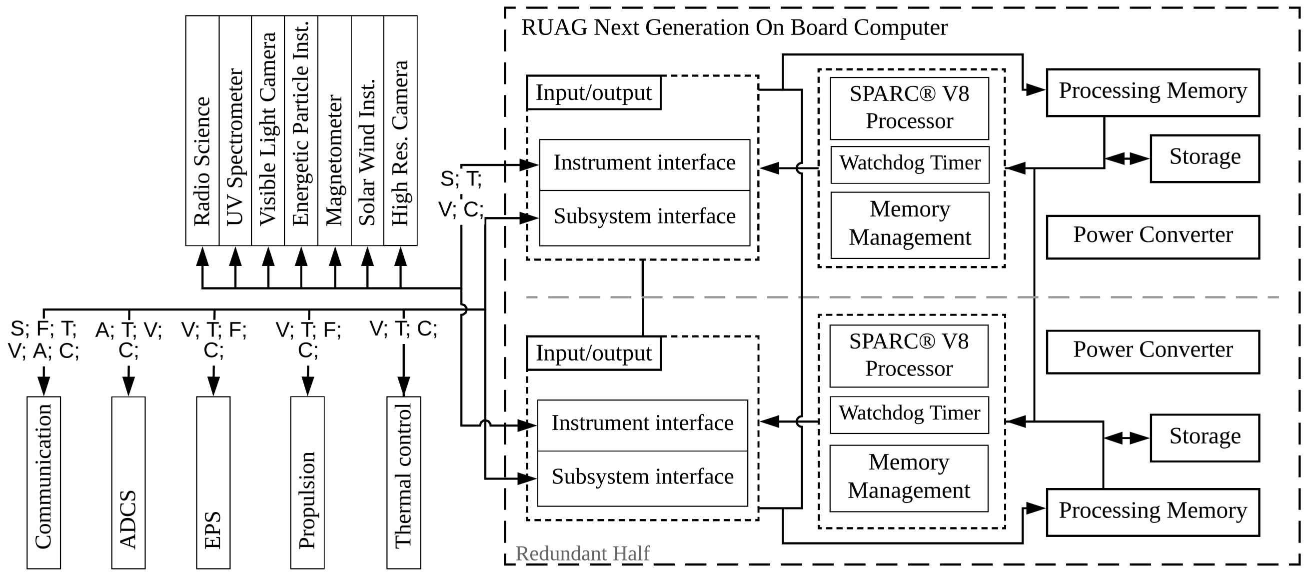

Figure 14.1: Data handling diagram, with data flow; S: Scientific Data; F: Fuel Level; T: Thermal Data; V: Voltage Data; A: Attitude Data; C: Commands.

In selecting the components for the on board computer, sustainability was considered an important criterion, especially hazardous substances and conflict materials (carbon based, such as the structures), which pose a challenge for these parts. As all components are acquired off the shelf, it is ensured that the manufacturers of the on board computer (RUAG) and of the processor (Oracle), have implemented sustainable procurement statements.

14.4 On Board Software

Nucleus RTOS (Real Time Operating System) by Mentor will be used as the operating system of the Orpheus spacecraft, as it has a high reliability and relatively low development cost. The software functionality can be divided into five modules, as portrayed in Figure 14.2.

The data processing module functions as the bridge between the information the instruments provide, and the transmitted data. This part of the software is responsible for the sorting, compression, encryption, storage and transmission of the instrument outputs.

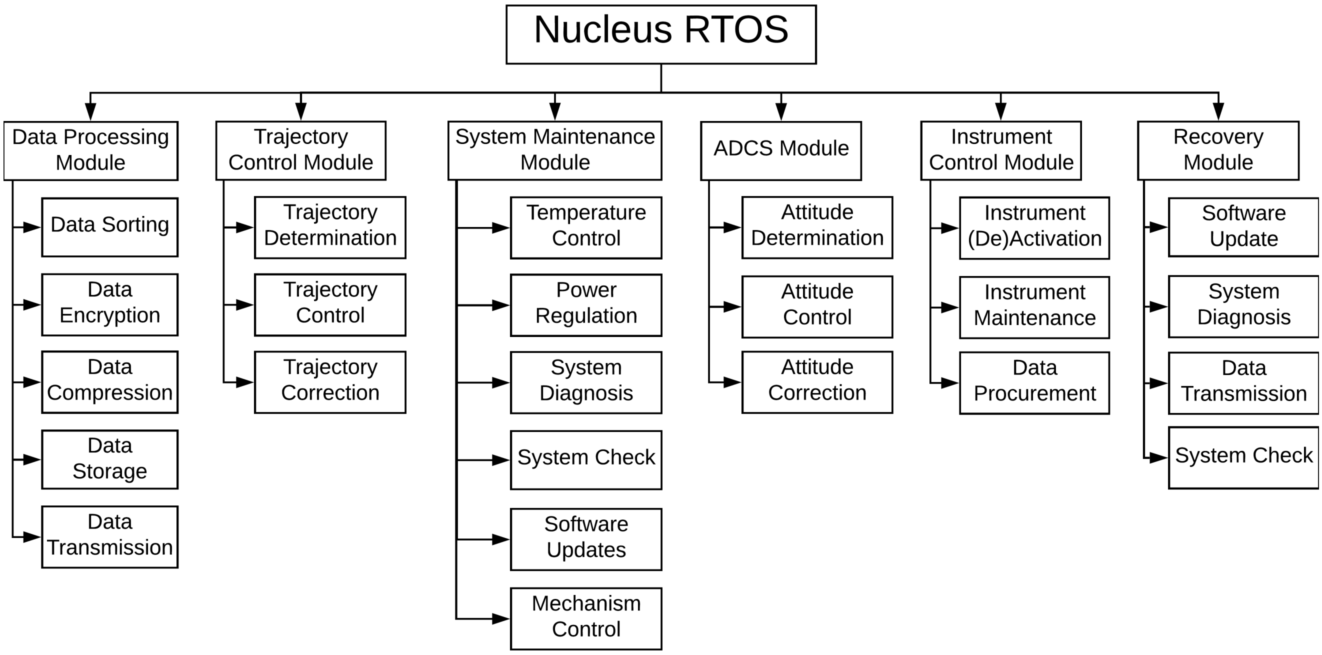

Figure 14.2: Software block diagram.

The trajectory control module is charge of engaging and maintaining the desired path to the Pluto-Charon system. This module works together with the Attitude Determination and Control Subsystem (ADCS) to achieve this, by controlling the propulsion subsystem.

The system maintenance module assures the functionality of all subsystems, and gathers information on their status. This module contains the thermal control, as well as power regulation and system check software. It also is able to perform software updates, and control the mechanisms, such as the magnetometer boom.

The ADCS is responsible with the orientation and stability of the spacecraft. It contains the stability control software, and collects data from sensors. It also facilitates scientific data recording by pointing the instruments in the desired direction.

The instrument control module is in charge of the duty cycle of the scientific payload, and decides its activation and deactivation. It also collects the scientific data from the instruments, and bridges it to the data processing module.

Finally, the recovery module serves as a separate entity of the Orpheus software. It is an operating system with limited functionality, and is only used when the on-board computer is in safe mode. It must be able to communicate with the ground station, and procure diagnosis data from the subsystems as well as from the main operating system. It is also able to update the main software, and perform limited commands (orienting spacecraft towards Earth), in order to keep the risk of complete software failure at a minimum.

14.5 Hibernation and Safe Modes

The software and hardware of the C&DH subsystem are responsible for initiating system hibernation and safe mode. These operational modes are implemented to increase the reliability, availability, maintainability and safety of the Orpheus spacecraft.

Hibernation mode consists of several actions that are performed by each subsystem. The C&DH subsystem will initiate hibernation during the coast phase of the mission, when most components are not needed. During hibernation, the subsystems are either turned off, or function in a low power state, except the thermal and EPS subsystems. The first must maintain the temperature of the spacecraft within operational levels, while the latter cannot be shut down, as the power source is nuclear, and must therefore be regulated.

During hibernation, the C&DH subsystem will function on a low power mode implemented in the software, that maintains a low clock speed and uses minimal resources. It therefore only operates the functions necessary to control the two subsystems mentioned above. This process will also extend the reliability of the on-board computer through lowering the wear of the components [30].

The hibernation mode implemented in the Orpheus mission will be similar to that of New Horizons, where the spacecraft will periodically send a beacon signal to Earth once per week, and a full systems check once per month

[64], by engaging the communication subsystem. This allows the ground station to fix potential problems in advance of the general operations phase.

A safe mode will also be implemented with the software of the system, with the purpose of acting as a safeguard measure in case of operating system failure. This mode consists of only using the essential functions for communication and diagnosis of the software. The process to perform spacecraft maintenance using safe-mode is explained in the Figure 14.3.

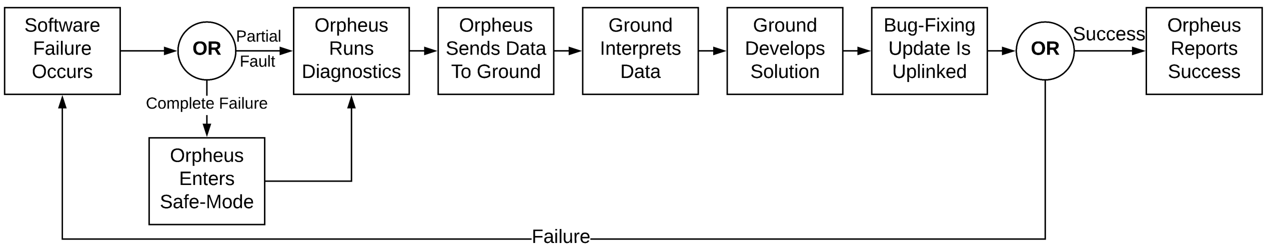

Figure 14.3: Safe mode software maintenance.

The safe mode, as operated by the software, is a stripped down version of the operating system installed on a separate memory partition (minimising the risk of failure due to memory malfunction), with limited functionality. It shall be able to send diagnostic data (hardware temperature, voltage, etc.) and software logs to ground. Furthermore, it shall be able to implement any potential software updates and reset the C&DH subsystem. The safe mode operating subsystem must be thoroughly tested, while maintaining a low complexity to maximise reliability.

14.6 Verification and Validation

First of all, the design choice must be verified. From the storage point of view, the choice made is very robust, as the storage data required by the Orpheus mission is 16 Gigabytes, and the available storage is 50 Gigabytes (excluding the redundant subsystem branch). This means that a change in the recorded data by more than 100% would be required in order to affect the C&DH design choice. Furthermore, as the required amount of storage is 63 Gigabits (8 Gigabytes), as described in chapter 6, which is considerably lower than the available space.

Furthermore, due to miniaturisation of electronic components, most of the subsystem is composed of the connectors and interfaces. Therefore, a change in storage requirements would not affect the mass nor the power, as solid state storage is light and consumes minimal power [24].

In order to ensure desired functionality and the high reliability of the C&DH, thorough verification and validation procedures are required both at a subsystem and a system integration level for both software and hardware. The operating system has to be verified through testing. This is done by using operation and failure scenarios and analysis of the reaction of the software. This kind of testing has been implemented in the New Horizons mission, especially when mitigating failure related bugs, by using “lights out” scenarios [7]. For example, the operating system is given the scenario that the sun sensor fails, and the process through which the problem is approached is observed and analysed. Potential software bugs are detected this way, and can be fixed.

Strain tests can be performed in different operational conditions, with different processor loads, in order to observe the deterioration rate of the components. These can be used to predict the behaviour of the computer over extended periods of time, up to the total mission duration. A hardware in the loop approach will be used for this, which can be applied to test both the C&DH and ADCS subsystems, by subjecting the two subsystems to mission conditions in a laboratory environment [118] continuously over a certain period of time.

Validation cannot be fully performed through tests, as the total expected mission time of 25 years cannot be physically attained before the launch date. However, certain elements can be verified through testing, such as vacuum survival (using a vacuum chamber) and radiation resistance (exposing the subsystem to radiation and recording the effects).

Validation can be performed at a system level by testing the integration of the on board computer with the other subsystems after their finalisation on the mock-up spacecraft. The compatibility of each subsystem can also be tested by connecting them separately throughout the assembly process to the computer and running diagnosis tests. The results can then be compared to the expected values, and the software and hardware can therefore be validated.

15 Launcher and Kick Stage

15.1 Launcher

To establish the Earth-Jupiter-Pluto transfer trajectory, a ΔV of 6726 m/s is required from low Earth orbit (180 km altitude). In the Midterm Report [27] it was concluded that the SpaceX Falcon Heavy is to be used for the Orpheus mission which is capable of providing a characteristic energy (C_3) as depicted in Figure 15.1. The data for the C_3 energy of the Falcon Heavy is obtained from the NASA Launch Vehicle Performance website[1]. The characteristic energy is converted to ΔV using Equation 15.1 [137], where r indicates the parking orbit altitude of 180 km and μ_E the gravitational parameter of Earth ($3.99 \times 10^{14}\,\mathrm{m^3/s^2}$).

$$\Delta V = \sqrt{\frac{2\mu_E}{r} + C_3} - \sqrt{\frac{\mu_E}{r}} \tag{15.1}$$

Using Equation 15.1 a required C_3 energy of $89.3\,\mathrm{km^2/s^2}$ is found. Studying Figure 15.1 it becomes clear there is no way the Falcon Heavy (expendable) can provide this C_3 (maximum possible $C_3 = 60\,\mathrm{km^2/s^2}$).

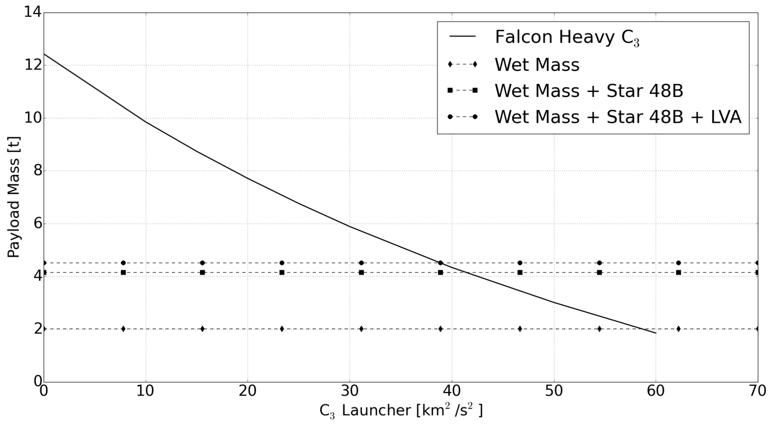

Figure 15.1: Characteristic energy of the SpaceX Falcon Heavy launcher in expandable mode.

15.2 Kick Stage

As shown in Figure 15.1, an additional rocket stage is required to obtain a C_3 of $89.3\,\mathrm{km^2/s^2}$. A common solution for a fourth stage of a launcher is a (solid) kick stage, which was also used for the New Horizons mission [121]. A kick stage uses solid propellant, making it reliable and allowing it to occupy a small volume in the launcher (given the high density of solid propellants). A kick stage produces high thrust and can only be fired once; once lit it can no longer be shut down.

Commonly-used solid kick stages suitable for the Orpheus mission are shown in Table 15.1. All Star kick stages are manufactured by Northrop Grumman (previously Orbital ATK) and are off-the-shelf products [112]. The first five columns of Table 15.1 list information about the performance of the particular kick stage. The last three columns provide information regarding the ΔV delivered by the launcher, kick stage and the excess ΔV (required 6726 m/s minus launcher ΔV minus kick stage ΔV). The launcher ΔV varies per kick stage given each stage has a different wet mass (hence there is a different in launcher payload mass).

Table 15.1: Considered Star kick stages for the Orpheus mission [112].

Kick stage	**Specific impulse [s]**	**Wet mass [kg]**	**Dry mass [kg]**	**Thrust [kN]**	**Launcher ΔV [m/s]**	**Kick stage ΔV [m/s]**	**Excess ΔV [m/s]**
Star 48A (short)	283.4	2574	127	77.1	4748	2130	137
Star 48A (long)	289.9	2581	133	79.0	4746	2175	180
Star 48B (short)	286.0	2134	111	67.2	4874	1887	21
Star 48B (long)	292.1	2141	117	68.6	4872	1924	56

[1] https://elvperf.ksc.nasa.gov/Pages/Default.aspx (June 19 2018)

The selected kick stage is the Star 48B in short configuration. Main reason for this is that this kick stage provides the lowest excess ΔV, hence making it the most optimal for the mission. In case a future mass growth outside margins is present, the kick stage could be re-evaluated to a more powerful configuration, like the Star 48B (long). The additional of the Star 48B (short) increases the launcher payload mass to 4131 kg, as depicted in Figure 15.1. A picture of the selected kick stage and thrust and pressure over time are shown in Figure 15.2.

Note that the excess ΔV should be 0 for the mission, as a non-zero excess would mean Orpheus will not be put on the right trajectory. This problem is solved by shutting down the third stage of the Falcon Heavy at an earlier point in the mission, meaning it delivers less ΔV. This is possible given the third stage of the Falcon Heavy can be turned on and off multiple times.

Before the kick stage is ignited, Orpheus together with the kick stage are spinned using the mono-propellant thrusters to stabilise the spacecraft. During the 1.4 minute burn of the Star 48B, the spacecraft can make very small corrections in attitude using the mono-propellant thrusters. The Star 48B is not equipped with a thrust vector control mechanism.

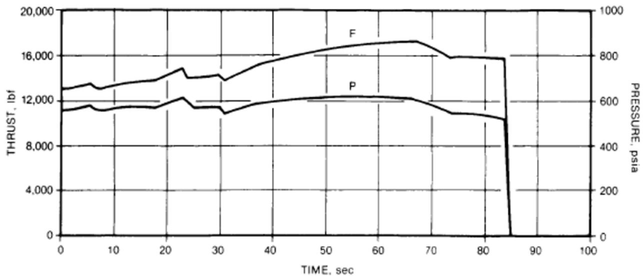

Figure 15.2: Star 48B (short) kick stage (left) with thrust and pressure performance data (right) [112].

Both the launcher and kick stage have TRL9 and do not require in-orbit refuelling, meaning `R-LCN-020` and `R-LCN-030` are met. Additionally, Orpheus can be put on the correct transfer trajectory with one single launch, which complies with `R-LCN-040`.

15.3 Launch Vehicle Adapter

The launch vehicle adaptor (LVA) is the adapter that connects Oprheus plus the kick stage to the Falcon Heavy rocket. The adaptor is provided by SpaceX, but is included in the payload mass of the rocket, given multiple configurations of these adaptors exist. Actual data regarding the mass of the Falcon Heavy LVA was not available to the public. Therefore, a statistical relationship provided by Brown [14] is used, as shown in Equation 15.2.

$$m_{LVA} = 0.0755 \cdot m_{wet} + 50 \tag{15.2}$$

Here, m_{LVA} indicates the mass of the launch vehicle adapter and m_{wet} the wet mass of Orpheus plus the Star 48B kick stage. Using a wet mass of 4131 kg, an LVA mass of 363 kg is obtained, also depicted in Figure 15.1.

16 Spacecraft Structural Support

The following chapter provides a detail analysis of the spacecraft structure. The launch loads, and the spacecraft internal architecture are presented, followed by the design of the magnetometer boom and the supporting structure.

16.1 Launch Loads & Requirements

Since there is no launch manual yet available for the Falcon Heavy following approach is used to determine the loads the structure has to withstand. By comparing launch loads of different launchers (Falcon 9 [130], Delta IV Heavy [142] and Ariane V [3]), it is found that the maximum and minimum lateral and longitudinal forces during launch do not differ much between launchers (confirmed during a person talk with Dr. Saullo (Tu Delft)). For instance, the maximum axial loading for the Falcon 9 and the Delta IV Heavy is 6 g, whereas for the Ariane V it is 4.25 g. Laterally, the maximum loading of 2 g occurs for the Falcon 9 and the Delta IV Heavy. For the Ariane V the maximum lateral load is 0.25 g. Chosing the maximum launch loads found for similar launchers, leads to a worst case scenario design of the structure. Since the Falcon 9 is designed by the space company (SpaceX) than the Falcon Heavy, it is decided that the launch loads of the Falcon 9 are used to estimate stresses on the structure. In addition, it is decided that the structure is designed for maximum lateral and longitudinal accelerations during launch as well as for the natural frequencies the launcher manual provides.

From the Falcon 9 launch manual for payloads with a fundamental lateral frequency greater 10 Hz and a fundamental longitudinal frequency greater than 25 Hz the given combined loading envelope presented in Figure 16.1 holds [130].

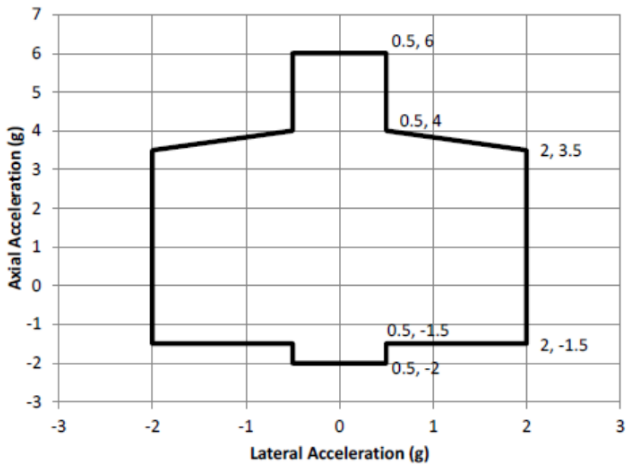

Figure 16.1: Falcon 9 payload design load factors for "standard" mass (over 4,000 lb) [130]

From the figure it is seen that the maximum axial acceleration is 6 g and the maximum lateral acceleration is 2 g in both directions. Since the sine vibrations are imposing a much lower lateral and axial acceleration on the spacecraft, they are not investigated during this preliminary sizing of the structure, but shall be tested once the structure is manufactured.

Therefore, using the information presented, the requirements presented in Table 16.1 are applied for the structural support of the Orpheus spacecraft.

Table 16.1: Requirements for the structure of the spacecraft.

Identifier	Requirement	Traceability
R-STR-010	The supporting structure shall mechanically align the spacecraft equipment	R-SYS-100
R-STR-020	The supporting structure shall have the strength to resist 6 g of axial acceleration.	R-SYS-120
R-STR-030	The supporting structure shall have the strength resist 2 g of lateral acceleration.	R-SYS-120
R-STR-040	The supporting structure shall carry the equipment during the mission.	R-SYS-100
R-STR-050	The supporting structure shall have a lifespan of at least 25 years	R-SYS-030
R-STR-060	The supporting structure shall protect hardware from external radiation.	R-SYS-100
R-STR-070	The supporting structure shall have a maximum mass of 120 kg.	R-SYS-010
R-STR-080	The supporting structure shall accommodate assembly of the spacecraft equipment.	R-MIS-180
R-STR-090	The supporting structure shall produce a system lateral natural frequency of more than 10 Hz.	R-SYS-130
R-STR-100	The supporting structure shall produce a system axial natural frequency of more than 25 Hz.	R-SYS-130

Requirements R-STR-010, R-STR-040, R-STR-060 and R-STR-080 represent main purposes of the structural support of the spacecraft, which is to accommodate all internal and external components. These are verified through inspection. Requirements R-STR-020, R-STR-030, R-STR-090 and R-STR-100 are given by the Falcon 9 launch manual, and is verified through a finite element method (FEM) (described in section 16.3. Finally, R-STR-050 and R-STR-070 are imposed by the mission goals and mass budget and can be verified through analysis using a render in CATIA V5 R21 and Ansys Workbench.

16.2 Spacecraft Architecture

The Orpheus spacecraft system architecture of Orpheus is presented in Figure 16.3, and is used to determine the required configuration from the point of view of placement and size integration. It should be noted, that the propulsion section of the diagram is a simplified version of the one presented in Chapter 10.

Before the supporting structure is designed, sizing is required. Using the approximate volume and size of the major spacecraft subsystem components, and the spacecraft architecture presented in Figure 16.3, the configuration presented in Figure 16.2 is produced. Therefore, the required size for the structure subsystem is determined.

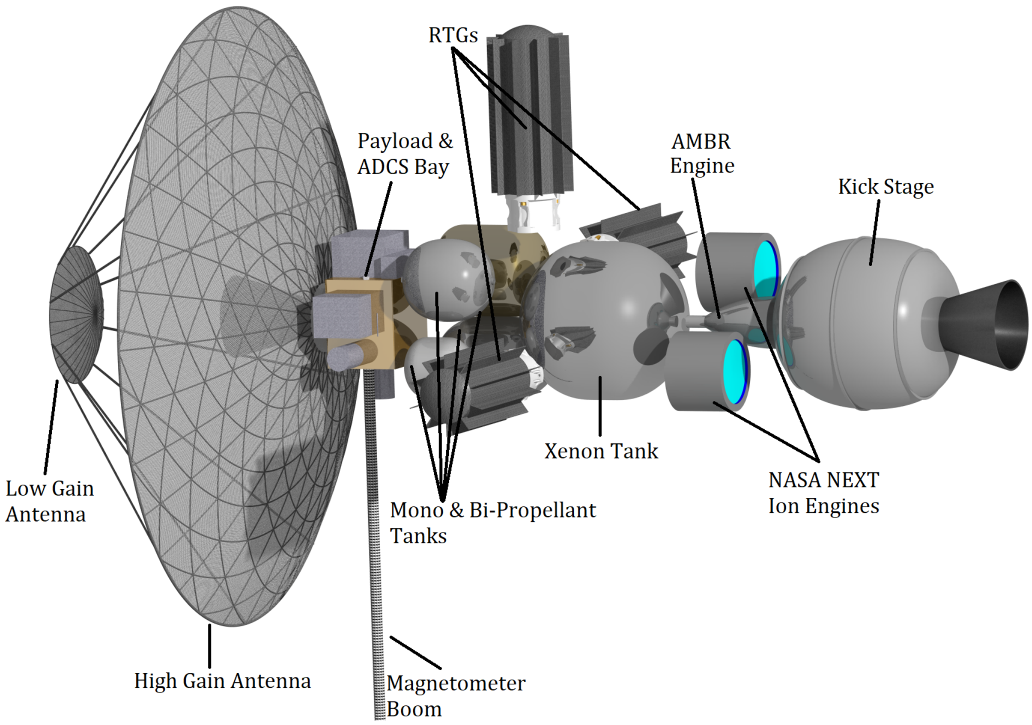

Figure 16.2: Main components placement.

16.3 Structural Analysis Method

In order to survive the critical mission loads and comply with weight requirements, the internal structure of Orpheus is designed with a compromise between mass and strength, while selecting materials appropriate for the space environment. In addition to that, the launcher fairing sets the maximum height of the spacecraft to 6.7 m [130].

First of all, an analytical approach is used to size the structure to withstand compression and lateral loads by using Equation 16.1, where σ is the local maximum stress, g is the acceleration in "z" and "y" direction (seen in Figure 16.4), m is the mass of the segment, L is the height of the section, I is the area moment of inertia and A is the cross sectional area perpendicular to the loading direction.

$$\sigma_{tot} = \frac{g_y \cdot m \cdot L}{I} + \frac{g_x \cdot m}{A} \tag{16.1}$$

The spacecraft is divided into three segments, assumed to be of homogeneous density and therefore a uniformly distributed mass, as shown in Figure 16.4. This will produce an over-designed structure, as the masses will only be attached towards the bottom of their segments. However, this decreases the failure risk of the structure.

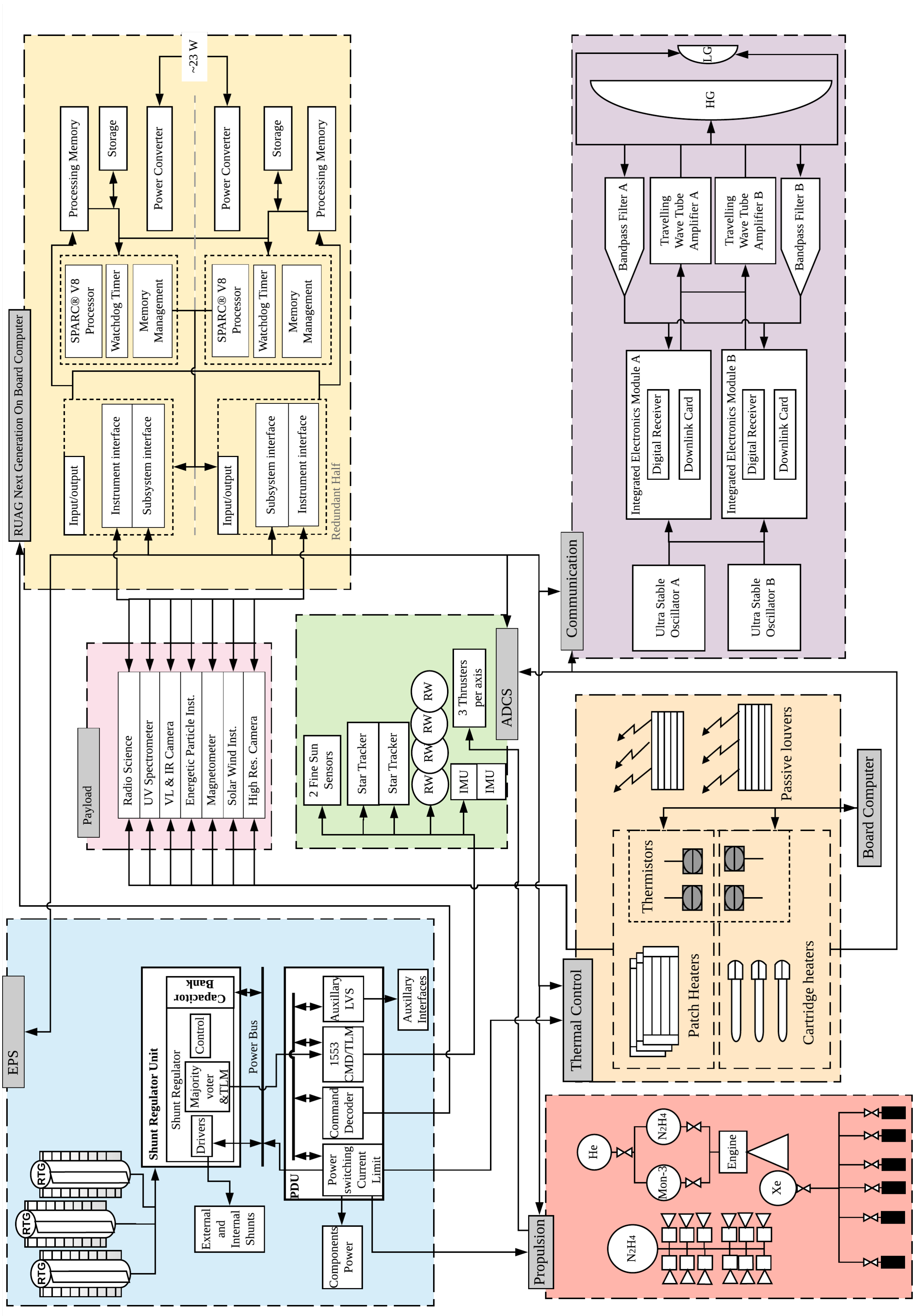

Figure 16.3: Orpheus spacecraft architecture.

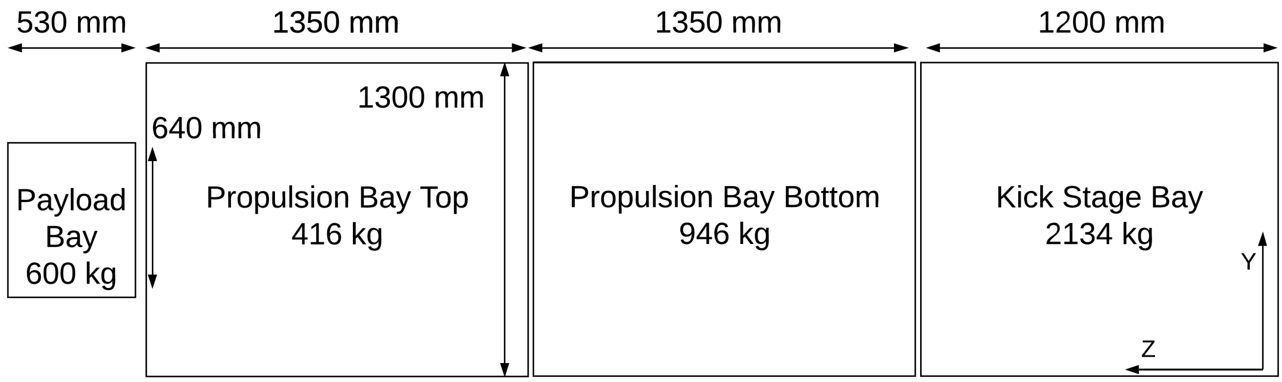

Figure 16.4: Structural layout used for analysis.

The design process used for the structures subsystem is described in Figure 16.5. Several feedback loops can be observed, as the design is iterated in order to comply with all requirements.

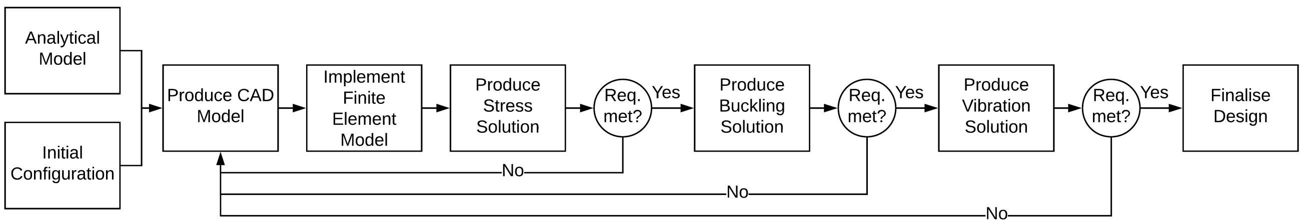

Figure 16.5: Structural subsystem design process, including iteration.

The output of the analytical approach are values for stresses that are then used to design the configuration of the structure itself using Equation 16.1. The cross sectional geometry is obtained by fixing certain dimensions known from the size of the components of Orpheus, as seen in Figure 16.4. According to Dr. Castro, researcher at the faculty of Aerospace Engineering at TU Delft, trusses are the most appropriate concept to be used in space structures, due to low weight and high strength.

A combination of square and I-beams is used for the spacecraft support skeleton beams, as the bending performance of these shapes can be higher than that of circular rods due to an increased moment of inertia (more area concentrated to the edges). Furthermore, a fail-safe approach is used for the design, meaning that no failure shall occur during the mission duration. Therefore, a preliminary sizing is developed analytically and implemented into the finite element analysis (FEM) program ANSYS Workbench 17.1.

The output provides insight in the other modes of failure that cannot be adequately analysed analytically, such as bucking, which proves to be the main source of structural failure during the launch, as shown by the FEM analysis. Hence, the design is iterated (shape, material, configuration, as seen in Figure 16.5) and analysed in ANSYS Workbench 17.1 in order to optimise for mass while fulfilling the strength and natural frequency requirements. The results of this process are presented in section 16.4.

16.4 Structural Analysis Results

The method presented in section 16.3 is applied on the structure shown in Figure 16.6a. The masses of the kickstage, tanks and payload are simulated as homogeneous boxes within the structure. It is important to note the three upper boxes (payload and tanks) are only supported by the horizontal trusses. The bottom box (kickstage) is radially connected to the diagonal trusses and vertical beams. The RTGs are modelled homogeneously and are attached externally to the main structure. For the mesh, the default 'fine' size function of Ansys Workbench 17.1 is used. Meshes and amount of nodes are further discussed in section 16.8. The vertical parts are made of aluminium, all other parts are carbon fibre, as shown in Figure 16.6b.

Figure 16.7a and Figure 16.7b show Orpheus experiencing maximum launch accelerations. As expected the largest stresses are located at the bottom of the structure. It is also noted that the horizontal and diagonal trusses are only loaded in bending. The vertical beams are loaded in any direction, depending on the direction of the lateral acceleration. Table 16.2 gives the resulting stresses and shows the structure has a safety margin of more than 25% as is customary for spacecraft structural design [153]. The critical stress is the shear stress in the carbon fibre. The other safety margins are excessive due to designing for this critical stress. As a result of normalising the stress

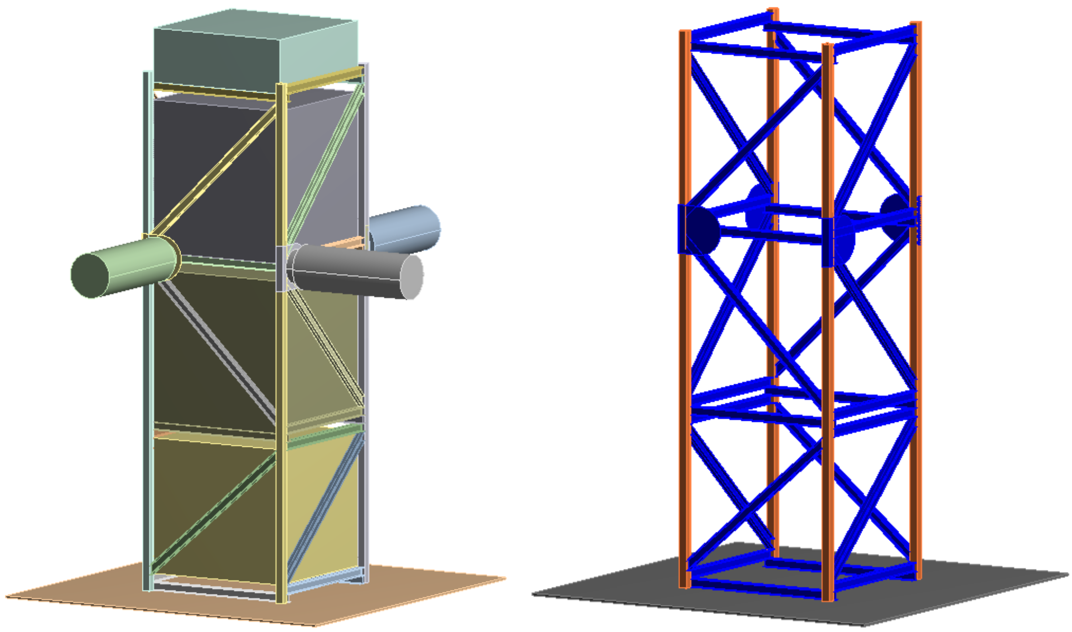

(a) Setup of the Ansys FEM analysis used for structural design of Orpheus.

(b) Materials in structure. Blue is carbon fibre, orange is aluminium 7075-T6.

Figure 16.6: Setup and application of materials for structures FEM.

Table 16.3: Buckling modes during launch.

Mode	Load Multiplier [-]
1	-10.4
2	-10.0
3	-8.7
4	-7.8
5	7.9
6	9.3

Table 16.4: Structure vibration modes.

Mode	Frequency [Hz]	Direction
1	10.6	Lateral
2	10.7	Lateral
3	28.2	Torque
4	31.1	Lateral
5	31.3	Lateral
6	40.6	Axial

with respect to the yield stress of carbon fibre, some areas in Figure 16.7a show stresses above 100%. However, these areas are in the aluminium parts of the structure, thus no failure occurs.

Table 16.2: Critical Stress and safety margins

	Aluminium 7075-T6			Carbon Fibre		
	Max. stress [MPa]	Yield [MPa]	Safety Margin [-]	Max. stress [MPa]	Yield [MPa]	Safety Margin [-]
Shear	60.8	331	444%	39.5	50.0	26.8%
Normal	-214	503	135%	182	829	355%

Next, buckling is evaluated for the first six buckling modes. The results are given in Table 16.3. The load multiplier refers to the amount of times the acceleration needs to be increased before any point of the structure buckles. A negative value indicates that a reversal of the direction of the loads is required to cause buckling. It is clear that no buckling is likely to occur in this structure.

Finally, vibrations are evaluated, using the Ansys specialised tool, to prevent resonance between the launcher and the spacecraft. Table 16.4 gives the six lowest eigenfrequencies of Orpheus. Requirement `R-STR-080` states that the lateral eigenfrequency shall be larger than 10 Hz, mode 1 and mode 2 are the lateral vibrations, a margin of 0.6 Hz or 6% is present. The other requirement corresponds to axial vibrations that must be bigger than 25 Hz (`R-STR-100`). This is easily met as shown by mode 6, the axial vibration, by a margin of 15.6 Hz or 62.4%.

16.5 Justification of Structural Design

Using the results from Ansys, it is possible to justify the design choices made for the structures. Starting with four vertical beams to support all the spacecraft elements, horizontal beams and diagonal beams are added to prevent buckling of the vertical beams. The horizontal and diagonal trusses are largely loaded in bending. They are therefore designed to have a large area moment of inertia around their bending axis. This results in I-beams

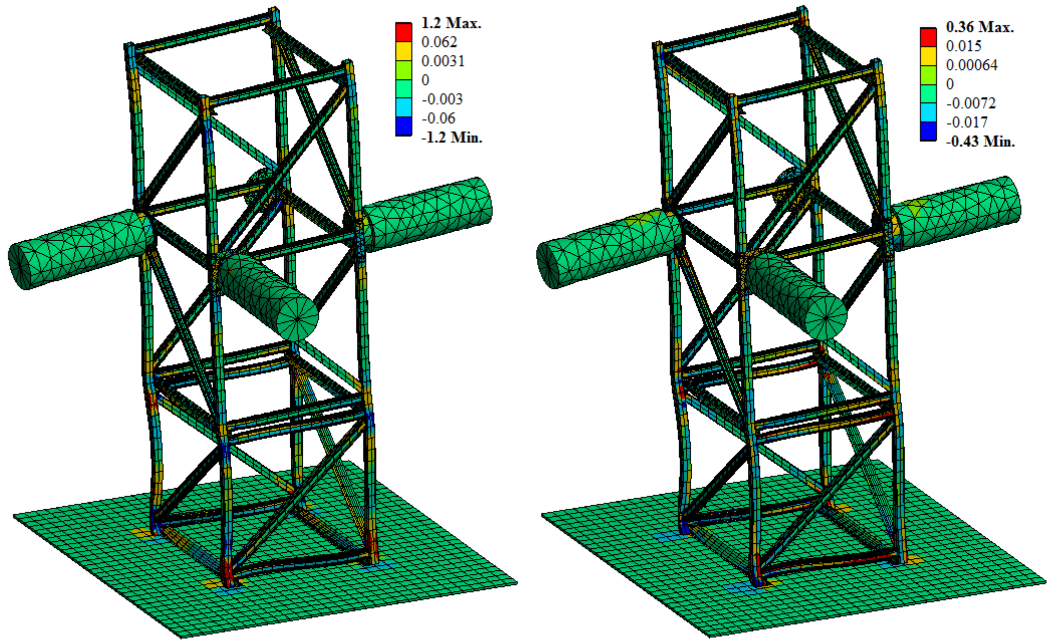

(a) Shear stresses throughout structure, normalized w.r.t. shear yield stress of carbon fibre.

(b) Normal stresses throughout structure, normalised w.r.t. normal yield stress of aluminium.

Figure 16.7: Stresses calculated by structures FEM.

with large webs and a small flange [36]. The vertical beams are square to allow for easier connections and to cope with stresses in any direction.

A stress concentration at the RTGs is dealt with by adding shear plates that transfer the bending loads into the rest of the structure at the attachment points. Getting the eigenfrequencies of Orpheus within the boundaries set by the launcher poses a big challenge. It is preferable to have as much of the spacecraft made of carbon fibre because of its high stress-low density qualities [104]. However, as Equation 16.2 to Equation 16.5 demonstrate, the frequency is dependent on the E-modulus. Carbon Fibre has a much lower shear E-modulus than aluminium, 9 GPa versus 26.9 GPa (taken from Ansys Workbench 17.1 Engineering Data Sources). A modal FEM analysis confirms lower frequencies for carbon fibre than for aluminium. Hence it is decided to change the materials of these beams to aluminium. The distribution of materials in the structure of Orpheus is shown in Figure 16.6b, materials are further discussed in section 16.6.

Table 16.5 gives a bill of materials for the structures of Orpheus

Table 16.5: Bill of material structures.

Item	**Lay-out**	**Qty.**	**Unit mass [kg]**	**Total Mass [kg]**
Vertical beam	70x70 square beam, 3mm thickness	4	10.2	40.8
Horizontal truss short	70x70 I-beam, 5mm web, 3mm flange	10	1.4	14
Horizontal truss long	70x70 I-beam, 5mm web, 3mm flange	8	1.6	12.8
Diagonal kickstage	70x70 I-beam, 5mm web, 3mm flange	4	2.4	9.6
Diagonal tanks	70x70 I-beam, 2mm web, 2mm flange	8	1.1	8.8
Shear plate	400x400 corner piece, 3mm thickness	4	0.76	3.0
Magnetometer boom	2 times 2 meter beam	1	2.0	2.5
Other	Connectors and Mechanics	-	-	28.5
Total				120
Total (+contingency)	20% contingency			144

16.6 Material Properties

As mentioned in the previous section, two materials are used for the configuration presented in Figure 16.6b. This selection is based on research done with regards to material strength to weight ratios and outgassing[1] properties.

As seen from Figure 16.8 (marked by the red line), carbon fibre reinforced polymers (CFRP) have comparable strengths to metals, but have a lower density, which gives them a better strength to weight ratio. As one of the

[1]The phenomena through which molecules trapped in the material escape due to the vacuum of outer space, creating weak points in the material.

limiting factor of the design is the total weight of the structure, this material is initially used for the first iteration of the design.

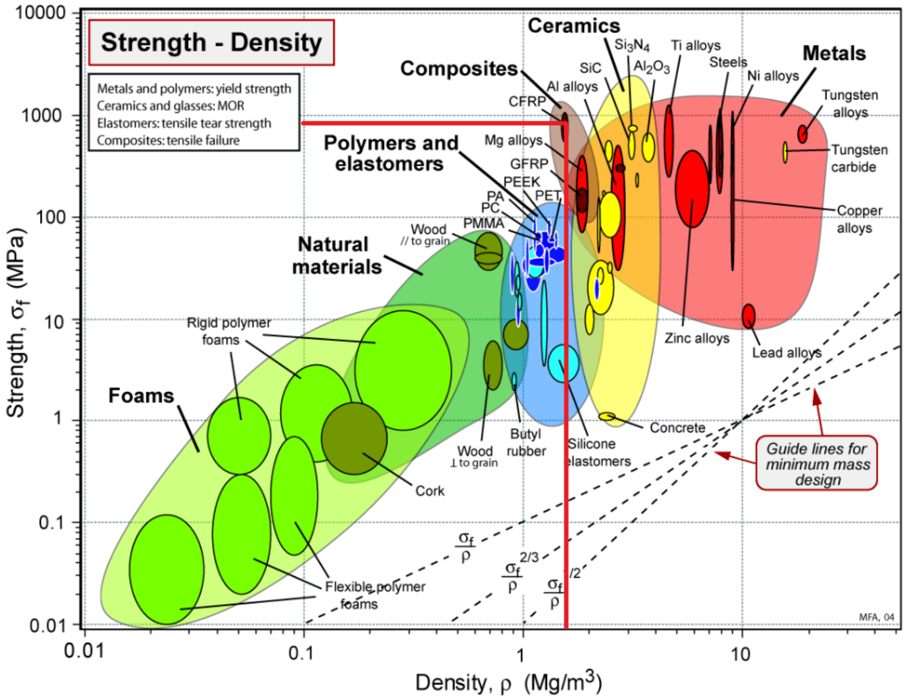

Figure 16.8: Strength vs density for various material groups [83].

Furthermore, as stated by Anwar [29], carbon fibre composites have a relatively low susceptibility to the outgassing effect. However, the properties of fibre reinforced composites are highly directional, as seen in Table 16.6, as the shear properties of the carbon based material are much lower than its axial properties when compared to the aluminium.

Therefore, aluminium elements are required in order to fulfil the lateral natural frequency requirement (more than 10Hz), as the shear modulus of Al-7075 T6 is greater than that of the composite, and therefore resists lateral motion, increasing the fundamental frequency. This material is selected for its high yield strength and low outgassing effect, as stated by Patrick [115]. The properties of aluminium 7075 T6 are presented in Table 16.6.

Table 16.6: Selected material properties: Al 7075 T6 [57], and carbon fibre prepreg from the ANSYS material database.

Material	Axial Modulus [MPa]	Shear Modulus [MPa]	Axial Strength [MPa]	Shear Strength [MPa]	Density [kg/m3]
Epoxy Carbon Woven Prepreg	91820	9000	829	50	1480
Aluminium 7075 T6	71700	26900	503	331	2810

There are several challenges posed by the combination of materials selected, one of which is the galvanic corrosion that would happen if carbon fibre is in contact with aluminium [8]. This phenomena happens due to the different potentials of carbon and aluminium causing material wear. Therefore, the two materials will have to be separated at joints with a layer of a resistant but non-conductive material, such as kevlar[101].

Another problem stems from the joining of the two materials, as welding cannot be performed to join a metal and a composite. Bolts are a good solution for metals, but are not recommended for composite joining. Furthermore, adhesives could prove to be a bad solution, as their strength is relatively small compared to metals and composites. Mechanical joints will then have to be used in order to ensure the reliability and strength of the structure [128]. These will have to be made out of a non conductive material, like kevlar, in order to avoid Galvanic corrosion. The effect of these joints on the structural strength of the satellite requires further investigation, but it is expected that these would not have a negative effect, as the greatest design consideration, buckling, does not apply for these joints due to their reduced size.

16.7 Magnetometer Boom

Since the GPHS-RTG and other spacecraft components generates a magnetic field, the magnetometer shall be placed sufficiently far away from the spacecraft to not encounter any interference leading to faulty data. According to test data of an GPHS-RTG, analysed by Bennett et al.[45], the maximum field strength was estimated to be 148 nT at 1 m from the geometric centre of the RTG and decreases to approximately 10 nT $\pm$4 nT at 2 m. These numbers are based on a particular RTG test. To account for possible variations in magnetic field from the source, a safety factor of 2 is used on the boom length. Hence, for the magnetometer to not be affected by the RTG and spacecraft magnetic radiation the boom is designed to have a length of **4 m**.

For the boom structure and material, Storable Tubular Extendible Member (STEM) booms, truss booms as well as carbon fibre reinforced polymer (CFRP) tube booms are considered. Truss boom structures are generally very large and require a canister for packaging that has a high volume, making it unsuitable to be attached to the Orpheus payload bay. Therefore, trusses are ruled out [72]. STEM booms are known to be used for deployment large spacecraft structures, such as solar sails or antennas, on small satellites. STEMs are sometimes preferred for their small packaging volume, however booms used for magnetometers or other sensors are still under development [31]. CFRP booms are used on many spacecrafts, such as the Solar Orbiter [110], the THEMIS satellite [33] and SWARM [103]. Therefore, carbon fibre composites tubes are used for the entire boom to minimise the weight of the structure and due to the reason that they are flight proven. Next to this, the high specific stiffness helps withstand the launch frequencies, and its low thermal expansion factor makes it suitable for different space environments. In addition, since carbon fibre is non-magnetic, the boom material does not interfere with the magnetometer [33].

It is decided to use high modulus Exel Crosslite^{TM} carbon fibre tubes manufactured by exel composites in Finland (Exel Composites Crosslite Brochure 2014) The mechanical properties of this specific carbon fibre tube can be found in Table 16.7

Table 16.7: Properties of the High Modulus Exel Crosslit^{TM} carbon fibre tube.

Property	Symbol	Value	Unit
Young's Modulus	E	120-195	GPa
Bending Strength	σ_{bend}	> 600	MPa
Yield Strength	σ_{yield}	> 800	MPa
Density	ρ	1.65	g/cm^3
Max. outer diameter	D_{outer}	60	mm
Wall thickness	t	1-2	mm

The deployment of the Orpheus boom is presented in Figure 16.9 where the grey circles present the deployment mechanisms and hinges necessary to unfold the boom. This concept is based on the Solar Orbiter instrument boom [110].

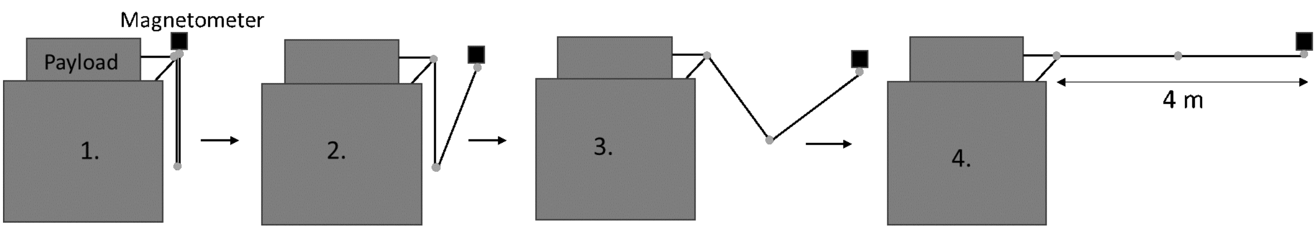

Figure 16.9: Deployment sequence of the magnetometer boom.

The boom is attached to the spacecraft by a simple hinge-spring system. The deployment mechanism is actuated by torsional springs which are pre-loaded to deploy the boom with sufficient torque margins as done for the Solar Orbiter instrument boom [110]. To damp the deployment motion a viscous damper is added into the mechanism. In addition, a latching system is implemented to lock the boom into its deployed position such that all interfaces can function correctly and the needed distance to the spacecraft is ensured. The connection of the two boom parts is also done by a hinge-spring system. Each of the hinges includes a hold-down and release mechanism used to release the folded boom once Orpheus is in Orbit. Further investigation is required to determine the effect of this boom on the controlability of the spacecraft. The chosen low-shock, non-explosive hold-down and release mechanism is taken from the off-the-shelf catalogue provided by NEA Electronics.

16.7.1 Natural Frequency Analysis

Since the boom is in a folded state during launch, it needs to be investigated whether its natural frequency in lateral and longitudinal direction complies to the constraint given by the launcher. This analysis is done to avoid resonance of the boom, leading to damage of the structure. From section 16.1 it is known that the fundamental bending mode of the spacecraft shall be greater than at least 10 Hz and the fundamental axial mode greater than 25 Hz. To simplify the analysis, the two booms of 2 m length have been modelled as presented in Figure 16.10 (boom half with magnetometer point mass) and Figure 16.11 (boom half, attached to the spacecraft). The masses indicated in the figures represent the boom mass (m_2) and the magnetometer mass of 1.5 kg (m_1). To simplify the calculations and design for a worst case scenario, all hinges are assumed to be rigid and translate the frequency loading of the launcher to the booms.

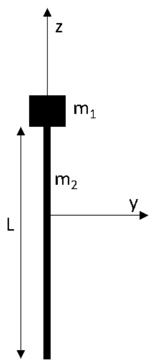

Figure 16.10: Folded boom part with tip mass.

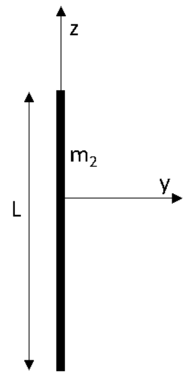

Figure 16.11: Folded boom part without tip mass.

To determine the natural frequencies of the boom parts with tip mass (Figure 16.10), Equation 16.2 and Equation 16.3, given by Zandbergen [153], In the equations below I is the area moment of inertia around the y-axis and x-axis, as displayed in the figure above. E is the Young's Modulus of the material, m_1 is the mass of the magnetometer, m_2 is the mass of the boom, and L is the lengths of each boom half. The numbers in front of the square root are factors derived by Zandbergen [153]. Using the properties provided in Table 16.7 the best combination of Young's Modulus and tube thickness is found that exceeds a lateral frequency of 10 Hz and a longitudinal frequency of 25 Hz as required by the launcher [130].

$$f_{nat,lat} = 0.276\sqrt{\frac{EI}{m_1 L^3 + 0.236 m_2 L^3}} \qquad (16.2)$$

$$f_{nat,lng} = 0.16\sqrt{\frac{AE}{m_1 L + 0.333 m_2 L}} \qquad (16.3)$$

Equation 16.4 and Equation 16.5 also given by Zandbergen [153], are used to evaluate the natural frequencies of the boom without tip mass. The same symbol explanation holds as mentioned above.

$$f_{nat,lat} = 0.56\sqrt{\frac{EI}{m_2 L^3}} \qquad (16.4)$$

$$f_{nat,lng} = 0.25\sqrt{\frac{AE}{m_2 L}} \qquad (16.5)$$

For the boom with tip mass a natural lateral frequency of about 13 Hz is achieved when the CFRP tube has an outer diameter of 60 mm, a thickness of 2 mm and a Young's Modulus of 195 GPa. For the second boom without tip mass, the natural frequency in lateral direction with the same tube dimensions is approximately 31 Hz. Therefore the lateral frequency requirement, given by the launcher manual in Section 16.1, is met. The longitudinal frequency for both booms is in any case larger than the required 25 Hz.

16.7.2 Boom Bending Analysis

First of all, the maximum compressive force is calculated by using Equation 16.6. F is the force, m the mass of the structure and a the acceleration. With a maximum axial acceleration of 6 g, as given by the launch manual, the magnetometer boom has to be able to carry a longitudinal compressive force of approximately 160 N. A bending moment at the connection point of each boom of around 106 Nm is calculated from the lateral launcher acceleration of 2 g using Equation 16.7. Here, d is the maximum distance of the applied force to the connection point (in this case, 2 m).

$$F = m \cdot a \quad (16.6) \qquad\qquad M = m \cdot a \cdot d \quad (16.7)$$

Critical stresses are therefore a compression stress of 437 kPa, determined with Equation 16.9 and a bending stress of 690 MPa, calculated with Equation 16.8. The moment of inertia, I, is found to be approximately 153423 mm^4. The CFRP tubes can be designed to withstand these stresses and are therefore qualifies as boom structure.

$$\sigma_{bending} = \frac{M}{I} \quad (16.8) \qquad\qquad \sigma = \frac{F}{A} \quad (16.9)$$

Concluding from the analysis above, the magnetometer boom is made out of Exel Crosslite^{TM} carbon fibre tubes with a diameter of 60 mm, a thickness of 2 mm and a Young's modulus of 195 GPa. With a density of 1.65 g/cm^3, the 4 m long boom weighs 2.5 kg, not including the hinges and mechanism used.

The load cases are also evaluated with an I-boom structure. However, it is found that even thought the bending analysis gives better results than for the tube, the natural frequencies determined for the I-boom do not comply with the launcher requirements.

16.8 Verification and Validation

Verification is performed throughout the design process in order to ensure the quality of the solution. The analytical model was unit tested and results were verified by hand with the equations used.

The numerical model (FEM) was verified by varying the mesh size and comparing the results. The relevant outputs are shown in Table 16.8. It can be concluded that a finer mesh gives more critical results for maximum stress and the eigenfrequency is closer to the minimum of 10 Hz. The buckling multiplier is less critical though. This proves that the FEM results are extremely sensitive to the mesh. It can be noted though that both results are in the same order of magnitude and thus, using the margins shown in section 16.4, the FEM is adequate for this preliminary design phase. However, due to time constraints, only two data points could be computed for the convergence analysis, and further investigation is required to confirm the validity of the results.

Table 16.8: Difference as result from different mesh settings

Mesh size	Nodes	Elements	Max. Stress [MPa]	Smallest Buckling Multiplier [-]	Lateral Vibration Frequency [Hz]
Coarse	40537	8384	277	4.7	11.38
Fine	104741	21884	356	7.9	10.6
Difference	-	-	22%	40%	7%

Three typical ways to validate the structural design [148]:

1. Test
2. Analysis (Finite Element Model, CAD models for mass, volume, interfaces)
3. Inspection

Stress and strain tests can be performed on the structure after production and assembly, from individual struts to the final product. The properties of the carbon fibre elements can then be verified for compliance, and check if the simulation matches the final product. Failed tests can lead to reiteration of the design.

Furthermore, thorough inspection is needed for the final product. De-lamination and cracks could lead to lower failure stresses, and could potentially lead to mission failure. Several techniques can be used for this, such as ultrasonic testing, x-ray testing and eddy current thermography [49].

The coating of the outer surface of the spacecraft shall be done such that limited release of paint and/or other debris is caused. In addition, the manufacturing of carbon fibres shall follow company health regulations and sustainability requirements as demanded by the Orpheus mission.

16.8.1 Verification of the Magnetometer Boom

To verify the boom structure a thermal vacuum test can be done. This ensures that the CFRP tubes can withstand the launch environment and the space environment. Next to this, a sine and random vibration test can be performed to verify the previously determined natural frequencies of the booms and ensure the boom survives the launch loads. A functional test on subsystem level ensures that the boom deploys correctly and is reliable. In addition, a magnetic measurement test is performed to evaluate the magnetic interference with the sensor of the magnetometer on the tip of the boom. This particular test can be done in the Maxwell Test Chamber at ESA ESTEC [48].

17 Budgets

The budgets per subsystem have to comply with the overall budgets of the spacecraft design, which are discussed within this chapter. An overview of the cost, power and mass and ΔV budget are given and explained.

17.1 Cost Breakdown Structure

The cost breakdown structure presented in Figure 17.1 is coherent with the budget presented in section 17.2. During a standard mission, the costs are allocated into seven different components, as shown in the figure. The focus within the DSE project lies mainly on component 1.0 and 2.0: the spacecraft design itself and the launcher. However, a lot more needs to be taken into account when carrying out a complete space mission. J.R. Wertz et. al describe a structure with seven main components, for which amongst others operations, program management and ground control are take into account. Where necessary, sub components have been indicated [148].

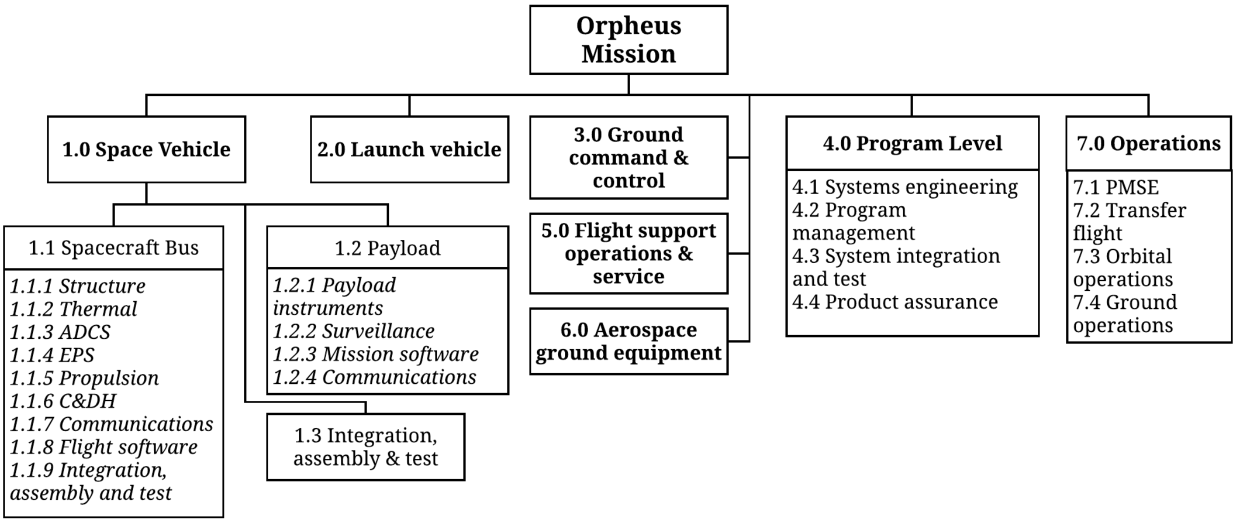

Figure 17.1: Cost breakdown structure Orpheus mission.

17.2 Cost Budget

The standardised contingency factor has been set at 20% [76], for which alternating percentages are indicated in Table 17.1 when applied. The 20% standard contingency will be reserved for unanticipated events that cause the cost of the single component to increase. These events can be for instance delay in schedule, design errors, logistic errors or other. The 10% budget contingency of the total cost of the mission is needed for 2 purposes. Either unanticipated cost factors will occur during later design phases, or events occur that cause an increased cost for the full budget. For instance, new requirements from customers in a later stage could influence all design choices, or a change in launch schedule can cause a delay in every department.

Table 17.1: Cost budget breakdown for the Orpheus mission [28] [148].

(Sub)system	Cost [USD]	Contingency	Total Cost[USD]
1.0 Space vehicle			
1.1 Spacecraft bus			
1.1.1 Structure	10,000,000 $	20%	12,000,000 $
1.1.2 Thermal	1,500,000 $	20%	1,800,000 $
1.1.3 ADCS	13,000,000 $	20%	15,600,000 $
1.1.4 EPS	352,790,000 $	5%	370,429,500 $
1.1.5 Propulsion	50,000,000 $	20%	60,000,000 $
1.1.6 C&DH	500,000 $	10%	550,000 $
1.1.7 Communications	7,000,000 $	20%	8,400,000 $
1.1.8 Flight Software	4,000,000 $	20%	4,800,000 $
1.1.9 Integration, assembly and Test	40,000,000 $	20%	48,000,000 $
Subtotal 1.1			521,571,100 $
1.2 Payload			
1.2.1 Payload Instruments	21,000,000 $	5%	22,120,000 $

1.2.2 Surveillance	2,000,000 $	20%	2,400,000 $
1.2.3 Mission software	2,000,000 $	20%	2,400,000 $
1.2.4 Communications	2,000,000 $	20%	2,400,000 $
Subtotal 1.2			29,320,000 $
1.3 Integration, assembly & test	30,000,000 $	20%	36,000,000 $
1.0 Subtotal			**586,891,100 $**
2.0 Launch Vehicle	150,000,000 $	5%	**157,500,000 $**
3.0 Ground command & control	10,000,000 $	20%	**12,000,000 $**
4.0 Program level			
4.1 Systems engineering	5,000,000 $	20%	6,000,000 $
4.2 Program management	3,000,000 $	20%	3,600,000 $
4.3 System integration and test	8,000,000 $	20%	9,600,000 $
4.4 Product assurance	5,000,000 $	20%	6,000,000 $
Subtotal 4.0			**25,200,000 $**
5.0 Flight support operations & service	10,000,000 $	20%	**12,200,000 $**
6.0 Aerospace ground equipment	15,000,000 $	20%	**18,000,000 $**
7.0 Operations			
7.1 PMSE	10,000,000 $	20%	12,000,000 $
7.2 Transfer flight	100,000,000 $	20%	120,000,000 $
7.3 Orbital operations	32,000,000 $	20%	38,400,000 $
7.4 Ground operations	15,000,000 $	20%	18,000,000 $
Subtotal 7.0			**188,400,000 $**
Subtotal budget			**999,999,500 $**
Contingency 10%			99,999,950 $
Total budget			**1,099,999,450 $**
Total budget, rounded off			**1,100,000,000 $**

Components 2.0, the launch vehicle, 1.1.4 (the EPS system including the three RTG's) and 1.2.1 (payload instruments) are given a contingency margin of 5%. This is due to the fact that these are 'off-the-shelf' components which are not designed specifically for the mission. For the command and data handling system (C&DH), the products are off the shelf as well. However, more integration into the subsystem is required, which leads to a margin of 10%.

17.3 Power Budget

The update of the power budget because of design iterations has made room for a better contingency management over all the budgets, and has allowed more systems to operate at a better level with more power. The total power budget comprises 670 Watts, readily including a 10% margin.

Table 17.2: Description of each power mode.

Power mode	Description
1	All on (reference frame)
2	Launch
3	Science mode
4	Burn mode
5	Nominal mode
6	Communications mode
7	Safe mode
8	Hibernation
9	Trajectory correction manoeuvre

Table 17.3: Power mode distribution.

Mode	1	2	3	4	5	6	7	8	9
PDU [W]	52.50	52.50	52.50	52.50	13.13	35	13.13	13.13	20.00
Duty cycle [%]	100	100	100	100	100	100	100	100	100
Average [W]	52.50	52.50	52.50	52.50	13.13	35	13.13	13.13	20.00
Thermal [W]	42.00	42.00	42.00	42.00	42.00	33.60	42.00	42.00	42.00
Duty cycle [%]	100	100	100	10	100	100	100	10	10
Average [W]	42.00	42.00	42.00	13.20	42.00	33.60	42.00	8.70	8.70
ADCS [W]	95.55	95.55	95.55	95.55	23.89	95.55	47.78	95.55	95.55
Duty cycle [%]	100	0	50	0	100	5	100	0	10
Average [W]	95.55	0	47.78	0	23.89	4.78	48.78	0	18.56
DHS [W]	29.4	29.4	29.4	29.4	29.4	29.4	29.4	29.4	29.4
Duty cycle [%]	100	0	100	0	10	20	5	5	10
Average [W]	29.4	0	29.4	0	2.94	5.88	1.47	1.47	2.94
Propulsion [W]	630.00	630.00	630.00	630.00	630.00	630.00	630.00	630.00	300.00
Duty cycle [%]	100	0	0	100	0	0	0	0	100
Average [W]	630.00	0	0	630.00	0	0	0	0	300.00
Communications [W]	176.00	176.00	176.00	176.00	176.00	176.00	176.00	176.00	176.00
Duty cycle [%]	100	0	20	0	0	100	1	0	0
Average [W]	176.00	0	35.20	0	0	176	1.76	0	0
Infrared & Visible light spectrometer [W]	7.08	7.08	7.08	7.08	7.08	7.08	7.08	7.08	7.08
Duty cycle [%]	100	0	100	0	0	0	0	0	0
Average [W]	6.74	0	6.74	0	0	0	0	0	0
Ultraviolet spectrometer [W]	4.73	4.73	4.73	4.73	4.73	4.73	4.73	4.73	4.73
Duty cycle [%]	100	0	100	0	0	0	0	0	0
Average[W]	4.73	0	4.73	0	0	0	0	0	0
Radio science & gravity experiment [W]	15.75	15.75	15.75	15.75	15.75	15.75	15.75	15.75	15.75
Duty cycle [%]	100	0	100	0	0	0	0	0	0
Average [W]	15.75	0	15.75	0	0	0	0	0	0
High resolution camera [W]	5.36	5.36	5.36	5.36	5.36	5.36	5.36	5.36	5.36
Duty cycle [%]	100	0	100	0	0	0	0	0	0
Average[W]	5.36	0	5.36	0	0	0	0	0	0
Solar wind instrument [W]	3.26	3.26	3.26	3.26	3.26	3.26	3.26	3.26	3.26
Duty cycle [%]	100	0	1000	0	0	0	0	0	0
Average [W]	3.26	0	3.26	0	0	0	0	0	0
Energetic particle analyser [W]	2.42	2.42	2.42	2.42	2.42	2.42	2.42	2.42	2.42
Duty cycle [%]	100	0	1000	0	0	0	0	0	0
Average [W]	2.42	0	2.42	0	0	0	0	0	0
Magnetometer [W]	2.10	2.10	2.10	2.10	2.10	2.10	2.10	2.10	2.10
Duty cycle [%]	100	0	100	0	0	0	0	0	0
Average [W]	2.0	0	2.10	0	0	0	0	0	0
Total [W]	1060.88	94.50	242.30	669.70	81.43	271.71	153.64	23.03	345.39

17.4 ΔV and Propellant Budget

The ΔV budget for Orpheus is shown in Table 17.4. From the specific impulse of entry, the corresponding engine can be determined:

- 230 s: Ariane Group monopropellant thruster.
- 286 s: Nortrop Grumman Star 48B (short) kick stage.
- 333 s: Aerojet AMBR bipropellant engine.
- 348 s: Falcon Heavy Merlin Vacuum engine.
- 1410 s: NASA NEXT ion thruster.

The required ΔV follows directly from the mission design. Following ESA margins [76], a 5% margin is added over accurately calculated manoeuvres (ESA `R-DV-11` [76]). Over orbital and attitude control manoeuvres a 100% is added (ESA `R-DV-12` and ESA `R-DV-13` [76]). For all manoeuvres of the ion propulsion system, an additional 5% margin is added (ESA `R-DV-6` [76]).

Additionally over all required propellant masses, a 2% mass margin is added for propellant residuals (ESA `R-M2-6` [76]). Given manoeuvres of the attitude and orbit control system are non continuous, no impulse time is added. Note that as all values in Table 17.4 are rounded, this contingency might sometimes not be visible as it is less than 1.

Table 17.4: Orpheus ΔV and propellant budget.

Manoeuvre	Specific impulse [s]	Required ΔV [m/s]	Margin [%]	Total ΔV [m/s]	Required propellant [kg]	Total propellant [kg]	Impulse time [-]
Interplanetary transfer (launcher)	348	4870	0%	4870			
Interplanetary transfer (kick stage)	286	1877	0%	1877	2134	2134	1.4 min
Earth-Jupiter transfer corrections	1410	100	10%	110	16	16	0.3 years
Jupiter-Pluto transfer corrections	1410	100	10%	110	15	16	0.3 years
Pluto insertion	1410	5860	10%	6446	715	729	12.1 years
Pluto science orbit circularisation	333	243	5%	255	90	92	7.9 min
Pluto orbit & attitude control	230	7	100%	14	7	7	
Charon transfer orbit injection	333	207	5%	217	71	72	6.2 min
Pluto-Charon transfer corrections	230	10	100%	20	9	9	
Charon insertion & circularisation	333	159	5%	167	51	52	4.5 min
Charon orbit & attitude control	230	71	100%	142	59	60	
End of life disposal	333	125	5%	131	36	37	3.6 min
Total		13648		14380			

17.5 Mass Budget

The mass budget for the Orpheus mission is presented in Table 17.5. For every different system, masses are allocated based on the current best estimate or commercial off-the-shelve (COTS) mass found in brochures or technical data sheets. Depending on the mass growth risk of different subsystem components, a margin is added based on ESA standards `R-M2-4` [76], either 5% (COTS), 10% (COTS with minor modifications) or 20% (complete new design). Special note for the propulsion- and communications system in Table 17.5. Given the ESA margin applied on the different components of the subsystem (Table 10.23 and Table 13.2) the average of all individual 5-10-20 margins is displayed in Table 17.5.

Additionally a 20% margin is added over the entire spacecraft dry mass, as stated in ESA standard `R-M2-1` [76].

Table 17.5: Orpheus mass budget.

Dry mass contribution	Without margin	Margin	Total	% Total
Structure & mechanisms	120 kg	20%	144 kg	19%
Thermal Control	40 kg	10%	44 kg	6%
Communications	32 kg	17.9%	38 kg	5%
Command & Data Handling	7 kg	5%	7 kg	1%
Attitude Determination and Control	14 kg	5%	14 kg	2%
Propulsion	206 kg	7.8%	222 kg	30%
Power source	168 kg	5%	176 kg	24%
Power Management & Distribution	43 kg	20%	51 kg	7%
Payload	36 kg	5%	37 kg	5%
Others	5 kg	20%	6 kg	1%
Total dry mass (excl. adapter)	669 kg		740 kg	100%
System margin		20%	134 kg	
Total dry mass with margin (excl. adapter)			874 kg	
Wet mass contribution				
Xenon propellant			761 kg	
Hydrazine propellant			243 kg	
MON-3 propellant			133 kg	
Helium pressurant			2 kg	
Total wet mass (excl. adapter)			2013 kg	
Kick stage			2134 kg	
Adapter mass (incl. separation mechanism)			363 kg	
Launch mass (incl. adapter)			**4510 kg**	

18 System Compliance, Verification and Validation

The following chapter presents the final considerations accounted for the design. Firstly, the compliance of the spacecraft with the requirements is checked, and unknown compliant requirements are discussed. Furthermore, a performance analysis is conducted on the parameters obtained. Lastly, the system-wide verification and validation procedures are described.

18.1 Request for Requirement Deviation

The following request for deviation is made, in order to still comply with the requirement on the dry mass and keep the progress of the mission design possible.

- R-SYS-010: The space system dry mass shall be in range of 401-650 kg.
- **R-SYS-011**: The space segment shall have a minimum dry mass of 401 kg.

The lower limit of requirement `R-SYS-010` is given by stakeholders, whereas the upper limit has been established in the baseline of the design to ensure the design of Orpheus does stay within mass limits such that no cost overruns occur. Through the more detailed design of each subsystem and the implementation of margins according to ESA standards [76] the dry mass increased to 870 kg and deviates therefore from requirement `R-SYS-010`. With deviation, the mission is still 100% feasible and no changes in system designs are necessary. Therefore, the requirement is changed to the form it takes from the stakeholder requirement `R-MIS-060`.

18.2 Compliance matrix

In order to verify if the design meets all the imposed requirements, a compliance matrix is developed, presented in Table 18.1. Requirements that cannot be verified at this stage of development are marked as unknown (UNK) and discussed in section 18.3. Sub-requirements mentioned in previous reports are omitted, as only the compliance of the parent is taken into consideration.

Table 18.1: Orpheus project requirement compliance matrix.

ID	Requirement Description	Met?
	Scientific Requirements	
R-SCI-010	The system shall provide UV spectroscopy of Pluto.	yes
R-SCI-020	The system shall provide UV spectroscopy of Charon.	yes
R-SCI-030	The system shall provide high resolution visible spectrum imagery of Pluto.	yes
R-SCI-040	The system shall provide high resolution visible spectrum imagery of Charon.	yes
R-SCI-050	The system shall provide high resolution hemispheric visible imagery of Nix.	UNK
R-SCI-060	The system shall provide high resolution hemispheric visible imagery of Hydra.	UNK
R-SCI-070	The system shall determine gravity harmonics of the Pluto-Charon system of at least degree 6 and order 6.	yes
R-SCI-080	The system shall measure the magnetospheric environment of Pluto.	yes
R-SCI-090	The system shall measure the magnetospheric environment of Charon.	yes
R-SCI-100	The system shall measure the time variability of Pluto.	yes
R-SCI-110	The system shall measure the time variability of Charon.	yes
R-SCI-120	The system shall perform topographic measurements of at least 70% of Pluto with a vertical resolution of at least 500 m.	yes
R-SCI-130	The system shall perform topographic measurements of at least 70% of Charon with a vertical resolution of at least 500 m.	yes
R-SCI-140	The system shall map the surface temperature of at least 70% of Pluto with a spatial resolution of at least 10 km/pixel.	yes
R-SCI-150	The system shall map the surface temperature of at least 70% of Charon with a spatial resolution of at least 10 km/pixel.	yes
R-SCI-160	The system shall provide hemispheric UV spectroscopy of Hydra.	UNK
R-SCI-170	The system shall provide hemispheric UV spectroscopy of Nix.	UNK
	Mission Requirements	
R-MIS-010	The exploration mission shall be an orbital exploration of the Pluto-Charon system.	yes
R-MIS-020	The vehicle shall be in orbit in the Pluto-Charon system for a minimum of one year.	yes
R-MIS-030	The selected in-space propulsion system shall have TRL 6 or higher.	yes
R-MIS-040	The total launch mass of the Pluto orbiter mission (including in-space propulsion subsystem) shall not exceed the launching capability of the selected launcher.	yes
R-MIS-050	The proposed exploration mission architecture and time-line is constrained by a single launch of a vehicle chosen by the team.	yes
R-MIS-060	The minimum nominal instrumentation load shall be 401 kg.	yes
R-MIS-071	The duration of the mission shall be no more than 25 years.	yes
R-MIS-080	The selected launch vehicle shall have TRL 9.	yes
R-MIS-091	The overall budget shall not exceed USD 1.1 billion (2018) with a risk of no more than USD 300 million (2018).	yes

R-MIS-100	Performance data of subsystems shall be shared with the corresponding (sub)contractors.	yes
R-MIS-110	The project shall adhere to the regulations set by the Fellowship building.	yes
R-MIS-120	The project shall not disturb other groups working on the DSE.	yes
R-MIS-130	The project shall adhere to the DSE deadlines set by the TU Delft.	yes
R-MIS-140	The project shall adhere to the DSE regulations set by the TU Delft.	yes
R-MIS-150	The project shall adhere to the treaties ratified by The United Nations.	yes
R-MIS-160	The mission shall abide by the rules imposed by the Office for Outer Space Affairs.	yes
R-MIS-170	The mission shall adhere to the space agency launch windows.	yes
R-MIS-180	The mission shall adhere to regulations set in place by regulatory agencies of the governments involved.	yes
R-MIS-190	The mission shall not violate export control / ITAR regulations.	yes
R-MIS-200	The mission shall adhere to planetary protection class II regulations.	yes
R-MIS-210	Measurement data shall be made available for educational purposes.	yes
R-MIS-220	The mission shall contribute to the advancement of society.	yes
R-MIS-230	Press release kits shall be made available for the media at key mission milestones.	yes
R-MIS-240	The mission shall avoid the production of toxic waste on Earth.	yes
R-MIS-250	The mission shall avoid the production of nuclear waste on Earth.	yes
R-MIS-260	The mission shall gather data about the Pluto-Charon system.	yes
	Launch Segment Requirements	
R-LCN-010	The launcher shall have a reliability of at least 0.95.	UNK
R-LCN-020	The launch vehicle shall have a technology readiness level of 9.	yes
R-LCN-030	The launcher shall not require in-orbit refuelling.	yes
R-LCN-040	The launcher shall get the space segment in a parking orbit with one single launch.	yes
R-LCN-050	The launcher shall be able to keep the space segment in a clean environment of ISO class 9.	yes
R-LCN-060	The launch segment shall not cost more than USD 150 million (2018).	yes
	Spacecraft Segment Requirements	
R-SYS-011	The space segment shall have a minimum dry mass of 401 kg.	yes
R-SYS-020	The space segment shall have a injected mass of no more than 8300 kg including a 5% launch margin.	yes
R-SYS-030	The space segment shall have a lifetime of at least 25 years in space from which at least one year of full-time scientific payload operations.	yes
R-SYS-040	The space segment shall have a lifetime of 3.3 years on Earth.	UNK
R-SYS-050	The space segment shall cost no more thanUSD 690 million (2018).	yes
R-SYS-060	In space, the space segment shall have a probability less than 10^{-4} of impact with any foreign object of mass larger than 0.1 kg .	UNK
R-SYS-070	The space segment shall adhere the requirements of planetary protection class II.	yes
R-SYS-080	The space segment shall have no single points that could lead to mission failure.	yes
R-SYS-090	The space segment shall include design margins as specified by ESA.	yes
R-SYS-100	The space segment shall be able to survive the space environment	UNK
R-SYS-110	The space segment shall enter hibernation mode during the orbital transfer.	yes
R-SYS-120	The space segment shall survive the loads during launch.	UNK
R-SYS-130	The space segment shall adhere to the constraints the launcher puts on the space segment as defined in the launcher manual	UNK
	Ground Segment	
R-GND-010	The ground segment shall be able to receive data from the space segment over a distance of no more than 50.305 AU with a transfer rate of at least 1 kbit/s.	yes
R-GND-020	The ground segment shall be able to transmit data to the space segment over a distance of no more than 50.305 AU with a transfer rate of at least 1 Mbit/s.	yes
R-GND-030	Ground segment operation over the entire mission duration shall not cost more than USD 192 million (2018).	yes
	Command & Data Handling Subsystem	
R-CDH-010	The software shall be update-able from the ground.	yes
R-CDH-020	The spacecraft shall send a confirmation signal when a command is successfully executed or failed.	yes
R-CDH-030	The C&DH subsystem shall implement system hibernation.	yes
R-CDH-040	The C&DH subsystem shall implement system safe mode.	yes
R-CDH-050	The C&DH subsystem shall contain more than 16 GigaBytes of storage.	yes
R-CDH-060	The C&DH subsystem shall transmit a weekly status update during hibernation.	yes
R-CDH-070	The real-time data system shall be able to monitor spacecraft health, safety and operational status.	yes
R-CDH-080	The C&DH subsystem shall be available a minimum of 99% of the mission time.	yes
R-CDH-090	The C&DH subsystem shall have a reliability of 0.99 or above.	yes
R-CDH-100	The C&DH subsystem shall have a mass of 10 kg or less.	yes
R-CDH-110	The C&DH subsystem shall use 30 W or less input power.	yes
R-CDH-120	The C&DH subsystem shall comply with size requirements set by the launcher.	yes
R-CDH-130	The C&DH subsystem shall not have any single points of failure.	yes
	Communication Subsystem	
R-COM-010	The communications array shall consume 50% of the available power or less.	yes
R-COM-020	Science data shall be downlinked by the spacecraft in X-band.	yes
R-COM-030	The maximum bit error rate during data downlink shall be equal or lower than 10^{-5}.	yes
R-COM-040	The communication subsystem shall not cost more than USD 7 million (2018).	yes
R-COM-050	The communication subsystem shall not weigh more than 44 kg.	yes
R-COM-060	The spacecraft shall downlink to Earth with a data rate of more than 1 kbps.	yes
R-COM-070	The spacecraft shall have a downlink frequency of 8.4 GHz.	yes
R-COM-080	The spacecraft shall have an uplink frequency of 7.145 GHz.	yes
R-COM-090	The antenna shall have a diameter equal or less than 4.5 m.	yes
R-COM-100	The communication subsystem shall have no single points of failure.	yes
R-COM-110	The communication subsystem shall operate within the temperature range 15-45 degrees Celsius.	yes
	Payload	
R-PLD-010	The payload shall fit inside the spacecraft structure where necessary.	yes

R-PLD-020	The payload mass shall be a maximum of 40 kg.	yes
R-PLD-030	The payload shall be in use for a minimum of 1 year after. reaching Pluto	yes
R-PLD-040	The payload shall contain a gravity experiment.	yes
R-PLD-050	The payload shall contain a magnetometer.	yes
R-PLD-060	The payload shall contain a radio science experiment.	yes
R-PLD-070	The payload shall contain a visible and infrared imager/spectrometer.	yes
R-PLD-080	The payload shall contain an ultraviolet imaging spectrometer.	yes
R-PLD-090	The payload shall contain a telescopic camera.	yes
R-PLD-100	The payload shall contain a solar wind and plasma spectrometer.	yes
R-PLD-110	The payload shall not exceed a total costs of USD 21 million (2018).	yes
R-PLD-120	The payload shall be functional for the duration of the entire mission.	UNK
R-PLD-130	The payload shall utilise a 0.8 code rate for data storage.	UNK
	Thermal Control Subsystem	
R-TCS-010	The TCS shall maintain the temperature of the payload between -40°C and 40°C.	Yes
R-TCS-020	The TCS shall maintain the temperature of the magnetometer between -40°C and 20°C.	Yes
R-TCS-030	The TCS shall maintain the temperature of the energetic particle instrument between 0°C and 40°C.	Yes
R-TCS-040	The TCS shall maintain the temperature of the solar wind analyser between 0°C and -20°C.	Yes
R-TCS-050	The TCS shall maintain the temperature of the energetic particle instrument between 0°C and 40°C.	Yes
R-TCS-050	The TCS shall maintain the temperature of the visible light/IR camera at 25°C.	Yes
R-TCS-060	The TCS shall maintain the temperature of the hydrazine propellant between 2.5°C and 12.5°C.	Yes
R-TCS-060	The TCS shall maintain the temperature of the MON-3 propellant between -6.3°C and 3.7°C.	Yes
R-TCS-070	The TCS shall fit inside the spacecraft structure.	Yes
R-TCS-080	The TCS mass shall be no more than 40 kg.	Yes
R-TCS-090	The active TCS shall be in use for the full duration of the scientific mission.	Yes
R-TCS-100	The TCS shall keep the spacecraft bus at a temperature between -20 and 20. °C	Yes
R-TCS-110	The TCS shall not exceed a total costs of USD 1.4 million (2018)	Yes
R-TCS-120	The active TCS shall not consume more than 41 W	Yes
	Structures Subsystem	
R-STR-010	The structures shall mechanically align the spacecraft equipment.	yes
R-STR-020	The structures shall have the strength to carry the equipment during 6 g of axial accelerations.	yes
R-STR-030	The structures shall have the strength to carry the equipment during 2 g of lateral accelerations.	yes
R-STR-040	The structures shall have the strength to carry the equipment during orbit.	yes
R-STR-050	The structures shall have a lifespan of at least 25 years.	yes
R-STR-060	The structures shall protect hardware from external radiation.	UNK
R-STR-070	The structures shall have a maximum mass of 120 kg.	yes
R-STR-080	The structures shall accommodate assembly of the spacecraft equipment.	yes
	Attitude Determination & Control Subsystem	
R-ADCS-010	The ADCS shall have a safe mode.	yes
R-ADCS-020	The ADCS shall fit inside the spacecraft structure.	yes
R-ADCS-030	The ADCS mass shall be a maximum of 28 kg.	yes
R-ADCS-040	The ADCS shall be functional for the duration of the entire mission.	UNK
R-ADCS-050	The ADCS shall have a minimum pointing accuracy of 0.1 degrees.	yes
R-ADCS-060	The ADCS shall be able to rotate the spacecraft 180° over any of the three axes within 1 hour.	yes
R-ADCS-070	The ADCS shall provide a minimum orientation accuracy of 0.1 degrees.	yes
R-ADCS-080	The ADCS shall be able to spin stabilise the spacecraft at an angular rate of at least 3 rad/s.	yes
R-ADCS-090	The ADCS shall not exceed a total cost of USD 13 million (2018)	yes
R-ADCS-100	The ADCS thrusters shall provide a minimum of 20 N per thruster at BOL.	yes
R-ADCS-110	The ADCS shall achieve the spin stabilisation spin rate within 1 hour.	yes
R-ADCS-120	The ADCS shall be able to counter the anticipated disturbance torques.	yes
	Propulsion Subsystem	
R-PRP-010	The propulsion system shall adhere to ESA margin standards (SRE-PA/2011.097/).	yes
R-PRP-020	The selected in-space propulsion system shall have TRL 6 or above.	yes
R-PRP-030	The electrical propulsion subsystem shall require a maximum peak power of below 640 watts at EOL.	yes
R-PRP-040	The propulsion system shall have total dimensions not exceeding 4x1.5x1.5 m.	yes
R-PRP-050	The electrical subsystem shall be able to provide thrust for minimum 12.1 years.	yes
R-PRP-060	The chemical subsystem shall be re-ignitable for a minimum of 5 times.	yes
R-PRP-070	The electrical subsystem shall provide minimum 6060 m/s .	yes
R-PRP-080	The bi-propellant subsystem shall provide minimum 986 m/s.	yes
R-PRP-090	The mono-propellant propulsion subsystem shall provide minimum 150 m/s.	yes
R-PRP-100	The fuel tanks shall be compatible with hydrazine.	yes
R-PRP-110	The oxidiser tank shall be compatible with Mon-3.	yes
R-PRP-120	The electrical ion thruster shall have a thrust vectoring system.	yes
R-PRP-130	The propulsion subsystem shall not exceed a total cost of USD 50 million (2018)	yes
R-PRP-140	The propulsion subsystem shall be a maximum of 215 kg	yes
	Electric Power Subsystem	
R-EPS-010	The EPS module shall be able to provide a mininum peak power of 670 W until the end of the electrical manoeuvre(24 years).	yes
R-EPS-020	The EPS module shall have a mass of no more than 220 kg.	yes
R-EPS-030	The EPS module shall not cost more than USD 351 million (2018).	yes
R-EPS-040	The EPS module shall be able to dissipate excess heat power .	yes
R-EPS-050	The EPS module shall be compatible with the hibernation mode.	yes
R-EPS-060	The EPS shall not pollute the Pluto or Charon environment.	yes

18.3 Compliance-Unknown Requirements

The following section lists and discusses all requirements where the compliance is still unknown at this stage of the project.

- **R-SCI-050, R-SCI-060, R-SCI-160, R-SCI-170:** It is unknown whether these requirements will be possible with the current level of analysis. A more in depth investigation is required to determine if all the objects orbiting Pluto can be visited.
- **R-LCN-010:** The reliability of the Falcon Heavy is ambiguous at this stage. It had one successful launch, but it failed the insertion trajectory. Therefore, the requirement is marked as unknown compliance for know.
- **R-SYS-040:** More information is required about the storage conditions and the assembly components themselves to determine if this requirement can be fulfilled.
- **R-SYS-060:** A more in depth trajectory analysis has to be performed in order to produce a complete mapping of the objects Orpheus might encounter on the route to Pluto. Therefore, it is unknown whether `R-SYS-060` is fulfilled.
- **R-SYS-100:** A more in depth investigation is required to determine if the spacecraft is able to survive the space environments, achieved through analysis or tests.
- **R-SYS-120:** While the structures were proven to survive the launch loads, more data, which is currently unavailable, is needed to determine if this applies to all other spacecraft components as well.
- **R-SYS-130:** As with `R-SYS-120`, the spacecraft would need prototype testing for each component to confirm if this requirement is complied with.
- **R-PLD-120:** The functionality of the payload over the entire mission has to be simulated in the next phase of the mission design life cycle. Hence, whether this requirement is fulfilled is still unknown.
- **R-PLD-130:** It is unknown whether the payload can output data at a 0.8 code rate. A more thorough investigation with the payload manufacturers is required to confirm compliance.
- **R-STR-050:** The structure shall be tested on whether it complies with the radiation exposure limits. This is done is the testing phase after the DSE. Hence, compliance cannot be verified with current data.
- **R-ADCS-040:** Only statistical data is available on the reliability and availability, therefore compliance cannot be verified.

18.4 System Performance Analysis

The following section summarises the performance of the Orpheus spacecraft after launch. The selected orbit, explained in Section 7.4.5, has a coverage of about 90% of Pluto and Charon, exceeding by far the scientific requirements `R-SCI-010-I`, `R-SCI-020-I`, `R-SCI-030-I` and `R-SCI-040-I`. In addition, the orbits are designed such that Orpheus can stay in the Pluto-Charon System for an entire year, meeting `R-MIS-020`. The trajectory is optimised to reach the system in at least 24 years and orbiting Pluto and Charon for maximum of 1 year, as verified in Section 7.7. This means `R-MIS-071` is fully met. The orbit visiting frequency is 15 days for Pluto as well as for Charon. Hence every 15 days the spacecraft will revisit the same point of the planet its orbits.

Data is sent down by means of a 4.5 m diameter high gain antenna with a maximum data rate of 5.3 kbps, five times faster than New Horizons. With this, Orpheus includes the largest antenna ever sent to the outer solar system.

The subsystem requirement `R-ADCS-050`, `R-ADCS-070`, `R-PRP-080` and `R-EPS-010`are verified during each subsystem analysis. It is notable to say, that `R-PRP-080` drives the propulsion system design to a high performance level. The ion-engine burn of 12.1 years is the longest ion-engine burn ever performed in space [54].

Performance requirement `R-EPS-010` determines the minimum peak power that shall be delivered by the RTGs after the ion-engine burn. Figure 18.1 displays the power delivered by the RTGs over the mission lifetime of 25 years. It is clearly visible that over the 25 years, the RTGs deliver enough power such that the system is able to operate in different modes. This gives indication that the power system is performing sufficiently for the proposed mission.

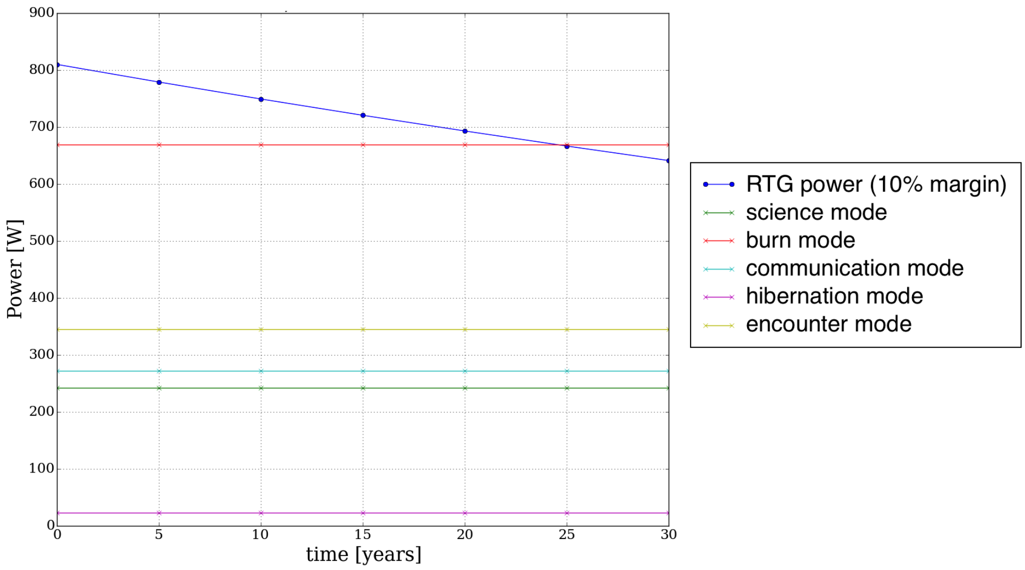

Figure 18.1: Power delivered/consumed over mission lifetime

Concluding from the compliance analysis as well as the performance analysis presented above, Orpheus is using groundbreaking technology to meet all requirements possible at this design phase.

18.5 System Verification & Validation

To verify the performance of Orpheus, several tests as well as simulations are performed. Tests include thermal vacuum testing, sine and random vibration testing as well as electromagnetic compatibility tests.

Orpheus is tested in the Large Space Simulator (LSS), a large vacuum chamber to model the vacuum environment in space. This particular chamber can be used to test thermal as well as mechanical properties. Already in 1988 the IRIS spacecraft was tested in the LSS [106]. Besides this, Orpheus shall be tested such that it survives the acoustic loads during launch. This may be done in the Large European Acoustic Facility (LEAF) at ESA ESTEC where they tested ENVISAT as well [131]. The electromagnetic compatibility of the spacecraft can be verified by testing it in the Maxwell Test Chamber at ESA ESTEC, as well [48]. Another test that is essential for the system to survive in the space environment is the radiation testing. This can be performed in the ESTEC Co-60 Facility at ESA.

Next to this, Orpheus needs to be verified in terms of system integration. This verification is done by inspection and demonstration. For instance the RTG interface with the spacecraft is inspected and it is demonstrated that the all systems receive power. All subsystems are tested on the ground as well as during the commissioning phase in Earth Parking Orbit again.

19 Operations and Logistics

The following chapter explains the logistics of the mission and the effect on cost and schedule, followed by the mission operations.

19.1 Logistics

As already presented in the Midterm Report [27], the logistics include all activities with implications on the timing and planning of the mission to ensure that the schedule and cost constraints are met. Figure 19.1 shows the logistics of the Orpheus mission. The loop between the 'manufacturing of parts' and the 'redesign' can be iterated as many times as necessary, for the spacecraft parts, the spacecraft subsystems, and the spacecraft as a whole. The activities related to logistics are explained in detail below, in the order of fulfilment.

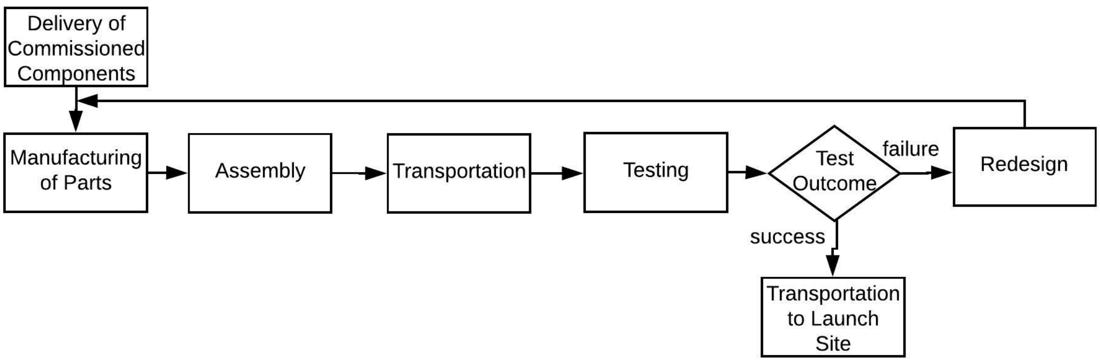

Figure 19.1: Logistics Flow Diagram.

Delivery of Commissioned Components: This step is done by subcontractors. It is essential that these are held to a strict schedule deadline, without affecting the quality of the products. Many of the components of Orpheus are procured from established contractors in the domain (Boeing, Thales), which can provide safe transport of the hardware to the assembly site.

Manufacturing of Parts: The production of parts is a time consuming process and shall be monitored such that deadlines are met. It is especially important, since Orpheus is to be launched in a specific launch window.

Transportation: To prevent cost overruns, transportation costs need to be included in the cost breakdown. Since the transportation may be affected by external factors, such as traffic delays and the risk of a crash in transit, sufficient amount of time needs to be included in the scheduling. Orpheus employs subcontractors from all over the world, therefore air transportation will probably be used. The nearest airport to the assembly site will be used in order to minimise the risks previously mentioned.

Testing: To prevent a redesign of parts or systems, the testing phase shall be done very thoroughly. In case of a redesign, cost overruns and schedule delays are usually unavoidable. It is therefore important that authorised testing facilities are chosen and accurate tests are performed.

By making use of Integrated Concurrent Engineering, engineering analysis and team communication are combined into one activity. This leads to less design iterations, more feedback within the team and a reduction in wasted effort. ICE can be considered a lean design approach, and is used during the initial design phase of Orpheus. [18].

19.2 Mission Operations

The following section presents the mission operations of Orpheus. A mission overview is given, followed by a concept development and a detailed description of the hibernation mode.

19.2.1 Mission Operations Overview

As mentioned in Chapter 7, Orpheus does a Jupiter gravity assist (JGA) 756 days after leaving Earth. Table 19.1 presents the different flight phases of Orpheus, based on New Horizons mission [64]. As can be seen, two beacon (warning signal) hibernation modes are implemented during the cruise phases. Objectives that have to be met in each phase are navigation and targeting (N&T). This ensures that Orpheus stays on the right trajectory and reaches Pluto in time.

Table 19.1: Mission Overview.

Mission Phase	Time Frame	Objective
Launch and Early Orbit Phase	Launch (24 November 2027)	Checkout, N&T
Commissioning	LEOP until 60 days before JGA (December 2027)	Instrument Commissioning, Redundancy Testing, N&T
Coast 1	756 days til Jupiter encounter (19 December 2029)	Beacon-Hibernation, Annual Checkouts, Precession Manoeuvres, N&T
Jupiter	Approx. 100 days of JGA (29 March 2030)	Science Observations, N&T
Coast 2	7898 days until Pluto encounter (29 March 2030 - 12 November 2051)	Beacon-Hibernation, Annual Checkouts, Precession Manoeuvres, N&T
Pluto-Charon Encounter	6 months operation around Pluto (end 12 May 2052)	Science Observations, N&T
Transfer to Charon	6 months operations around Charon (end 12 November 2052)	Science Observations, N&T
Data Retrieval	During transfer to Charon	Return Pluto and Charon Data, N&T
End of Mission	S/C EOL (November 2052)	Heliocentric Orbit until end of life, extend of mission if possible

The operations before the launch such as transport to the pad and pad integration have not been included in detail as they are not the focus of this project. However they are mentioned in Section 21.

19.2.2 Operation Concept

Since Orpheus is a deep space exploration mission the operation phase of the spacecraft is the longest period of the mission. Due to the long flight time to Pluto, a hibernation mode is included. During hibernation it is essential that the operations are done autonomously, especially along the trajectory from Jupiter to Pluto in coast phase 2 [70].

Commissioning: During commissioning Orpheus' functioning is checked on a subsystem level. All subsystems as well as their redundant components are tested on whether they operate correctly. This is done in the Earth Parking Orbit.

Autonomy: It is decided that Orpheus has an implemented autonomy subsystem that monitors the health of the spacecraft throughout the entire mission. A level 1 closed-loop system is used. This implies, that for instance the thermal control system is automated and heats the spacecraft when the temperature drops. In addition, actions to prevent and detect anomalies are included [148]. For the execution of the mission a level 3 closed-loop system is added. This provides that event-based operations are carried out and on-board operations control procedures are executed [148]. A level 1 automation ensures that the validation of the system is done easily and cost effectively. The autonomy subsystem transitions Orpheus into encounter mode when Pluto is reached.

Beacon-Hibernation Mode: To save mission costs, preserve the spacecraft and instrument hardware and limit the usage of the Deep Space Network, Orpheus will enter and exit a beacon-hibernation mode during the long coast phases of the mission. Thermal control is then done on spacecraft level rather than checking each single instrument, since they are turned off [6]. The fist hibernation lasts for 2 year, leaving 1 year to check whether instruments and systems unction correctly before encountering Jupiter. In the second hibernation mode however, the ion-engine is required to fire for more than 12.1 years, as stated in section 10.5, imposing a risk of failure if not monitored correctly. This mode is referred to as "Burn-mode" and is further explained below. Before each hibernation mode a sequence of autonomous activities needs to be done which is presented in Figure 19.2 [64].

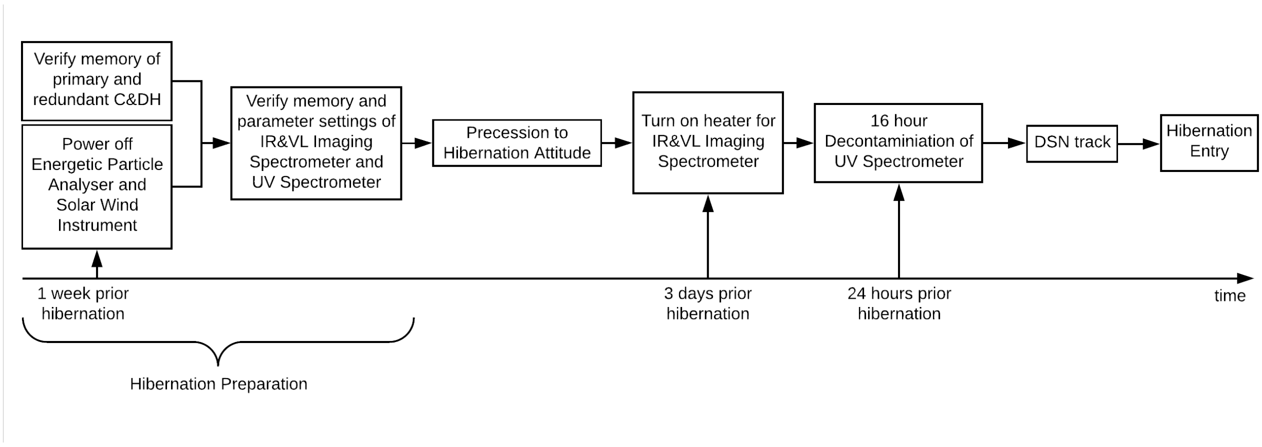

Figure 19.2: Pre-Hibernation activities.

Beacon-hibernation is done by weekly beacon tracks and 10 bps telemetry tracks each month, similar to New Horizons [64]. The weekly beacon tone broadcast is done discontinuously over a period of 36 hours using the low gain antenna, with an accuracy requirement of up to 3.8 degrees.

Burn Mode: The burn mode is entered during cruise phase 2, when the ion engine needs to operate to achieve the arrival of Orpheus at Pluto. During this phase the beacon-hibernation is still operational as most of the other systems do not require to be turned on.

Payload Operations Planning Since Orpheus is doing a fly-by at Jupiter part of the payload is turned on during this fly-by to gather scientific data of Jupiter and to test the instruments. Because exiting the hibernation mode requires time, activities are started 3 days before hibernation is fully ended. By turning off the heaters of the instruments, switching on the ADCS and the spacecraft entering normal operation phase, hibernation is ended [64]. When orbiting the Pluto-Charon system the on-board instruments are operating at specified times, as already mentioned in section 6.2. Ones per orbit, the sequence of commands to turn on or off the payload are loaded on the ground based command scheduler.

End of Life After spending 1 year in the Pluto-Charon system, the Orpheus spacecraft will fire its main engine for the last time. This burn will propel the spacecraft into a heliocentric orbit in the outer solar system. Once in its final orbit, the spacecraft will become less active. The payload system will still operate to acquire more data of the outer solar system. However it will not be as active as the system was in the Pluto-Charon system.

20 Technical Risk Analysis

The following chapter presents the updated technical risks of the mission, which stem from the risks presented and then expanded upon in the Baseline and Midterm Reports [27] [28]. This is followed by the risk map and mitigation techniques that are implemented.

20.1 Analysis Approach

Risk is the product of the likelihood of an event and the consequence of that event happening (financial loss), or otherwise. In order to identify the risks associated with the Orpheus mission, the following approach is applied (described in more detail in the Baseline Report [28]):

- **Step 1. Identification:** For each category, potential risks are identified.
- **Step 2. Assessment:** The identified events are analysed in terms of likelihood and effect on the mission.
- **Step 3. Mitigation:** Mitigation techniques are applied on risks that are deemed too high.

For assessing the likelihood of the potential events, the following scale was used:

- **(1) Almost Impossible:** The event is extremely unlikely to occur and does not require preventive measures.
- **(2) Not Likely:** The event has a small probability to occur, preventive measures are minor.
- **(3) Could Occur:** The event has a medium probability to occur, preventive actions are recommended.
- **(4) Known to Occur:** The event is very likely to occur, preventive actions are strongly suggested.
- **(5) Common Occurrence:** The event is near certain to occur, strong preventive actions are required.

Furthermore, the assessment of the severity of the risks is done using the following scale:

- **(1) Insignificant:** Has no noticeable impact on the mission.
- **(2) Minor:** Has a very low impact on the mission, to be avoided if possible.
- **(3) Moderate:** Impact is relatively large, requires mitigation actions.
- **(4) Major:** Has severe consequences on the mission, strong mitigation is required.
- **(5) Catastrophic:** Might lead to mission failure, catastrophic cost overruns or schedule delays. Mitigation is a priority.

Using these criteria, the risks relating to the entirety of the mission are identified, ranked and mitigated.

20.2 Top-Level Risks

The top level risks are risks associated with the cost and scheduling of the mission, presented in Table 20.1. In Table 20.2, they are plotted on a risk map, before and after (in bold) the mitigation techniques are implemented. In Table 20.1 there are risks that are both in the cost and schedule section, as they overlap in category.

Most risks are mitigated by keeping a close relationship and good communication within the project team and with the user. In addition to that, accurate documentation and proper planning is essential to prevent schedule delays, thereby mitigating the risk of the development of new technologies. Inflation rate, as well as the funding, need to be monitored during the entire project. This can be done by making sure that inflation is accounted for when doing a cost analysis and that no cost overruns occur.

Table 20.1: Top-level risks associated with scheduling and cost

Risk ID	Risk Description	Risk ID	Risk Description
(C)	**Cost**	C-12	Inflation
C-1	Funding cuts	**(S)**	**Scheduling**
C-2	Unavailability of validation facilities	S-1	Subcontractor delivery issues
C-3	Unavailable validation methods	S-2	Transportation issues
C-4	Redundancy	S-3	Having to develop new technologies
C-5	Wrong choice of design margins	S-4	Unavailability of facilities
C-6	Having to develop new technology	S-5	Unavailable validation methods
C-7	Change in mission requirements	S-6	Request for deviation
C-8	Underestimating amount of work	S-7	Change in stakeholder requirements
C-9	Employee status	S-8	Change in mission requirements
C-10	Too little workers employed for the mission	S-9	Funding cut
C-11	Price fluctuations	S-10	Launch provider issues

Table 20.2: Cost and Scheduling Risk Map

	Probability				
Potential Consequences	1. Almost Impossible	2. Not Likely to Occur	3. Could Occur	4. Known to Occur	5. Common Occurrence
5. Catastrophic	**C-1**	**C-7** C-1,C-7, S-10	C-2		
4. Major	C-9	**S-10**, C-6, S-8, S-9	C-5, S-3		
3. Moderate	**C-9**	**C-2**,**C-3**,**C-4**,**C-5**,**C-6** **S-3**,**S-8**,**S-9**,C-3,C-4, S-7	C-10,C-11, S-1, S-4, S-5, S-6		C-12
2. Minor		**C-8**,**S-1**,**S-6**,**S-7**,S-2	**S-4**,**S-5**C-8	**C-11**	
1. Insignificant		**S-2**		**C-10**	**C-12**

Low Risk	Medium Risk	Significant Risk	High Risk

20.3 Mission Success Risks

Table 20.3 lists all risks that affect the mission success on a subsystem level, as well as the design level. In the table, 'O' represents the likelihood of occurrence, and 'C' represents the consequence of the event happening. The scale used is taken using the scale shown in sec:approach (1-lowest, 5-highest). Choices are made on engineering judgement and experience. The risks are then plotted in Table 20.5, with the risks after mitigation in bold.

All risks are, at least partially, mitigated through verification and validation, as well as peer evaluation. More specific measures taken are explained in Table 20.4.

Table 20.4: Specific mitigation strategies

Risk ID	**Mitigation Strategy**
T-1.3, T-1.9, T-1.11, T-4.10, T-4.11	Monitor Risk
T-1.1, T-4.2.2-6, T-4.3.2-3, T-4.4.1, T-4.4.4, T-4.5.2, T-4.7.3, T-4.7.5, T-4.7.11, T-4.7.12, T-4.9.1-2	Redundancy of components
T-4.3.4	Ensure bit error rate $< 10^{-5}$
T-4.6.2-5	Mitigation included in design choices (Material choice etc.)
T-1.7, T-2.2, T-4.3, T-4.5, T-4.5.1, T-4.5.3, T-4.6, T-4.6.2-3, T-4.6.6-7, T-4.7, T-4.7.2, T-4.7.4, T-4.7.6-9, T-4.8, T-4.8.2, T-4.9, T-4.9.3, T-4.9.4, T-5.8	Verification testing
T-2.4-5, T-2.7, T-4.2.1, T-4.3.1, T-4.5.4, T-4.6.1, T-4.8.1, T-4.9.5, T-4.12, T-4.12.1-3, T-4.13, T-4.14, T-4.15	Verification simulation
T-4.1	Implement a protection system
T-4.7.10	Implement filters
T-3.3, T-3.4. T-3.5, T-4.7.1, T-4.12.1-3, T-5.1-7, T-5.10-11, T-5.13-17	Documentation and peer review
T-3.1	Introduce margins

Table 20.3: The risks associated with mission success

Risk ID	Risk Description	O	C	Risk ID	Risk Description	O	C
(1)	**Ground**			T-4.6.5	Degassing	5	3
T-1.1	Control equipment failure	4	4	T-4.6.6	Magnetometer boom deployment failure	2	4
T-1.2	Insufficient data	4	5	T-4.6.7	Truss failure	3	5
T-1.3	Poor override command	5	5	T-4.7	Propulsion failure		
T-1.4	Spacecraft structural failure	3	5	T-4.7.1	Propellant calculation error	1	5
T-1.5	Worker strike	2	4	T-4.7.2	Propellant leak	2	4
T-1.6	Crash in transit	2	5	T-4.7.3	Valve failure	4	5
T-1.7	Hardware failure	3	4	T-4.7.4	(Re)-ignition failure	2	5
T-1.8	Wrong signal acquisition	3	4	T-4.7.5	Propellant mixing in feedystsem	2	5
T-1.9	DSN availability	2	3	T-4.7.6	Tank Rupture	1	5
T-1.10	Signal mismatch	3	3	T-4.7.7	Bipropellant engine failure	2	5
T-1.11	Software threats/hacking	1	3	T-4.7.8	Elevated helium leakage	2	3
(2)	**Launch**			T-4.7.9	Electrical engine failure	2	5
T-2.1	Payload issues	4	5	T-4.7.10	Feed system blockages	2	5
T-2.2	Structural failure	4	5	T-4.7.11	Monopropellant thruster failure	2	4
T-2.3	Launcher failure	4	5	T-4.7.12	Propellant freezing	2	5
T-2.4	Decoupling failure	2	5	T-4.8	Payload failure		
T-2.5	Separation failure	2	5	T-4.8.1	Failure to switch on	2	5
T-2.6	Weather	5	4	T-4.8.2	Aperture/lens blockage	1	5
T-2.7	Orbit Insertion	2	4	T-4.8.3	Inaccurate data	1	5
(3)	**Manufacturer**			T-4.9	Thermal control failure		
T-3.1	Defects outside tolerances	1	3	T-4.9.1	Louver failure	2	5
T-3.2	Assembly missmatches	2	4	T-4.9.2	Heater failure	4	4
T-3.3	Non-manufacturable designs	3	4	T-4.9.3	Insulator layer damage	3	5
T-3.4	Improper design margins	2	4	T-4.9.4	Thermistor failure	3	4
T-3.5	Issues with contractors	3	4	T-4.9.5	Degredation of MLI	5	4
(4)	**Space**			T-4.10	High-energy particle radiation	5	4
T-4.1	Foreign object/debris impact	4	5	T-4.11	Solar wind	5	4
T-4.2	ADCS failure			T-4.12	ΔV calculation error		
T-4.2.1	Spacecraft instability	2	5	T-4.12.1	Incorrectly modelled dynamics	2	5
T-4.2.2	Reaction wheel failure	4	5	T-4.12.2	Modelled dynamics less accurate than required	2	5
T-4.2.3	Sun sensor failure	4	5	T-4.12.3	Coordinate system conversion issues	2	5
T-4.2.4	Star tracker failure	4	5	T-4.13	Mapping less accurate than required	3	4
T-4.2.5	IMU failure	4	5	T-4.14	Spacecraft inserted into incorrect trajectory	3	5
T-4.2.6	Thruster failure	4	5	T-4.15	Trajectory calculation error	1	5
T-4.3	Communication failure			**(5)**	**Design**	2	5
T-4.3.1	Data rate lower than expected	3	4	T-5.1	Poor trade-off criteria selection	2	3
T-4.3.2	Antenna damage	2	5	T-5.2	Poor criteria weighting	2	3
T-4.3.3	Antenna pointing failure	2	4	T-5.3	Skipping required trade-off	2	3
T-4.3.4	Bit switching	5	2	T-5.4	Poor judgement/justification	2	3
T-4.4	TT&C failure			T-5.5	Not all design options considered	1	2
T-4.1	Memory failure	4	4	T-5.6	Availability of facilities	1	4
T-4.4.2	CPU failure	3	5	T-5.7	Final product test failure	2	5
T-4.4.3	OS bugs, errors	4	4	T-5.8	Unverifiable requirements	2	3
T-4.4.4	Component failure	2	5	T-5.9	Infeasible requirements	1	3
T-4.5	EPS failure			T-5.10	Incomprehensive requirements	1	3
T-4.5.1	Circuitry failure	3	5	T-5.11	Unresolved test anomalies	1	5
T-4.5.2	RTG failure	1	5	T-5.12	Incomplete requirements	2	5
T-4.5.3	System overheating	1	5	T-5.13	Unvalidated (sub)-system	3	5
T-4.5.4	Higher power degradation	1	5	T-5.14	Unverified requirements	2	5
T-4.6	Structural failure			T-5.15	Reliability overestimation	3	4
T-4.6.1	Degradation of materials	5	4	T-5.16	Maintainability underestimation	3	4
T-4.6.2	Thermal expansion/contraction	5	4				
T-4.6.3	Magnetic failure/induction	3	4				
T-4.6.4	Galvanic corrosion	5	4				

Table 20.5: The mitigated risks associated with mission success

	Probability				
Potential Consequences	1. Almost Impossible	2. Not Likely to Occur	3. Could Occur	4. Known to Occur	5. Common Occurrence
5. Catastrophic	T-4.5.2-4, T-4.7.1, T-4.7.6,T-4.8.2-3, T-4.15,T-5.12	T-1.6, T-2.4, T-2.5, T-4.2.1, T-4.3.2, T-4.7, T-4-5,T-4.7.7, T-4.7,T-4.9-10, T-4.7.12,T-4.8.1, T-4.9.1,T-4.12.1-3, T-5.8,T-5.13,T-5.15	T-.4.5.1,T-1.4, T-4.5.7,T-4.9.3, T-4.13,T-5.14	T-1.2,T-2.1,T-2.2, T-2.3,T-4.1, T-4.2.2-6,T-4.7.3	T-1.3
4. Major	T-5.7, **T-3.3**, **T-4.5.1**, **T-4.5.3-4**, **T-4.7.2**, **T-4.9.3-4**, **T-4.14**, **T-5.8**	T-1.5,T-2.7,T-3.2, T-3.4,T-4.3.3, T-4.6.6,T-4.7.2, T-4.7.11,T-4.9.4, **T-1.7**, **T-4.6.3**	T-1.7-8,T-3.3, T-3.5,T-4.3.1, T-4.6.3,T-4.13, T-5.16-17, **T-2.6**, **T-4.6.2**, **T-4.6.4**, **T-4.10-11**	T-1.1,T-4.4.1, T-4.4.3,T-4.9.3	T-2.6, T-4.6.1-2, T-4.6.4, T-4.9.5-11
3. Moderate	T-1.11,T-3.1, T-5.10-11, **T-1.9**, **T-4.5.2**, **T-5.1-.4**, **T-5.12**	T-1.9,T-4.7.8, T-5.1-4,T-5.9, **T-2.3-5**, **T-4.3.2**, **T-4.4.4**, **T-4.7.5**, **T-4.7.12**, **T-4.9.1**, **T-4.12.1-3**, **T-5.13**, **T-5.15**	T-1.10, **T-4.6.5**, **T-4.13**, **T-5.14**	**T-4.2.2-6**, **T-4.2.6**, **T-4.7.3**	T-4.6.5, **T-1.3**
2. Minor	T-5.5-6, **T-3.1**	**T-4.3.3**, **T-4.7.11**, **T-4.9.2**	**T-4.3.4**, **T-5.16-17**	**T-1.1**, **T-4.4.1**	T-4.3.4, **T-4.9.5**
1. Insignificant					

Low Risk	Medium Risk	Significant Risk	High Risk

21 Project Design and Development

The following chapter presents the logical order of activities to be performed after the Design Synthesis Exercise (DSE).

The Orpheus mission follows the standards set by European Cooperation for Space Standardisation (ECSS) in which following project phases are defined [77].

- **Phase 0:** Mission Analysis/Need Identification
- **Phase A:** Feasibility
- **Phase B:** Preliminary Definition
- **Phase C:** Detailed Definition
- **Phase D:** Qualification and Production
- **Phase E:** Utilisation/Operations
- **Phase F:** Disposal

During the DSE the phases 0 to B are completed and a preliminary design of the Orpheus spacecraft is finished. After that, in the detailed design definition phase C, the engineering model is prepared and tested. In addition, hardware is manufactured and software is developed. The test plan is established and the system is then ready to be qualified and produced in phase D. Phase E and F are the in-orbit operations and the spacecraft disposal, respectively. A more detailed description of the operations can be found on Section 19.2. It is assumed that the mission proposal is already accepted by the prime contractor. Figure 21.1 presents the activities executed after the end of the DSE.

In order to estimate the time available for each step in the design and development logic, a Gantt chart can be set up. The chart shows the estimated time for all high-level activities and the schedule in Figure 21.2. The days shown in the figure indicate conventional working days on which tasks are performed, as in design phase C and D external contractors and companies will be collaborated with. Therefore, the required one-year orbit around the Pluto-Charon system is visible as 262 days rather than 365. Predecessors of other tasks can be found using the task ID, or via the arrow indication in the diagram. As unforeseen events can cause delays, the preceding steps to the launch date have been scheduled with slack in between design phases. Slack is considered necessary as well when external factors have influence on the schedule, which is mainly during phase D.

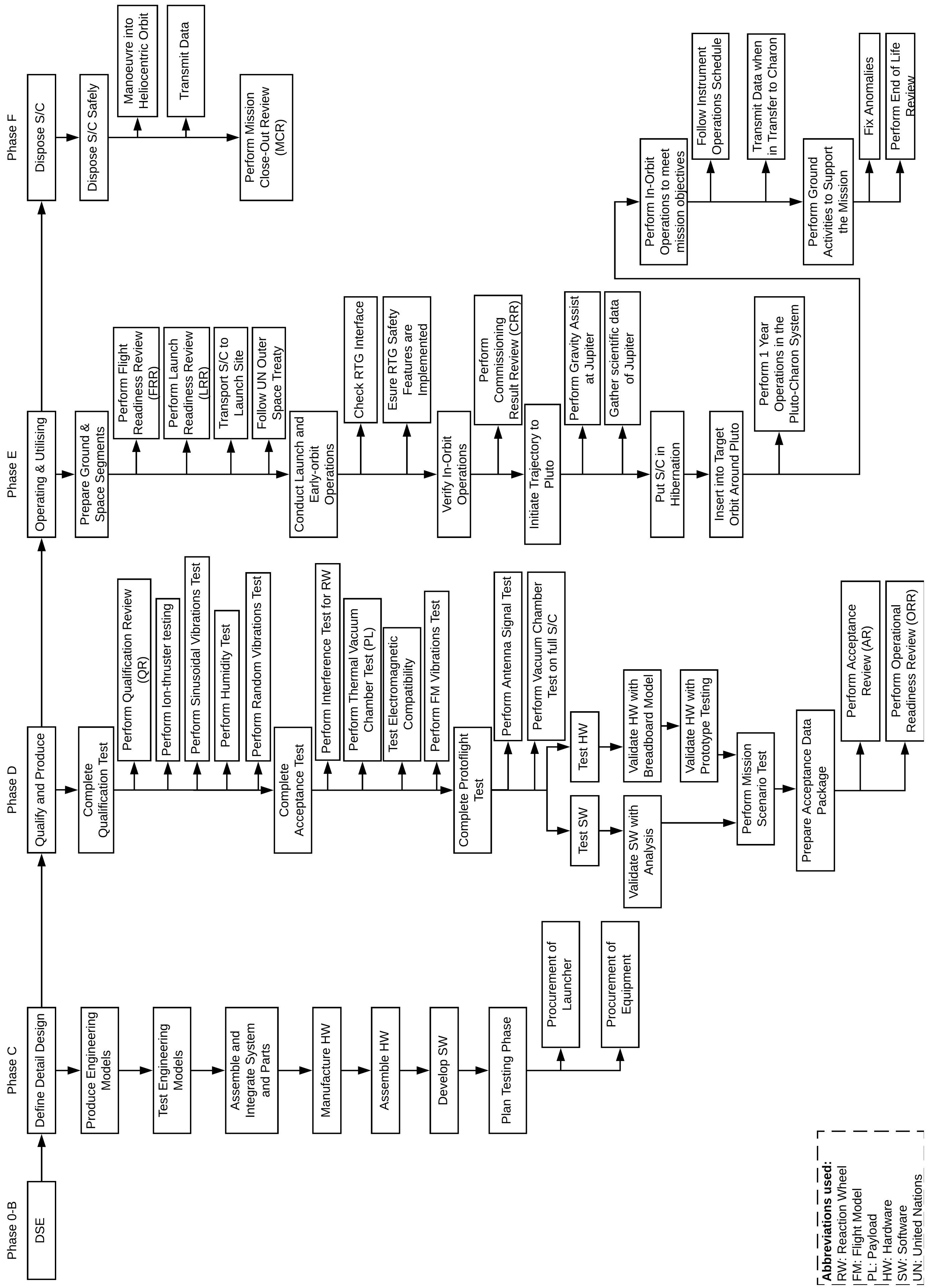

Figure 21.1: Design and Development Logic.

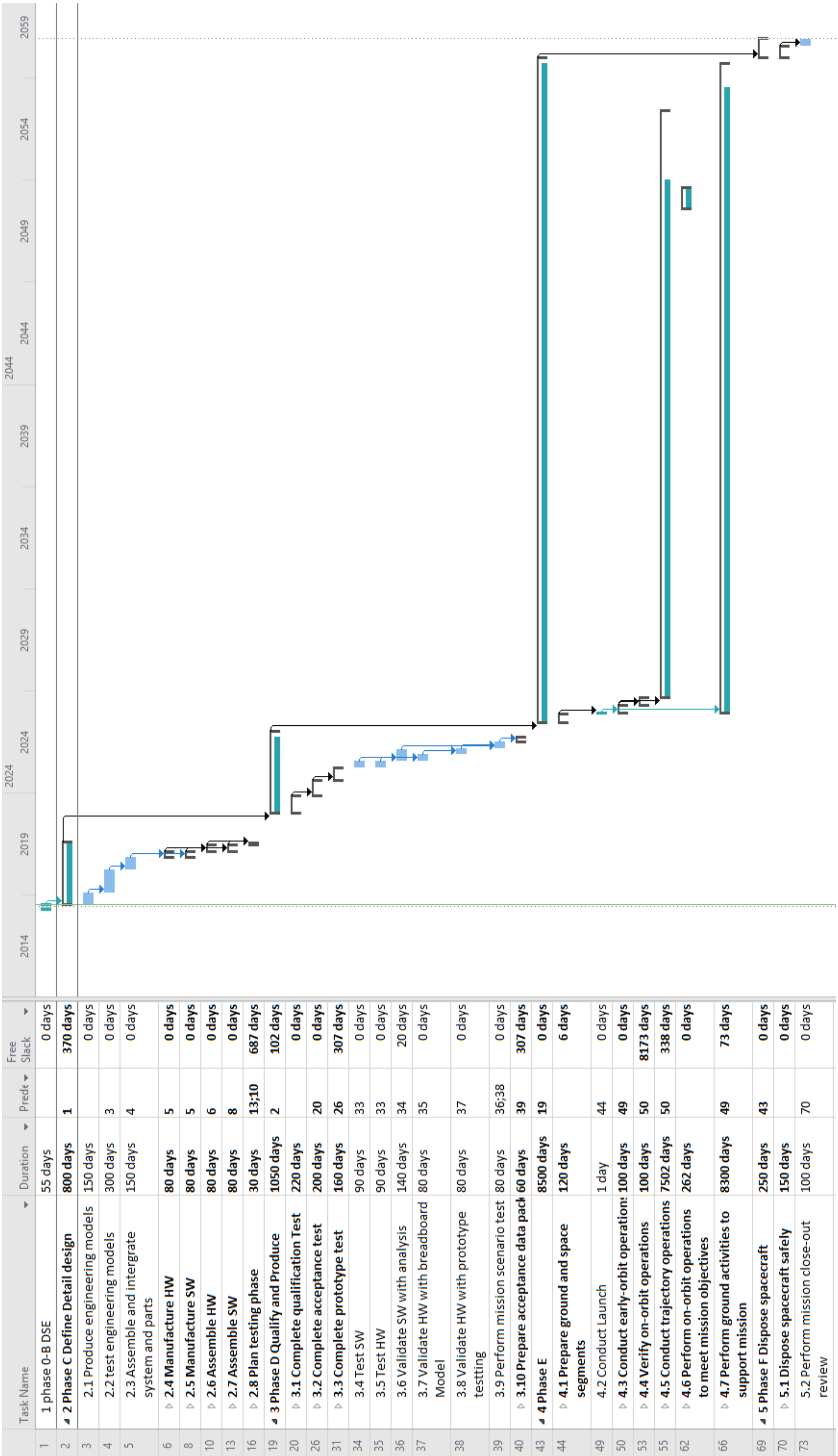

Figure 21.2: Orpheus project Gantt chart

22 Conclusion and Recommendations

Based on the design challenge set by the American Institute of Aeronautics and Astronautics and following up on NASA's New Horizons fly-by of Pluto, the Orpheus spacecraft is designed to orbit the Pluto-Charon system and gather scientific data from close proximity. In particular, it is intended to investigate whether Pluto or Charon have a magnetic field, to determine their atmospheric cycles, and the origin and behaviour of the (possible) internal oceans. The greatest challenge is posed by minimising both the amount of energy required for the transfer to the system and the time required to get there.

The initial key specifications of the spacecraft can be found in Table 22.1.

Table 22.1: Spacecraft specifications

Parameter	Value	Unit
Dry mass	874	kg
Wet mass	2016	kg
Max. thrust	623	N
Peak power	670	W
Total ΔV mission	14.4	km/s
Time to get to Pluto from Earth	24	years
Max. rotational rate	5	rpm
Max. data rate	5.3	kbps
Max. data storage	2x50	GB
High gain antenna diameter	4.5	m

Table 22.2: Keplerian parameters of the target orbits.

Keplerian Parameters	Pluto	Charon	Unit
Semi-major axis	1588	1000	km
Eccentricity	0.18	0.05	-
Inclination	77	65	deg
Argument of periapsis	0	0	deg
Longitude of ascending node (type I)	190-250	10-70	deg
Longitude of ascending node (type II)	30-65	210	deg

The use of 3 GPHS-RTGs makes it possible to power the spacecraft for a total mission lifetime of at least 25 years. In addition, a hybrid propulsion system, consisting of a chemical bi-propellant stage (Aerojet AMBR) and two electric ion engines (NASA NEXT) is used, resulting in an overall propellant mass of 1142 kg.

Orpheus travels from Earth to Pluto over a period of 24 years, performing a gravity assist at Jupiter. The trajectory, determined by a Lambert solver, is optimised by a genetic algorithm search and verified with the mission analysis tool GMAT. After a 12 year slowdown manoeuvre of the ion propulsion system, the bi-propellant high thrust propulsion systems brings Orpheus into its Pluto target orbit. Further analysis is required on this phase of the mission, as only high impulse analysis was conducted in the context of the DSE.

The chosen target orbit parameters around Pluto and Charon are presented in Table 22.2. Orbital specifications are selected to fulfil the scientific requirement to map at least 95% of the dwarf planet and its moon, achieve a stable orbit to be able to stay in the system for at least 1 year, and minimise the required ΔV to transfer from Pluto to Charon. The longitude of ascending node is determined such that Orpheus is constantly able to see Earth, making it easier to transmit data. Orpheus maps the surfaces in ultra-violet, infrared and visible light and additionally gathers data about Pluto's and Charon's time variability, as well as their magnetic- and gravity-field.

Transmission of the scientific data is achieved by using a high gain antenna with a diameter of 4.5 m, allowing a data rate of 5.3 kbps, five times higher than New Horizons [121]. Accurate pointing of the antenna is obtained by an attitude system containing 4 reaction wheels. Additionally, twelve 20 N chemical mono-propellant thruster are present for orbit maintenance, momentum dumping and spin-up/de-spin manoeuvres of the spacecraft. A low gain antenna is included for redundancy.

To prevent contamination of the celestial bodies, Orpheus performs an end of life manoeuvre, putting the spacecraft in a heliocentric orbit. Therefore the mission complies with the policy imposed by the Committee of Space Research (COSPAR).

The next step is manufacturing, verifying and validating the systems. During this phase it is recommended to ensure good documentation and outstanding systems engineering, to be able to trace back requirements and methods used. For future deep space missions, a system worth investigating further is the NASA nuclear fission reactor [97]. Besides this, the research into green propellant is suggested. This is the next step in making space missions more sustainable. For the trajectory verification done with GMAT it is recommended to evaluate further how to interface GMAT and Python in an efficient way in order to facilitate the optimisation of the orbital path. This prevents schedule delays and makes it easier for third parties to work with the software and codes generated by the team. The team further advises to create a list of lessons learned from the project design, after phase D (qualification and production). In addition, it encourages future Design Synthesis Exercise students to believe in their knowledge and have courage to be innovative in their design.

Although the mission requirements imposed unprecedented challenges on the team, the revolutionary solutions employed (the use of composite materials and ion propulsion) managed to produce a feasible design. This shows that such a mission should be on the agenda of the scientific community in the near future.

Bibliography

[1] C. C. Addison and B. C. Smith. The Viscosity of Dinitrogen Tetroxide and its Binary Mixtures with Organic Solvents. *Journal of the Chemical Society*, pages 1783–1788, 1960.

[2] R.C. Ahlert, G.L. Bauerle, and J.V. Lecce. Density and Viscosity of Anhydrous Hydrazine at Elevated Temperatures. *Journal of Chemical and Engineering Data*, 7(1):158–160, 1962.

[3] Ariane Space. Ariane 5 user's manual, 2016.

[4] B. Coppin. *Artificial Intelligence Illuminated*. Jones and Bartlett Publishers, Boston, 2004.

[5] Richard H. Battin. *Introduction to the Mathematics and Methods of Astrodynamics*. AIAA, 2000.

[6] A.B. Bauer. Automating the Pluto Experience: An Examination of the New Horizons Autonomous Operations Subsystem. In *IEEE Aerospace Conference Proceedings*. IEEE, 2007. DOI: 10.1109/AERO.2007.352645.

[7] B.A. Bauer. Lights-Out Scenario Testing for the New Horizons Autonomous Operations Subsystem. pages 1–8. 2008 IEEE Aerospace Conference, 2008. DOI:10.1109/AERO.2008.4526485.

[8] F. Bellucci. Galvanic Corrosion between Nonmetallic Composites and Metals II. Effect of Area Ratio and Environmental Degradation. *Corrosion Journal*, 48(4):281–291, 1992. DOI: 10.5006/1.3315934.

[9] R.S. Bokulic. A Decade of Advancements in Spacecraft Communication Technology at APL. *Johns Hopkins APL Technical Digest,*, 25(4):286–294, 2004.

[10] T. Bondo, R. Walker, and A. Willig et al. Preliminary Design of an Advanced Mission to Pluto. Technical report, ESA, 2004.

[11] A. Brekke. *Physics of the Upper Polar Atmosphere*. Springer-Verlag GmbH, Berlin Heidelberg, 2013.

[12] D. Brennan. *Sustainable Process Engineering: Concepts, Strategies, Evaluation and Implementation*. Pan Stanford, 1st edition, 2013.

[13] C.D. Brown. *Spacecraft Propulsion*. AIAA, 1996.

[14] C.D. Brown. *Elements of Spacecraft Design*. AIAA, 1st edition, 2002.

[15] G. Carr and A. Ging. The Cassini Power System Performance over the Last Decade. *5th International Energy Conversion Engineering Conference and Exhibit (IECEC)*, 2007.

[16] V. A. Chobotov. *Orbital Mechanics*. AIAA, third edition, 2002.

[17] Q.P. Chu. Spacecraft Attitude Dynamics and Control AE4313 course notes No. 2 Part 1. Presentation, 2017.

[18] T. Coffee. The Future of Integrated Concurrent Engineering in Spacecraft Design. Technical report, Massachusetts Institute of Technology, 2006.

[19] Sierra Nevada Corporation. Space Technologies Product Catalog. Media Kit, 2015.

[20] H. Curtis. *Orbital Mechanics for Engineering Students*. Elsevier, Embry-Riddle Aeronautical University, Florida, 2005.

[21] D. Byron et al. *Statistical Orbit Determination*. Academic Press, Burlington, 2004. DOI: 10.1016/B978-012683630-1/50021-7.

[22] C. Darwin. *Origin Of Species*. Castle, 2004.

[23] A. Debus. Planetary Protection Requirements. *CNES*, 2002. Reference: RNC-CNES-R-14.

[24] Delkin Devices. Secure Digital Cards Data Sheet, 2018.

[25] Dave Doody. *Deep Spacecraft, an Overview of Interplanetary Flight*. Springer and Praxis Publishing, Chichester, UK, 2013.

[26] The Economist. Interplanetary Settlement. The World is not Enough. 2016.

[27] A. Badea et al. AE3200 Design Synthesis Exercise Midterm Report. Technical report, 2018.

[28] A. Badea et al. Baseline Report Version 1.1. Technical report, Delft University of Technology, 2018.

[29] Anwar et. al. Outgassing Effect on Spacecraft Structure Materials. 2:34–38, 2015.

[30] A.T. Tai et al. On-board Preventive Maintenance for Long-life Deep-space Missions: a Model-based Analysis. *Computer Performance and Dependability Symposium, 1998. IPDS '98. Proceedings. IEEE International*, pages 196–205, 1998. DOI: 10.1109/IPDS.1998.707722.

[31] B.L. Davis et al. Big Deployables in Small Satellites. In *28th Annual AIAA/USU Conference on Small Satellites*, 2014. SSC14 VII-4.

[32] C. C. DeBoy et. al. The RF Telecommunications System for the New Horizons Mission to Pluto. 3:1478, 2004. 10.1109/AERO.2004.1367922.

[33] D. Auslander et al. Instrument Boom Mechanism on the THEMIS Satellite, magnetometer, radial wire and axial boom. *Space Science Review*, 2008. DOI: 10.1007/s11214-008-9386-4.

[34] D. Eakman et al. Small Spacecraft Power and Thermal Subsystems. NASA Contractor Report 195029, McDonnell Douglas Aerospace, National Aeronautics and Space Administration Langley Research Center Hampton, Virginia 23681-0001, 1994.

[35] D. J. McComas et al. Solar Wind Electron Proton Alpha Monitor (SWEPAM) for the Advanced Composition Explorer. *Space Science Reviews*, 86:563–612, 1998.

[36] D. Pasini et al. Structural efficiency maps for beams subjected to bending. *Proceedings of the Institution of Mechanical Engineers*, L:207–220, 2003.

[37] D.D. Morabito et al. *Cassini Downlink Ka-Band Carrier Signal Analysis*. IPN Progress Report 42-208. Jet Propulsion Laboratory, 2017.

[38] D.J. Anderson et al. Status and Mission Applicability of NASA's In-Space Propulsion Technology Project. *45th AIAA/ASME/SAE/ASEE Joint Propulsion Conference & Exhibit*, 2009.

[39] D.W. Scott et al. Hydrazine: Heat Capacity, Heats of Fusion and Vaporization, Vapor Pressure, Entropy and Thermodynamic Functions. *J. Am. Chem. Soc.*, 71(7):2293–2297, 1949.

[40] E.D. Schaefer et al. Spacecraft Packaging. Technical Report 1, John Hopkins Apl, 2008.

[41] G. Chin et al. Lunar Reconnaissance Orbiter Overview: The Instrument Suite and Mission. *Springer Science*, 110:1–36, 2007.

[42] G. Weaver et. al. Enhancing the Art of Space Operations-Progress in JHU/APL Ultra-Stable Oscillator Capabilities. 2008.

[43] G.H. Fountain et al. The New Horizons Spacecraft. *Space Science Review*, 140:23–47, 2008. DOI: 10.1007/s11214-008-9374-8.

[44] G.L. Bennett et al. Mission of Daring: The General-Purpose Heat Source Radioisotope Thermoelectric Generator. *4th International Energy Conversion Engineering Conference and Exhibit (IECEC)*, 2006.

[45] G.L. Bennett et al. Mission of Daring: The General-Purpose Heat Source Radioisotope Thermoelectric Generator. In *4th International Energy Conversion Engineering Conference and Exhibit (IECEC)*. AIAA, 2006.

[46] H.A. Weaver et al. Overview of the New Horizons Science Payload. *Space Science Review*, 140:75–91, 2008. DOI: 10.1007/s11214-008-9376-6.

[47] J. Dever et al. Degradation of Spacecraft Materials. *Handbook of Degradation of Materials*, 2011.

[48] J. Suchail et al. Maxwell, the ESA-ESTEC New Large EMC Facility. Technical report, 2004.

[49] J. Wu et al. Surface Crack Detection for Carbon Fiber Reinforced Plastic (CFRP) Materials Using Pulsed Eddy Current Testing. *IEEE Far East Forum on Nondestructive Evaluation/Testing*, 2014.

[50] J.E. Werner et al. Cost Comparison in 2015 Dollars for Radioisotope Power Systems Cassini and Mars Science Laboratory, 2016.

[51] J.F. Zakrajsek et al. Radioisotope Power Systems Program Status and Expectations. 2017. DOI = 10.2514/6.2017-4609.

[52] J.W. Dankanich et al. Advanced Xenon Feed System (AXFS) Development and Hot-fire Testing. *45th AIAA/ASME/SAE/ASEE Joint Propulsion Conference & Exhibit*, 2009.

[53] L.J. Hastings et al. Analytical Modeling and Test Correlation of Variable Density Multilayer Insulation for Cryogenic Storage. *Marshall Space Flight Center*, 2004.

[54] M.W. Crofton et al. Characterization of the NASA NEXT Thruster. *45th AIAA/ASME/SAE/ASEE Joint Propulsion Conference & Exhibit*, 2003.

[55] M.W Leeds et al. Development of the Cassini Spacecraft Propulsion System. *AIAA*, 1996.

[56] P. Li et al. Compatibility of Hydrazine and EPDM Rubber Containing Polybutadiene Coagent. *Journal of Elastomers & Plastics*, 46(6):499–513, 2014.

[57] R. Clark et al. On The Correlation of Mechanical and Physical Properties of 7075-T6 Al Alloy. *Engineering Failure Analysis*, 12(4):520 – 526, 2005. DOI: 10.1016/j.engfailanal.2004.09.005.

[58] R. Fimmel et al. Pioneer odyssey encounter with a giant. *SP-349*, 1974. Washington, D.C.

[59] R. Masse et al. GPIM AF-M315E Propulsion System. *51st AIAA/SAE/ASEE Joint Propulsion Conference*, 2015. DOI: 10.2514/6.2015-3753.

[60] R.E. Gold et al. The MESSENGER Mission to Mercury: Scientific Payload. *Planetary and Space Science*, 2001.

[61] R.J. Hamann et al. AE3-S01 - Systems Engineering & Technical Management. 2006.

[62] S. Guarro et al. The Cassini mission risk assessment framework and application techniques. *Reliability Engineering and System Safety*, 49(1905):293–302, 1995.

[63] S. Hamilton et al. New Horizons Hibernation Ooerations: It takes a Lot of Work to Sleep. *2015 IEEE Aerospace Conference*, pages 1–15, 2015. DOI: 10.1109/AERO.2015.7119154.

[64] S. Hamilton et al. New Horizons Hibernation Operations: It Takes A Lot Of Work To Sleep. pages 1–15, 2015. DOI:10.1109/AERO.2015.7119154.

[65] S. Henderson et al. Performance Results for the Advanced Materials Bipropellant Rocket (AMBR) Engine. *46th AIAA/ASME/SAE/ASEE Joint Propulsion Conference & Exhibit*, 2010.

[66] S.A. Stern et al. The Pluto system: Initial results from its exploration by New Horizons. *Science*, 350(6258), 2015. DOI: 10.1126/science.aad1815.

[67] S.A. Stern et al. The Pluto System After New Horizons. *Annual Reviews of Astronomy and Astrophysics*, 2018. DOI: arXiv:1712.05669.

[68] Shenand et al. Optimal Two-Impulse Rendezvous Using Multiple-Revolution Lambert Solutions. 26:50–61, 2003.

[69] S.J. Bolton et al. The Juno Mission. *Springer Science*, 2017.

[70] T. Uhlig et al. *Spacecraft Operations*. Springer, 2015. DOI 10.1007/978-3-7091-1803-0.

[71] W. Tam et. al. Low Cost Derivative Tanks for Spacecraft and Launch Vehicles. *35th AIAA/ASME/SAE/ASEE Joint Propulsion Conference and Exhibit*, 1999.

[72] W.K. Belvin et al. Advanced Deployable Structural Systems for Small Satellites. 2016.

[73] Xun Zhu et al. The Density and Thermal Structure of Pluto's Atmosphere and Associated Escape Processes and Rates. *Icarus*, 228:301 – 314, 2014. DOI: 10.1016/j.icarus.2013.10.011.

[74] Y. Zhang et al. The Imaging Stability Enhancement of Optical Payload Using Multiple Vibration Isolation Platforms. 21, 2013.

[75] V. Chandelier et.al. New Miniature Ultra-Stable Oscillators. 1:383–388 vol.1, 1999. DOI: 10.1109/FREQ.1999.840787.

[76] European Space Agency. Philosophy for Science Assessment Studies, 2012.

[77] European Cooperation for Space Standardisation. Space Project Management, Project Planning and Implementation. Technical report, Noordwijk, The Netherlands, 2009. ECSS-M-ST-10C Rev. 1.

[78] P. Fortescue, J. Stark, and G. Swinerd. *Spacecraft Systems Engineering*. Wiley, third edition, 2003.

[79] E. Gill. Systems engineering and aerospace design, verification & validation for spacecraft propulsion. University Lecture, 2018.

[80] E. Gill. Systems Engineering and Aerospace Design, Verification and Validation for the Attitude and Orbit Control System. University Lecture, 2018.

[81] E. Gill. Systems engineering methods. University Lecture, 2018.

[82] D.G. Gilmore. *Spacecraft Thermal Control Handbook, Volume 1 - Fundamental Technologies*. AIAA/Aerospace Press, second edition, 2002.

[83] Granta. CES 2010 EduPack: Material and Process Selection Charts, 2010.

[84] C.D Griffin. Vibration Testing of the Pluto/New Horizons Radioisotope Thermoelectric Generator. *4th International Energy Conversion Engineering Conference*, 2006.

[85] H. Curtis. *Orbital Mechanics for Engineering Students*. Butterworth-Heinemann, Amsterdam, 2010. p359 - 397.

[86] H. Curtis. *Orbital mechanics for engineering students*. Elsevier, 3rd edition, 2014.

[87] C.Y. Han and J.M. Choi. Thermal Analysis of Spacecraft Propulsion System and its Validation. *KSME International Journal*, 18(5):847–856, 2004.

[88] C. B. Haskins and W. P. Millard. X-band Digital Receiver For The New Horizons Spacecraft. 3:1488 Vol.3, 2004. DOI: 10.1109/AERO.2004.1367923.

[89] R.L. Heacock. The voyager spacecraft. *Proceedings of the Institution of Mechanical Engineers*, 194, 1980.

[90] R.J.G. Hermsen. Cryogenic Propellant Tank Pressurization. Master's thesis, Delft University of Technology, 2017.

[91] D. Huzel and D. Huang. *Flow Control Balancing Orifices*. Fives North American Combustion, Inc, 1992.

[92] I.E. Idelchik and E. Fried. *Handbook of Hydraulic Resistance*. Israel Program for Scientific Translations Ltd., second edition, 1966.

[93] L. Iess, S. Asmar, and P. Tortora. MORE: An Advanced Tracking Experiment for the Exploration of Mercury with the Mission BepiColombo. *Acta Astronautica*, 65:666 – 675, 2009.

[94] Dario Izzo. Revisiting lambert's problem. *Celestial Mechanics and Dynamical Astronomy*, 121(1):1–15, 2015. DOI: 10.1007/s10569-014-9587-y.

[95] R.D. Karam. *Satellite Thermal Control for Systems Engineers*, volume 181. AIAA, 1998.

[96] V. P. Koutras and A. N. Platis. Applying Software Rejuvenation in a Two Node Cluster System for High Availability. *2006 International Conference on Dependability of Computer Systems*, pages 175–182, 2006. DOI: 10.1109/DEPCOS-RELCOMEX.2006.7.

[97] D. Poston L. Mason, M. Gibson. Kilowatt-Class Fission Power Systems for Science and Human Precursor Missions. *NASA*, 2013.

[98] Jet Propulsion Laboratory. Juno telecommunications. *DESCANSO Design and Performance Summary Series*, 16, 2012.

[99] K. Lindstrom. *Draft Environmental Impact Statement for the New Horizons Mission*. NASA, 2005.

[100] James M. Longuski and Steve N. Williams. Automated Design of Gravity-assist Trajectories to Mars and the Outer Planets. *Celestial Mechanics and Dynamical Astronomy*, 52(3):207–220, 1991. DOI: 10.1007/bf00048484.

[101] A. M. Ismail M. H. Abd-El Salam. Electrical Conductivity and Electric Modulus of Stable Kevlar Fiber Loaded HAF/NBR Rubber Composite. *Wiley Online Library*, 2011. DOI: 10.1002/app.34620.

[102] R.D. McCarty, H.U. Steurer, and C.M. Daily. The Thermodynamic Properties of Nitrogen Tetroxide, 1986.

[103] P. McMahon, H.-J. Jung, and J. Edwards. Swarm Deployable Boom Assembly (DBA) Development of a Deployable Magnetometer for the SWARM Spacecraft. In *15th European Space Mechanisms & Tribology Symposium*, 2013.

[104] U. Meier. Strengthening of Structures Using Carbon Fibre/Epoxy Composites. *Construction and Building Materials*, 09:341–351, 1995.

[105] J. Melman. *Trajectory Optimization for a Mission to Neptune and Triton*. Master's Thesis, TU Delft, 2007.

[106] P. Messidoro, M. Ballesio, and J.P. Vessaz. IRIS Thermal Balance Test Within ESTEC LSS. In *15th Space Simulation Conference Support the Highway to Space through Testing*, pages 253–267, 1988.

[107] R.N. Miyake. Spacecraft Design Thermal Control Subsystem. University Lecture, 2008.

[108] United Nations. Space Debris Mitigation Guidelines of the Committee on the Peaceful Uses of Outer Space. 2010.

[109] B. Nufer. Hypergolic Propellants: the Handling Hazards and Lessons Learned From Use. Technical report, National Aeronautics and Space Administration, 2018.

[110] X. Olaskoaga and J.A. Andión. Solar Orbiter Instrument Boom Subsystem. In *17th European Space Mechanisms and Tribology Symposium*, 2017.

[111] Omnidea-RTG. Space Propulsion Components Product Catalogue, 2016.

[112] Orbital ATK. ATK Space Propulsion Products Catalog, 2008.

[113] G K. Ottman and C B. Hersman. The Pluto-New Horizons RTG and Power System Early Mission Performance. *AIAA*, (4029), 2006.

[114] J.L Ridihalgh P. EOGERS. Cost-Effective Radioisotope Thermoelectric Generator Designs involving Cm-244 and Pu-238 Heat Sources. *AIAA*, 11(10), 1974.

[115] T.J. Patrick. Outgassing and the Choice of Materials For Space Instrumentation. *Vacuum*, 23(11):411 – 413, 1973. DOI: 10.1016/0042-207X(73)92531-1.

[116] M. M. Peet. Spacecraft Dynamics and Control. Arizona State University Lecture Slides, 2009.

[117] E. Price and D.P. Woodruff. Applications of the Shannon-Hartley Theorem to Data Streams and Sparse Recovery. *2012 IEEE International Symposium on Information Theory Proceedings*, pages 2446–2450, 2012.

[118] A. Ptak and K. Foundy. Real-time Spacecraft Simulation and Hardware-in-the-loop Testing. pages 230–236, 1998. DOI: 10.1109/RTTAS.1998.683207.

[119] Defense Quality and Standardization Office. Performance Specification Propellant, Hydrazine. Technical Report 925-7847, Defense Quality and Standardization Office, 1014 Billy Mitchell 1 Blvd STE 1 Kelly AFB TX 78241-5603, 1989.

[120] H. Richter and D. Schmidt. *Rohrhydraulik: Ein Handbuch zur praktischen Strömungsberechnung*. Springer, fifth edition, 1971.

[121] C.T. Russell. *New Horizons: Reconnaissance of the Pluto-Charon System and the Kuiper Belt*. Springer, first edition, 2009.

[122] Stuart Russell and Peter Norvig. *Artificial Intelligence: A Modern Approach (3rd Edition)*. Pearson, 2009.

[123] Amir Salaree. Pluto. *EARTH-450, Satellites of Saturn & Jupiter*, 2013.

[124] R.M.H. Schlijper. *The Gravity-Assist, Literature Report*. Faculty of Aerospace Engineering, TU Delft, 2002.

[125] R. Schulz and J. Benkhoff. BepiColombo: Payload and Mission Updates. *Advances in Space Research*, 38:572–577, 2006.

[126] F. Schwartz. X band TWTA Specification, 2011. Ref: EXM-OM-EQP-AF-0380.

[127] ECSS Secretariat. Space Engineering: Radio Frequency and Modulation, 2011. ECSS-E-ST-50-05C Rev. 2.

[128] J. Sinke. AE3211-II Production of Aerospace Systems . University Lecture, 2018.

[129] RUAG Space. Next Generation On Board Computer, 2017. Document ID: R-COMM-NOT-1238507-RSE.

[130] SpaceX. Falcon 9 Launch Vehicle: Payload User's Guide, 2015.

[131] F. Spoto. The ENVISAT Satellite and its Integration. 2001.

[132] S.A. Stern. The Pluto-Charon System. *Annual review of astronomy and astrophysics*, 30:185–233, 1992.

[133] Nathan J. Strange and James M. Longuski. Graphical Method for Gravity-Assist Trajectory Design. *Journal of Spacecraft and Rockets*, 39(1):9–16, 2002. DOI: 10.2514/2.3800.

[134] G. Sutton and O. Biblarz. *Rocket Propulsion Elements*. John Wiley & Sons, seventh edition, 2001.

[135] M. Tafazoli. A Study of On-orbit Spacecraft Failures. *Acta Astronautica*, 64:195–205, 2009.

[136] J. Taylor. *Deep Space Communications*. Jet Propulsion Laboratory, 2014.

[137] T.S. Taylor. *Introduction to Rocket Science and Engineering*. Taylor & Francis Inc, second edition, 2017.

[138] The GMAT Development Team. General Mission Analysis Tool (GMAT): User Guide, 2017.

[139] M.A. Toral. Payload Performance of TDRS KL and Future Services, 2017. Presentation.

[140] Lin Tze Tan and Sergio Pellegrino. Ultra Thin Deployable Reflector Antennas. 45th AIAA/ASME/ASCE/AHS/ASC Structures, Structural Dynamics & Materials Conference, 2004.

[141] P.E. Uney and D.A. Fester. Material Compatibility with Space Storable Propellants. Design guidebook, Jet Propulsion Laboratory, 1972.

[142] United Launch Alliance. Delta iv launch services user's guide, 2013.

[143] Vacco. Low Pressure Latch Valves. Company Product Brochure, 2004.

[144] David A. Vallado. *Fundamentals of Astrodynamics and Applications*. Primis, 1997.

[145] D.A. Vaughan. Gimbal Development for the NEXT Ion Propulsion System. *41st AIAA/ASME/SAE/ASEE Joint Propulsion*, 2005.

[146] C.B. Vining and G.L. Bennett. Power for Science and Exploration: Upgrading the General-Purpose Heat Source Radioisotope Thermoelectric Generator (GPHS-RTG). *46th AIAA/ASME/SAE/ASEE Joint Propulsion Conference & Exhibit*, 2010.

[147] H.A. Weaver, W.C. Gibson, and M.B. Tapley at al. Overview of the New Horizons Science Payload. *Space Science Review*, 140:75–91, 2008.

[148] J.R. Wertz, D.F.Everett, and J.J. Puschell. *Space Mission Analysis and Design, The New SMAD*. Space Technology Series. Microcosm Press, 1st edition, 2011.

[149] J.R. Wertz and W.J. Larson. *Space Mission Analysis and Design*. Space Technology Series. Microcosm Press, 3rd edition, 1999.

[150] B. Wie. *Space Vehicles and Control*. American Institute of Aeronautics and Astronautics, Inc., 1998.

[151] M. Williamson. Spacecraft Thermal Design. *Physics in Technology*, 18:120–127, 1987.

[152] A. Yuhas. The New Space Race: How Billionaires Launched the Next Era of Exploration. 2018.

[153] B.T.C. Zandbergen. *Aerospace Design & Systems Engineering Elements I, Part: Spacecraft (Bus) Design and Sizing*. Delft University of Technology, Faculty of Aerospace Engineering, 2015.

[154] B.T.C. Zandbergen. *Thermal Rocket Propulsion*. Delft University of Technology, second edition, 2017.

A: Constraint Satisfaction Problem (CSP)

Variables (X)

1) *Planetary nodes*: The set of planetary bodies that interact with the spacecraft during the interplanetary trajectory. This includes the departure and rendezvous body as p_0 and p_{N+1} respectively.	$P = \{p_0, p_1, ..., p_N, p_{N+1} \mid N \in \mathbb{Z},\ N > 0\}$
2) *Interplanetary legs*: Sequence of duration's describing the time of flight between each planetary node's periapsis manoeuvre (departure, powered gravity assist or capture).	$L_i = \{l_1, l_2, ..., l_N, l_{N+1} \mid N \in \mathbb{Z},\ N > 0\}$
3) *Planetary legs*: Sequence of duration's describing the time of flight within the spheres of influence of each planetary node.	$L_p = \{l_1, l_2, ..., l_{N+1}, l_{N+2} \mid N \in \mathbb{Z},\ N > 0\}$
4) *Delta-V impulses*: List of ΔV impulses at each planetary radius of periapsis (r_p), excluding the possibility of deep space manoeuvres (DSM).	$\Delta V = \{\Delta V_0, \Delta V_1, ..., \Delta V_N, \Delta V_{N+1} \mid N \in \mathbb{Z},\ N > 0\}$

Domains (D)

1) Potential planetary flybys	$D_p = \{Mercury, Venus, Earth, Mars, Jupiter, Saturn, Uranus, Neptune\}$
2) Launch day after 2025 1st of January	$D_l = \{1, 2, 3, ..., 9998, 9999\}[days]$
3) Duration of each interplanetary leg	$D_{ld} = \{1, 2, 3, ..., 9998, 9999\}[days]$

Constraints (C)

1) Constraints on flybys: no repeats, Earth is not the first flyby	$C_p =< P,\ p_i \neq p_{i+1},\ p_1 \neq Earth >$
2) Total duration of trajectory	$C_l =< L_i, L_p,\ \sum l_i < 24\ \ [years] >$